THE ROLE OF FREE-STREAM TURBULENCE ON HIGH PRESSURE TURBINE AERO-THERMAL STAGE INTERACTION

A Dissertation Presented

By

James Earl Kopriva

to

The Department of Mechanical and Industrial Engineering

in partial fulfillment of the requirements
for the degree of

Doctor of Philosophy

in the field of

Mechanical Engineering

Northeastern University
Boston, Massachusetts

March 2017

Abstract

Turbulence plays an important role on the aero-thermal performance of modern aircraft engine High Pressure Turbines (HPT). The role of the vane wake and passage turbulence on the downstream blade flow field is an important consideration for both performance and durability. Obtaining measurements to fully characterize the flow field can be challenging and costly in an experimental facility. Advances in Computational Fluid Dynamic (CFD) modeling and High Performance Computing (HPC) are providing opportunity to close these measurement gaps. In order for CFD to be adopted, methods need to be both accurate and efficient. Meshing approaches must also be able to resolve complex HPT geometry while maintaining quality adequate for scale-resolved simulations. Therefore, the accuracy of executing scale-resolved simulations with a second-order code on a mesh of prisms and tetrahedrals in Fluent is considered.

Before execution of the HPT computational study, a building block approach is taken to gain quantified predictive performance in the modeling approach as well as understanding limitations in lower computational cost modeling approaches. The predictive capability for Reynolds Averaged Navier Stokes (RANS), Hybrid Large Eddy Simulation (LES), and wall-resolved LES turbulence modeling approaches are first assessed for a cylinder in cross-flow at a Reynolds number of 2580. The flow condition and simple geometry facilitate a quick turn-around for modeling assessment before moving the HPT vane study at high Reynolds and Mach number conditions. Modeling approaches are then assessed relative to the experimental measurements of Arts and Rouvroit (1992) on a pitch-line HPT uncooled vane at high Mach and Reynolds numbers conditions with low (0-6%) free-stream turbulence. The current unstructured second-order LES approach agrees with experimental data and is found to be within the equivalent experimental uncertainty when compared to the structured high-ordered solver FDL3DI. The unstructured Hybrid LES aero-thermal predictions are found to be in close agreement with LES predictions and 4 times more computationally efficient.

A sliding mesh approach is then used to understand the complex HPT vane and blade stage aero-thermal interaction at 0 and 20% inlet turbulence. A HPT blade has been designed to pair with the uncooled vane of Arts and Rouvroit (1992) to evaluate the impact of passage turbulence and vane wake on the downstream blade boundary layer as well as wake formation and evolution. The learnings from the statistical 2D pitch-line stage simulations are applied to a 3D annular representation of the geometry including endwalls and blade tip clearance to demonstrate the impact of secondary flows on the overall aero-thermal performance. Compared to the 2D pitch-line predictions, the vane and blade overall mass average relative total pressure loss for the 3D geometry increases by 73 and 107%, respectively. The blade loss is shown to be largely driven by the formation of the tip vortex. Hybrid LES predictions show that by increasing stage inlet turbulence by 20% results in up to a 40% increase for the surface heat flux on the vane. However, the impact of stage inlet turbulence is found to be secondary compared to the periodic unsteadiness generated by the vane wake on the downstream blade surface heat transfer and mixing.

Acknowledgments

I would like to express my sincere gratitude to Dr. Gregory Laskowski, who has been a friend and mentor in industry and academia. Thank you for encouraging my continued comprehension of the applications, benefits, and limitations of computational fluid dynamics. This has promoted my understanding of the complex physics within a gas turbine and the capability to utilize CFD to enhance design. I am grateful for his time and contribution to my career growth as a researcher and engineer. I would also like to thank Dr. Reza Sheikhi for his support and encouragement. The completion of this work would not have been possible without his support in balancing academic, professional, and personal obligations. I am also grateful to the members of my doctoral committee, Professors Hameed Metghalchi and Professor Mehdi Abedi for their support.

I would like to thank to my colleagues and friends at the Computational Energy and Combustion Laboratory, Mehdi Safari, Fatemeh Hadi, and Ronak Ghandriz. I appreciate their encouragement and support during our time at NEU. I would also like to thank the many GE collaborators who provided insight, suggestions, and comments. Special thanks to Bhanu Reddy for technical insightful throughout the project. The LES and HLES pitch-line sliding mesh simulations were run on NCSA Blue Waters and I would like to thank the Private Sector Program and the Blue Waters sustained-petascale computing project at the National Center for Supercomputing Applications (NCSA). Blue Waters is supported by the National Science Foundation (award numbers OCI 07-25070 and ACI-1238993) and the state of Illinois.

Finally, I would like to thank my family for their constant support. I am extremely fortunate to have the persistent and unwavering support of my Mom, Dad, and brother Tom. My mother continuously provides the characterization of strength and selflessness. I am also privileged to have an amazing wife, Sarah, and children, Tyler and Payton. I appreciate their understanding and sacrifice of many nights and weekends to help me complete my work. I look forward to the additional time we will have together.

Dedicated to my remarkable wife Sarah and
children Tyler and Payton without whom
this work would not have been completed...ever

Contents

List of Figures

List of Tables

Chapter 1

Introduction

1.1 Motivation

Over 2.2 billion passengers are transported annually by aircraft, a vast majority of which are powered by jet engines based on turbofan technology. According to the United States Department of Transportation, US carriers consumed 10.3 billion gallons of fuel domestically and 5.9 billion gallons internationally in 2014. The current average fuel cost is approximately \$2/gallon [1, 2]. Therefore, technologies that can enable even a 0.1% Specific Fuel Consumption (SFC) savings can have on the order of a billion-dollar impact on the US economy while reducing carbon-based emissions.

Commercial aviation is projected to have robust growth over the next 20 years, where Boeing anticipates the size of the fleet growing by 58% [3, 4] equating to 21,000 airplanes by 2033. With this growth comes the broad-based desire to improve fuel efficiency and reduce the environmental impact of aircraft engines. Some examples of industry, government, and institutional collaboration are:

- FAA Continuous Lower Energy, Emissions, and Noise (CLEEN) program, which aims to reduce fuel burn by 33% [5].
- EU FACTOR 7 program that projects optimization of the combustor and gas turbine module can be worth up to 2% SFC, 1.5% reduction in weight, 3% reduction in cost, and 20% improved component life [6].

However, to achieve such technology improvements for aircraft engines requires better understanding of the flow physics and improved predictive aero-thermal performance. Gas turbines are equipped with a high-pressure turbine (HPT) and a low-pressure (or power) turbine (LPT). The HPT generally drives the compressor, while the LPT typically drives a propulsion device (for example, a propeller or fan). The LPT and HPT are exposed to different pressures, temperatures, and Reynolds numbers (Re) but they share similar aero-thermal challenges due to the strong interaction between the stationary vanes and rotating blades.

One of the primary challenges of characterizing the turbine module is the tremendous cost to build test facilities that operate at engine scale conditions. Detailed measurements are required to understand the underlying physics in order to identify an optimized, yet robust design. However, direct inter-stage measurements prove difficult to obtain. To compensate for the limited data sets, designers incorporate safety margins into their calculations to ensure adequate turbine performance and component life during operation [7, 8]. Recent advances in computational fluid dynamic (CFD) modeling have allowed the ability to bridge these measurement gaps. This has also led to a lower number of experimental rig tests and provides an opportunity for understanding the complex turbine physics, allowing for design optimization [9, 10, 11].

According to a recent publication by NASA, on the 2030 vision for CFD, the last decade has seen stagnation in simulation capabilities for the aerospace industry [9]. Even with the continuous reduction in computational costs, steady Reynolds-average Navier-Stokes (RANS) methods have remained the primary modeling choice. Advances in RANS modeling approaches have focused on larger meshes, more complex geometries, and more runs for design optimization or flow condition uncertainty [12]. RANS methods have seen success for fully turbulent attached flows [12, 13]; however, the well-known limitations of RANS methods for separated flows restrict their use to a limited design space [14]. More precisely, modeling challenges include smooth body separation for high-speed stall, low-speed high-lift, compressor stall, turbulence migration, and impact on momentum and enthalpy mixing through the HPT [15, 16, 17**?**

, 35, 9]. These examples require the accurate prediction of regions of wakes, flow separation, and/or boundary layer transition. Slotnick et al. [9] states the current most critical item and likely pacing item for 2030 is the ability to adequately predict turbulent flows with possible boundary layer transition and flow separation present. Fortunately, in the advent of supercomputing, Large Eddy Simulation (LES) can play a key role in maturing the physical understanding of these complex flow fields. The accuracy of LES makes it very attractive for targeted applications and assessment of lower computational cost turbulence modeling approaches such as RANS.

Although LES can accurately predict the desired flow regimes (wakes, flow separation, and boundary layer transition), industrial applications still require a lower computation cost approach. In order for RANS models to better capture boundary layer transition, purely empirical two equation transition models have been derived [18, 19, 20]. Each model requires a level of empiricism; therefore, the turbulence model is dependent on the data set used to calibrate it. Hybrid unsteady RANS/LES methods provide improved predictive capability for wakes and other regions of separated flows at a lower computational cost than LES. Hybrid models evoke RANS or wall modeled (WM) LES near the wall, lowering the grid requirement and therefore computational cost. This also allows for the use of RANS based transition models; however, the integration of transition modeling with hybrid models has not been well vetted [9]. The significant benefit of the hybrid models is the employment of LES in regions of separation for improved accuracy. It should be noted that for hybrid methods to be routinely used, a fluid RANS-to-LES transition in the boundary layer is required. Wall resolved LES can play a key role in assessing boundary layer transition regions for hybrid models and is addressed in this thesis.

Finally, given the complexity of typical turbine designs, a robust solver and meshing is required. Discretization schemes must be tolerant of localized poor mesh quality in regions of complex geometry, while at the same time be capable of delivering accurate results for Hybrid or wall resolved LES approaches. Also, modeling techniques must be robust enough to deliver converged solutions over a range of design conditions with minimal user intervention. Additionally, automated meshing for optimization is

becoming more common for complex design features where unstructured meshing is required [10, 11].

The present study takes an industrial HPT modeling approach using the commercial solver Fluent and unstructured meshing [21]. RANS, Hybrid LES (HLES), and LES approaches are first assessed to experimental measurement and higher fidelity numerical approaches (for example, structured meshing and higher-order solvers). LES serves as a benchmark for lower computational cost turbulence models where experimental measurements could not be obtained. Each modeling approach is assessed on its ability to capture the role of free-stream turbulence on boundary layer development and impact on wake formation, evolution, and decay. This understanding is a critical building block before extending the study to vane/blade stage interaction to understand the impact of periodic unsteadiness on the downstream blade. A downstream blade has been designed by the author and paired with the uncooled HPT vane of Arts and Rouvroit [22]. Therefore the current computational vane and downstream blade studies are anchored to the HPT vane experimental measurements of Arts and Rouvroit [22]. This also ensures numerical and measurement comparisons are first understood before exploring increasingly complex physics due to the coupled vane/blade interaction.

Before further discussion on the approach, a brief literature review of studies completed on the flow physics of interest is provided.

1.2 Review of Experimental & Numerical Studies

Turbulence plays an important role on the flow physics through the HPT yet its evolution through the stage is still poorly understood. Furthermore, achieving combustor level turbulence and length scales can be both challenging and costly in an experimental facility. Figure 1-1 shows an example of complex combustor and single stage HPT engine interface. Numerous experimental efforts have been undertaken to mimic the turbulence levels exiting a combustor. Barringer et al. [24] achieved intensity of 18% and non-dimensional integral length scale of 0.11 based on true chord

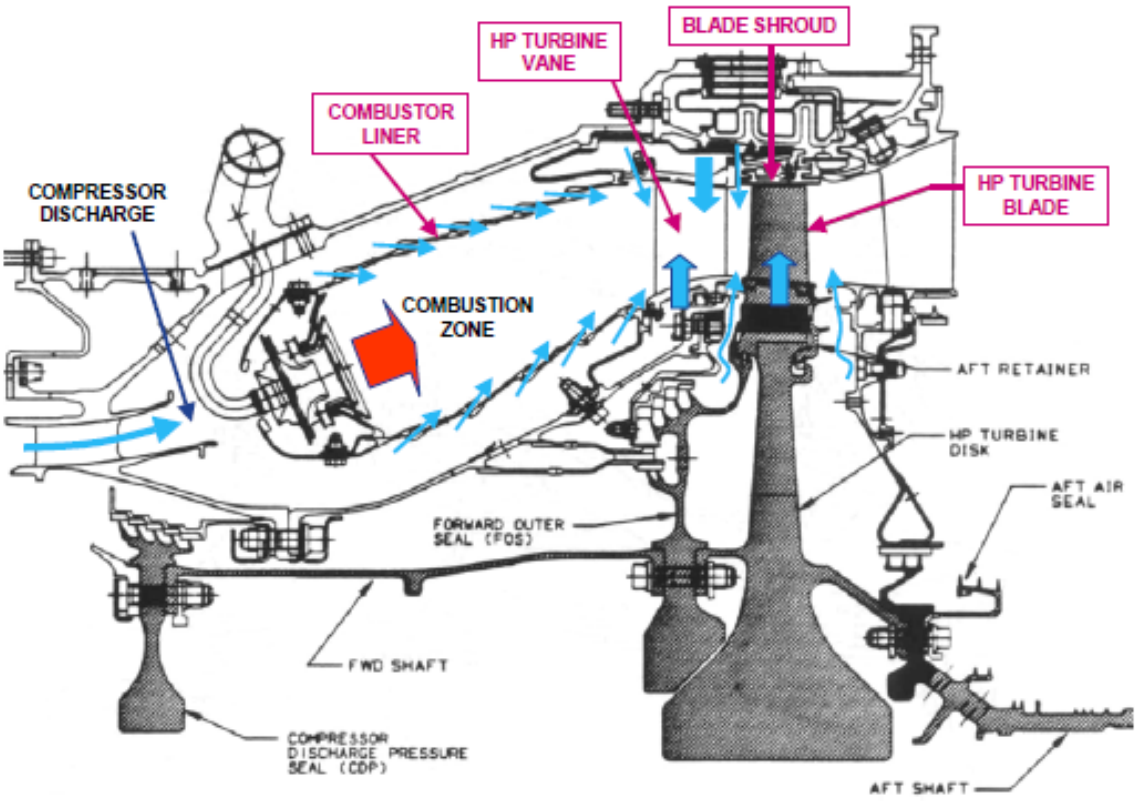

Figure 1-1. Combustor and a single stage HPT engine cross-section [23].

for the downstream vane with a combustor simulator and large jets. Giel et al. [25] achieved levels of 10% and non-dimensional length scale of 0.17 with an active grid. Polanka [26] reached levels of 20% with a passive bar array and large blockage. Thole et al. [27] achieved levels of 20% with a blown bar array with integral and dissipation length scale based on vane true chord of 0.09 and 0.21, respectively.

In general, the impact of free-stream turbulence for gas turbines has a pronounced effect on boundary layer (BL) development and resulting heat transfer. Other primary drivers for BL transition in HPT are elevated Reynolds numbers, pressure gradient, film cooling, and periodic-unsteady wake driven transition. Turbulent compared to laminar boundary layers typically result in 3-5 times greater surface heat transfer. When film cooling is introduced into a laminar boundary layer, Mayle [28] showed downstream heat transfer on the level of turbulent flow. Secondary effects on BL transition are surface roughness, curvature, compressibility, and heat transfer for

the HPT [28]. Furthermore, the BL state plays an important role in downstream wake mixing [29]. Rehder [30] demonstrated that the contribution of loss due to the BL represented up to 50% of the overall loss for a TE cooled transonic vane. A significant amount of experimental work has been done regarding HPT vane and blade uncooled and cooled trailing-edge (TE) designs and the impact on local heat transfer and downstream wake mixing. Sieverding and Heinemann [31] demonstrated that the fundamental frequency of large-scale vortex shedding downstream of a linear transonic turbine airfoil is a strong function of the BL state. The Strouhal number changed by nearly 80% based on the BL that formed the shear layers on the suction and pressure side surfaces at the TE. Cicatelli and Sieverding [32] investigated the impact of unsteady vortex shedding on the pressure side and suction side surfaces in the vicinity of a thick TE without cooling. The pressure fluctuations impacted the BL flow developing on these surfaces approaching the TE. The Root Mean Square (RMS) values of the fluctuations were dominated by the periodic component with a smaller contribution coming from the random component. Later, Sieverding et al.[33] attributed strong suction side pressure variations to downstream vortex shedding.

The impact of turbulence levels on HPT vane wall heat transfer continues to be a focus both experimentally and computationally. Arts and Rouvroit [34, 22] conducted a detailed study of uncooled transonic vane at exit Re of 5×10^5 - 2×10^6 and exit Mach numbers of 0.7 - 1.12 for turbulence intensities of 1%, 4% and 6%. The wall heat transfer measurements clearly demonstrated the free-stream condition impact on BL state (laminar, transitional, and turbulent). Arts and Rouvroit [34, 22] showed an increase in the heat transfer coefficient with increasing Re and inlet turbulence. For example, increasing the inlet turbulence from 1 to 6% at $Re = 1 \times 10^6$ raised the local heat transfer on the pressure and suction side by 2 and 4 times, respectively. Suction side heat transfer was found to be extremely sensitive due to BL transition location. For select cases, Bhaskaran [35] then Collado et al. [16] showed improved heat transfer prediction by better capturing the transitional BL with LES. Recently, DNS and LES was completed by Wheeler et al. [36] and Pichler et al [37] at a Re of 5×10^5 at 4% turbulence intensity.

On a different HPT vane geometry, Boyle et al. [14] experimentally investigated vane heat transfer coefficients with inlet turbulence levels up to 20%. Nix [38] showed increasing inlet turbulence increased the pressure side heat transfer by 50% while having less impact on the suction side surface near the throat. This suggests that strong acceleration reduced the local turbulence intensity near the suction side surface. Radomsky and Thole [39] measured BL profiles on a vane at turbulence intensities of 0.6% and 19%. Low turbulence levels resulted in laminar BL profiles along the pressure side surface. Elevated turbulence values yielded a mean profile that was laminar in nature with non-zero RMS velocity fluctuations, suggesting a transitional BL. Only on the suction side surface, at high levels of turbulence, was a true turbulent BL observed at a surface distance normalized to the true chord of $s/C = 1.2$ (just upstream of the TE). Dees et al. [40] demonstrated a transitional BL on the suction side surface by measuring wall heat transfer with and without a BL trip. Laskowski et al. [41] showed improved metal temperature predictions compared to measurements on the suction side surface for a conjugate heat transfer analysis by including a transition model. Clearly, the ability to accurately predict the impact of free-stream turbulence on BL state is critical in understanding the wall heat transfer and the formation of the downstream wake formation.

The effect of the upstream vane wake on blade heat transfer was studied by Ou and Han [42]. An upstream wake generator was used to generate the wakes and in general had a stronger impact on suction side heat transfer coefficients than on pressure side heat transfer coefficients. Although insightful, fully coupled high pressure turbine vane/blade interaction studies at engine relevant Mach and Re are challenging and costly. Didier et al. [43] conducted an experimental evaluation of an HPT vane/blade interaction at realistic engine conditions. Compared to a stationary blade subjected to high values of isotropic turbulence, they found that the coupled vane/blade interaction led to significantly higher leading-edge (LE) heat transfer due to periodic fluctuations of shocks and wakes. For the vane, inlet turbulence and unsteadiness play an important role in momentum and thermal migration through the turbine. Sharma et al. [44] showed the need to capture combustor like turbulence and the migration

of temperature distortion through the turbine. This was shown to be a first order impact on vane/blade temperature fields. Unsteady RANS (URANS) was also performed and highlighted the need for unsteady turbulence modeling to capture vane wake unsteadiness and thermal segregation impact on the downstream blade temperature. Recently, Wang et al. [45] reported a LES result for an HPT vane/blade sliding mesh simulation. The analysis was for an entire vane/blade including endwall and tip effects utilizing unstructured grids and wall-functions. The authors acknowledge future work is required on near-wall modeling and grid resolution, but the analysis demonstrated the capability of conducting such simulations.

1.3 Approach and Objective

This study presents CFD studies used to systematically understand the impact of turbulence and the uncoupled and coupled vane/blade interaction on BL development, resulting heat transfer, and downstream wake mixing in the absence of cooling. This research provides a better understanding of stage aero-thermal interaction which, in turn, can allow for improved engine performance. Before the computational study can be executed, a building block approach is taken to gain confidence in the modeling approach and understand limitations in lower computational cost modeling approaches. This is done by assessing computational cost and accuracy for RANS, HLES, and LES modeling approaches but also the accuracy of LES using an unstructured mesh of tetrahedral and prism elements with second-order spatial and temporal schemes. The need for the turbulence modeling, meshing, and solver studies are driven by the aerospace industry design phases described by Slotnick et al. [9]:

- Conceptual Design Phase: CFD can be used to guide design decisions for new concepts where no data is available. Studies must minimize time consuming optimization and deliver reasonably accurate results to guide the design decision. Therefore, there is a need to assess modeling approaches that can be afforded in this early phase of the design and their limitations.

- Preliminary & Detailed Design Phase: Multi-component and multi-physics simulations are performed leading to larger meshes and more complex geometries. RANS methods have remained the primary modeling choice given the detailed and larger, more costly computational domains. However, for targeted cases HLES or LES can often be afforded allowing for improved predictive accuracy. The challenge of complex HPT geometry still remains and detailed features must be captured (for example, blade tip geometry). Therefore, robust solver and meshing approaches need to be assessed to determine any compromises in accuracy.

Chapter 2 first provides details on the various turbulence models selected for this study. Next, Chapter 3 assesses each of the selected turbulence models to experimental measurements for the canonical case of a cylinder in cross-flow. A key motivation for the current work is to understand the capability of executing scale-resolved simulations with a second-order code on a mesh of prisms and tetrahedral. This study is the first step in demonstrating accurate scale-resolved results provides adequate mesh resolution and quality. Turbulence modeling approaches conducted on a cylinder in cross-flow under low Mach and Reynolds number conditions facilitated quick turnaround for modeling assessment. Robust and computationally cost effective modeling approaches are considered. The former is addressed by assessing scale resolving turbulence models with the commercial code Fluent on both structured and unstructured meshes. This helps address concerns of mesh topology on numerical dissipation and spatial order accuracy. The latter is addressed by assessing HLES models allowing for a computational cost reduction from wall resolved LES. In addition, deficiencies in the modeling assumptions for the low cost steady RANS approach are presented and quantified.

Chapter 5 compares predictions from RANS, HLES, and LES turbulence models to HPT vane experimental measurements performed by Arts and Rouvroit [34]. Lessons learned from the cylinder in cross-flow studies are applied to a pitch-line HPT uncooled vane that is representative of engine operating conditions. Modeling sensitivities are executed to build confidence in the approach at engine operating

conditions for RANS, HLES, and LES modeling approaches. This is done to assess each computational approach before moving to the expanded computational studies with elevated inlet turbulence in Chapter 6. Predictions are assessed relative to experimental measurement along with understanding computational cost and accuracy of RANS, HLES, and LES modeling approaches. The work described here has been presented in several conferences and publications [46, 47, 17, 48, 49, 50]. LES serves as a benchmark for lower computational cost turbulence models where measurements are not provided. The current work executes scale-resolved simulations with a second-order code on a mesh of prisms and tetrahedral elements. The selected meshing approach must be able to resolve complex HPT geometry while maintaining mesh quality adequate for scale-resolved simulations. The accuracy of unstructured meshing using the commercial code Fluent for LES is compared to a structured high-ordered solver as part of an ongoing effort at GE [48, 49, 50, 51, 37]. This approach is extrapolated to higher levels for free-stream turbulence to better understand the role of turbulence and Reynolds number impact on:

- Boundary layer development.
- Vane and blade wall heat flux.
- Development of downstream wake formation and decay.

Ultimately, the goal is a better understanding of the impact of turbulence on an 3D engine centerline stage design. Uncoupled and coupled vane/blade interaction studies are presented in Chapters 7 and 8. Chapter 7 focuses on stage interaction of the vane/blade for a pitch-line section. This is done to isolate the coupled interaction and impact on loss generating mechanisms (i.e., profile and wake mixing) and thermal loading in the absence of endwall secondary flows and rotational effects. HPT stage interactions are further isolated by the following stepwise study:

- Vane in absence of downstream blade interaction.
- Blade in absence of upstream vane interaction.
- Fully coupled vane/blade.

Focus is placed on identifying different mechanisms contributing to BL, heat transfer, and mixing losses at various levels of free-stream turbulence.

The selected vane geometry for this stage design is that of Arts and Rouvroit [34] shown in Figure 1-2. A downstream blade has been designed by the author to be coupled with the upstream uncooled vane where details of this design are provided in Appendix B. The blade has been designed with a blade/vane count of 2:1 to maintain computational domain periodicity. The simulations are focused on HPT engine scale conditions where the vane and blade Re, based on exit condition and chord, are 1×10^6 and 5×10^5, respectively. Inlet turbulence of up to 20% is pursued to address engine level conditions and the impact on BL development and wake formation.

In Chapter 8, endwalls and blade tip clearance is added to the stage design to assess secondary flow span-wise penetration and impact on the propagation of turbulence through an uncooled 3D engine centerline stage design. The vane of Arts and Rouvroit [34] is linearly stacked with the addition of endwall to the computational domain. The 50% span of the 3D vane and blade airfoil geometries are matched to the pitch-line case in Chapter 7. The inlet and exit boundary conditions at the pitch are also matched in order to evaluate the impact of the 3D flow field and rotational effects between the 3D and linear pitch-line geometries. Initial findings for Chapters 7 and 8 have been presented and published at the European Turbomachinery Conference [52].

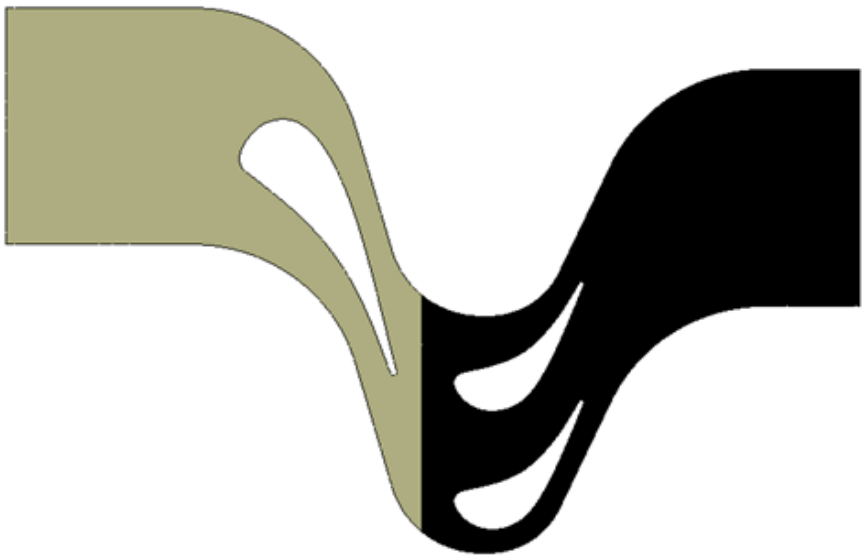

(a)

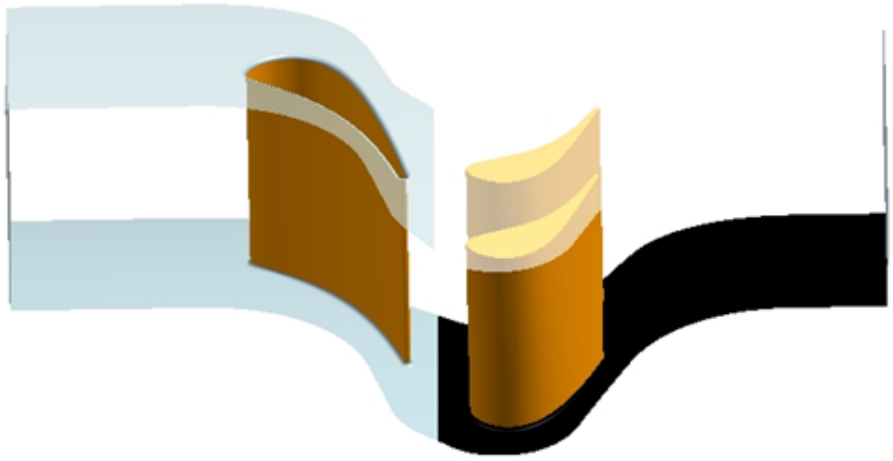

(b)

Figure 1-2. Stage design: (a) pitchline and (b) 3D annular.

Chapter 2

Modeling Overview

2.1 Governing Equations

Prior to the introducing turbulence models, a statement on the founding conservation equations of mass, momentum, and energy is required. The first governing equation is the continuity equation that governs the conservation of mass for a compressible fluid. Next, the compressible Navier-Stokes equations are invoked to describe the motion of a viscous fluid. These equations arise from applying Newton's second law to fluid motion, comprised of surface and body forces acting on the fluid element. Body forces act directly on the mass which includes gravity. The surface forces include the assumption that the stress in the fluid is the sum of a diffusing viscous term (proportional to the gradient of velocity) and a pressure. The energy conservation principle for a fluid volume can be formulated for a fluid element in a similar manner to the mass and momentum conservation equations where heat flux of thermal conduction, and internal heat generation are included. The unsteady compressible flow equations for mass, momentum, and energy are

$$\frac{\partial \rho}{\partial t} + \frac{\partial \rho U_i}{\partial x_i} = 0 \tag{2.1}$$

$$\frac{\partial \rho U_i}{\partial t} + \frac{\partial \rho U_i U_j}{\partial x_j} = -\frac{\partial p}{\partial x_i} + \frac{\partial \tau_{ij}}{\partial x_j} \tag{2.2}$$

$$\frac{\partial \rho E}{\partial t} + \frac{\partial \rho U_i E}{\partial x_i} = \rho \dot{q} - \frac{\partial U_i p}{\partial x_i} + \frac{\partial \tau_{ij} U_j}{\partial x_i} + \frac{\partial}{\partial x_i}\left(k \frac{\partial T}{\partial x_i}\right) \tag{2.3}$$

where k, ρ, U, p, and T are the thermal conductivity, density, velocity, pressure, and temperature of the fluid, respectively. Stress and the total energy term are defined as

$$\tau_{ij} = \mu\left(\frac{\partial U_i}{\partial x_j} + \frac{\partial U_j}{\partial x_i} - \frac{2}{3}\frac{\partial U_k}{\partial x_k}\delta_{ij}\right) \tag{2.4}$$

and

$$E = h - p/\rho + U_i U_i/2 \tag{2.5}$$

where μ and h are the kinematic viscosity and enthalpy, respectively. The equations are closed using the ideal gas equation

$$p = \rho R T. \tag{2.6}$$

where R is the ideal gas constant.

Next, Reynolds ($\phi = \overline{\phi} + \phi'$) and Favre ($\phi = \widetilde{\phi} + \phi"$) decompositions are applied to the governing equations to obtain the Favre-averaged Navier-Stokes equations. For a scalar quantity, ϕ' and $\overline{\phi}$ are the fluctuating and mean component. $\widetilde{\phi} = \overline{\rho\phi}/\overline{\rho}$ defines density weighted values for compressible flow and $\phi"$ is the density weighted fluctuating component. By introducing Reynolds decomposition for ρ and p and Favre decomposition for U, the following equation is derived from Equation(2.2)

$$\frac{\partial \overline{\rho}\widetilde{U}_i}{\partial t} + \frac{\partial \overline{\rho}\widetilde{U}_i\widetilde{U}_j}{\partial x_j} = -\frac{\partial \overline{p}}{\partial x_i} + \frac{\partial \overline{\tau_{ij}}}{\partial x_j} - \frac{\partial \tau_{ij}^{RANS}}{\partial x_j} \tag{2.7}$$

where

$$\tau_{ij}^{RANS} = \overline{\rho u_i" u_j"} \tag{2.8}$$

is introduced as an unclosed term. The equation is closed using the Boussinesq or turbulent-viscosity hypothesis [53] where

$$\tau_{ij}^{RANS} = -2\mu_t\left(\widetilde{S}_{ij} - \frac{1}{3}\frac{\partial \widetilde{U}_k}{\partial x_k}\delta_{ij}\right) + \frac{2}{3}\overline{\rho}k\delta_{ij} \tag{2.9}$$

the turbulent kinetic energy is

$$k = \frac{1}{2}\overline{u_i u_i} \tag{2.10}$$

and the Favre averaged strain rate tensor is

$$\widetilde{S}_{ij} = \frac{1}{2}\left(\frac{\partial \widetilde{U}_i}{\partial x_j} + \frac{\partial \widetilde{U}_j}{\partial x_i}\right). \tag{2.11}$$

This closure is employed for all turbulence models in this study where μ_t is the eddy viscosity.

2.2 Turbulence Modeling and Numerical Approach

Aero-thermal flows in high pressure turbines (HPT) are extremely challenging to compute because the flow is intrinsically multi-scale, unsteady, and turbulent. Next, the meshing approach must be able to resolve the blade tip clearance, leakage paths, and other complex geometries features in the HPT. Finally, the numerical solvers must be tolerant of localized poor mesh quality for these complex geometries. Given these challenges, this study includes a robust commercial solver and unstructured meshing to access the predictive capability using scale-resolved methods. Computational studies are performed using ANSYS Fluent v16 using RANS, HLES, and LES turbulence models [21]. The turbulence models are selected to understand the trade-off between computation efficiency and accuracy. The lower cost Shear-Stress Transport (SST) RANS turbulence model is considered relative to the Wall Adapted Local Eddy (WALE) LES model and the Improved Delayed Detached Eddy Simulation (IDDES) HLES model [54, 55, 56, 57]. Figure 2-1 characterizes the flow field resolved by the different turbulence modeling approaches. The spectrum of turbulent scales are representative of the energy cascade process involving the transfer of turbulent kinetic energy from larger eddies to smaller eddies. Dissipation of the energy to heat through molecular viscosity occurs at the smallest scales. In general, RANS models the entire range of turbulence coming at a reduced computational cost but reduced accuracy. At increased computational cost, LES resolves the large turbulent eddies improving

accuracy where the small scales are modeled. HLES is used to resolve the large scale turbulent quantities in separated flow regions. Cost savings, relative to LES, are due to the wall treatment where a switching function is used to revert to URANS near the wall. This size of the computational mesh directly impacts the computational cost where Chapman [58] estimated the near-wall grid points for a structured mesh is $N_{xyz} \propto Re^{1.8}$. N_{xyz} defines the number of grid points in three dimensions. Using a HLES or wall-modeled LES (WMLES) approach, Piomelli et al. [59] estimated $N_{xyz} \propto Re^{0.4}$, providing a significant computational cost savings due to the coarser near-wall grid.

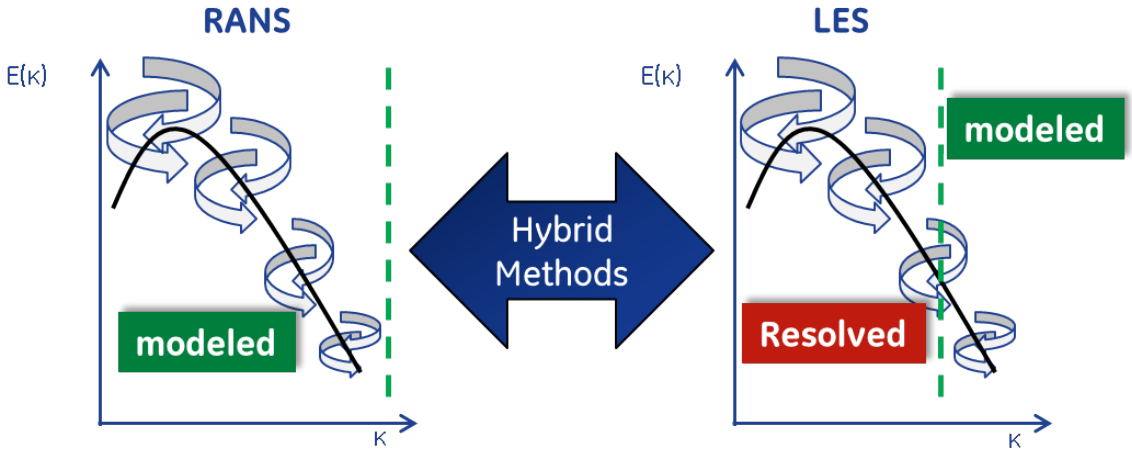

Figure 2-1. Conceptual representation of the energy cascade and resolved vs modeled flow quantities.

A wall resolved WALE LES model is used as a benchmark for RANS and HLES modeling approach. This LES model was selected based on the work of Medic et al. on an LPT [15]. For RANS or HLES models, in order to predict transitional boundary layers, Menter's $\gamma - Re_\theta$ transition model is coupled with the two-equation $k - \omega$ model with SST correction [60].

The pressure-based solver of Fluent is utilized with the pressure velocity coupled scheme [21]. Second-order bounded central differencing scheme is applied for the spatial discretization of the momentum in WALE and IDDES calculations. The bounded central differencing scheme is based on the normalized variable diagram (NVD) approach [61] along with convection boundedness criterion (CBC). The bounded central

differencing scheme is a composite NVD-scheme that consists of a pure central differencing, a blended scheme of the central differencing, and the second-order upwind scheme. The same scheme is used for all other transport equations for the WALE calculations. IDDES modeling utilizes second-order upwind discretization scheme for all other transport equations. The second-order upwind discretization scheme is used for all transport equations for the SST RANS turbulence models. A bounded second-order implicit time advancement scheme is used for WALE and IDDES models.

2.2.1 RANS Modeling

The RANS turbulence model chosen for this study is the standard SST $k-\omega$ model [54, 55]. Due to the robustness and good performance for attached and simple shear flow, this model has become one of the main workhorses for industrial engineering CFD [62, 53]. The SST model is a blend of the $k-\varepsilon$ and $k-\omega$ turbulence models [53]. The model includes a limiter to transition from the $k-\omega$ model near the wall to the $k-\varepsilon$ model in the core or shear flow regions. For attached turbulent BL the $k-\omega$ model has shown superior prediction when compared to the law of the wall. The $k-\varepsilon$ has shown improvement for simple shear flows compared to the $k-\omega$ [62].

Critical assumptions to close the SST two-equation model is:

1 Boussinesq hypothesis or turbulent-viscosity hypothesis.

2 Isotropic turbulence.

3 Standard gradient-diffusion hypothesis.

4 Empirical constants used to address the closure problem.

Item 1) assumes the Reynolds-stress is linearly and instantaneously related to the mean strain rate, S_{ij}. Item 2) results in the assumption that the turbulence is isotropic. The two-equation model uses turbulent kinetic energy and specific dissipation rate transport equations to define the eddy viscosity

$$\mu_t = \frac{\overline{\rho}k}{\omega}\frac{1}{max\left(\frac{1}{\alpha^*}, \frac{\widetilde{S}F_2}{a_1\omega}\right)} \tag{2.12}$$

where ω is the specific turbulence dissipation rate and

$$\widetilde{S} = \left(2\widetilde{S}_{ij}\widetilde{S}_{ij}\right)^{1/2} \tag{2.13}$$

is the local strain rate invariant. Further definitions for functions F_2 and α^* are provided by Menter et al. [55]. Constant a_1 and others empirical constants used for the SST model formulation can be found in Appendix A. The max operation with the limiter term $\frac{\widetilde{S}F_2}{a_1\omega}$ is used by the SST formulation.

Assumptions 1) and 2) are well known to be limiting in accelerating, boundary layer, and separating flow field [62]. Tavoularis and Corrison [63] showed for shear flow the near and far wake contained anisotropic turbulence. Tucker [64] showed for a simple contraction the Reynolds stress was not linear dependent on the local mean rate of strain but the total amount of the mean strain experienced. These deficiencies are further highlighted in Chapter 3 and 5.

The standard gradient-diffusion hypothesis is used to model the pressure diffusion and turbulent transport in the turbulent kinetic energy transport equation. The gradient-diffusion hypothesis within an incompressible BL can be approximated by

$$\overline{v'T'} = -\alpha_T \frac{\partial \overline{T}}{\partial y} \tag{2.14}$$

where y, v, T, and α_T are the normal coordinate to the wall, normal fluctuating velocity component, fluctuating temperature, and the eddy thermal diffusion, respectively. The turbulent Prandtl number,

$$Pr_T = \frac{\nu_T}{\alpha_T} \tag{2.15}$$

is used to determine α_T for the SST model where the current simulations assume $Pr_T = 0.85$. Specifically in the BL this assumption fails due to the non-linear relationship of the Pr_T relative to the distance from the wall.

The SST model is briefly discussed here. The reader is referred to Wilcox [53] for derivation and discussion of the standard $k-\omega$ model which the SST model is

founded. The SST turbulent kinetic energy transport equation is

$$\frac{\partial \overline{\rho} k}{\partial t} + \frac{\partial \overline{\rho} \widetilde{U}_j k}{\partial x_j} = P^* - \overline{\rho} \beta^* k \omega + \frac{\partial}{\partial x_j} \left[\left(\mu + \frac{\mu_t}{\sigma_k} \right) \frac{\partial k}{\partial x_j} \right] \tag{2.16}$$

Two modifications are considered for the productions term (P^*). The first is the production limiter [55]

$$P^* = min \left(\mu_t \widetilde{S}^2, 10 \overline{\rho} \beta^* k \omega \right) \tag{2.17}$$

where the ANSYS default clip factor of 10 is used. The second modifier is the Kato-Launder correction [65]

$$P^* = \mu_t \widetilde{S} \widetilde{\Omega} - \frac{2}{3} \overline{\rho} k \delta_{ij} \frac{\partial \widetilde{U}_i}{\partial \widetilde{x}_j} \tag{2.18}$$

where the Favre Averaged rotation rate tensor is

$$\widetilde{\Omega}_{ij} = \frac{1}{2} \left(\frac{\partial \widetilde{U}_i}{\partial x_j} - \frac{\partial \widetilde{U}_j}{\partial x_i} \right), \tag{2.19}$$

and the local rotation rate invariant is

$$\widetilde{\Omega} = \left(2 \widetilde{\Omega}_{ij} \widetilde{\Omega}_{ij} \right)^{1/2}. \tag{2.20}$$

The Kato-Launder correction was developed to reduce over-prediction of turbulent production in regions of large normal strain. Benefits are seen near the LE stagnation region for airfoils [65] and this correction is applied to all presented results for the current effort.

The second transport equation is from the specific dissipation rate.

$$\frac{\partial \overline{\rho} k}{\partial t} + \frac{\partial \overline{\rho} \widetilde{U}_j k}{\partial x_j} = P^* - \overline{\rho} \beta^* k \omega + \frac{\partial}{\partial x_j} \left[\left(\mu + \frac{\mu_t}{\sigma_k} \right) \frac{\partial k}{\partial x_j} \right] \tag{2.21}$$

Coefficients used for the $k - \omega$ and SST models are found in Appendix A. Further description can be found in references [60, 21].

2.2.2 RANS Transition Modeling

The $\gamma - Re_\theta$ transition model is selected for its wide use in industrial flows with varying Re and free-stream turbulence. The model has been calibrated to natural, bypass, and separation induced transitional flows. The model formulation allows application on both structured and unstructured meshing. In this study, focus is placed on the impact of free-stream turbulence and wake-induced transition, that are primary drivers for gas turbine flows. This model has not been validated for wake-induced transition. In addition, the $\gamma - Re_\theta$ transition model has also not been calibrated for roughness, free-stream turbulent length scale, and streamline curvature impact. However, it is shown that there is a substantial improvement in RANS and HLES predictions by including this transition model and a cost and accuracy opportunity in further developing transition modeling for HLES application.

In order to predict the impact of free-stream conditions on boundary layer state with RANS modeling, Menter's $\gamma - Re_\theta$ transition model is coupled with the two-equation SST model [60, 21]. The additional transport equation for the intermittency (γ) model is needed to turn on the production term of the turbulent kinetic energy downstream of the transition point.

$$\frac{\partial \overline{\rho}\gamma}{\partial t} + \frac{\partial \overline{\rho}\widetilde{U}_j\gamma}{\partial x_j} = P_{\gamma 1} + E_{\gamma 1} + P_{\gamma 2} + E_{\gamma 2} + \frac{\partial}{\partial x_j}\left[\left(\mu_t + \frac{\mu_t}{\sigma_\gamma}\right)\frac{\partial \gamma}{\partial x_j}\right] \tag{2.22}$$

The transition source terms are $P_{\gamma 1}$ and $E_{\gamma 1}$. The destruction or relaminarization source terms are $P_{\gamma 2}$ and $E_{\gamma 2}$.

The transport equation for the transition momentum thickness Reynolds number is

$$\frac{\partial \overline{\rho} Re^*_{\theta t}}{\partial t} + \frac{\partial \overline{\rho}\widetilde{U}_j Re^*_{\theta t}}{\partial x_j} = P_{\theta t} + \frac{\partial}{\partial x_j}\left[\sigma_{\theta t}\left(\mu + \mu_t\right)\frac{\partial Re^*_{\theta t}}{\partial x_j}\right] \tag{2.23}$$

The source term $P_{\theta t}$ forces the transported scalar to represent the local value of the transition momentum thickness Reynolds number which is calculated from an empirical correlation outside the boundary layer.

The $\gamma - Re_\theta$ is coupled with the SST model by modification of the production

and destruction terms in the k equation.

$$\frac{\partial \overline{\rho} k}{\partial t} + \frac{\partial \overline{\rho} \widetilde{U}_j k}{\partial x_j} = P^* - D_t^* + \frac{\partial}{\partial x_j}\left[\left(\mu + \frac{\mu_t}{\sigma_k}\right)\frac{\partial k}{\partial x_j}\right] \tag{2.24}$$

where

$$P_t^* = \gamma_{eff} P^* \tag{2.25}$$

$$D_t^* = min\left[max\left(\gamma_{eff}, 1.0\right), 1.0\right]\overline{\rho}\beta^* k\omega \tag{2.26}$$

No attempt has been made to modify the transition model coefficients for the current study. Further details into the development and calibration of this model can be found in Menter et al. [60, 20].

Primary development of this model has been for LPT [60]. This model has been applied to HPT conditions with moderate success, including the experimental study of Arts and Rouvroit [34] uncooled vane case. However, limited knowledge of turbulence decay was available at the time for the studies of Menter et al. [60, 20]. Turbulence decay is available for the current study and is characterized and applied at the computational inlet for the uncooled vane case in Chapter 5.

2.2.3 LES Modeling

The unstructured finite volume code of Fluent filtering operation is defined as

$$\overline{\phi}\left(x\right) = \int_{Domain} \phi\left(x'\right) G\left(x, x'\right) dx' = \frac{1}{V}\int_V \phi\left(x'\right) dx', x' \in V \tag{2.27}$$

where V is the local volume,

$$G\left(x, x'\right) = \begin{cases} 1/V & x \in V \\ 0 & x' \text{otherwise} \end{cases} \tag{2.28}$$

and

$$\widetilde{\phi}\left(x\right) = \frac{1}{V}\frac{\int_V \rho\left(x'\right)\phi\left(x'\right) dx'}{\overline{\rho}}, x' \in V. \tag{2.29}$$

The LES Favre filtered Navier-Stokes equation is

$$\frac{\partial \overline{\rho}\,\widetilde{U}_i}{\partial t} + \frac{\partial \overline{\rho}\widetilde{U}_i\widetilde{U}_j}{\partial x_j} = -\frac{\partial \overline{p}}{\partial x_i} + \frac{\partial \overline{\tau_{ij}}}{\partial x_j} - \frac{\partial \tau_{ij}^{LES}}{\partial x_j} \tag{2.30}$$

where the equation is of the same form as the RANS Favre Averaged Equation 2.7. However, the overbar quantities now represent the filtered flow field. LES Favre filtered equation resolves large scale structures proportional to the local element size where the smallest portion of the turbulent energetic content, that cannot be resolved on the grid, are modeled. For the current LES approach, the Boussinesq approximation is used to close the Favre filtered equations. The modeling differences is the eddy viscosity formulation where the RANS eddy viscosity is redefined as the sub-grid scale viscosity for LES. For LES approaches on unstructured meshes (such as Fluent) the local mesh volume is used as the LES filter size. Using the Boussinesq approximation the value of the eddy viscosity determines the contribution of the unclosed term. Depending on the contribution, Equations 2.7 or 2.30 operates in a RANS (large μ_t) or LES mode (small μ_t), respectively. This is the basis for hybrid RANS/LES models discussed in the next section.

The WALE eddy viscosity defined as the sub-grid scale viscosity (μ_{SGS}) is modeled using the one equation WALE model of Nicoud and Ducros [56] where

$$\mu_{SGS} = \overline{\rho} L_w^2 \frac{\left(S_{ij}^d S_{ij}^d\right)^{3/2}}{\left(\widetilde{S}_{ij}\widetilde{S}_{ij}\right)^{5/2} + \left(S_{ij}^d S_{ij}^d\right)^{5/4}} \tag{2.31}$$

where

$$S_{ij}^d = \frac{1}{2}\left[\left(\frac{\partial \widetilde{U}_i}{\partial x_j}\right)^2 + \left(\frac{\partial \widetilde{U}_i}{\partial x_j}\right)^2\right] - \frac{1}{3}\delta_{ij}\left(\frac{\partial \widetilde{U}_k}{\partial x_k}\right)^2 \tag{2.32}$$

and

$$L_w = min\left(\kappa d, C_w \Delta_{SGS}\right). \tag{2.33}$$

Filter size, mesh size, time step, space discretization scheme, and time marching scheme are all factors that have been shown to affect the quality of the LES solution

[66, 50]. These factors are considered in the following chapters for the second order unstructured Fluent code. In cases where the filter size is equal to the mesh size the truncation error is dominant and the SGS model error is relatively small [67]. In order to model complex geometries found in turbine designs, an unstructured meshing approach is required. In the current study, Fluent uses explicit filtering bases on the local grid refinement when Δ_{SGS} is equal to the cubic root of the local element. Equation 2.33 dependence on the wall distance (d) is a slight modification from the original model of Nicoud and Ducros [56]. C_w is set to 0.325 with a turbulent Prandtl number (Pr_t) equal to 0.85 to close the energy equation. C_w differs from other published work on HPT flow, ranging from 0.49 - 0.6, with various numerical solvers where a Pr_t as low as 0.6 was used [56, 16]. Sensitivity to the coefficient C_w is addressed in Chapter 5.

A significant advantage of the WALE model in comparison with the widely used Smagorinsky model is due to an improved formulation of the SGS turbulent viscosity. This approach assures the proper damping of the turbulent viscosity near to solid walls. The WALE model is designed to return the correct wall asymptotic (y^3) behavior for wall bounded flows where y is the distance from the wall. Another advantage is for laminar shear flows where a zero turbulent viscosity is returned. This allows the correct treatment of laminar zones in the domain which is important for the current study with laminar to turbulent boundary layer transition.

2.2.4 Hybrid LES Modeling

Hybrid RANS/LES methods are currently being very intensively explored in the academic and industrial CFD communities. These models resolve the large-scale flow structures ("LES-mode") in shear or separation type flow regions. However, for wall resolved LES, turbulent length scales become very small near the wall and LES can becomes prohibitively expensive due to the number of grid points near the wall scaling with $Re^{1.8}$ [58]. HLES models utilizes a RANS modeling approach allowing for reduced computational cost due to relaxed meshing requirements where the number of near-wall grid points now scale with $Re^{0.4}$ [59]. Three types of hybridization tech-

niques are described by Frohlich et al. [68]: 1) blending, 2) hard interface, and 3) soft interface models. IDDES falls under the category of a blending model. Improvements over the previous DDES model were directed towards fixing the "log-layer mismatch" problem of DES and DDES and a new definition of a subgrid length scale that takes into account the near-wall distance [57]. Additionally, given an unsteady inlet boundary condition, the IDDES model operates in a wall-modeled LES (WMLES) mode where near-wall mesh resolution requirements must be met [69]. Therefore, there is an intentional non-uniqueness to the IDDES solution due to their DDES and WMLES branches. WMLES is triggered with unsteady boundary condition where DDES mode occurs in steady inflow conditions.

The SST-IDDES model is selected for this study where the k-equation of the SST model is modified resulting in the following equation,

$$\frac{\partial \overline{\rho} k}{\partial t} + \frac{\partial \overline{\rho} \widetilde{U}_j k}{\partial x_j} = P^* - \overline{\rho} \beta^* k \omega F_{IDDES} + \frac{\partial}{\partial x_j} \left[\left(\mu + \frac{\mu_t}{\sigma_{k3}} \right) \frac{\partial k}{\partial x_j} \right]. \tag{2.34}$$

The variable F_{IDDES} is defined as

$$F_{IDDES} = \left[\max \left(\frac{L_t}{C_{DES} \Delta_{DES}} \left(1 - f_{IDDES} \right), 1 \right) \right] \tag{2.35}$$

where this function is dependent on the RANS turbulent length scale ($L_t = k^{1/2}/c_\mu \omega$), filter size ($\Delta_{DES}$), shielding functions ($f_{IDDES}$), and constant ($C_{DES}$). For the current study using Fluent applies the constant $C_{DES} = 0.61$. The reader should refer to Shur et. al [57] and Gritskevich et al. [70] for detailed discussion of this function and the model's development. This function allows for a cost reduction from LES by employing unsteady RANS modeling within the BL and switching to LES treatment in the regions of unsteadiness with adequate grid resolution. In order to model BL transition, the SST-IDDES model allows the ability to include the $\gamma - Re_\theta$ transition model (IDDES-T) in Fluent. The implementation of the transition model follows from the previous RANS modeling discussion. It should be noted that the transition model is dependent on the model's kinetic energy. Therefore, the impact of the

resolved unsteadiness when operating in a WMLES mode near the wall is not directly accounted for when using the transition model for IDDES. The resolved and modeled kinetic energy within the boundary layer for the IDDES-T is studied in Chapters 3 and 7.

Chapter 3

Cylinder in Cross-flow

Simulations of the experimental study by Konstantinidis et al. [71, 72] are presented in this chapter (Figure 3-1). Konstantinidis et al. [71] performed PIV experimental measurements of the flow field behind a cylinder in a 72 x 72 mm water tunnel. The cylinder diameter is kept to 7.2 mm to avoid any tunnel wall effects on the cylinder's wake. Therefore the tunnel span extent was large enough to allow statistical quantities to decorrelate at mid-span, resulting in a statistically two-dimensional flow in the direction parallel to the cylinder axis. The Reynolds number based on the free-stream velocity, U_∞, and the cylinder diameter, D, is $Re_D = 2580$. The reported experimental uncertainty is $\pm 5\%$ and $\pm 10\%$ for mean and fluctuating velocity components, respectively. This uncertainty includes test to test repeatability. The PIV image resolution is on the order of 10 μm, corresponding to 0.14% of the cylinder diameter.

This is a fundamental test case for shear flow and serves as a benchmark case for computational codes. Given the low Reynolds number, incompressible flow, and simple geometry this test case facilitates a quick turn-around for modeling assessment. Recently, the high-order spectral implicit LES code of Mohammad et al. [73] was shown to be within the experimental measurement uncertainty of Konstantinidis et al. [71, 72]. Here the experimental results are used to quantify the impact of grid topology, turbulence model, and non-conformal interface using the commercial CFD code Fluent. A key motivation for the current work is to understand the capability of

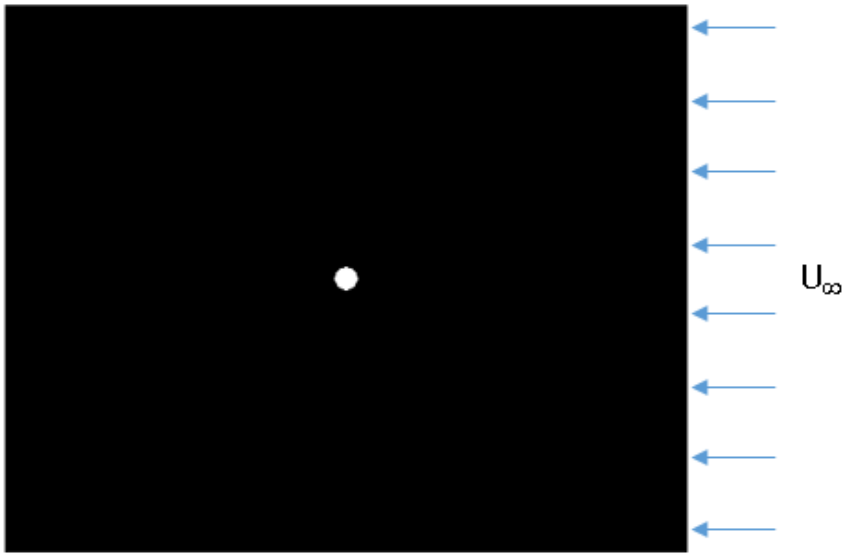

Figure 3-1. Schematic of the computational domain used for the cylinder in cross-flow study.

executing a scale-resolved simulation with a second-order code on a mesh of prisms and tetrahedral. LES serves as a benchmark for lower computational cost turbulence models (RANS and HLES) for HPT studies in the next chapter. Therefore, it is demonstrated that the current modeling approach can provide predictions within the experimental uncertainty for first-order statistics and second-order statistics. This is done to access the desired modeling and meshing approach prior to moving to the additional complexity of HPT simulations. These lessons learned for modeling shear flows are applied in two primary regions of the HPT simulations: 1) shedding wake behind the TE of a HPT vane or blade, and 2) simulating bars used to generate turbulence upstream of a HPT experimental test vane.

Even though the flow for the cylinder in cross-flow is incompressible, simulations are carried out using a compressible solver. The same solver approach is used for the compressible HPT flow simulations. The pressure-based solver of Fluent is utilized with the coupled scheme for the pressure-velocity coupling [21]. Second-order bounded central differencing scheme is applied for the spatial discretization of the momentum in WALE and IDDES calculations. The bounded central differencing scheme is based on the normalized variable diagram (NVD) approach [61] along with

convection boundedness criterion (CBC). The bounded central differencing scheme is a composite NVD-scheme that consists of a pure central differencing, a blended scheme of the central differencing, and the second-order upwind scheme. The same scheme is used for all other transport equations for the WALE calculations. IDDES modeling utilizes second-order upwind discretization scheme for all other transport equations. The second-order upwind discretization scheme is used for all transport equations for the SST RANS turbulence models. A bounded second-order implicit time advancement scheme is used for WALE and IDDES models.

Simulations are executed with an uniform inlet velocity, constant static exit pressure, and a no slip condition on the cylinder wall. The domain is periodic in span and uses slip boundary conditions on the top and bottom wall. The x-axis is along the stream-wise flow direction and the z-axis is along the cylinder axis (i.e. span-wise direction). The domain is shown in Figure 3-1 where the origin of the coordinate system is at the cylinder center.

For LES and HLES simulation, the domain computational span divided by the cylinder diameter is $S/D = 2.2$. The selected domain extent is based on the previous computational studies of Mohammad et al. [73]. The non-dimensional time step, $t_0 = \Delta t(U/D)$, and iterations per time step are 0.035 and 9, respectively. The time step for shear flows was estimated by the fundamental shedding frequency. The St of 0.21 for the cylinder is used to determine the time step needed to achieve approximately 100 time steps per wake shedding period. This approach is revised in Chapter 5.

At the end of this chapter, a separate experimental study, to measure the cylinder wall heat flux, was performed by Nakamura and Igarashi [74]. The heat flux was measured as a function of angle, where 0 degrees is found at the upstream stagnation point of the cylinder. Computationally, the surface of the cylinder is treated as a fixed temperature wall where T_{wall}/Tt_{∞}=1.1. T_{wall} is the cylinder surface temperature and Tt_{∞} is the free-stream inlet total temperature.

3.1 Mesh Study

In order to deal with complex geometries for industrial applications, robust mesh topologies and solvers are often required. In particular, the focus of this effort is modeling HPT stage geometry to better understand vane/blade interaction. The cylinder study is attractive because of the quality of the measurements, modest Reynolds number, and separation flow physics of interest for the HPT. The current case study is used to determine the required mesh refinement, then quantify the impact of three mesh topologies using the LES WALE SGS model [56] in Fluent [69]. The LES grid density requirement is first evaluated on an unstructured tetrahedral core mesh with near-wall prism layers to capture the boundary layer. The grid requirement for this study has been established by achieving predictions within the experimental uncertainty first and second-order statistics. The core tetrahedral element edge length was refined by 50% for three cases shown in figure 3-2 and summarized in Table 3.1. The tetrahedral element edge length is defined as dL. The size of the near-wall prism elements are fixed for the three mesh refinements where the surface prism element edge length divided by the cylinder diameter is $D/ds = 28.2$. A separate study on the near-wall mesh has been conducted to identify the optimal sizing. The regions of the near and far wakes are defined to be within 2 and 6 diameters downstream, respectively. The cylinder wall total prism layer thickness is selected to meet maximum boundary layer thickness where the first cell height results in a $y+$ less than 1. The prism layer expansion ratio was set to 1.1 that includes 21 layers before transitioning to tetrahedral elements.

Table 3.1. Cylinder mesh refinement summary.

Model	Fine	Medium	Coarse
Cylinder Wall D/ds	28.2	28.2	28.2
Near Wake D/dL	16.9	11.3	8.5
Far Wake D/dL	9.2	6.2	4.5

The grid sensitivity of the unstructured meshes are compared to measured velocity profile data at different locations downstream of the cylinder ranging from

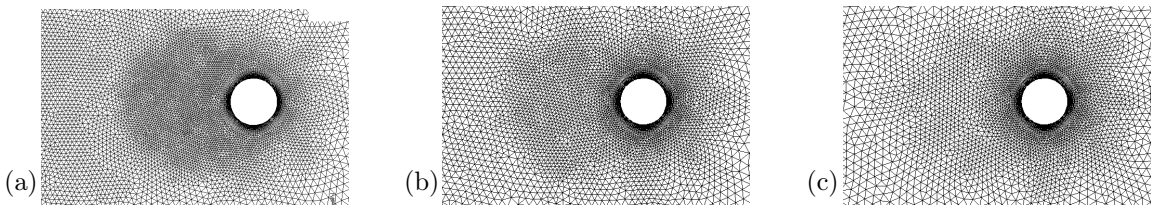

Figure 3-2. Grid refinement comparison for (a) fine (b) medium, and (c) coarse unstrucutred tetrahedral meshes.

$X/D = 0.7 - 3.0$ in Figure 3-3. In order to show all X/D planes, an offset for each plane is applied to the y-axis. This offset is -1.0 and -0.5 for the stream-wise and cross-stream figures, respectively. Agreement within the experimental uncertainty is found for both medium and fine grids. This establishes grid requirement but also shows that an unstructured tetrahedral element mesh using second-order numerics in Fluent can capture wake mixing to within the experimental uncertainty of the mean shear flow predictions for this canonical case. Next, the grid sensitivity of the unstructured meshes are compared to measured fluctuating velocities' profile data at different locations downstream of the cylinder in Figure 3-4. Agreement within 2X the experimental uncertainty is found for the fine grid showing the meshing approach using second-order numerics in Fluent can also capture turbulent quantities in the wake.

The impact of mesh topology is now evaluated for both first and second-order statistics. The fine unstructured grid is compared to a structured mesh and a 2D extrusion of the unstructured span domain topology. Figure 3-5 qualitatively compares the topology, instantaneous flow structure, and mean stream-wise velocity. The magnitude of the density gradient over the density, or numerical Schlieren, is used to show the instantaneous flow structure (images do not represent the same instant in time). The Numerical Schlieren image for the structured mesh is notably different from the two unstructured results. However, this seems to have little impact on the mean flow field. The mean stream-wise and cross-stream velocities predictive capability is quantified in Figure 3-6. Both unstructured meshes, relative to the structured mesh, are found to be in better agreement with the data. However, a mesh density study was

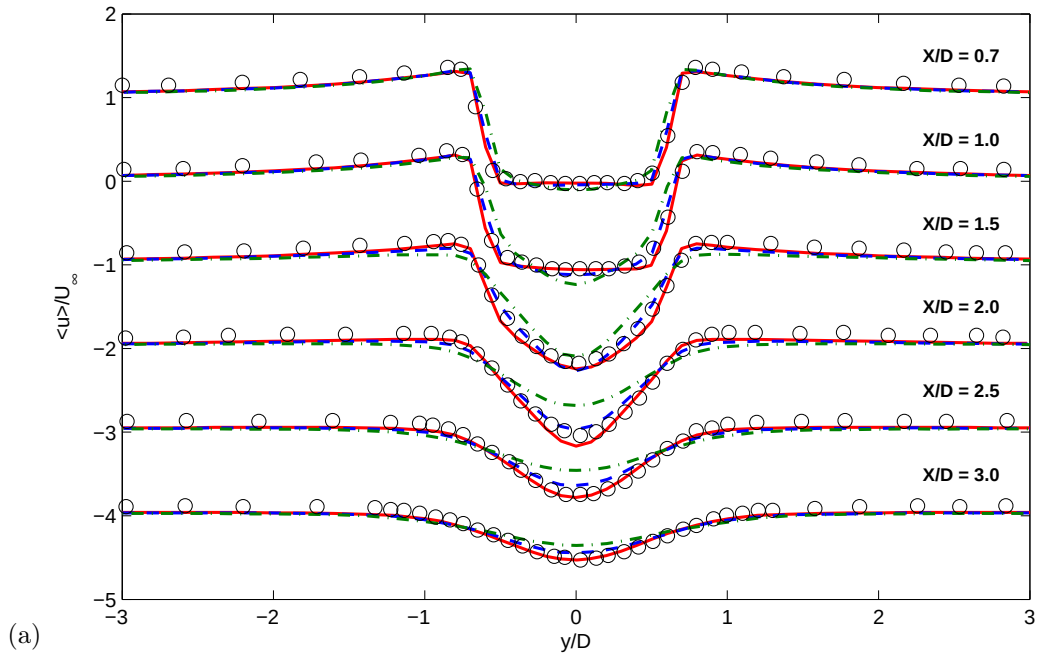

(a)

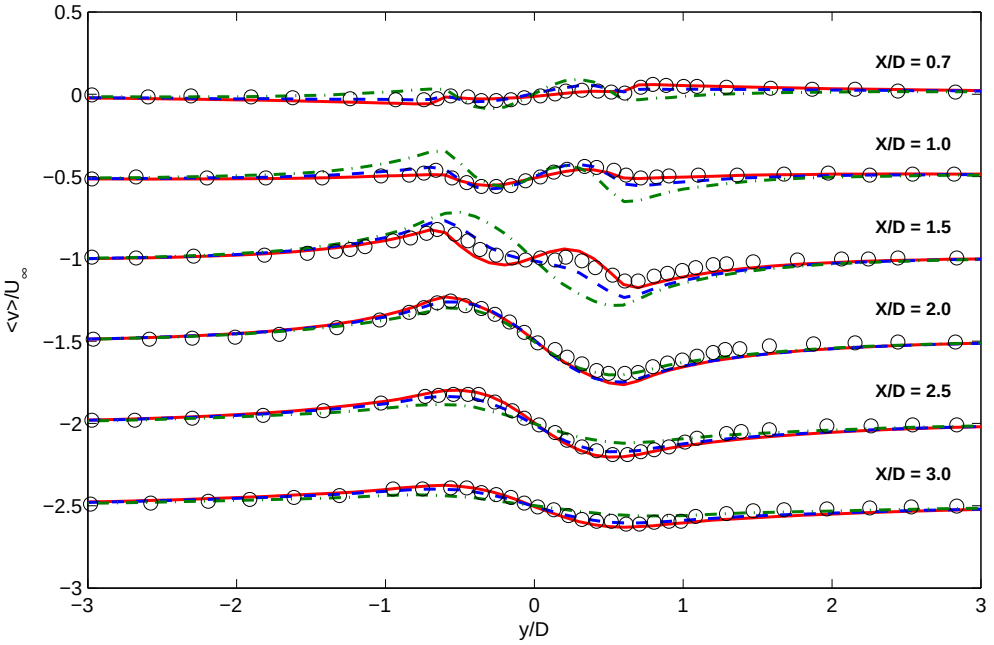

(b)

Figure 3-3. Experiment measurement (○) compared to unstructured tetrahedral sensitivity for coarse (· - ·), medium (- - -), and fine (——) mesh densities for (a) stream-wise and (b) cross-stream normalized mean velocities at different stream-wise planes downstream of cylinder.

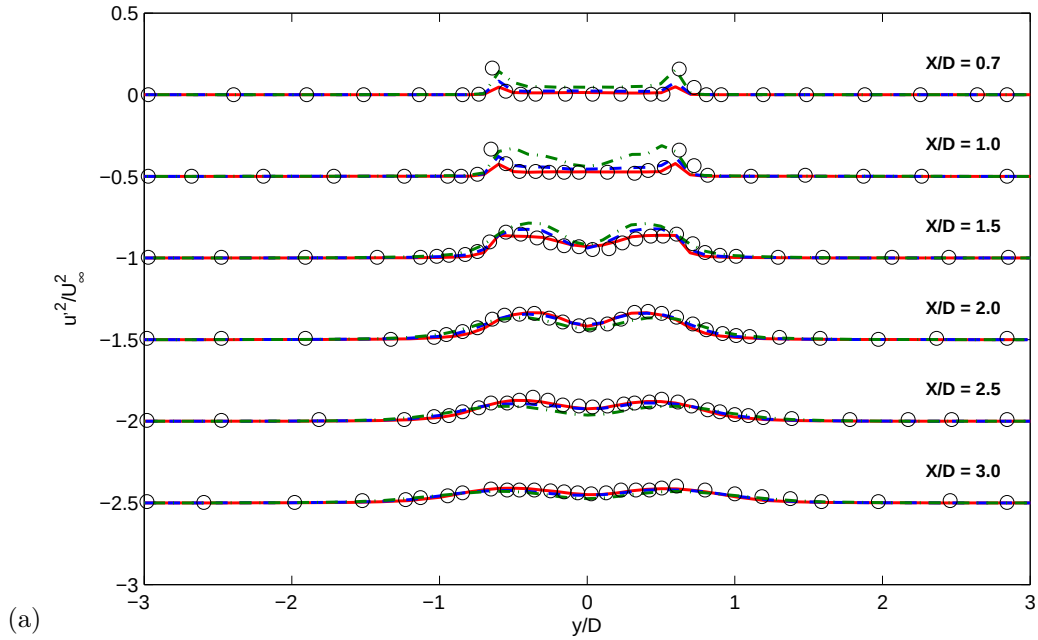

(a)

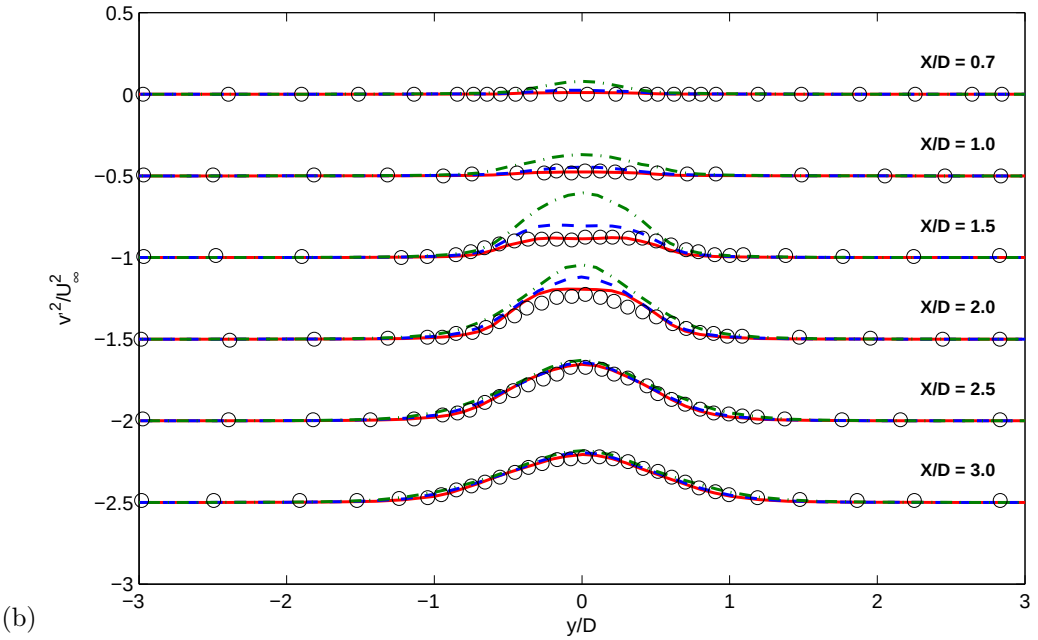

(b)

Figure 3-4. Experiment measurement (○) compared to unstructured tetrahedral sensitivity for coarse (· - - ·), medium (- - -), and fine (——) mesh densities for (a) stream-wise and (b) cross-stream normalized fluctuating velocities at different stream-wise planes downstream of cylinder.

not completed to optimize the structured mesh. Table 3.2 shows that the structured mesh local maximum cell edge length is in general coarser than the fine unstructured case. A finer structured mesh was not pursued given the accuracy found using an unstructured tetrahedral mesh. However, the 2D extrusion of the unstructured mesh is run with edge lengths matched to the structured mesh, providing a comparison between structured and unstructured approaches using the same local element edge lengths. In addition, a negligible change in element count was found when moving from a structured to the extruded unstructured approach. This is due to localized mesh refinement capability of an unstructured approach where the structured grid can lead to over refined regions away from the region of interest. In the current case, the region of interest is wake shedding downstream of the cylinder.

Table 3.2. Cylinder mesh topology summary.

Model	Structured	Extruded Unstructured	Fine Unstructured
Cylinder Wall D/ds	40	40	28.2
Cylinder Wall D/dz	80	80	28.2
Near Wake D/dL	25.4	25.4	8.5
Far Wake D/dL	12.7	12.7	4.5

A key objective identified in Chapter 1 is to better understand the role of turbulence on the HPT aero-thermal flow field. Prediction of second-order statistics is essential for understanding the developing turbulent flow field for shear flow. Figure 3-7 compares the WALE model and PIV resolved fluctuating components. The fine tetrahedral unstructured results are found to be in excellent agreement with the data showing the validity of the unstructured meshing approach. The two locations where the predictions fall outside the experimental uncertainty are found for the stream-wise fluctuating velocity at $X/D = 0.7$ and the cross-stream fluctuating velocity at $X/D = 2.0$. The stream-wise deviation at $X/D = 0.7$ is where the shear layer begins to develop. Mesh refinement in the shear layer would likely improve predictions based on structured results. The structured mesh is found to have approximately a 2 to 1 element edge length ratio compared to the fine unstructured case where the shear layer is initially formed. However, given the minimal impact on the down-

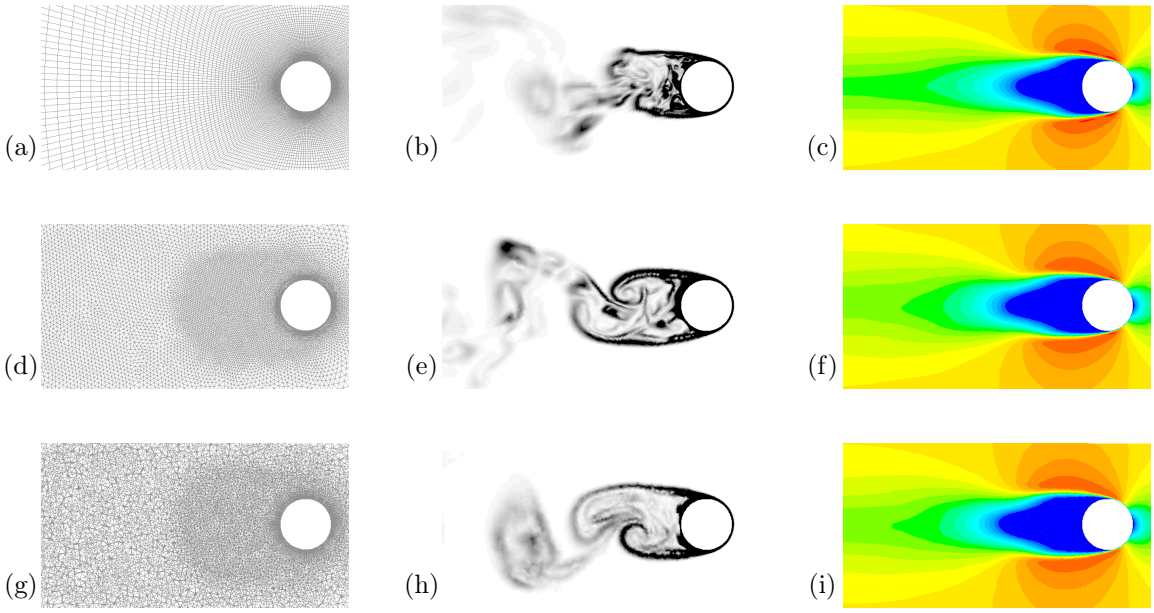

Figure 3-5. Grid topology comparison study. Structured (a) mesh (b) numerical Schlieren and (c) mean stream-wise velocity. 2D extruded near-wall prisms and tetrahedral core (d) mesh (e) numerical Schlieren and (f) mean stream-wise velocity. Near wall prisms with tetrahedral core (g) mesh (h) numerical Schlieren and (i) mean stream-wise velocity.

stream predictions this was not pursued. The cross-stream deviation at $X/D = 2.0$ is in the end of separation region where large vortical structures are developing. Any experimental or computational positional uncertainty results in a significant change in profile shape. This is highlighted by the unstructured predictive agreement with measurement both up and down stream of $X/D = 2.0$. In addition, small differences in Reynolds number, surface roughness, and cylinder profile could impact the separation region. A shift of $0.1D$ would result in the predictions falling within the experimental uncertainty.

3.2 Time Averaging and Statistically Steady State

Monitoring points were distributed in the domain to provide an understanding of the statistical evolution of the flow to enable high quality averaging of the statistics. Figure 3-8 and 3-9 present results for WALE and IDDES, respectively. Instantaneous

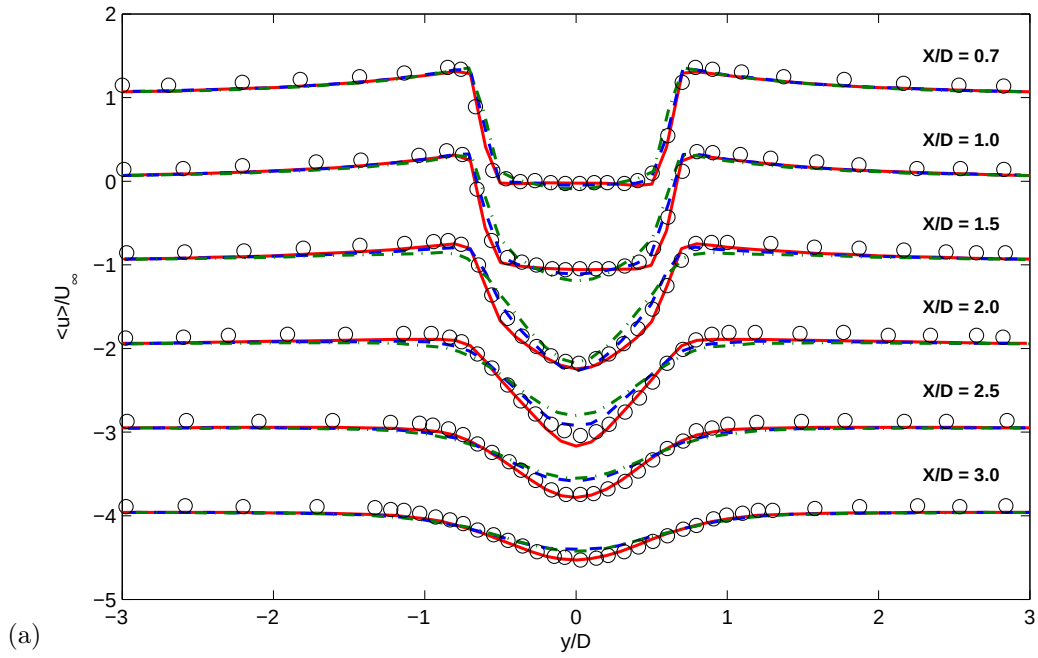

(a)

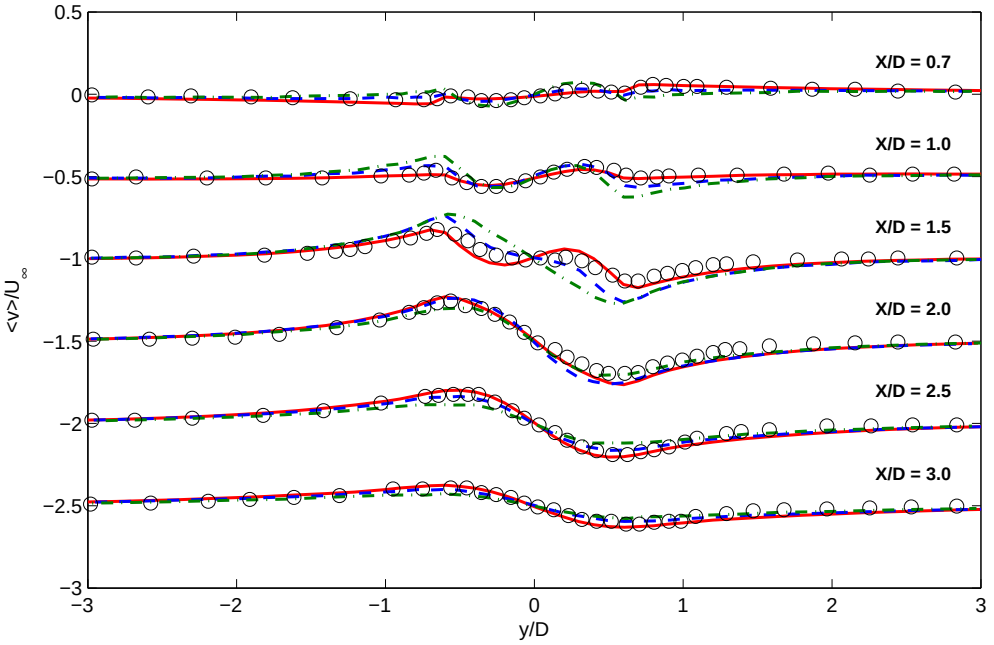

(b)

Figure 3-6. Experiment measurement (○) compared to mesh topology for unstructured tetrahedral (——), extruded tetrahedral (- - -), and structured (· - ·) for (a) stream-wise and (b) cross-stream normalized mean velocities at different stream-wise planes downstream of cylinder.

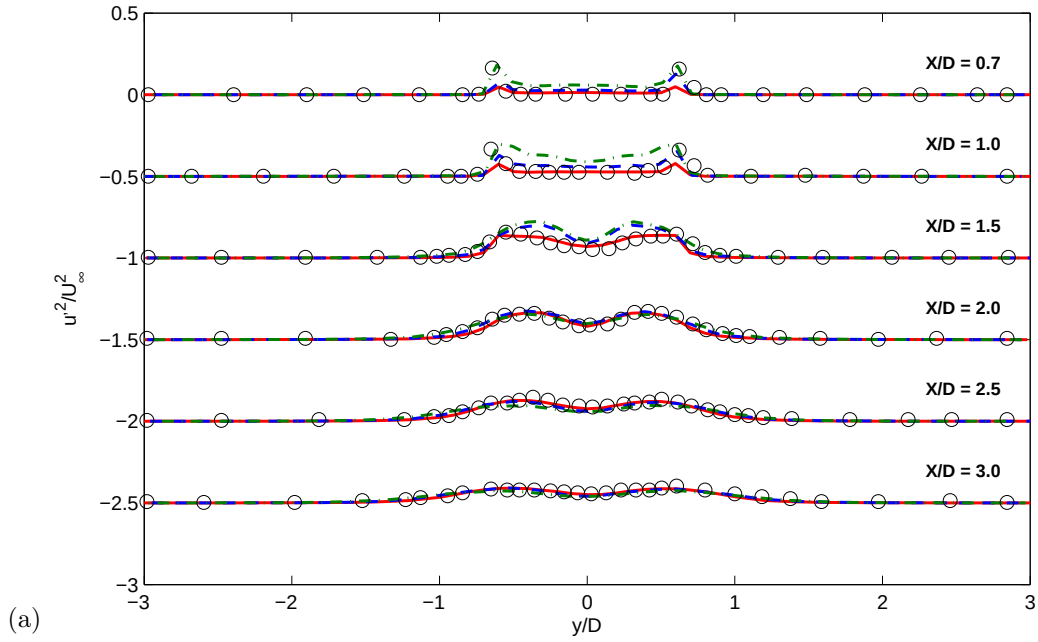

(a)

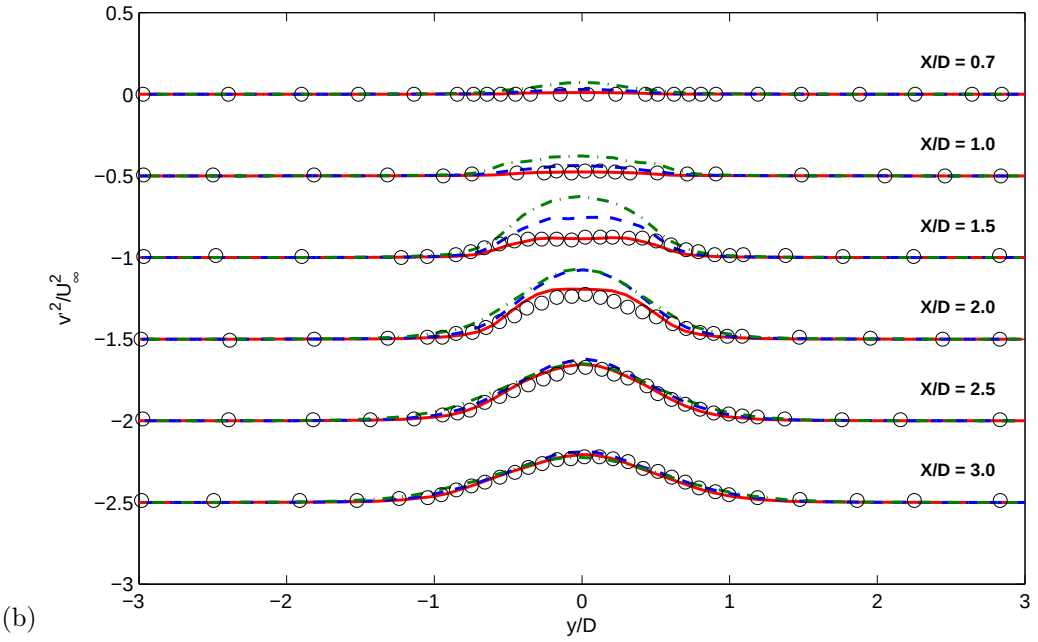

(b)

Figure 3-7. Experiment measurement (○) compared to mesh topology for unstructured tetrahedral (——), extruded tetrahedral (- - -), and structured (· - ·) for (a) stream-wise and (b) cross-stream normalized fluctuating velocities at different stream-wise planes downstream of cylinder.

pressure normalized to the exit pressure, p_2, was monitored as a function of time down-stream of the cylinder at X/D of 2.0 and 3.0. Time averaging is initiated at $t_0 = 165$ where statistics are collected for over 100 cylinder flow passing. It is shown that the solutions reach statistically steady state prior to $t_0 = 165$ and sufficient time averaging has been applied.

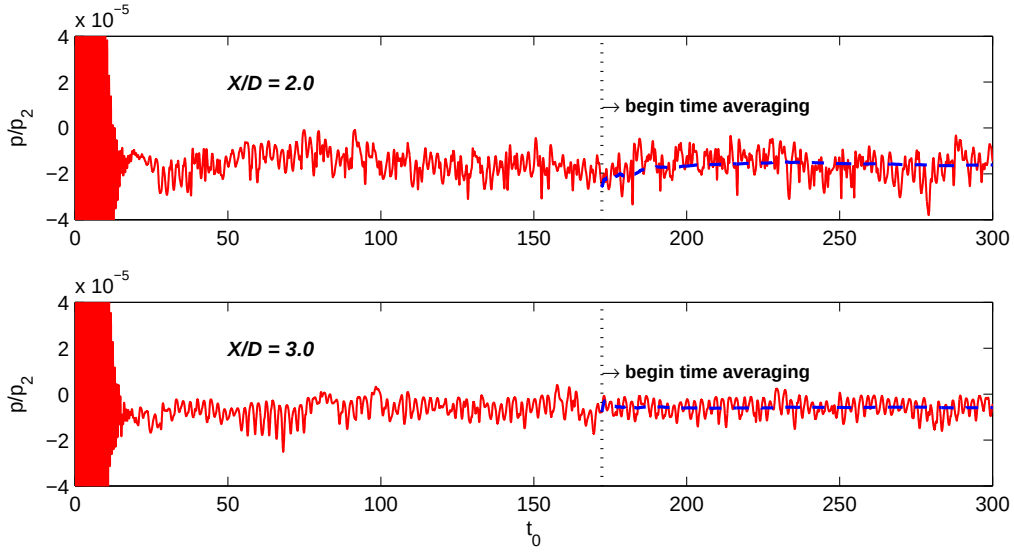

Figure 3-8. WALE time averaging. Running time average (- - -), and instantaneous value (——)

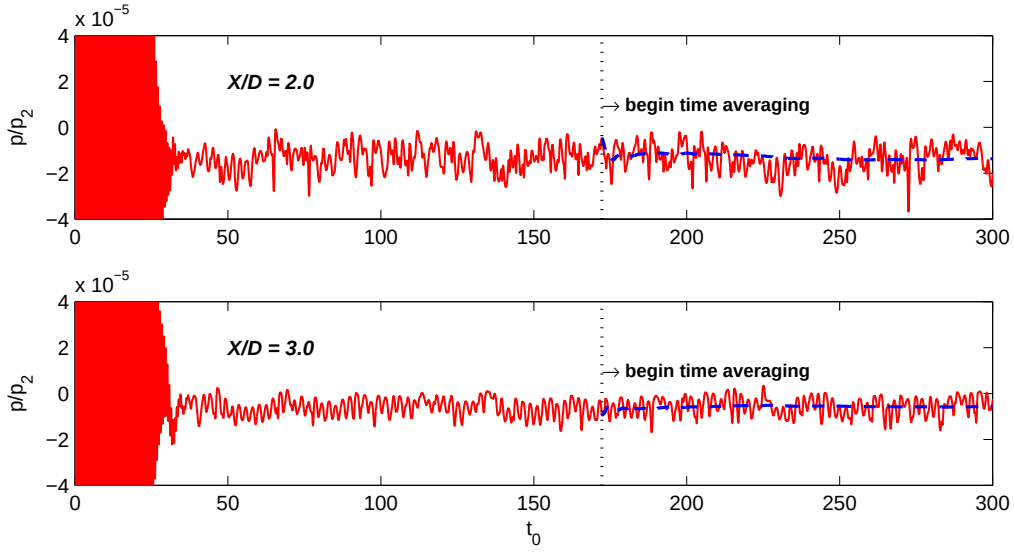

Figure 3-9. IDDES time averaging. Running time average (- - -) and instantaneous value (——).

3.3 Model Study

Wall resolved LES has been demonstrated to be very accurate, but the computational requirement limits the impact this method can have for industrial applications. An alternative approach is to model the boundary layer with RANS, where the computational cost of LES is too high. Two additional turbulence models are evaluated beyond the WALE model. The SST model is evaluated given its wide use in industrial turbine flows and significant reduction in computational cost. However, the RANS SST model is well known to be limiting in separating and wake mixing flow [62] as previously discussed in Chapter 2. The IDDES model resolves the large scale turbulent quantities in separated flow regions but near the wall switches to the SST model. The primary interest in the IDDES model, relative to LES, is the cost reduction in mesh requirement at the wall. Additional discussion on the selection of the HLES IDDES model for this study was previous discussed in Chapter 2.

For the current cylinder study, no attempt is made to reduce near-wall mesh size for the IDDES model. The focus is instead on the model's near-wall treatment and switching function impact on the wake flow field relative to the LES WALE solution. The near-wall mesh resolution requirement is evaluated in the following chapters on the HPT vane. Each turbulence model (SST, IDDES, WALE) is run on the same fine unstructured tetrahedral mesh to remove grid sensitivity between the WALE and IDDES comparison. The fine mesh also provides a grid independent solution for the SST predictions.

The results of the steady RANS SST model shows the inability to predict both the stream-wise and cross-stream mean velocity (Figure 3-10). It should be highlighted that these near wake measurement planes are within $X/D = 3.0$ of the cylinder. The next chapter looks at downstream measure planes for a HPT vane wake where $X/D > 10$ (D being the TE diameter of the vane). This helps quantify the SST model predictive capability in the far wake. However, it is clear that the model is not calibrated to predict the near wake flow field accurately. The SST predictive miss could be contributed to the modeling of boundary layer or wake mixing. However,

the IDDES model use of the SST model near the wall results in the same boundary layer. IDDES predictions for stream-wise and cross-stream velocity are within the experimental uncertainty for 10 out of the 12 downstream wake plane locations. Therefore, the modeling of the wake mixing for the steady RANS SST model is the primary contribution to the significant predictive miss.

Isotropic turbulence is one of the major assumptions for the RANS SST model. The limitations of this assumption is well known, where the WALE model in Figure 3-11 shows the anisotropic behavior in the downstream wake of the cylinder. The three components of resolved Reynold stress are normalized to the kinetic energy, k and each plane is offset by -3.0 on the y-axis. The deviation between u'^2/k, v'^2/k, and w'^2/k show the anisotropic turbulence remaining at the furthest down-stream location plotted at $X/D = 3.0$.

Figures 3-10 and 3-12 provide confidence in the IDDES model predictive capability relative to the experimental data. IDDES mean flow is found to fall slightly outside the experimental uncertainty at $X/D = 1.5$. Therefore, the predictive miss can be quantified by either an error in flow value or an error in position. The flow quantity error is 10% or 2 times the experimental uncertainty. The positional error is $0.1D$. This shift would result in the flow value falling within the experimental uncertainty. However, when only comparing turbulence models at $X/D = 1.5$, the IDDES model is found to have it largest deviation from the WALE model. This can be attributed to the difference in the turbulence model formulation. Instantaneous images of the flow field are presented in Figure 3-13. The numerical Schlieren images can be used to compare the instantaneous flow fields of WALE and IDDES. Similar large scale vortical structures are resolved. Differences can be seen in the smaller flow structures in the separation region, where the IDDES model results in less resolution of these small-scale structures. This is a direct result of turbulence subgrid scale model, since the identical mesh is used for both IDDES and WALE. It is important to note these differences between IDDES and WALE but also acknowledge both models accurately predict the mean flow field. Throughout this thesis IDDES is compared back to the WALE model to understand modeling impact.

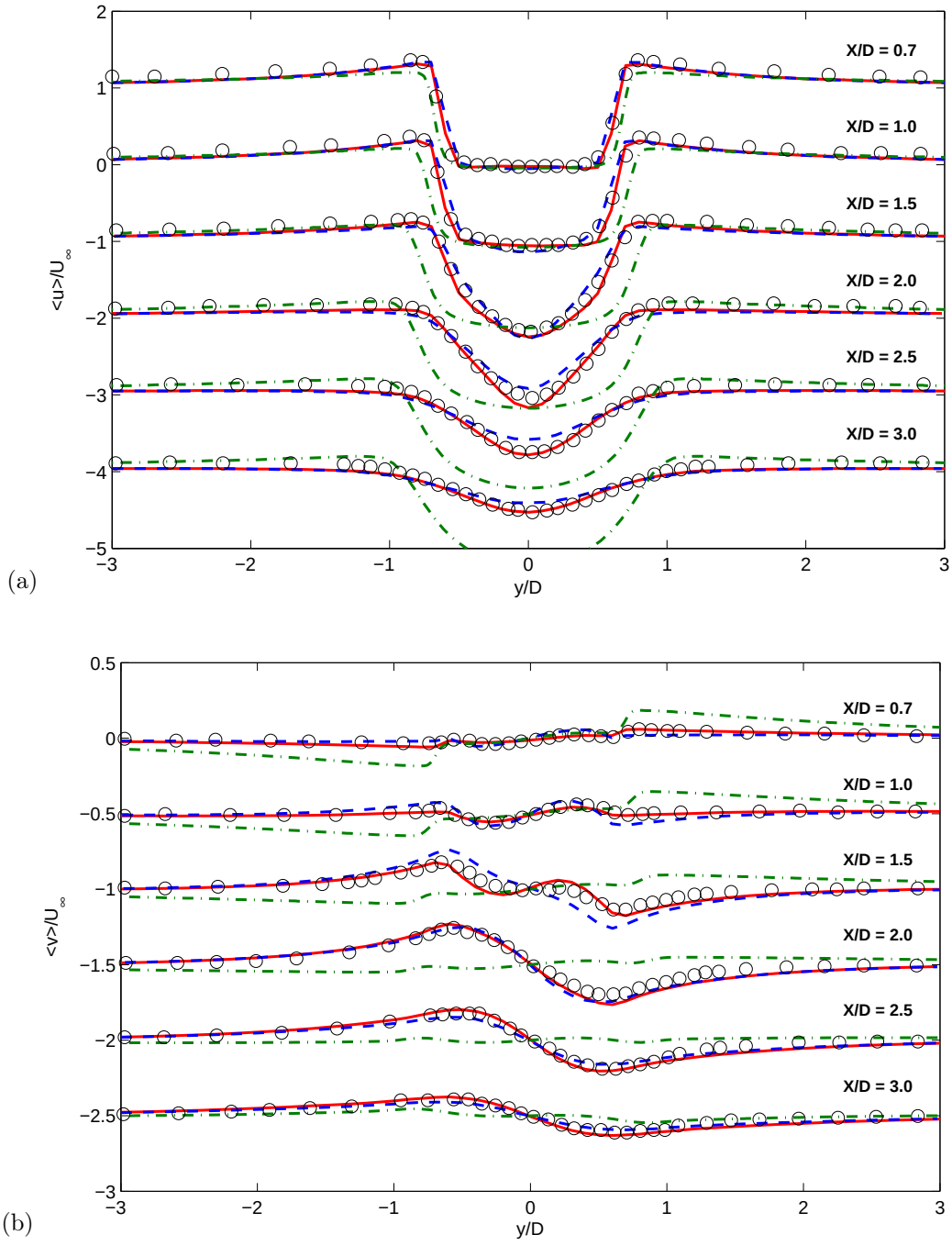

Figure 3-10. Experiment measurement (○) compared to RANS SST (· - ·), IDDES (- - -), and WALE (——) for (a) stream-wise and (b) cross-stream normalized mean velocities at different stream-wise planes downstream of cylinder.

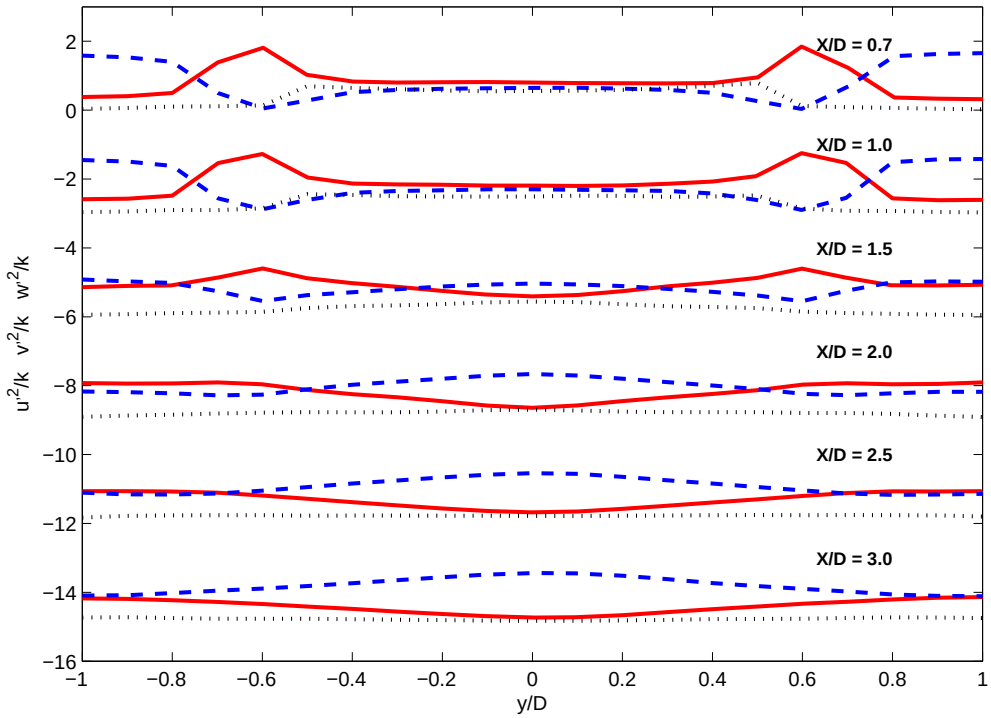

Figure 3-11. WALE resolved Reynolds Stress u'^2/k (——), v'^2/k (- - -), and w'^2/k ($\cdot\ \cdot\ \cdot$) at different stream-wise planes downstream of cylinder.

Figure 3-12 compares the fluctuating velocity components between IDDES and WALE. The largest variation between the models is found for the cross-stream component at $X/D = 1.5$, where prediction is $1.5X$ the experimental uncertainty. This deviation is consistent with early transitioning of the wake for the IDDES mean cross-stream flow. For both the WALE and IDDES models, only the resolved fluctuating component are plotted in Figure 3-12. For the IDDES model the resolve, modeled, and total turbulent kinetic energy (k) is shown in Figure 3-14 where for the majority of the wake, 95% of the total k is resolved. The experimental uncertainty is $\pm 10\%$, therefore the resolve k is a good representation of the total predicted k. At plane location $X/D = 0.7$, the outer shear layer is found to have 75% of the total k is resolved. This drop in resolution is consistent with the largest miss in Figure 3-12 where both WALE and IDDES under-predict the fluctuation stream-wise velocity.

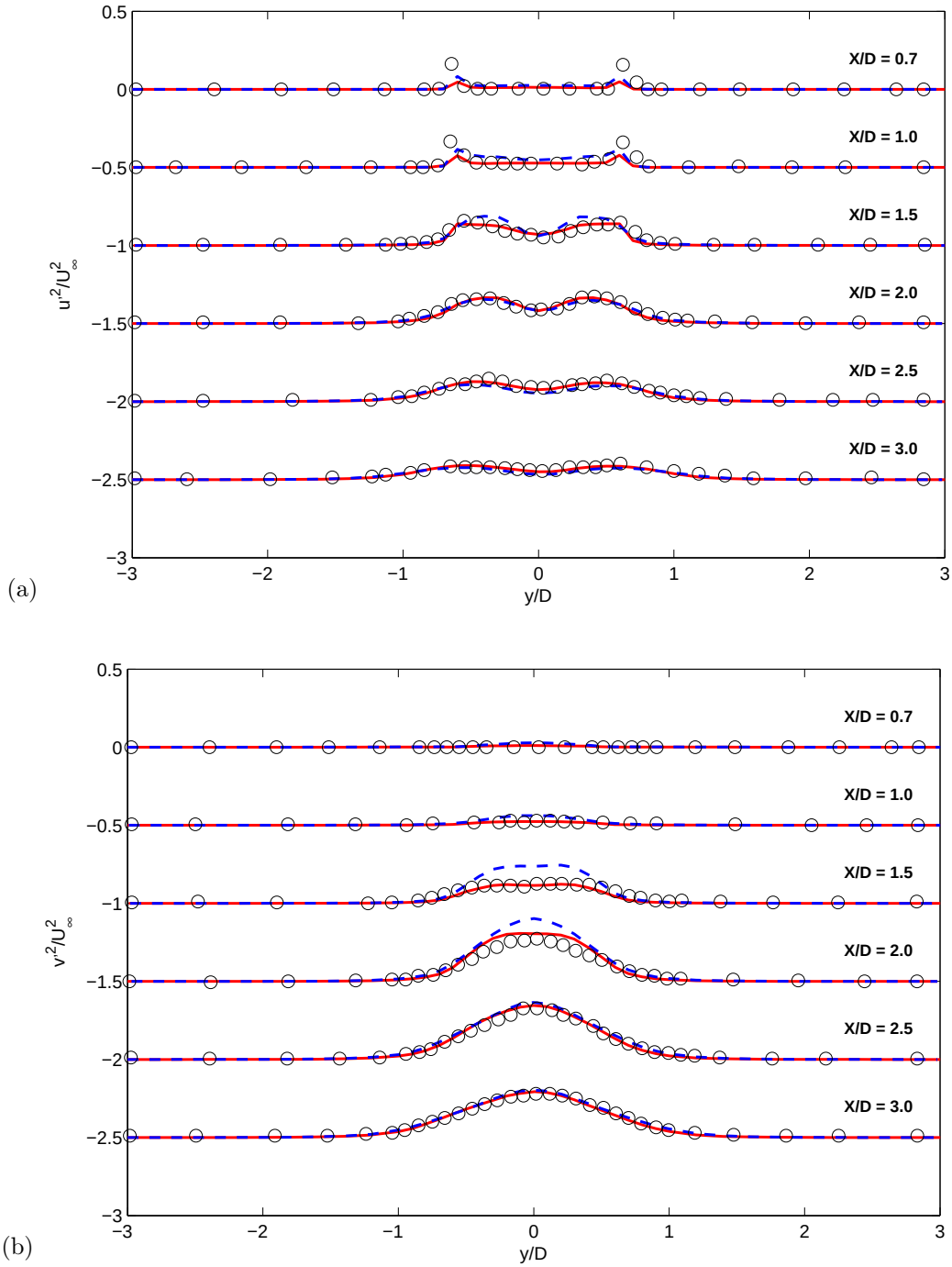

Figure 3-12. Experiment measurement (○) compared to IDDES (- - -) and WALE (——) for (a) stream-wise (b) and cross-stream normalized velocities fluctuations at different stream-wise planes downstream of cylinder.

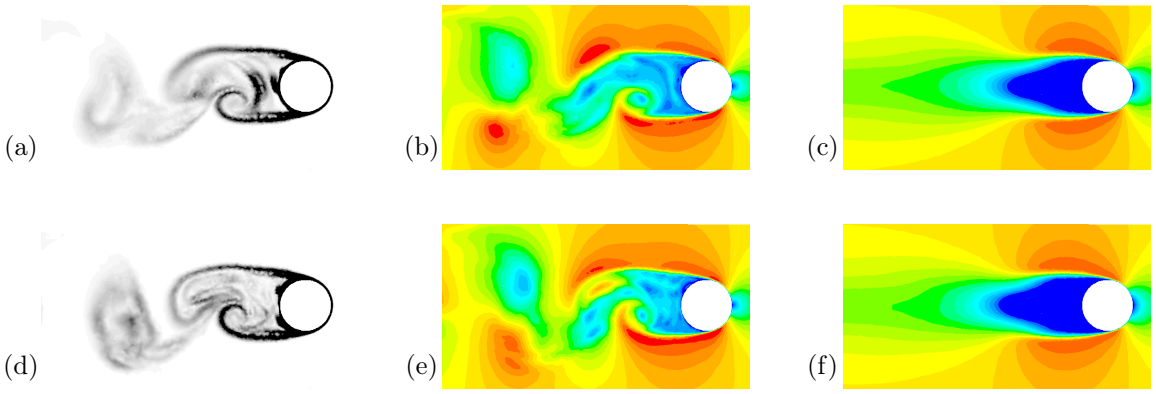

Figure 3-13. Scale resolved model comparison. IDDES (a) numerical Schlieren, (b) instantaneous velocity, and (c) mean stream-wise velocity. WALE (d) numerical Schlieren, (e) instantaneous velocity, and (f) mean stream-wise velocity.

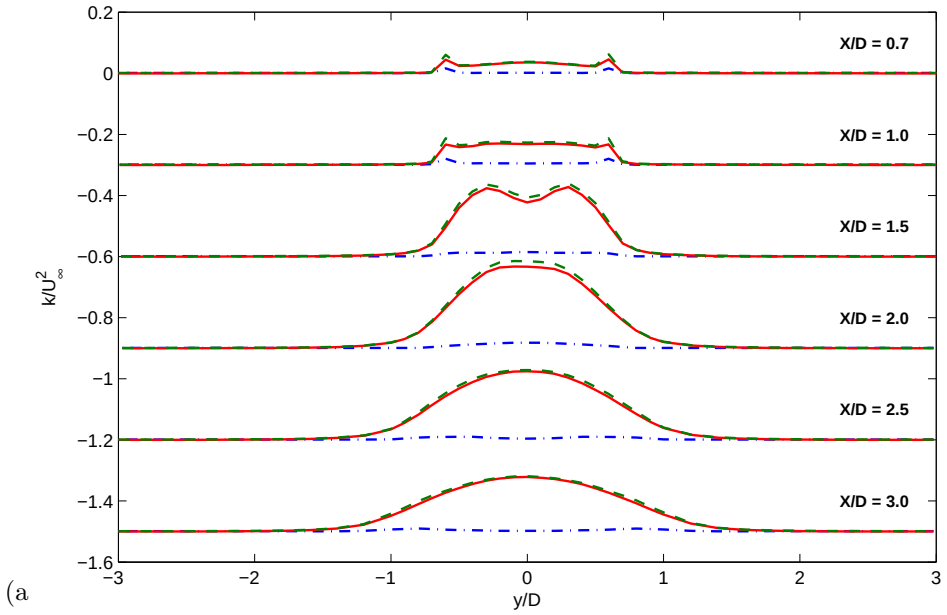

Figure 3-14. IDDES resolved (——), modeled (· - - ·), and total (- - -) turbulent kinetic energy at different stream-wise planes downstream of cylinder.

3.4 Non-conformal Interface

In order to look at a vane/blade interaction computationally, a sliding mesh approach is taken. There is also a need to use periodic interfaces to limit the computational

domain size and cost. In both cases a non-conformal mesh interface is employed. This canonical case is used to assess the impact of a non-conformal mesh interface on turbulent eddies crossing the interface placed at $X/D = 1.25$. The tetrahedral element size is maintained upstream and downstream of the interface however, one to one nodal connection is not maintained. Figure 3-15 shows there is no impact to the mean velocity due to the non-conformal interface. This is also true for the fluctuating velocity components. Therefore, this approach is applied to the HPT cases at the sliding mesh or periodic interfaces.

3.5 Cylinder Surface Heat Transfer

A separate experimental study, to measure the cylinder wall heat flux, was performed by Nakamura and Igarashi [74]. The heat flux is measured as a function of angle, where 0 degrees is found at the upstream stagnation point of the cylinder. Computationally, the surface of the cylinder is treated as a fixed wall temperature where T_{wall}/Tt_{∞}=1.1. Figure 3-16 compares the IDDES and WALE model results of $Re_D = 2580$ to the experimental results of $Re_D = 3000$. The difference in Re_D is not address at this time. Agreement between CFD and data is found for the upstream face of the cylinder. However, after the separation point on the cylinder surface both IDDES and WALE over-predict the non-dimensional heat flux where the difference in Re_D likely contributions to the predictive miss. Predictions of Bose et al. [75] using the Dynamic SGS model also predicted higher wall heat flux after the separation point where surface roughness or free-stream turbulence were also believed to influence the predictive miss. The predictive capability of wall heat flux is again quantified in the next chapter on a HPT vane surface subjected to different levels of free-stream turbulence.

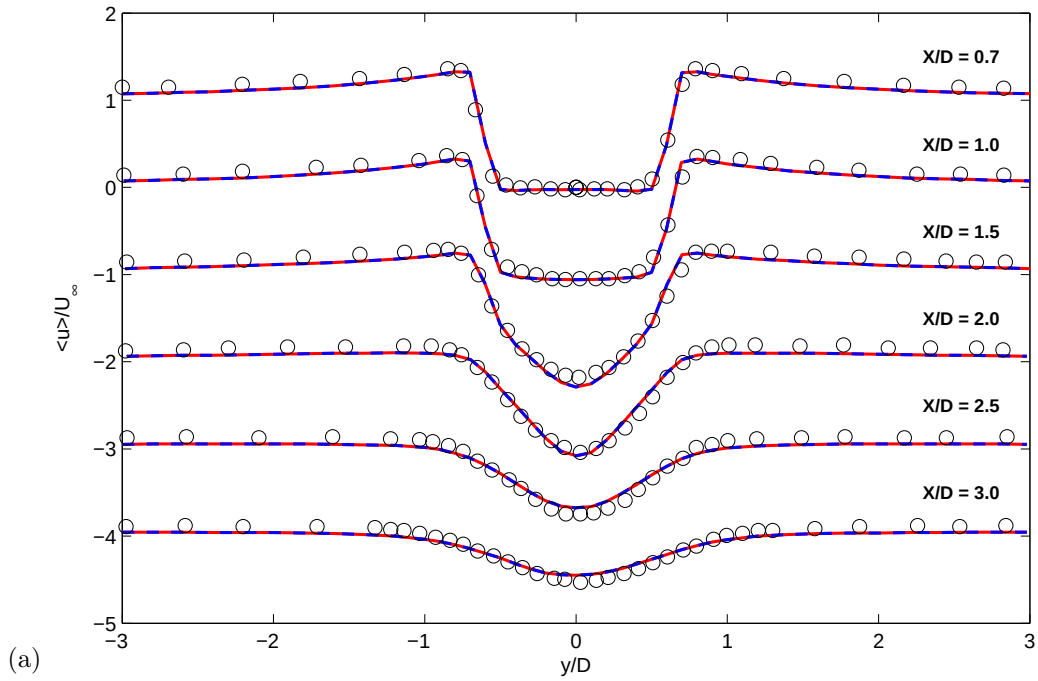

(a)

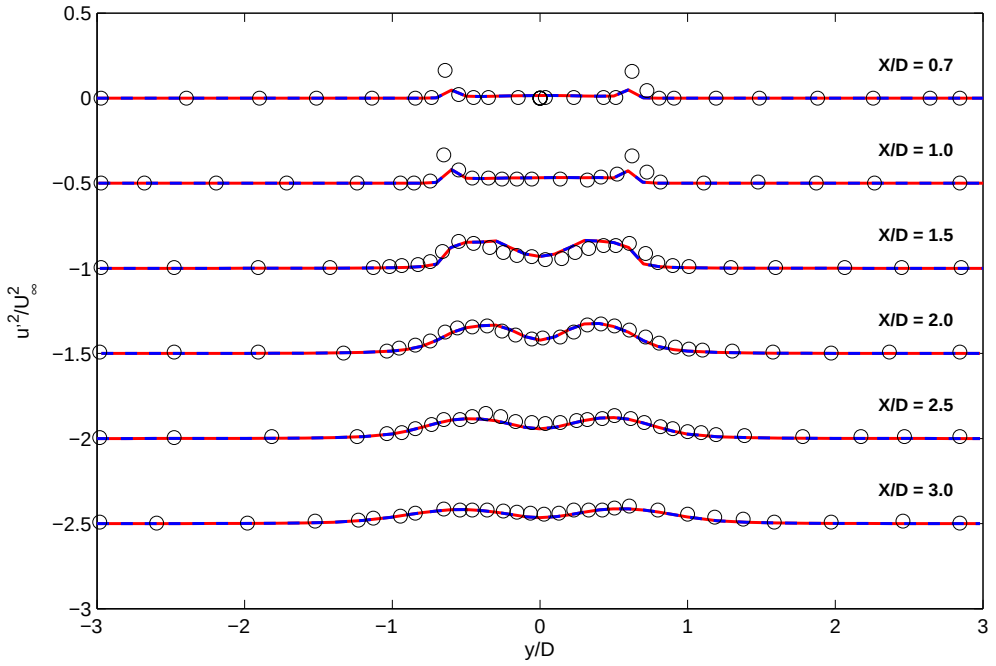

(b)

Figure 3-15. Experiment measurement (○) compared to non-conformal (- - -) and comformal (——) interfaces at $X/D = 1.0$ for stream-wise (a) mean and (b) fluctuating normalized velocities at different stream-wise planes downstream of cylinder.

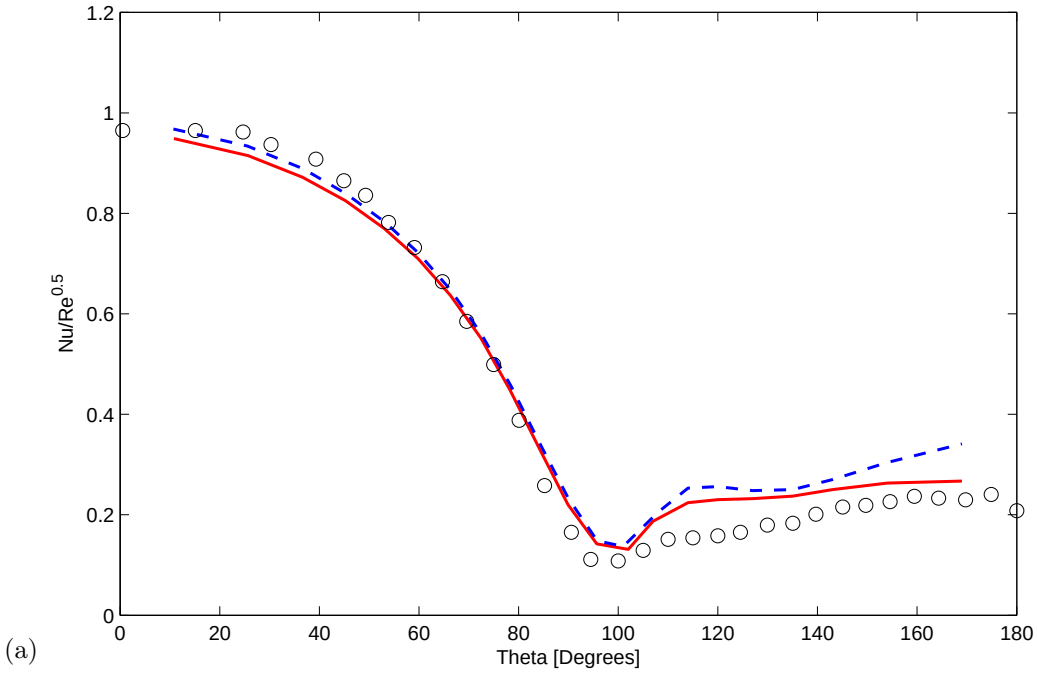

(a)

Figure 3-16. Experiment measurement (○) compared to IDDES (- - -) and WALE (——) predictions of non-dimensional wall heat flux.

3.6 Summary

For the current fundamental test case, WALE and IDDES show accurate predictions of first and second-order velocity statistics on unstructured tetrahedral meshes with Fluent using a pressure-based coupled second-order solver. The low Reynolds number and simple geometry allowed for a quick turn-around for modeling assessment. Comparison to the experimental results of Konstantinidis et al. [71] demonstrated Fluent WALE predictions were within the experimental uncertainty for first-order statistics and 2X experimental uncertainty for second-order statistics regardless of mesh topology. This helps address concerns of mesh topology on numerical dissipation and spatial order accuracy. This is a key motivation for the current work where we wanted to understand the capability of executing a second-order code on a mesh of prisms and tetrahedral. This study is the first step in demonstrating accurate scale-resolved results with a secondary order code provided adequate mesh resolution and quality. It should also be noted that the Fluent WALE results are found to have the same

level of predictive agreement found with the high-order spectral code of Mohammad et al. [73] for the same geometry and conditions.

It is found that the Fluent IDDES model was able to provide mean flow predictions within the experimental uncertainty with the exception of $X/D = 1.5$. The cross-stream fluctuating velocity prediction was within $1.5X$ the experimental uncertainty at locations $X/D = 1.5$ and 2.0, all other locations are within experimental uncertainty for IDDES. This provides confidence to next move to the more complex flow field of a HPT vane using the IDDES model. The cylinder study provided quality measurements with uncertainty, well posed boundary conditions, and detailed geometry essential for turbulence modeling assessment. Accurately capturing the developing shear layer is necessary for the prediction of HPT vane and blade trailing-edge wakes that will be addressed in the next chapters. Focus is placed on the far wake locations ($X/D > 20$) where capturing the precise wake separation region ($X/D < 1$) is secondary.

Chapter 4

Review of HPT Vane Experimental and Computational Studies

The experimental study of Arts and Rouvroit [34] has received significant attention by the academic and industrial communities given the well-characterized experiment for assessment of heat transfer coefficient (HTC) prediction for a HPT vane at engine scale conditions. In addition, the range of tested Reynolds numbers and free-stream turbulence conditions provide a challenging but well-suited case for the prediction of BL transition and resulting surface heat transfer. This chapter provides an overview of the experimental studies of Arts and Rouvroit [34] and related computational studies.

4.1 Experimental HPT Vane Study

Uncooled turbine vane experimental studies, reported by Arts and Rouvroit [34], have been carried out in a linear cascade in the von Karman Institute Isentropic Light Piston Compression Tube facility shown in Figure 4-1. Studies were performed at an inlet angle of attack of 0 degrees and run at Re_2 and $M_{2,is}$ conditions representative of a high pressure turbine vane. The Reynolds number, Re_2, is a function of the vane true chord and isentropic exit conditions and the Mach number, $M_{2,is}$, is dependent on the isentropic exit conditions. The linear cascade consisted of 5 vanes where the center vane was instrumented either for static pressure or heat flux measurements. The span

of the tunnel is 1.48 times the chord of the vane to eliminate the impact of end-wall effects on the pitch-line measurements. The vane geometry is summarized in Table 4.1 and shown in Figure 4-2 where the vane true chord (C), axial chord (C_{ax}), throat (g), pitch (p), and trailing-edge diameter (D_{TE}) are provided. The complete vane description and coordinates can be found in the publications of Arts and Rouvroit [34, 22]. The primary focus of the experimental study is the measurement of the convective heat transfer coefficient. The experiment definition is

$$h = \frac{q_{wall}}{T_{t1} - T_{wall}} \tag{4.1}$$

where q_{wall} is the measured wall heat flux, T_{t1} is the inlet total temperature, and T_{wall} is the local wall temperature. T_{wall} is reported and assumed constant over the entire vane due to the short test duration time (<400 ms) in the VKI CT-2 blow down facility.

Table 4.1. VKI uncooled vane geometry summary.

C $[mm]$	C_{ax} $[mm]$	o/C	g/C	D_{TE}/C
67.65	36.8	0.221	0.850	0.021

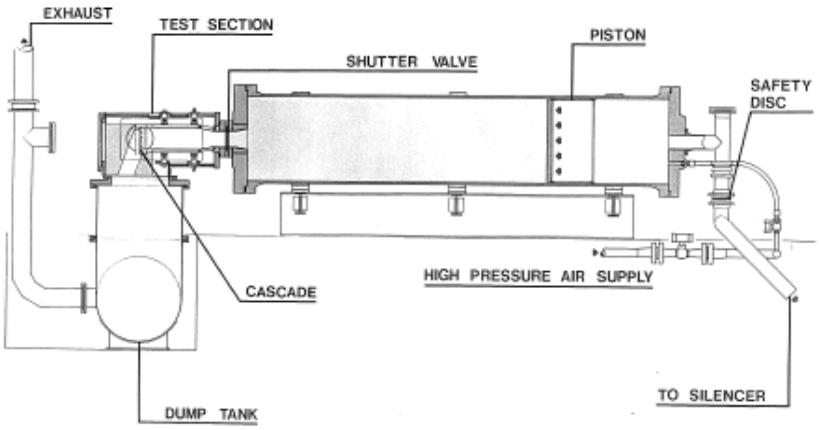

Figure 4-1. VKI Compression Tube VKI CT-2 facility [34].

A range of Reynolds, Mach numbers, and free stream TI conditions have been experimentally investigated. In order to generate free-stream turbulence in excess

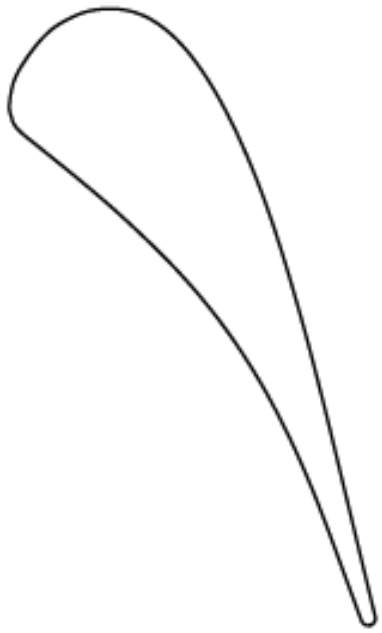

Figure 4-2. Geometry of the VKI uncooled HPT vane.

of 1%, evenly spaced bars were placed in the upstream flow [34, 76]. The upstream position of the bars, relative to the vane LE, is adjusted to vary the turbulence level. Vane inlet turbulence was measured at $X/C_{ax} = -1.49$ upstream of the leading edge of the vane. Only the stream-wise RMS velocity component was measured experimentally, therefore the turbulence reported experimentally is defined as $\frac{u'}{U_\infty}$. The reference velocity, U_∞, is based on the inlet free-stream mean velocity and u' is the stream-wise RMS component.

4.2 Summary of Prior Computational Studies

The experimental study of Arts and Rouvroit [34] provides a comprehensive range of Re, Mach, and free-stream turbulence levels to assess CFD turbulence modeling predictive capability. Near-wall mesh requirements for wall-resolved LES approaches are computationally demanding, therefore RANS approaches have included transitional models with some success [20]. One, two, and Reynolds-stress RANS equations have all been assessed over the range of test conditions. In general, results have shown

agreement with experimental measurement over a finite range of conditions showing the largest deviation at high free-stream turbulence levels [77, 20, 78]. This is a concern for industrial design where the design space may fall outside the range of the validity of the model. Additionally, up to this point, turbulence boundary conditions have been incomplete computationally where only turbulence level has been based on experimental report values. Turbulence length scale and/or decay rate has been assumed computationally. The current study uses turbulence length scale and decay provided by Arts [76] and WALE simulations to evaluate the SST with $\gamma - Re_\theta$ model. In addition, RANS modeling predictions for this case were not understood beyond HTC where the impact of BL development on wake formation are studied in the current effort.

For selected cases, Bhaskaran [35] then Collado et al. [16] showed improved heat transfer prediction by better capturing the transitional BL with LES. Each of their computational approaches are summarized in Table 4.2. For reference, the current computational approach is included in the table. Studies leading to the current approach are discussed in detail in Chapter 5. A summary of the predictions from previous work is compared to the experiment measurements in Figure 4-3 and 4-4. Case MUR129, Nu_C is representative of subsonic vane with generation of no free-stream turbulence where

$$Nu_C = \frac{hC}{k} \tag{4.2}$$

where C is the true chord of the vane and k is the thermal conductivity. The surface heat flux is indicative of a laminar BL at $s/C = 1$ on the suction side (SS) surface (region of $dp/ds \approx 0$) based on the laminar flat plate correlation

$$Nu_x = 0.332 Re^{1/2} Pr^{1/3} \tag{4.3}$$

where $Nu_x \approx 330$ at $s/C = 1$ [79]. However, an increase in Nu_C is found near the TE on the SS. Bhaskaran [35] is found to be in good agreement with measurement, where Collado et al. [16] is found to predict early transition on the SS. Collado et al. [16] did note further improvement was needed in the near-wall mesh for the unstructured

Table 4.2. Previous and current LES based approaches for case MUR235. Case MUR129 is include in parenthesis.

Case	Bhaskaran [35]	Collado [16]	Collado [16]	Current
Case	235(129)	235(129)	235(129)	235(129)
TI Inlet X/C_{ax}	-1.4	-1.3	-1.3	-1.49
TI%	7.0(0)	6.0(0)	6.0(0)	5.5(0)
TI Generation	Synthetic	Synthetic	Synthetic	Bars
LES SGS Model	Dynamic	WALE	WALE	WALE
Spatial Scheme	6th order	4th order	3rd order	2nd order
Mesh Type	Structured	Structured	Unstructured	Unstructured
Mesh Cell Count	$130M$	$30M$	$30M$	$120M(50M)$
$Span/C$	17	15	10	24(12)
Max $\Delta y+$	0.5	2.5	8	0.8
Max $\Delta s+$	140	250	32	60
Max $\Delta z+$	25	50	32	60
Temporal Scheme	Implicit	Implicit	Explicit	Implicit
$dt_o = tU/D_{TE}$	7.4×10^{-2}	2.9×10^{-2}	3.7×10^{-3}	4.9×10^{-2}

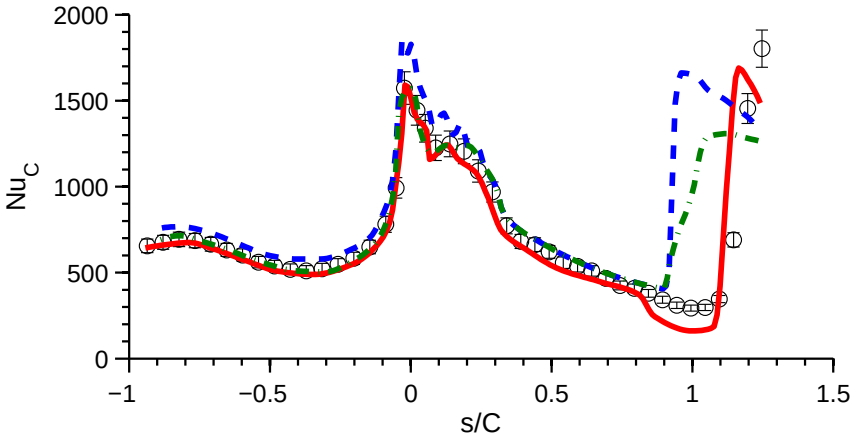

Figure 4-3. Experimental measurement of vane Nu (○) compared to Bhaskaran [35] (——), Collado et al. [16] structured (- - -), and Collado et al. [16] unstructured (· - ·) predictions for case MUR129.

cases, where $\Delta y+$ well exceeds a value of 1.

The impact of increasing inlet turbulence and Mach number is clearly seen for condition MUR235. Collado et al. [16] noted a correlation with the transition location to the SS shock on the vane for MUR235. Unfortunately, the impact of an under-resolved near-wall mesh on the prediction accuracy was not addressed. Predictions by Bhaskaran [35] are found to under-predict Nu in Figure 4-4. A sensitivity study to

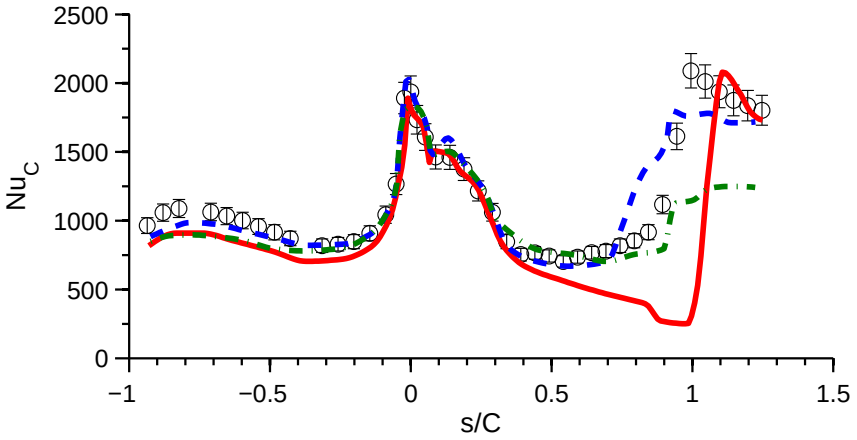

Figure 4-4. Experimental measurement of vane Nu ($\circ$) compared to Bhaskaran [35] (——), Collado et al. [16] structured (- - -), and Collado et al. [16] unstructured ($\cdot$ - $\cdot$) predictions for case MUR235. Case MUR217 ($\triangle$) with free-stream $TI = 4\%$ is also shown.

turbulent length scale was completed showing lead-edge Nu increased with decreasing length scale normalized to the vane true chord from 0.011 to 0.085.

Questions still remain from the previous LES studies completed and can be summarized as follows. Collado et al. [16] noted structured versus unstructured comparisons were incomplete due to open questions on the near-wall mesh density used. For case MUR235, synthetic turbulence was used by both Collado et al. [16] and Bhaskaran [35]. Therefore, the free-stream turbulence length scale and decay difference between prediction and experimental measurement was not closed. Current simulations include upstream bars to generate the inlet turbulence matched to the experimental setup used by Arts [76]. Finally, the previously published work has focused on the impact of free-stream turbulence on HTC and BL. Studies going forward are expanded to attenuation of turbulence and BL development and the impact on wake formation and HPT stage interaction.

Chapter 5

HPT Vane Computational Approach

Computational modeling approaches are now assessed for the current effort relative to the HPT experimental studies of Arts and Rouvroit [34]. Chapter 3 presented evaluations of different turbulence modeling approaches conducted on a cylinder in cross-flow under low Reynolds number and incompressible conditions. These flow conditions and simple geometry facilitated quick turn-around for modeling assessment. Lessons learned are now applied to a pitch-line HPT uncooled vane that is representative of real engine operating conditions. Modeling sensitivities are executed to build confidence in the approach at engine operating conditions for RANS, HLES, and LES modeling approaches. These established modeling approaches are also extrapolated to higher levels for free-stream turbulence. Ultimately, the objective is to establish an approach to develop a better understanding of the impact of turbulence on a 3D engine centerline stage design with axisymmetric endwalls and blade tip clearance.

5.1 Current Study Computational Approach

Two computational domains used for the pitch-line aero-thermal study of the Arts and Rouvroit [34] HPT uncooled vane are shown in Figure 5-1 and 5-2. The domain shown in Figure 5-2 is used for LES and Hybrid LES simulations where upstream bars generate free-stream turbulence to match the experimental set up of Arts [76]. This is done to properly represent generated turbulence level, scales, and decay. The inlet

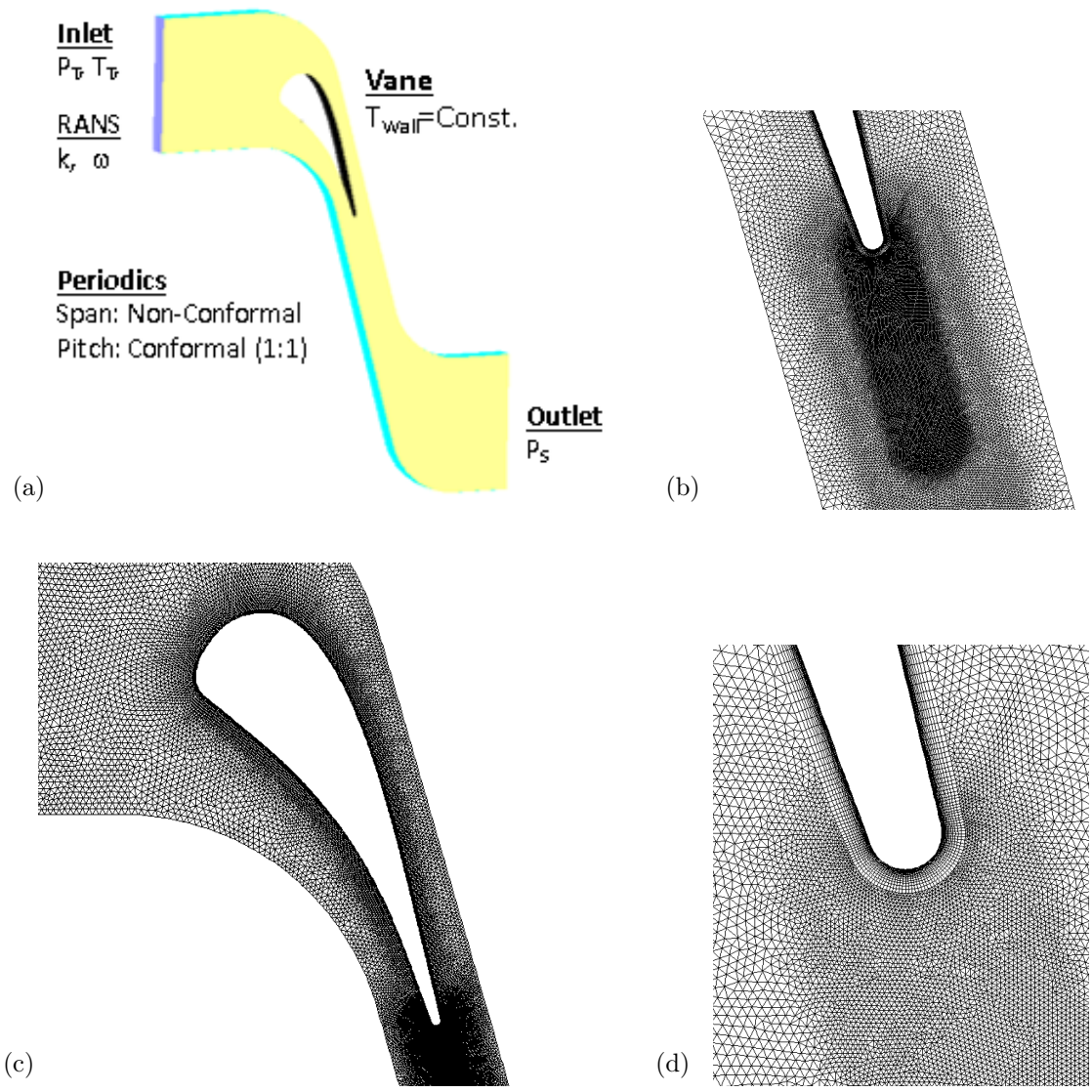

Figure 5-1. Uncooled vane (a) computational domain, (b) wake mesh, (c) airfoil mesh, and (d) trailing edge mesh.

of the computational domain in Figure 5-1 is set to the experimental measurement plane at $X/C_{ax} = -1.49$ where $X = 0$ is the LE of the vane. This approach is used for simulation with no inlet turbulence or when specifying k and ω for RANS inlet boundary conditions. RANS inlet boundary conditions for k are based on the experimentally measured inlet turbulence. For the cases of elevated turbulence, ω is tuned to match the decay of the bar generated turbulence at plane $X/C_{ax} = -1.49$.

The computational domain exit is placed at $X/C_{ax} = 3.0$ to allow the domain to

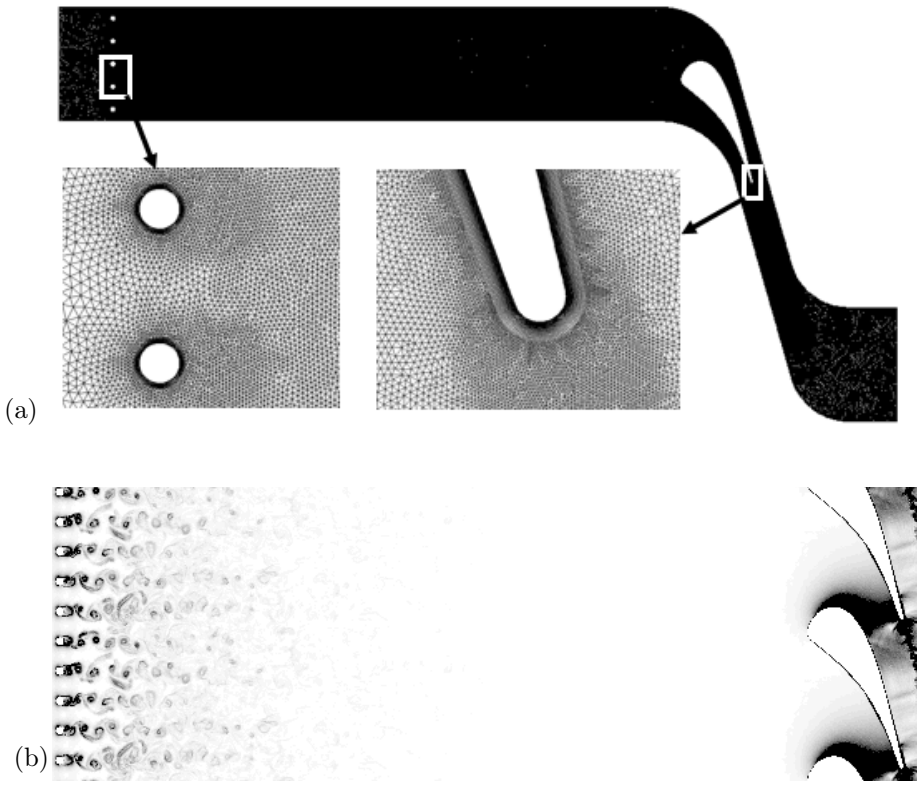

Figure 5-2. Vane case MUR226 (a) meshed domain and (b) numerical Schlieren $C|\Delta\rho|/\rho$, where C is chord.

include the wake measurement plane at $X/C_{ax} = 1.44$. Pitch-line measurements of HTC and downstream wake total pressure were made for the linear cascade with a span to chord ratio of 1.48 removing end-wall effect. The span extent was therefore large enough to allow statistical quantities to decorrelate, resulting in a statistically two-dimensional flow at the pitch. Additionally, the 5 vane (7 passage) cascade ensure periodic pitch-wise flow conditions. Therefore, the computational domain uses both span and pitch-wise periodic interfaces. The unstructured mesh approach uses a conformal interface in pitch and non-conformal in span. A conformal pitch-wise interface was driven by the Fluent solver requirement when moving to slide mesh simulation in Chapters 7 and 8. Non-conformal interfaces are not compatible for sliding mesh simulations in Fluent v16. The extent of the LES span-wise domain requirement was driven by either the vane TE vortex generation or the vortex structures generated from the upstream bars. The bar diameter was approximately 2X the vane TE

thickness which resulted in a span-wise domain increase of 2X when including the upstream bars (see Table 4.2). Further justification in span-wise domain requirement is discussed later in this chapter.

Uniform boundary conditions are provided for inlet total pressure and temperature where the flow enters normal to the domain inlet plane. Uniform static pressure is provided at the domain exit plane. The non-dimensional conditions for each simulation case is provided in Table 5.1. A fixed wall temperature and no-slip condition is prescribed at the vane wall. The wall temperature, provided by Arts and Rouvroit [34], is assumed constant due to the $< 400ms$ test time duration for the blow-down facility.

Table 5.1. VKI uncooled vane modeled test conditions.

$Case$	$Re_{C,2}$	$M_{2,is}$	$u'/U\%$	$T_{wall}[K]$
MUR129	1.14×10^6	0.84	0.8	300
MUR217	1.16×10^6	0.93	4.0	300
MUR235	1.15×10^6	0.93	6.0	300
MUR228	0.59×10^6	0.93	1.0	300
MUR226	0.58×10^6	0.92	4.0	300
MUR224	0.59×10^6	0.93	6.0	300

LES, HLES, and RANS simulations are run using ANSYS Fluent v16. Table 5.2 provides the list of turbulence models used to generate results presented in this chapter. Further detail of the turbulence model and numerical scheme selected were provided in Chapter 2. Unstructured meshing is used consisting of prism elements near the solid wall and tetrahedral elements in the core flow regions. There are no resulting pyramid elements in the transition from prism to tetrahedral elements. Mesh cell maximum skewness was above 0.5. Additional meshing metrics are presented in Table 5.3. The total prism layer thickness is selected to meet maximum BL thickness across all conditions run. The values of $\Delta y+$, $\Delta s+$, and $\Delta z+$ as a function of vane surface distance for each turbulence modeling approach is presented later in this chapter. LES and HLES cases were typically run by reaching statistical steady state after 12,000 time steps followed by time averaging the flow solution an additional 12,000 iterations, at a time step of 2×10^{-7} seconds. This is equivalent to averaging over 4 flow through times from the vane LE to TE. The LES predicted Strouhal number for

the vane wake shedding was found to be 0.28 based on the TE thickness and exit velocity for the vane. This resulted in approximately 100 time step per shedding period. The current LES computational approach, for MUR129 and MUR235, is summarized and compared to previous studies in Table 4.2. Justification of the mesh resolution, domain extent, time step selection, and convergence criteria is a focus of this chapter.

Table 5.2. Turbulence model summary.

Model	Description
SST	SST with KL production term modifier [54]
SST-T	SST with $\gamma - Re_\theta$ transition model and KL[60]
IDDES-T	IDDES with $\gamma - Re_\theta$ transition model and KL [57]
WALE	WALE SGS model [56]

Table 5.3. Mesh quality summary.

Model	WALE	IDDES & RANS
Prism Skewness	<0.6	<0.5
Tetrahedral Skewness	<0.80	<0.5
Prism Orthogonality	>0.60	>0.55
Tetrahedral Orthogonality	>0.20	>0.20
Tetrahedral Quality	>0.15	>0.15

Second-order bounded central differencing scheme is applied for the spatial discretization of the momentum equation in WALE and IDDES calculations. The bounded central differencing scheme is based on the normalized variable diagram (NVD) approach [61] along with convection boundedness criterion (CBC). The bounded central differencing scheme is a composite NVD-scheme that consists of a pure central differencing, a blended scheme of the central differencing, and the second-order upwind scheme. It should be noted that the first-order scheme is used only when the CBC is violated. The same scheme is used for all other transport equations for the WALE calculations. IDDES modeling utilizes second-order upwind discretization scheme for all other transport equations. The second-order upwind discretization scheme is used for all transport equations for the SST and SST-T turbulence models. A bounded second-order implicit time advancement scheme is used for WALE and IDDES models.

LES serves as a computational benchmark for RANS and HLES studies, when experimental data is not available. The numerical error associated with an unstructured second-order approach is addressed by comparing to the higher order code LES solver FDL3DI performed by Bhaskaran et al. [49]. Computational domain and boundary conditions were matched between Fluent and FDL3DI for cases MUR228 and MUR226 as part of an ongoing effort at GE [48, 49, 50, 51, 80, 37]. FDL3DI is a compact finite difference method with structured overset meshing. It uses a sixth order compact finite difference scheme in space along with an implicit Beam-Warming scheme for time advancement [35, 50].

Six cases are considered computationally in this work and summarized in Table 5.1. These conditions were selected to focus on the impact of inlet turbulence and Reynolds number on the development of the vane's boundary layer (BL) and resulting local surface heat transfer and downstream wake mixing. Arts and Rouvroit [34] reported the experimental measured HTC for each conditions in Table 5.1.

Loading and wake profiles are also reported matching Re and Mach number conditions of case MUR129. The measured total pressure wake profile provides an opportunity to assess the impact of BL development on downstream wake mixing loss. The uncertainties reported by Arts and Rouvroit [34] are based on a 20:1 confidence interval. The measurement uncertainties were $\pm 0.5\%$ for pressure, $\pm 1.5\%$ for temperature, $\pm 5\%$ for the heat transfer coefficient, ± 0.2 points on the integrated loss coefficient, and ± 0.5 degrees on the exit flow angle. The current study computes the experimental uncertainty bars for both the vane surface Nu number and the downstream normalized total pressure wake. The computed total pressure wake uncertainty presented in this study is based on reported wake to wake variation and reported uncertainties above. The largest uncertainty was found for the reported wake to wake variation. This may be a result of loading variation vane to vane for the cascades or the blow down facility having some level of inlet flow variation contributing to the uncertainty of the referenced inlet total pressure.

Figure 5-3 provides the domain locations where computational comparisons of boundary layers and flow field profiles are presented in this chapter. Both mean

and RMS components are presented where LES and HLES only contain the resolved contributions. TI is defined as

$$TI = \frac{\sqrt{1/3\left(u'^2 + v'^2 + w'^2\right)}}{\langle U \rangle} \tag{5.1}$$

where u', v', and w' are each of the RMS velocity components and $\langle U \rangle$ is the local mean velocity.

No BL measurements specific to this vane are available. However, the predictions are assessed indirectly through vane surface heat flux and wake total pressure loss experimental measurement. The BL is directly assessed to theory, empirical correlations, and past published experimental findings. Linear-log plots are used to assess the state of the BL which includes the empirical correlations for the viscous sublayer

$$u+ = y+ \tag{5.2}$$

and the log layer for turbulent flow

$$u+ = \frac{1}{\kappa}\log\left(y+\right) + C \tag{5.3}$$

where $\kappa = 0.41$ and $C = 5.2$. Temperature plots include the viscous sublayer

$$T+ = Pr \cdot y+ \tag{5.4}$$

and the log layer for turbulent flow

$$T+ = \frac{1}{\kappa_t}\log\left(y+\right) + B_t \tag{5.5}$$

where $\kappa_t = 0.47$ and

$$B_t = \left(3.85\left(Pr\right)^{1/3} - 1.3\right)^2 + 2.12\log\left(Pr\right) \tag{5.6}$$

as discussed in the Fluent Theory Guide [21]. By definition a laminar boundary layer

matches Equations 5.2 and 5.4 into the log layer region. For a turbulent BL the viscous layer is $y+ \lesssim 6$ followed by the buffer layer and then the log layer $y+ \gtrsim 11$.

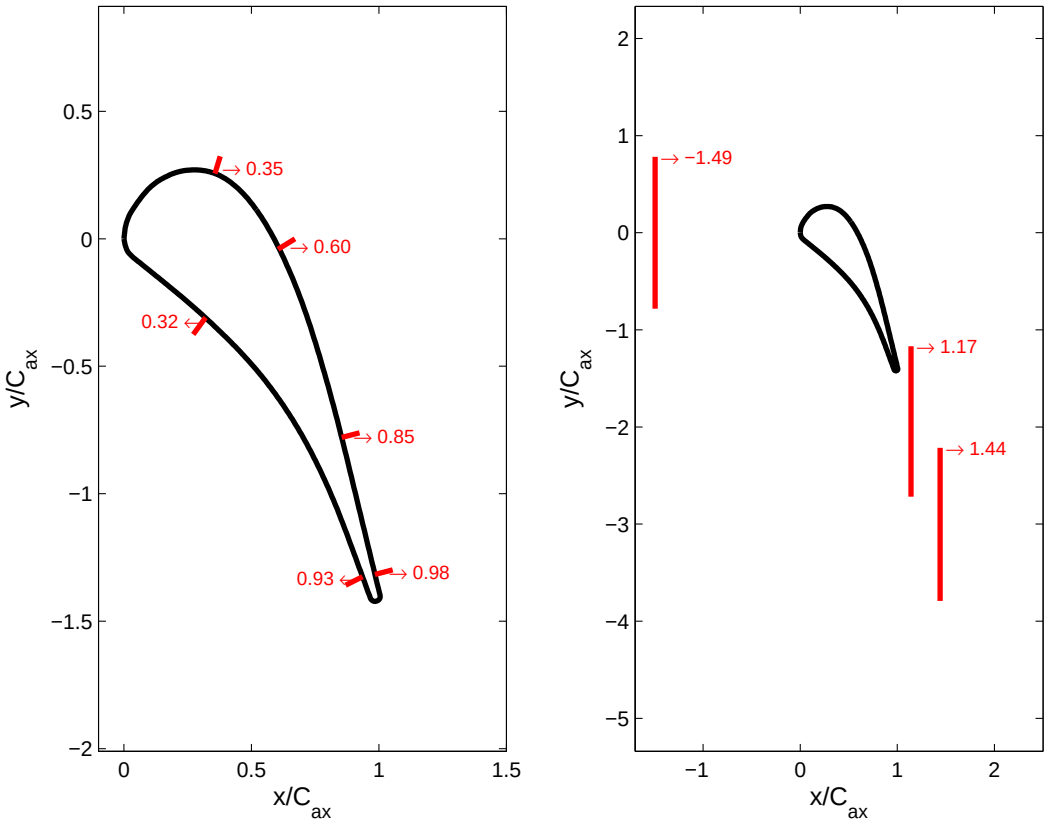

Figure 5-3. Boundary layer (left) and axial plane (right) locations for computational comparisons.

5.1.1 Zero Inlet Turbulence Generation Approach

Modeling predictions are assessed to HTC measurement for cases MUR129 and MUR228 at inlet TI of less than 1.0%. Experimental data is also available for loading and wake total pressure profile for MUR129. This allows for understanding of turbulence model capability before including additional complexity of elevated free-stream TI. The natural turbulence for the experimental facility resulted in an inlet TI<1%. However, no frequency spectrum was provided. The low inlet TI was not modeled or resolved for the current HLES and LES simulation. This is supported by running the SST-T model at 0.8 and 0% inlet TI. Since no experimental spectral analysis was provided

for case MUR129, a range of specific turbulence dissipation rates were also run corresponding to L_e/C equal to 5, 0.5, and 0.05. The dissipation length scale is defined as $L_e = k/e$ and is normalized to vane true chord, C. The SST-T sensitivities are presented in Figure 5-4 and show a negligible impact on the surface Nu and SS transition.

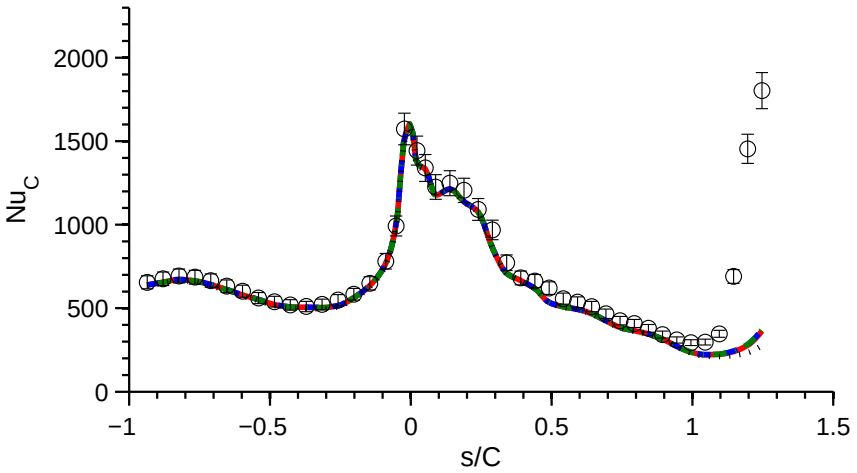

Figure 5-4. Vane mean Nu at low inlet turbulence for RANS-T inlet boundary conditions of TI=0.8% $L_e/C = 0.05$ (——), TI=0.8% $L_e/C = 0.5$ (- - -), and TI=0.8%, $L_e/C = 5.0$ (· - ·), and TI=0% (· · ·) compared to experimental cases MUR129 (○).

5.1.2 Moderate Inlet Turbulence Approach

Experimentally, elevated turbulence is generated by upstream bars with 3 mm diameter and a pitch of 12 mm [22]. The upstream location of the bars, relative to the vane leading edge, is varied to obtain two levels of inlet TI of 4% (MUR217, MUR226) and 6% (MUR235, MUR224) based on the bar locations provided by Arts [76]. Since inlet turbulence is expected to have an effect on the vane performance, it is important to accurately model the incoming turbulence structures and decay. The bars are included in the scale-resolved simulations to accurately account for the turbulence intensity, length scale, and decay. The LE of the vane is 7.8 and 5.4 X/C_{ax} downstream of the bars for cases MUR217/226 and MUR235/224, respectively. As can be seen for case MUR224 in Figure 5-2, a long inlet domain is required given the

upstream position of the bars.

In Figure 5-2 the coherent structures generated by the bars and subsequent breakdown into turbulence are illustrated. The Re_D based on the bar diameter is 6000 for case MUR226. Building from the cylinder in cross-flow study (Chapter 3), a mesh density was identified to capture the turbulence level and decay rate. While not computationally efficient, due to the long development length, the approach captures the turbulent scales, decay, and anisotropic behavior generated from the bars.

Only the stream-wise RMS velocity component was measured experimentally, therefore the turbulence reported experimentally is defined as u'/U_∞, where the reference velocity, U_∞, is based on the inlet free-stream mean velocity and u' is the stream-wise RMS component [22]. The turbulence and decay are plotted for cases MUR235, MUR224, and MUR226, where the experimentally measured values of u'/U_∞ at $X/C_{ax} = -1.49$ are shown in Figure 5-5. The placement of the upstream bars were matched to the experimental locations for each condition [76]. In general, LES results under-predict u'/U_∞ by 8 to 10% of the measure value. In addition, FDL3DI [49] is included in the comparison to quantify the impact of mesh type and code where Fluent is found to be within 5% of the turbulence level.

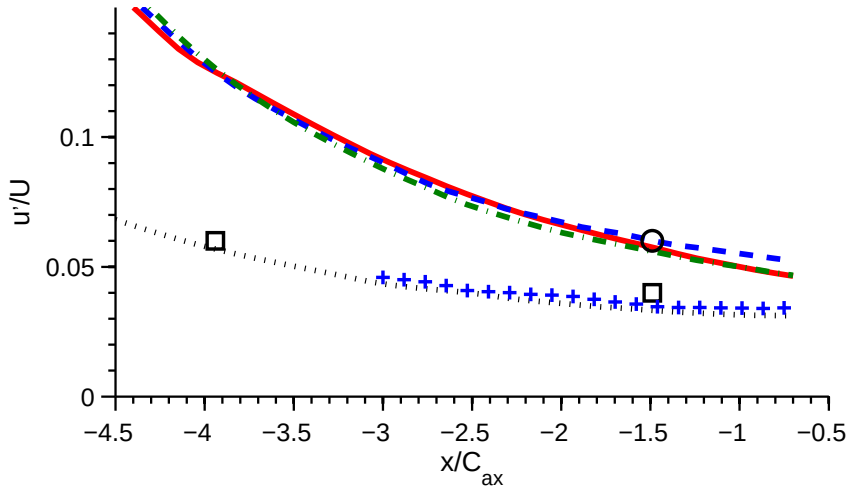

Figure 5-5. Plane averaged resolved u'/U_∞, where $X/C_{ax} = 0$ is the vane LE. WALE MUR235 (——), IDDES-T MUR235 (- - -), WALE MUR224 (· - ·), and WALE MUR226 (· · ·) are compared to experimental measurements for MUR235/224 (○) and MUR217/226 (□). FDL3DI (+) presented for case MUR226 [49].

Experimentally measured frequency peaks near 5,500 and a 2nd harmonic near 11,000 Hz were reported at $X/C_{ax} = -1.49$ [76]. Based on the free-stream velocity ($U_\infty \approx 60m/s$) and the bar diameter of 3 mm, the Strouhal number is 0.27 for the 1st harmonic. This is in good agreement with cases MUR235, MUR224, and MUR226 where frequency spectrum downstream of the bars have peak Strouhal numbers between $0.25 - 0.26$.

5.1.3 High Level Inlet Turbulence Approach

As discussed in Chapter 1, achieving combustor level turbulence and length scales can be both challenging and costly in an experimental facility. Barringer et al. [24] achieved intensity of 18% and non-dimensional integral length scale over the vane true chord of $L_I/C = 0.11$ downstream vane with a combustor simulator. For the current simulation, high level turbulence is created by moving the upstream bars closer to the vane LE, which resulted in TI=20% at $X/C_{ax} = -1.0$. Using Taylor's hypothesis for frozen turbulence, a length scale of $L_I = 0.011$ meters is calculated. Given the bar shedding frequency of 5,500 Hz and free-stream velocity of 60 m/s this results in $L_I/C = 0.16$. These conditions are in line with experimental measurements of Barringer et al. [24]. The two computational conditions are defined in Table 5.4. $Re_{C,2}$ and $M_{2,is}$ are based on the experimental cases MUR129 and MUR224 with the addition of high level turbulence.

Table 5.4. High level turbulence conditions for computation only.

$Case$	$Re_{C,2}$	$M_{2,is}$	$u'/U\%$	$T_{wall}[K]$
NB129	1.14×10^6	0.84	20	300
NB224	0.59×10^6	0.93	20	300

5.2 Modeling Sensitivity Studies

Before computational modeling approaches can be accurately assessed relative to the HPT experimental studies of Arts and Rouvroit [34], modeling sensitivity are com-

pleted for RANS, HLES, and LES approaches. This is done to build confidence in the approach at engine operating conditions along with understanding of required computational cost. First a grid independent RANS solution is confirmed. Next the mesh resolution, domain extent, time step selection, and convergence criteria is assessed for HLES and LES scale-resolved simulations. Finally, scale-resolved guidelines are provided based on lessons learned. The findings from these studies are done to provide confidence in the computational setup and approach while isolating predictive misses due to turbulence model, mesh type, and solver.

5.2.1 RANS

RANS SST-T mesh dependency studies are now performed for case MUR129. The intent was not to optimize the RANS mesh but to confirm a grid independent solution. The mesh is globally refined with exception to the first wall cell height for the vane where $\Delta y+$ remains less than 1 to maintain a wall integrated mesh approach. First cell values of $\Delta y+$, $\Delta s+$, and $\Delta z+$ are provided in Figure 5-6. Given the unstructured meshing approach $\Delta s+$ and $\Delta z+$ are equal. Mesh resolution are evaluated where an edge length change of 25% is applied.

The impact on mesh resolution is evaluated for surface Nu and wake mixing. Figure 5-7 shows a negligible change in surface Nu for all three mesh refinements. The total pressure (Figure 5-8) and TI (Figure 5-9) wake profiles are also found to be insensitive between the medium and fine mesh refinements. Figure 5-8 presents the local total pressure normalized to the inlet mass plane average total pressure, Pt_1, at $X/C_{ax} = -1.49$. Relative to the experimental uncertainty for case MUR129, the minor variation of Nu and wake total pressure due to mesh resolution are well within this uncertainty. Therefore, the RANS solution is considered to be grid converged. The proceeding chapters only present results for the fine mesh to demonstrate how the SST and SST-T models performed on the common mesh used for HLES.

The Kolmogorov scale (η) is used to quantify the local average element edge length relative to the smallest turbulent length scale. At this length scale, viscosity dominates the turbulent kinetic energy that is dissipated into heat. Figure 5-10

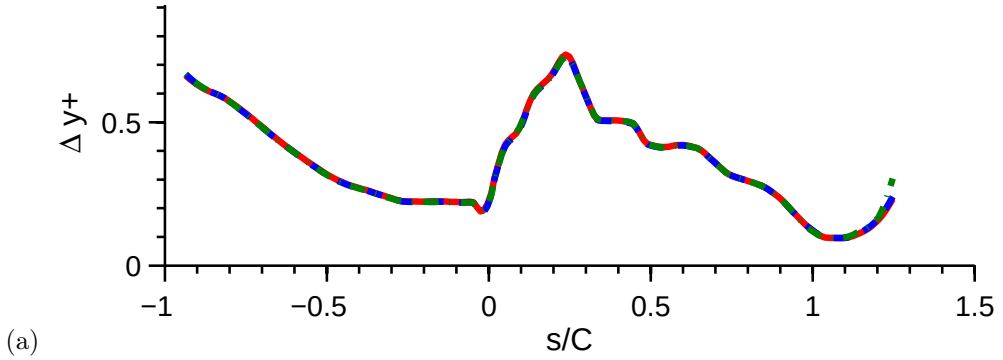

(a)

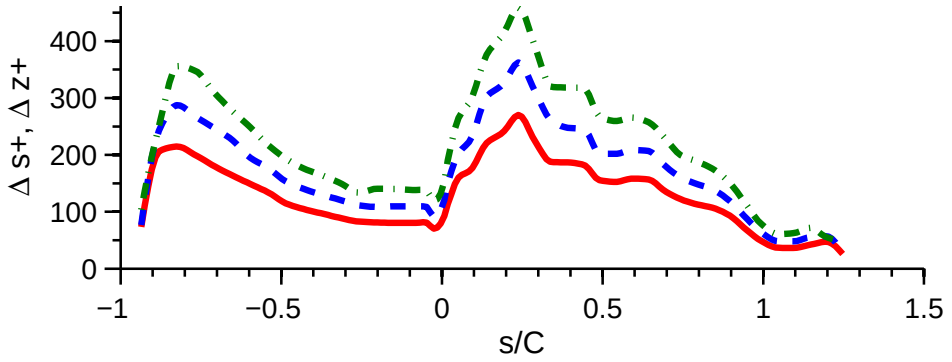

(b)

Figure 5-6. Vane (a) $\Delta y+$ and (b) $\Delta s+$ ($= \Delta z+$) for no inlet turbulence mesh study. SST-T case MUR129 for Fine (——), Medium (- - -), and Coarse (· - ·) meshes.

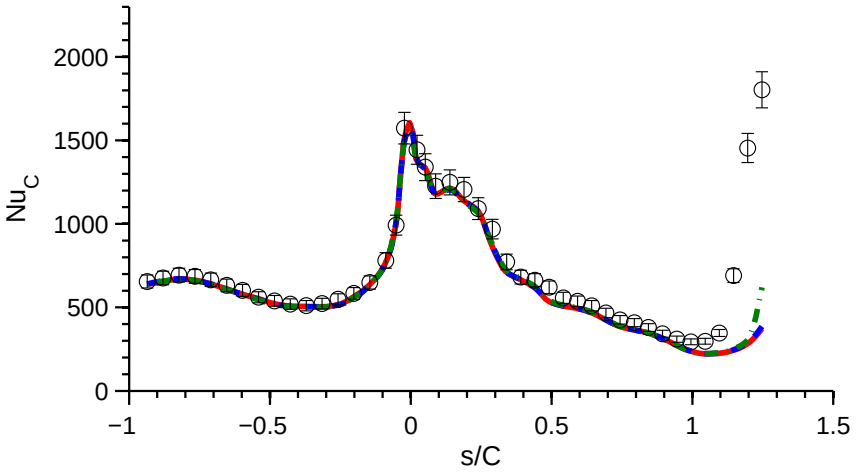

Figure 5-7. Vane mean Nu for no inlet turbulence mesh study. SST-T case MUR129 for Fine (——),) Medium (- - -), and Coarse (· - ·) meshes compared to experimental cases MUR129 (○).

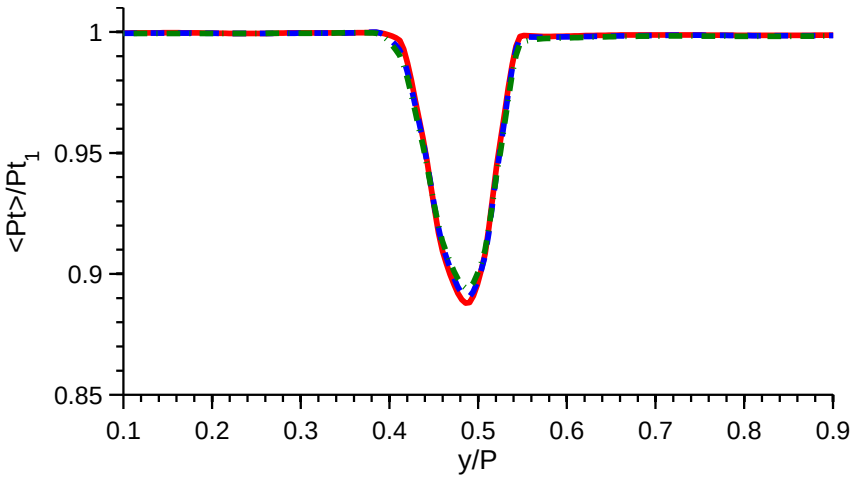

Figure 5-8. Vane normalized mean total pressure profiles for no inlet turbulence at $X/C_{ax} = 1.17$ mesh study. SST-T case MUR129 for Fine (——), Medium (- - -), and Coarse (· - ·) meshes.

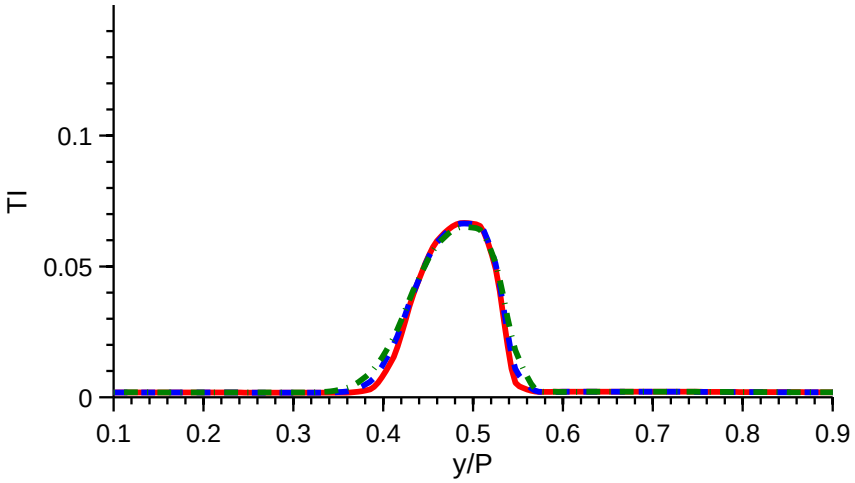

Figure 5-9. Vane local TI profiles for no inlet turbulence at $X/C_{ax} = 1.17$ mesh study. SST-T case MUR129 for Fine (——), Medium (- - -), and Coarse (· - ·) meshes.

provides contour plots of the cube root of the local element volume normalized to the Kolmogorov scale for the vane TE wake. Turbulence is generated downstream of the vane TE which is represented by the modeled kinetic energy for the SST-T model. As the mesh is refined the $V^{1/3}/\eta$ ratio is reduced in the TE region. This can be used to help target mesh resolution for scale-resolved approaches and is further discussed later in this chapter.

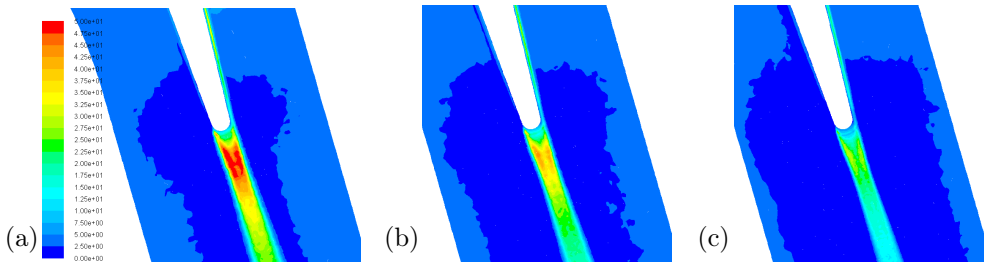

Figure 5-10. Contours of $V^{1/3}/\eta$ for (a) Coarse, (b) Medium, (c) and Fine meshes.

5.2.2 LES

The impact of mesh resolution, domain extent, time step selection, and convergence criteria is now evaluated for surface Nu and wake mixing for the LES WALE modeling approach. This is first done for case MUR129 where no inlet TI is imposed at the domain inlet. The mesh is globally refined with exception to the vane near-wall mesh where $\Delta y+$, $\Delta s+$, and $\Delta z+$ are held constant based on Table 4.2. The near mesh target for the LES simulations are revisited at the end of this section for a case with elevated inlet TI.

The impact of computational domain span (S) on the surface Nu is first assessed. Three span-wise extents relative to the vane chord are shown in Figure 5-11. Domain independence is reached for $S/C = 12$, where S/C of 12 and 18% show no change in prediction. Results are in good agreement with MUR129, capturing the transition location on the SS. However, the WALE model does over-predict the Nu on the PS and is addressed here before moving to additional sensitivities.

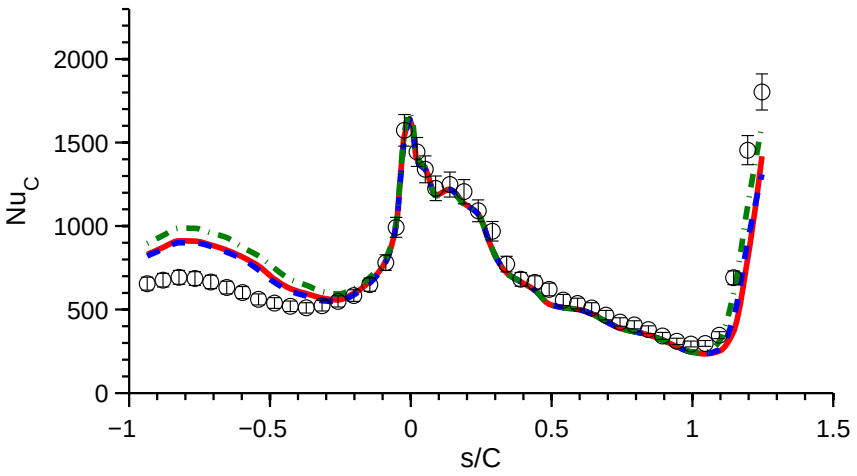

Figure 5-11. Vane mean Nu for no inlet turbulence computational span study. WALE case MUR129 for $S/C = 18\%$ (——), $S/C = 12\%$ (- - -), and $S/C = 6\%$ (· - ·) compared to experimental cases MUR129 (○).

The over-prediction of the Nu on the PS is believed to be caused by over-predicted strength of the Gortler vortex forming on the PS surface. The Gortler instability occurs under applied centrifugal force on a curved surface in the BL. The instability results in a counter rotating vortex pair. The stream-wise vortex pair is plotted along the PS surface in Figure 5-12. The resulting instantaneous Nu highlights the PS surface streaks due to the counter rotating stream-wise vorticity formed in the BL. This shows the relationship between the near-wall Gortler vortex pair and impact on the wall heat flux. The Gortler number is defined as

$$Go = \frac{U_e \theta}{\nu} \left(\frac{\theta}{R} \right)^{1/2} \tag{5.7}$$

where U_e is the velocity at the edge of the BL, R is the local radius, and θ is the BL momentum thickness. The vortical structures have been shown experimentally to form if $Go > 0.3$ [81, 82]. The Gortler number on the PS ranges from 3 to 20 for MUR129, confirming the conditions are sufficient to develop this flow instability. The wavelength of the vortex can also be compared to the experimental measurements of Winoto [83]. Winoto performed measurement over a range of concaved surfaces to determine the resulting wave length of the vortex pair for a given Gortler number. The radius of curvature was normalized to the channel height which can be compared

to the current vane PS curvature normalized to the vane throat, where $4 < R/o < 8$ is found for the vane. This results in a wavelength for case MUR129 of 0.7-1.4 mm based on the studies of Winoto [83]. Referring back to Figure 5-12 it is found the wavelength is approximately 0.8 mm where the computational span shown is 12 mm. Each vortex pair is visualized by a positive (red) and negative (blue) iso-surface of stream-wise vorticity.

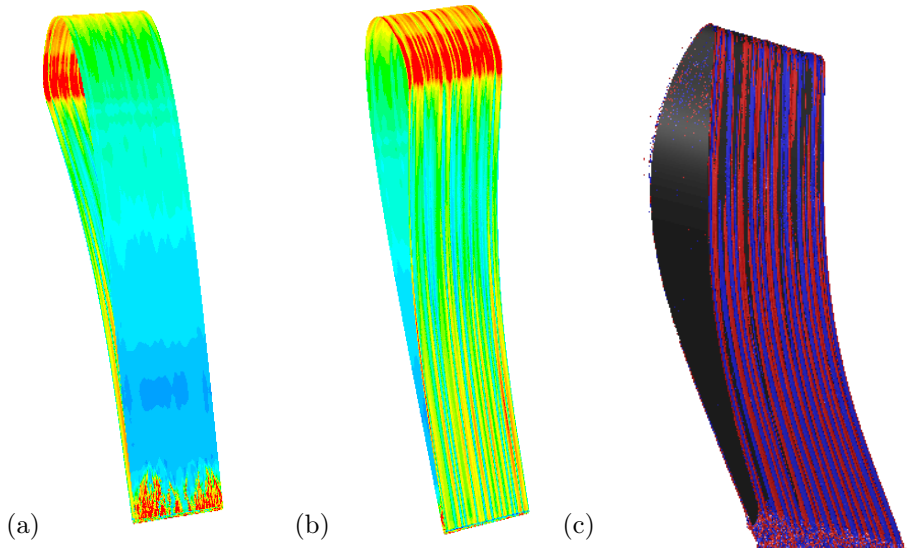

Figure 5-12. Images of (a) SS location instantaneous Nu, (b) PS instantaneous Nu, and (c) PS stream-wise vorticity iso-surface.

The contribution of the vortical structure on the pressure side Nu is further quantified by running the WALE model with a coarse near-wall mesh (Figure 5-13). The coarse mesh resolution is adequate for capturing a mean laminar BL. However, the mesh is not adequate to capture near-wall flow instabilities including BL transition. The PS surface Nu now agrees within experimental uncertainty for the under-resolved mesh where no PS vortical structures are predicted. In addition, the contribution of the SGS model was evaluated by changing C_w from 0.325 to 0. No impact on the Nu is shown on the PS, and the SS transition location has moved slightly upstream but is within the level of experimental uncertainty. A possible cause for the over-prediction

of the PS Nu is that no inlet TI was included in the WALE simulation. Low levels of roughness or TI ($\sim 1\%$) could break-up the growth of the PS vortex lowering Nu. The impact of higher free-stream TI (6%) on Nu is expected to increase Nu but computationally found to have a lower maximum PS Nu then MUR129. This elevated TI case is presented in Chapter 6.

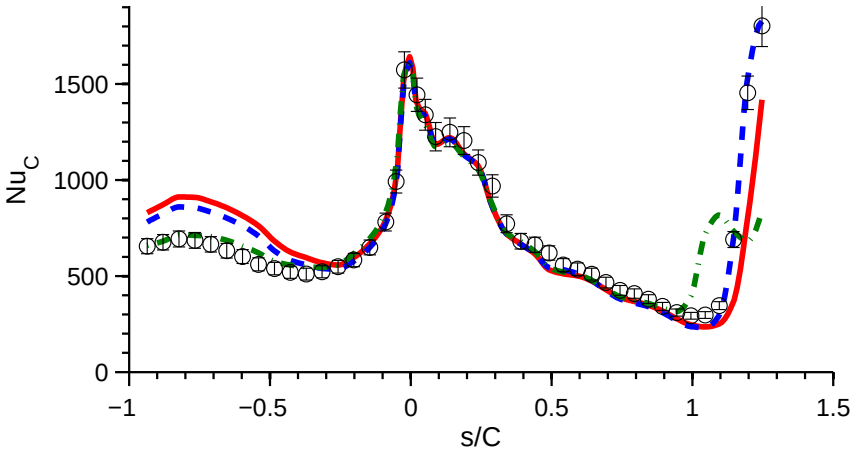

Figure 5-13. Vane mean Nu for WALE $C_w = 0.325$ & $\Delta s{+}_{max} = 50$ (——), WALE $C_w = 0$ & $\Delta s{+}_{max} = 50$ (- - -), and WALE $C_w = 0.325$ & $\Delta s{+}_{max} = 275$ (· - ·) for case MUR129 with no inlet turbulence generation. CFD compared to experimental measurement (∘).

Using the $S/C = 18$ domain, the impact time step selection and iteration per time step are presented in Figures 5-14 and 5-15, respectively. The largest impact on surface Nu is found for a time step of $\Delta t = 8 \times 10^{-7}$ where the transition is delayed on the SS. Overall, the selected range of time steps and iteration per time step have little impact on the surface Nu.

The impact of mesh resolution and domain extent are now evaluated for wake mixing. Three levels of mesh refinement are presented where the local edge length is refined by 50% in the wake. It should be noted that the fine LES and fine RANS mesh use identical refinement in the wake. Both the near (Figure 5-16) and far (Figure 5-17) wake show deviation in the wake prediction for the coarse mesh. All mesh resolutions are found to fall within the experimental uncertainty at the far wake location of $X/C_{ax} = 1.44$ relative to the vane LE. The fine mesh is then run at the 3 computational spans where S/C equals 6, 12, and 18% and shown for the near wake

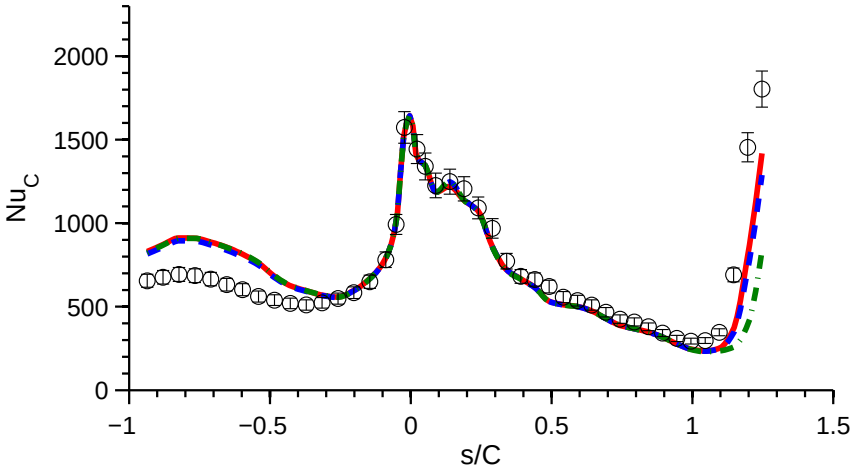

Figure 5-14. Vane mean Nu for no inlet turbulence time step study. WALE case MUR129 for $\Delta t = 2 \times 10^{-7}$ (——), $\Delta t = 4 \times 10^{-7}$ (- - -), and $\Delta t = 8 \times 10^{-7}$ (· - ·) compared to experimental cases MUR129 (○).

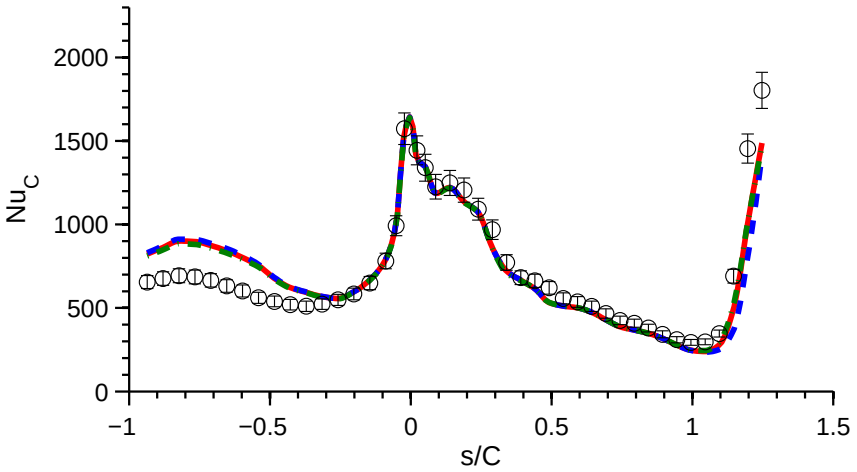

Figure 5-15. Vane mean Nu for no inlet turbulence iteration per time step study. WALE case MUR129 for 12 (——), 9 (- - -), and 6 (· - ·) iterations per time step.

location in Figure 5-18. S/C of 6 slightly deviates from the other domains but is again found to be within the relative experimental uncertainty.

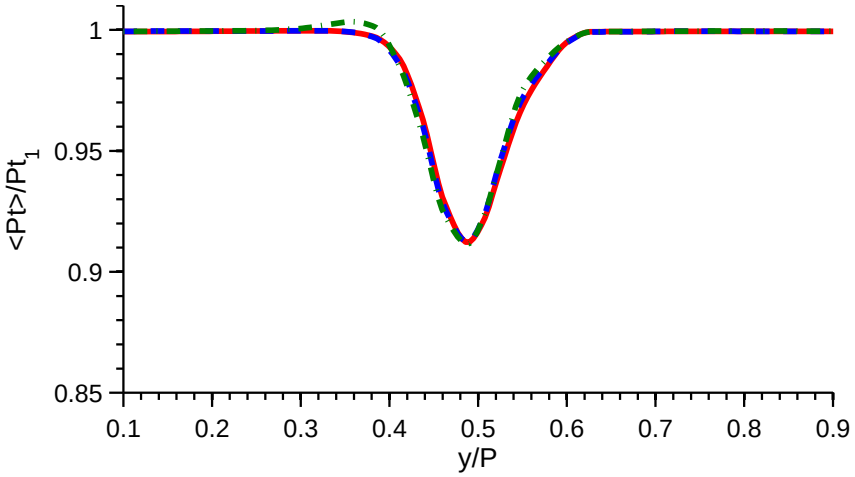

Figure 5-16. Vane normalized mean total pressure profiles for no inlet turbulence at $X/C_{ax} = 1.17$ mesh study. WALE case MUR129 for Fine (——), Medium (- - -), and Coarse (· - ·).

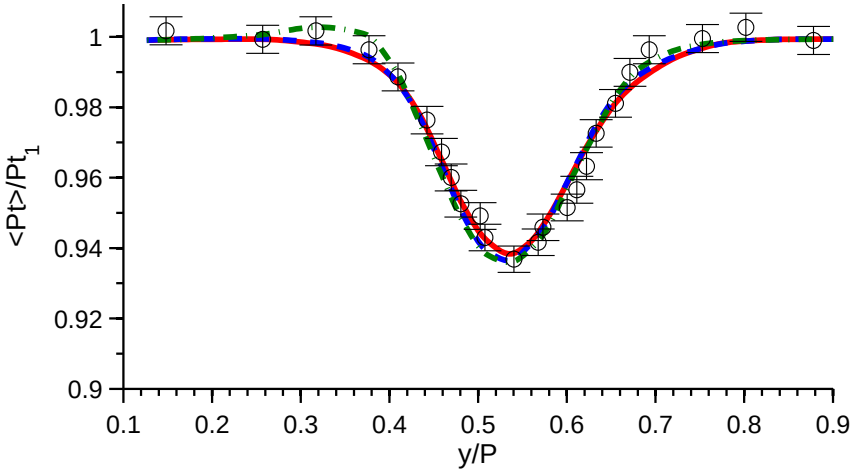

Figure 5-17. Vane normalized mean total pressure profiles for no inlet turbulence at $X/C_{ax} = 1.44$ mesh study. WALE case MUR129 for Fine (——), Medium (- - -), and Coarse (· - ·) compared to experimental cases MUR129 (○).

Next, time step and iterations per time step studies are completed using the fine mesh and $S/C = 18$ domain. As previously discussed, LES predicts a Strouhal number for the vane wake shedding of 0.28 based on the TE thickness and exit velocity for the vane. For a time step of $\Delta t = 2 \times 10^{-7}$ this resulted in approximately 100 time

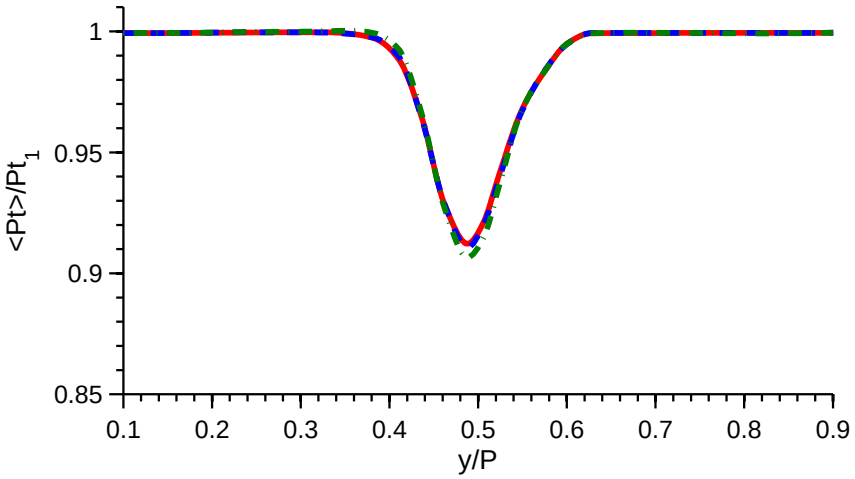

Figure 5-18. Vane normalized mean total pressure profiles at $X/C_{ax} = 1.17$ computational span study. WALE case MUR129 for $S/C = 18\%$ (——), $S/C = 12\%$ (- - -), and $S/C = 6\%$ (· - ·).

step per shedding period. This is compared to two larger time steps of $\Delta t = 4 \times 10^{-7}$ and $\Delta t = 8 \times 10^{-7}$ in Figure 5-19. A significant impact on the selected time step is found, highlighting the number of time step per shedding period required for the second-order implicit time advancement scheme. However, it is found that as low as 6 iterations per time step does not impact near wake mixing predictions in Figure 5-20.

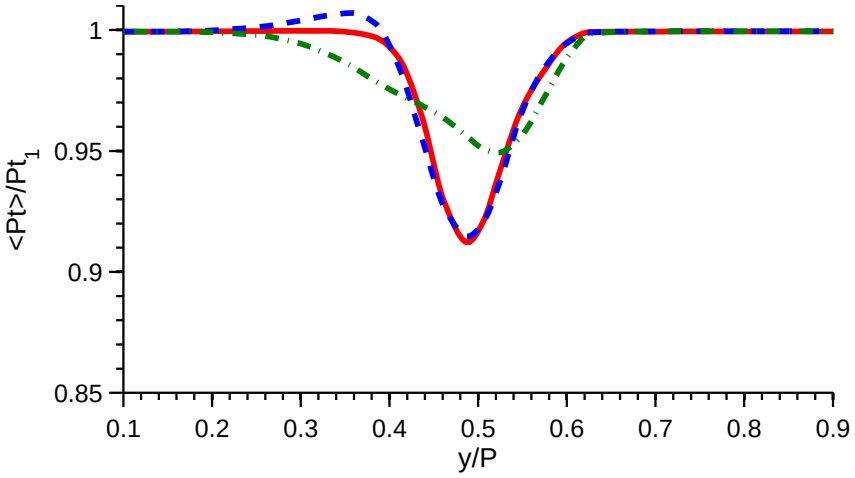

Figure 5-19. Vane normalized mean total pressure profiles for no inlet turbulence at $X/C_{ax} = 1.17$ time step study. WALE case MUR129 for $\Delta t = 2 \times 10^{-7}$ (——), $\Delta t = 4 \times 10^{-7}$ (- - -), and $\Delta t = 8 \times 10^{-7}$ (· - ·).

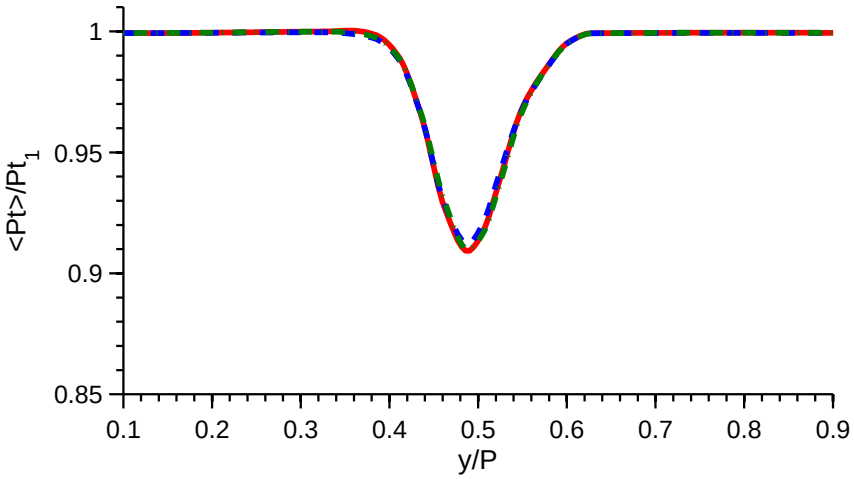

Figure 5-20. Vane normalized mean total pressure profiles for no inlet turbulence at $X/C_{ax} = 1.17$ iteration per time step study. WALE case MUR129 for 12 (——), 9 (- - -), and 6 (· - ·) iterations per time step.

Elevated Inlet Turbulence

Elevated turbulence is generated by upstream bars with 3 mm diameter and a pitch of 12 mm [22]. The bars are included in the scale-resolve simulations to accurately account for the turbulence intensity, length scale, and decay. The cylinder in cross-flow study (Chapter 3) is leveraged to determine the mesh density to capture the turbulence level and decay rate. The stream-wise TI was only measured experimentally (u'/U_∞). However, it is important to ensure each fluctuating velocity component is independent of the domain's span. Figure 5-21 plots the 3 components of RMS velocity normalized to the free-stream velocity. It is found that S/C of 24% is required to reach domain independence. The bar diameter is approximately 2X the vane TE thickness which agrees with the span-wise domain increase of 2X for the vane only case (MUR129).

The impact of near-wall mesh resolution is now evaluated for surface Nu, boundary layer formation, and wake mixing for the LES WALE modeling approach. This is done for case MUR224 where inlet TI of 6% is generated from the upstream bars. The vane near-wall mesh in the stream-wise ($\Delta s+$) and span-wise ($\Delta z+$) directions are refined by 50% where $\Delta y+$ is held constant. The near-wall values of $\Delta y+$ and $\Delta s+$ are plotted in Figure 5-22. The approach taken here is to understand the near-wall

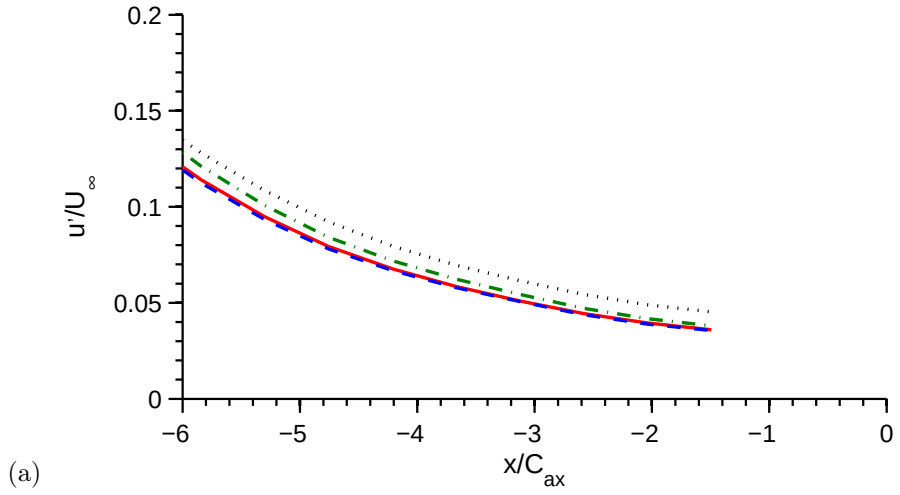

(a)

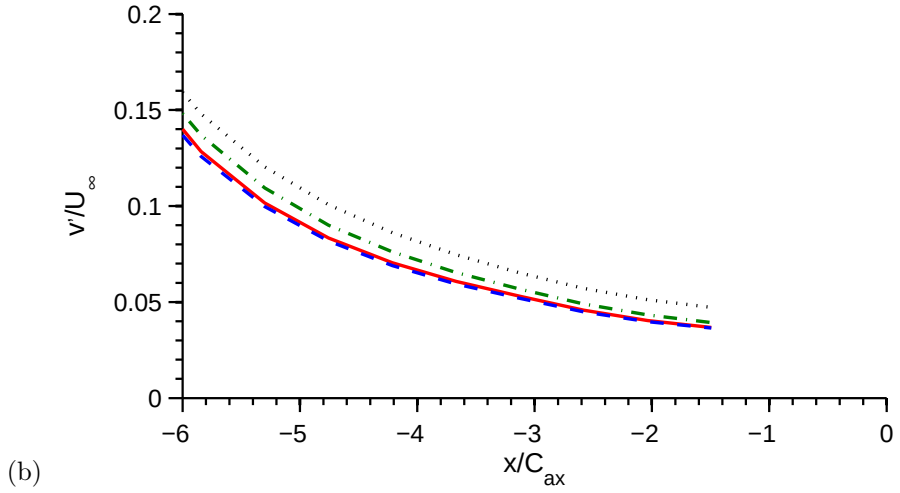

(b)

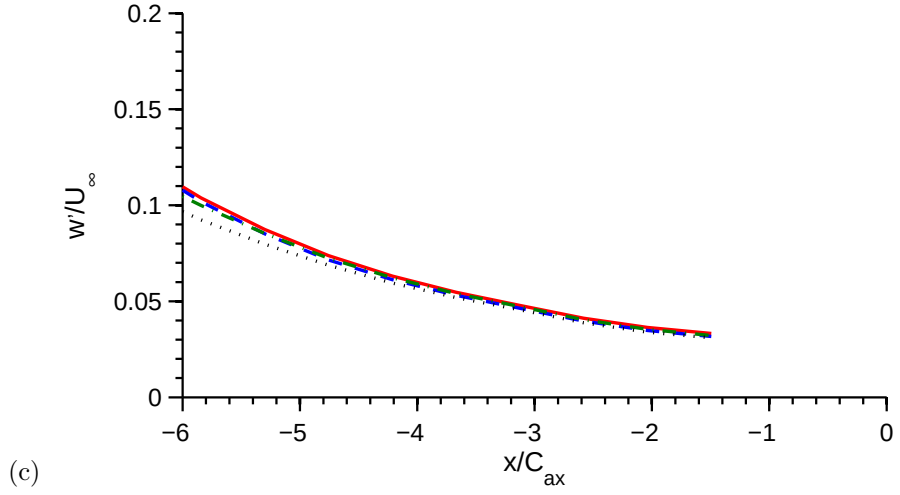

(c)

Figure 5-21. Computational span study for bar generated turbulence. WALE case MUR226 $S/C = 30\%$ (——), $S/C = 24\%$ (- - -), $S/C = 18\%$ (· - ·), and $S/C = 12$ (· · ·) for (a) u'/U_∞, (b) v'/U_∞ , and (c) w'/U_∞.

mesh requirement on the lower Re cases MUR226. After the desired near-wall mesh is determined, the values of $\Delta y+$ and $\Delta s+$ are targeted for the higher Re case MUR235.

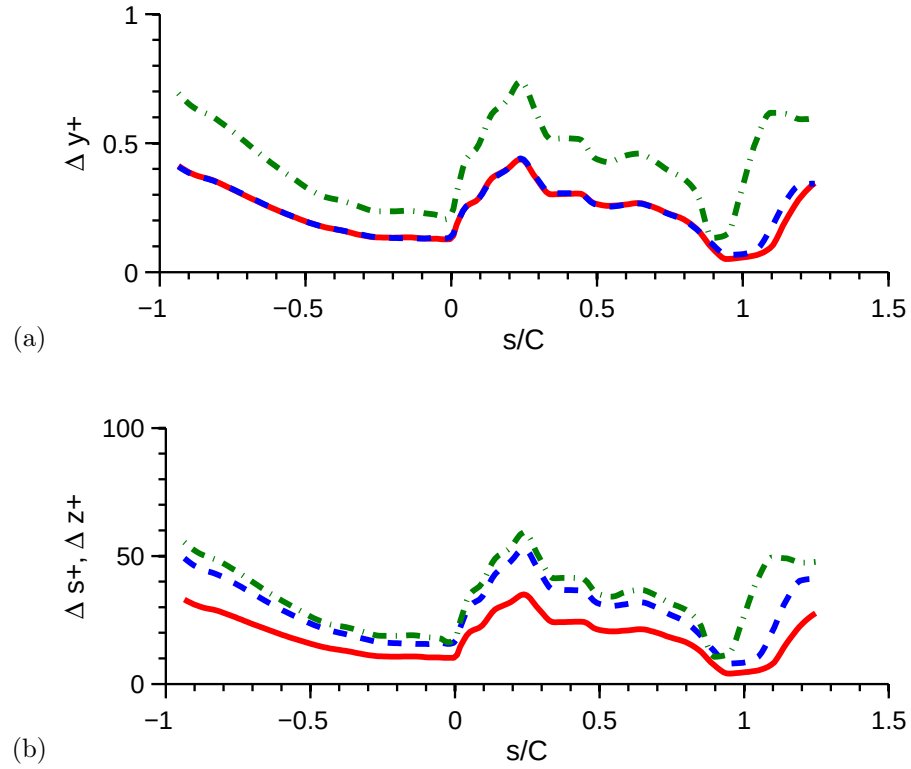

Figure 5-22. Vane (a) $\Delta y+$ and (b) $\Delta s+$ $(= \Delta z+)$ targets for $Re = 1 \times 10^6$ based on studies at $Re = 0.5 \times 10^6$. WALE case MUR224 medium mesh (——), MUR224 coarse mesh (- - -), and selected MUR235 medium mesh (· - ·).

The impact of near-wall mesh resolution on the surface Nu is first assessed in Figure 5-23. This shows an under-prediction of Nu for both mesh resolutions relative to the experimental data. However, the difference between the two computational cases is well within the cases experimental uncertainty. This suggests the WALE modeling deviation relative to the experimental measurement is due to turbulence model, mesh type, and/or solver, but not mesh density. Mesh type and solver impact are addressed in Chapter 6 by comparing to the structured mesh results from the computational code FDL3DI. There are also experimental unknowns that are not accounted for in the current study, such as the vane surface roughness.

Given the insensitivity to the change in near-wall mesh for case MUR226 the

values of $\Delta y+$ and $\Delta s+$ are targeted for the higher Re case MUR235. Additionally, the impact of the SGS model is evaluated by setting the WALE coefficient, C_w, to 0. This eliminates the use of the SGS model where the numerical schemes becomes the LES low-pass filter, therefore operating as an implicit LES filter. Given the dissipative second order scheme used, it is not surprising that setting C_w to 0 has no impact on the LES predictions. This shows that the SGS model could be eliminated to save on computational cost.

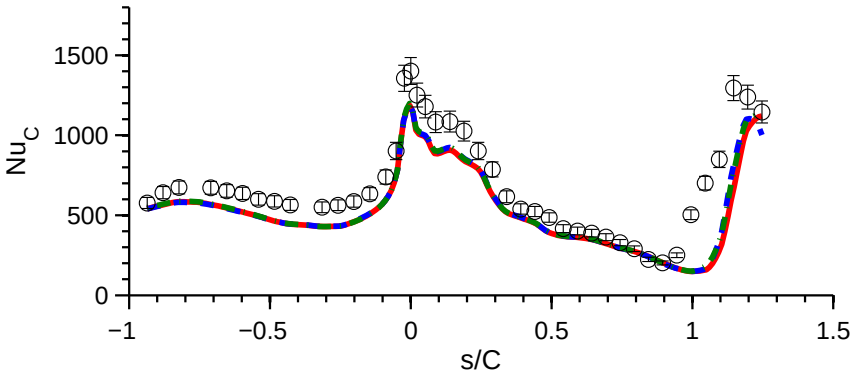

Figure 5-23. Vane mean Nu for moderate inlet turbulence mesh and model study. WALE case MUR224 for Medium mesh $C_w = 0.325$ (——), Coarse mesh $C_w = 0.325$ (- - -), and Medium mesh $C_w = 0.0$ (· - ·).

No BL measurements specific to this vane are available. However, the BL can be directly assessed to empirical correlations. Linear-log plots are used to assess the state of the BL which includes the empirical correlations for the viscous sublayer in Figure 5-24. The two mesh densities predict identical laminar BL at the PS TE, where the thickness is found to be around 10% of the TE thickness. The SS BL is found to transition to a turbulent boundary layer at the TE based on the law of the wall. Differences in the boundary layer profile between mesh resolutions are found to be insignificant for the BL as well as the dependent prediction of Nu. The negligible variation in BL prediction are further confirmed based on the contribution to the downstream wake mixing. Setting C_w to 0 is again found to have no impact on the LES predictions.

The impact of mesh resolution and SGS model coefficient are now evaluated for wake mixing. The total pressure (Figure 5-25) and TI (Figure 5-26) in the wake are

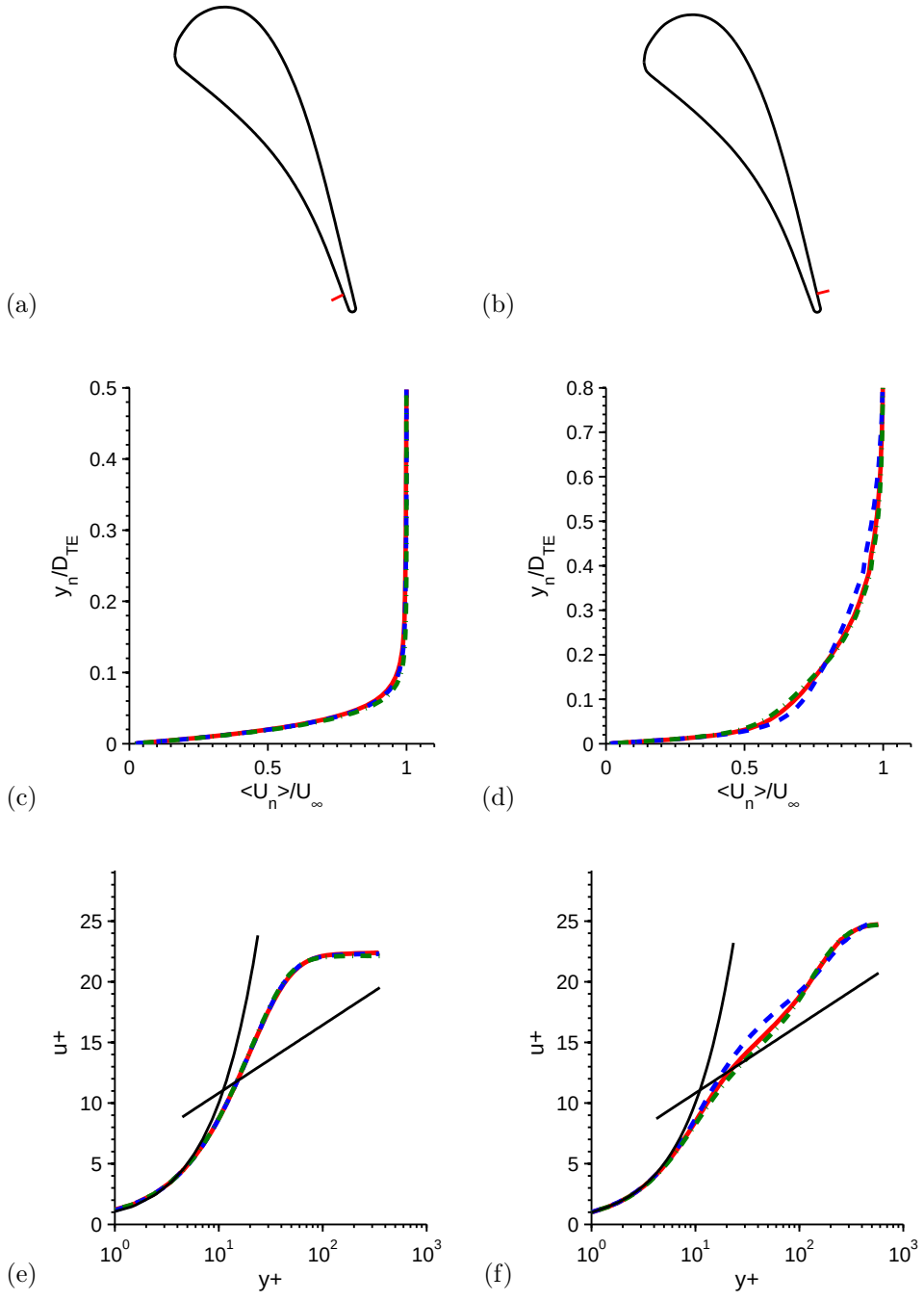

Figure 5-24. WALE case MUR244 mean velocity boundary layer profiles for Medium mesh $C_w = 0.325$ (——), Coarse mesh $C_w = 0.325$ (- - -), and Medium mesh $C_w = 0.0$ (· - ·) with moderate inlet turbulence. Images shown are (a) PS location $X/C_{ax} = 0.93$, (b) SS location $X/C_{ax} = 0.98$ from the blade LE, (c) PS velocity BL, (d) SS velocity BL, (e) PS linear-log BL, and (f) SS linear-log BL.

presented at $X/C_{ax} = 1.17$. Relative to the reported experimental uncertainty, the predicted total pressure wake is within this variation.

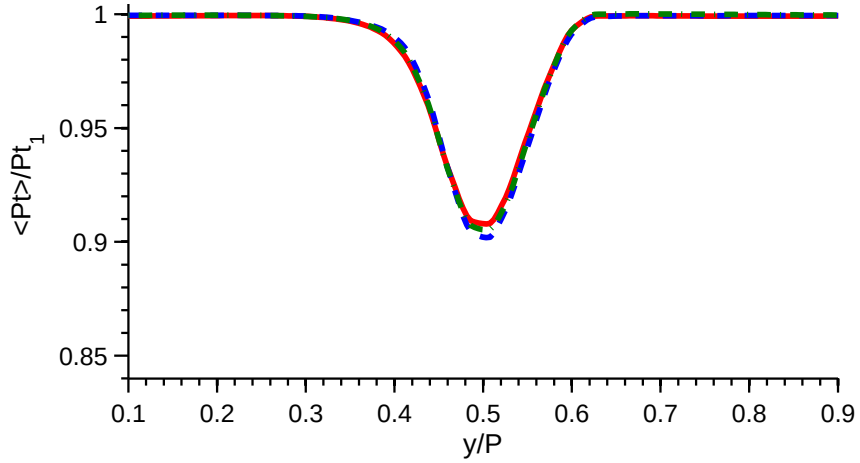

Figure 5-25. Vane normalized mean total pressure profiles at $X/C_{ax} = 1.17$ for moderate inlet turbulence mesh and SGS model study. WALE case MUR224 for Medium mesh $C_w = 0.325$ (——), Coarse mesh $C_w = 0.325$ (- - -), and Medium mesh $C_w = 0.0$ (· - ·).

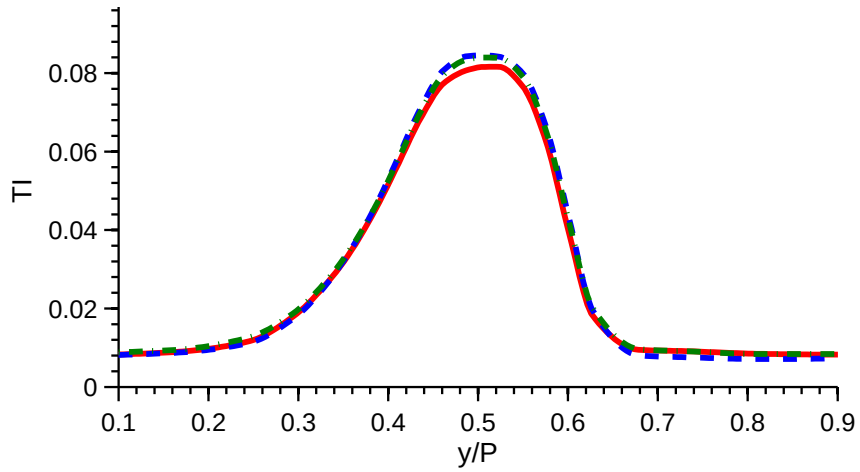

Figure 5-26. Vane local TI profiles at $X/C_{ax} = 1.17$ for moderate inlet turbulence mesh and SGS model study. WALE case MUR224 for Medium mesh $C_w = 0.325$ (——), Coarse mesh $C_w = 0.325$ (- - -), and Medium mesh $C_w = 0.0$ (· - ·).

5.2.3 Hybrid LES

Hybrid RANS/LES methods resolve the large-scale flow structures ("LES-mode") in shear or separation type flow regions. Therefore, the previous sections' LES learnings of mesh resolution, domain extent, time step selection, and convergence criteria can be applied in shear or separation flow regions for HLES. However, HLES model utilizes a RANS modeling approach near the wall allowing for reduced computational cost due to coarser meshing requirements. IDDES-T is then dependent on a blending function to transition between LES and RANS regions as discussed in Chapter 2.

Before we can move to detailed aero-thermal studies using the IDDES-T modeling approach for the HPT vane, an understanding is needed for:

- Near wall modeling prediction when including the $\gamma - Re_\theta$ transition model.
- Near wall mesh resolution impact on boundary layer development and wake generation.

In order to address this, three near-wall mesh resolutions are first considered for IDDES-T. These meshes are identical to the ones used for the RANS in the previous section. Figure 5-27 shows the resulting wall units for the 3 cases. A wall integrated approach was maintained by fixing the first cell height ($\Delta y+$) below 1. The remaining mesh edge lengths were increased by 25% for each cases.

Figure 5-28 shows the impact of near-wall mesh on IDDES-T predictions. PS and LE surface Nu predictions are found to be within the experimental uncertainty for each mesh resolution. However, the SS Nu predication varies in location and magnitude near the TE for case MUR129. This shows the IDDES model near-wall blending function sensitivity to local grid. It can be noted that $\Delta s+$ decrease sharply at $S/C = 1.2$ by an order of magnitude in Figure 5-27. This is because a fine mesh at the TE is required to resolve the developing shear flow in "LES-mode". It is recommended that $\Delta_{max} > 0.2\delta$, where δ is the thickness of the BL [21]. This recommendation is not met for $S/C > 1.2$. However, in Figure 5-28, the predicted Nu transition location is upstream of $S/C = 1.2$, showing the separation location and local mesh refinement does not coincide. Further understanding is needed of the

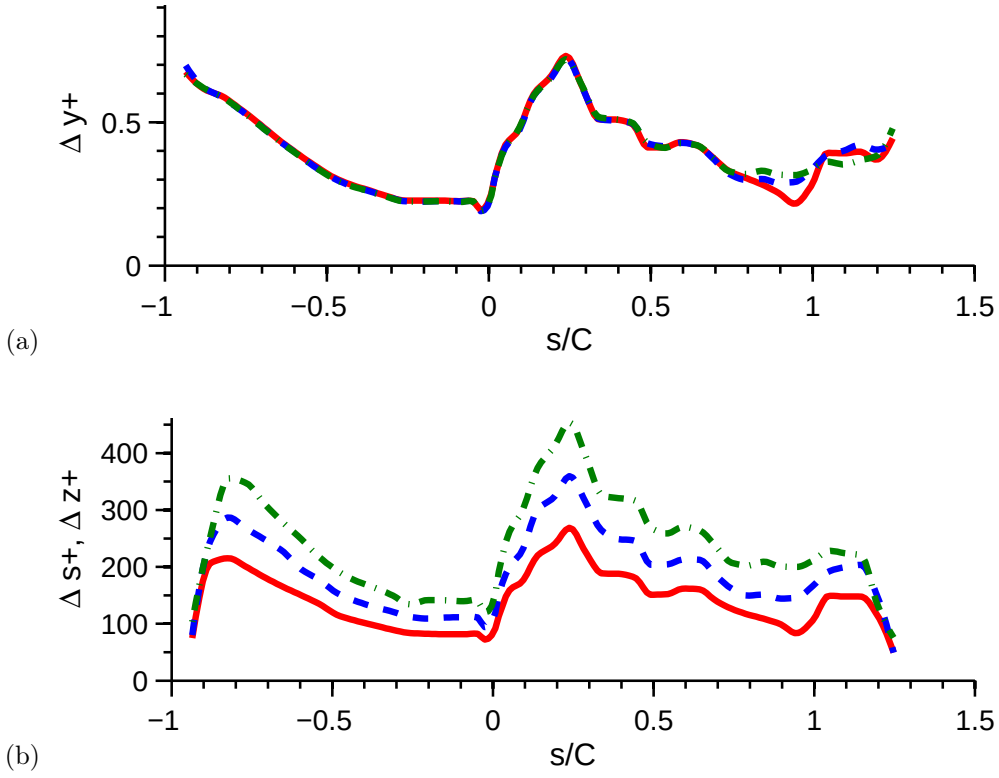

Figure 5-27. Vane (a) $\Delta y+$ and (b) $\Delta s+$ ($= \Delta z+$) for no inlet turbulence mesh study. IDDES-T case MUR129 for Fine (——), Medium (- - -), and Coarse (· - ·) meshes.

model contribution to the TE predictions of Nu.

Agreement in the SS TE Nu is found when comparing the IDDES-T fine mesh prediction to the WALE $\Delta s+_{max} = 275$ results in Figure 5-13. This can be explained by the LES part of the IDDES formulation leading to a Smagorinsky-type model with different definition of filter size (Δ). The filter size is based on maximum cell length or the cube root of the volume for IDDES or Smagorinsky models respectively [69]. The WALE model filter size is also based on the cube root of the volume. The IDDES-T fine mesh case is found to be operating in the LES regime at the TE due to the near-wall mesh density and unsteadiness generated from TE wake shedding. The resolved unsteadiness then leads to different BL transitioning behavior seen in Figure 5-28. This cannot be avoided due to the TE mesh refinement needed to resolve the developing shear flow. The fine mesh is therefore selected going forward for all

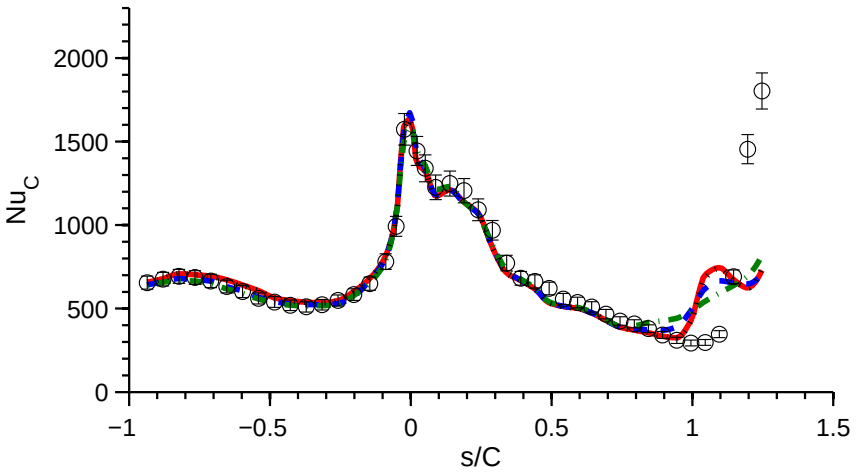

Figure 5-28. Vane mean Nu for no inlet turbulence mesh study. IDDES-T case MUR129 for Fine (——),) Medium (- - -), and Coarse (· - ·) meshes compared to experimental cases MUR129 (○). Fine mesh also run with $C_{DES} = 0.2$ (· · ·)

IDDES-T simulations presented to satisfy the resolution desired to predict the wake development and decay.

Before a comparison to the wake predictions are made, the IDDES filtering function is assessed. Due to the different definition of local length scale for the IDDES filter size compared to the WALE model, an additional sensitivity case is completed. The blending coefficient C_{DES} is reduced from 0.61 to 0.2. The models eddy viscosity is a function of C_{DES} multiplied by the filter size. Since IDDES is based on the maximum cell length and WALE is based on cube root of the volume, IDDES filter size is always larger than that of the WALE model for an identical mesh. Therefore, a reduction in C_{DES} was selected to lower the IDDES eddy viscosity to understand the model sensitivity for the fine mesh. C_{DES} can also be modified in the inner and outer wall regions. Here we wish to only impact the shear flow region where scale-resolved flow is desired. Therefore, only the outer C_{DES} was modified. Figure 5-13 shows no impact of lowering the outer C_{DES} term to 0.2 on surface Nu confirming the inner near-wall IDDES treatment has not been impacted. This also shows the SGS model for IDDES in the shear flow LES region has a negligible impact.

Figures 5-29 and 5-30 show total pressure and TI wake profile predictions at

$X/C_{ax} = 1.44$ downstream of the vane LE. The mesh in the wake for the fine IDDES-T is matched to the resolution of the LES fine mesh case required to resolve the developing shear flow. Relative to the experimental data, the fine IDDES-T predictions are within the experimental uncertainty with the exception of the center of the wake. At the wake center, IDDES-T is 2X the experimental uncertainty. Further, deviation for experimental measurements is found with the medium and coarse meshes where the depth of the wake increases. As the mesh coarsens and the computed eddy viscosity increases the wake solution moves from a LES to URANS solution. This is in agreement with the over-prediction of the wake depth. The contribution of the SS TE BL difference also contributes to the shift in the wake profile. Additionally, no impact is found when changing the C_{DES} from 0.61 to 0.2. This shows the SGS model for IDDES in the shear flow LES region has a negligible impact for the fine mesh.

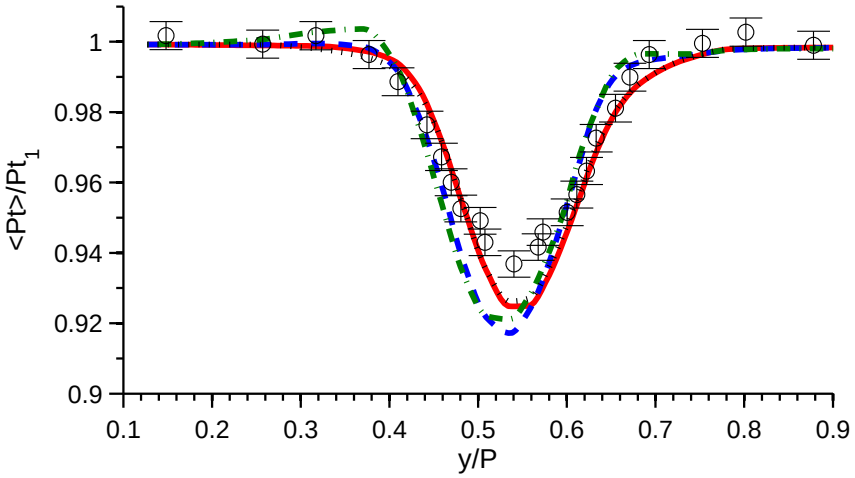

Figure 5-29. Vane normalized mean total pressure profiles for no inlet turbulence at $X/C_{ax} = 1.44$ mesh study. IDDES-T case MUR129 for Fine (——), Medium (- - -), and Coarse (· - ·) meshes. Fine mesh also run with $C_{DES} = 0.2$ (· · ·)

As previously discussed, $V^{1/3}/\eta$ can be used to target mesh resolution for scale-resolved simulation. Figure 5-31 compares $V^{1/3}/\eta$ in the wake SST-T and IDDES-T for the identical mesh. Wake mesh density can be estimated with RANS by targeting $V^{1/3}/\eta$ below 40. Due to the vortex shedding, the width of the wake as a function of

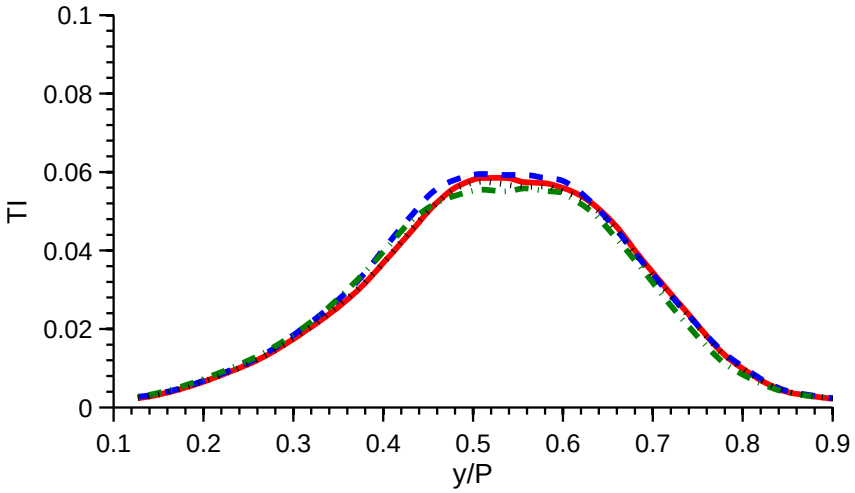

Figure 5-30. Vane normalized mean total pressure profiles for no inlet turbulence at $X/C_{ax} = 1.44$ mesh study. IDDES-T case MUR129 for Fine (——), Medium (- - -), and Coarse (· - ·) meshes. Fine mesh also run with $C_{DES} = 0.2$ (· · ·)

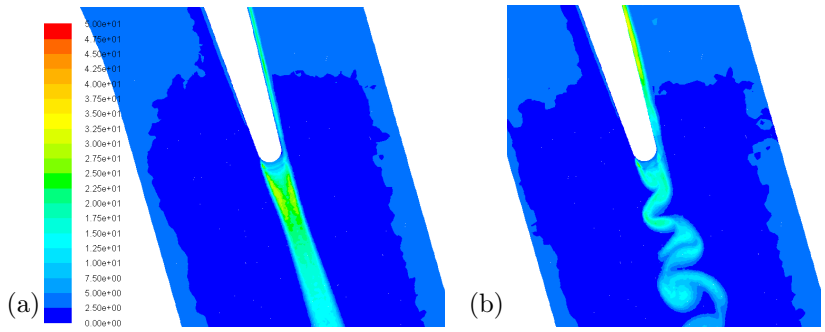

Figure 5-31. Contours of $V^{1/3}/\eta$ for (a) SST-T and (b) IDDES-T Fine meshes.

downstream distance must be accounted for where the IDDES-T contour provides a relative comparison to the steady RANS solution.

5.3 Unsteady Modeling Approach

Guidelines have been established for selecting time step, iteration per time step, and time averaging of unsteady scale-resolved modeling approaches. These guidelines are leveraged for aero-thermal studies presented in Chapters 6, 7, and 8.

5.3.1 Time Step Selection and Convergence

The required time step for shear flows can be estimated by the fundamental shedding frequency. Typically a range of Strouhal numbers are known for the given flow conditions. Table 5.5 demonstrates how the St is used for both the cylinder in cross-flow (Chapter 3) and uncooled vane studies. The time step was previously confirmed in both cases by evaluating the impact of time step on the desired flow quantities. A final check of the maximum CFL number with the selected mesh and time was found to typically be under 5. Based on the St number, an estimated time step is determined by setting 100 time steps per wake shedding period. This estimated time step is found to be in agreement with the selected time step for the previous model sensitivities for WALE and IDDES for both the cylinder and HPT vane studies.

Table 5.5. Estimation of required time step based on Strouhal Number.

Case	Cylinder	Vane (MUR129)
St	0.22	0.29
D (meter)	0.0254	0.00142
U_2 (m/s)	1.75	319
Period, $T = 1/f$ (sec)	6.6×10^{-2}	1.5×10^{-5}
Target $T/\Delta t$	100	100
Estimated Δt	6.6×10^{-4}	1.5×10^{-7}
Selected Δt	5.0×10^{-4}	2.0×10^{-7}

Figure 5-32 shows the iteration per time step convergence of momentum, continuity, and energy iteration for the WALE model. It was previously found that iteration per time step of 6, 9, and 12 resulted in no impact to surface Nu and wake mixing. The same result was found for the cylinder in cross-flow.

Finally, local quantities were monitored to determine when statistically steady state is reached and when the qualities have been sufficiently averaged. Three locations of interest are shown in Figure 5-33 where the flow is highly unsteady. The surface Nu is monitored on the SS surface near the TE where the BL flow is transitional and also in the separation flow region on the TE surface. A location is also shown in the wake at $X/C_{ax} = 1.07$ downstream of the vane LE. Based on Figure 5-33, the flow is allowed 4 flow through times to reach statistically steady state. The

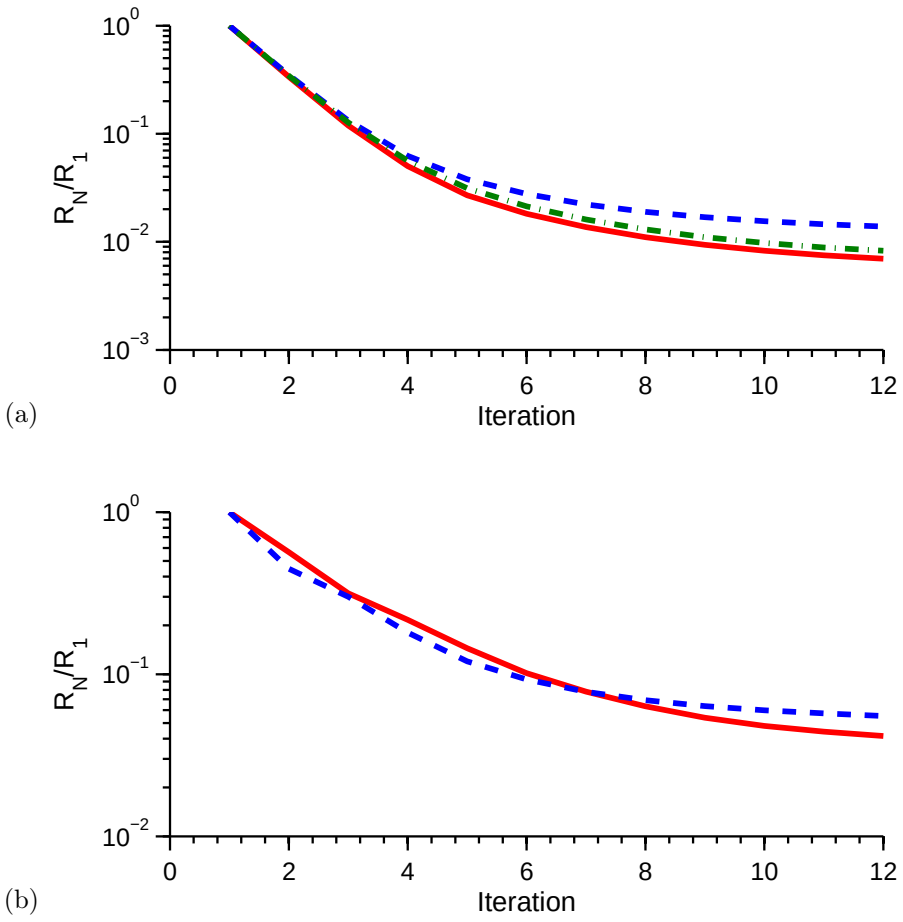

Figure 5-32. WALE inner iteration convergence for the uncooled vane (MUR129) for (a) x (——), y (- - -), z (· - ·) momentum and (b) continutiy (——) and energy (- - -).

flow through time is based on the inlet velocity to the vane, vane axial chord, and simulation time. Therefore, one flow through time is approximately the flow time from the LE to TE of the vane. The results also suggest a maximum of 2 flow through times are required. In addition, the solution was averaged over 4 flow through times to achieve a time average variation of less than 1% relative to the experimental uncertainty for Nu ensuring the collection of statistics has a negligible contribution to the model prediction error.

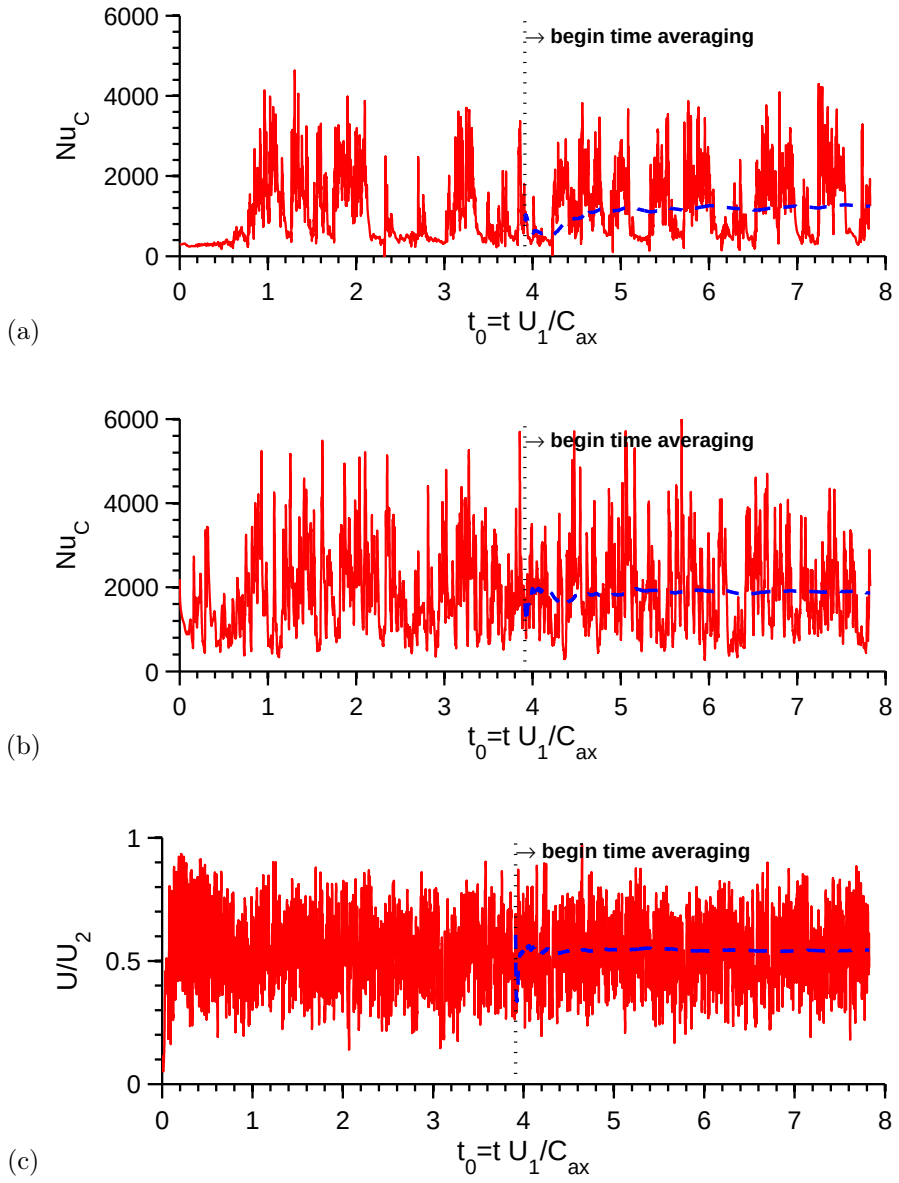

Figure 5-33. WALE time averaging. Running time average (- -), and instantaneous value (—) for the (a) Nu at the SS surface $X/C_{ax} = 0.98$, (b) vane Nu at the TE surface, and (c) vane normalized velocity in the near wake at $X/C_{ax} = 1.07$

5.3.2 Post Processing

Variables must be created for unsteady simulations to allow for plane mass average quantities. A plane mass-weighted averaged quantity of a scalar, ϕ, can be approximated numerically with the following equation,

$$\langle \phi \rangle_x = \frac{\int \rho V_x \phi dA}{\int \rho V_x dA} \approx \frac{\sum \rho V_x \phi \delta A}{\sum \rho V_x \delta A}. \tag{5.8}$$

This requires the creation of the variable $\rho V_x \phi$ and ρV_x, where V_x is normal to the plane of interest. The time average variables are then applied to Equation 5.8 for the mass averaged quantity.

5.4 Summary

Modeling sensitivity has been completed for RANS, HLES, and LES approaches. This was done to build confidence in the approach at engine operating conditions for an uncooled HPT vane. A summary of these finding is provided in Table 5.6.

Table 5.6. VKI uncooled vane RANS, HLES, and LES model approach.

Model	SST-T (SST)	IDDES-T	WALE
Max $\Delta y+$	1.0	1.0	1.0
Max $\Delta s+$	250	250	60
Max $\Delta z+$	250	250	60
Wake $V^{1/3}/\eta$	N/A	40	40
S/C No Inlet TI	N/A	12%	12%
S/C w/ Inlet TI	N/A	24%	24%
Δt	N/A	2×10^{-7}	2×10^{-7}
Iteration per time step	N/A	9	9
Minimum Averaging FTT	N/A	4	4

First, a grid independent RANS solution was confirmed. The intent was not to optimize the cost of the RANS mesh, but to confirm a grid independent solution. The mesh is globally refined by 25% with exception to the first wall cell height for the vane where $\Delta y+$ is held constant to maintain a wall integrated mesh approach. Negligible impact to surface Nu and wake mixing was found for all three meshes. However, the

fine RANS mesh was selected as the target mesh for future studies in Chapters 6, 7, and 8. This is done to compare RANS and HLES on an identical mesh.

Next, the mesh resolution, domain extent, time step selection, and convergence criteria were established for the LES scale-resolved simulation. This was first done for zero inlet TI levels. For a fixed near-wall mesh resolution, domain extent of $S/C = 12\%$, time step selection of $\Delta t = 4 \times 10^{-7}$, and iteration per time step of 6 were found to be sufficient for Nu predictions. This is based on the prediction varying less then the equivalent experimental uncertainty. Next mesh resolution, domain extent, time step selection, and iteration per time step were evaluated for the wake. Time step was found to have the most significant impact on wake mixing, requiring a time step of $\Delta t = 2 \times 10^{-7}$. This was due to the time steps per shedding period required for the current second order code approach. A guideline of 100 time steps per shedding frequency was determined and shown to agree with findings from the cylinder in cross-flow in Chapter 3. The medium and fine mesh cases were also within the equivalent experimental uncertainty suggesting the medium mesh in the wake is sufficient. However, as a conservative approach, the fine mesh is targeted for future studies. In addition, the results suggested a maximum of 2 flow through times are required, where averaging over 4 flow through times achieved a time average variation of less than 1% relative to the experimental uncertainty for Nu.

A sensitivity study was also completed for the LES near-wall mesh resolution and domain span-wise extent required for a case with elevated inlet TI. Elevated turbulence is generated by upstream bars with 3 mm diameter and a pitch of 12 mm [22]. It was shown that all three RMS velocity components were independent of the domain span, S/C of 24%. The impact of near-wall mesh resolution was then evaluated for surface Nu, boundary layer formation, and wake mixing for the LES WALE modeling approach. The difference in prediction between the two near-wall mesh resolutions was well within the equivalent experimental uncertainty for this case. The near-wall mesh values of $\Delta y+$, $\Delta z+$, and $\Delta s+$ at the lower Re case MUR226 is used as targets for the higher Re cases (i.e. MUR235).

HLES then leveraged learnings for near-wall and wake mesh resolution from RANS

and LES approaches, respectively. In addition, studies were completed to understand the model sensitivity to near-wall mesh density and its impact on boundary layer development and wake generation. Surface Nu and wake predictions were assessed for three mesh resolutions, matching those used for the RANS study, where it was noted that the fine LES and fine RANS mesh use identical refinement in the wake. PS and LE surface Nu prediction are found to be within the experimental uncertainty for each mesh resolution. However, the SS Nu prediction varies in location and magnitude near the TE for case MUR129, providing the near-wall blending function sensitivity to local grid. The wake depth was found to shift and increase in depth for both the coarse and medium meshes. The fine HLES mesh was therefore selected as the target mesh for future studies to match the targeted wake resolution used for LES.

Finally, scale-resolved guidelines were established for the wake mesh resolution based on RANS predictions. This allows for a low computational cost to assess mesh targets before moving to a scale-resolve approach. As previously discussed, $V^{1/3}/\eta$ can be used to target mesh resolution for scale-resolved simulation. Wake mesh density can be estimated with RANS by targeting $V^{1/3}/\eta$ below 40. Due to the vortex shedding, the width of the wake as a function of downstream distance must be also be considered. These completed studies provide confidence in the computational setup and approach for LES using an unstructured mesh of tetrahedral and prism elements with second-order spatial and temporal schemes in Fluent. This allows the assessment of predictive misses due to turbulence model, mesh type, and solver in the following chapters.

Chapter 6

Pitch-line Vane Aero-Thermal Study

Computational modeling approaches are now assessed relative to the HPT experimental studies of Arts and Rouvroit [34]. Established modeling practices from Chapter 5 are applied to a pitch-line HPT uncooled vane that is representative of engine operating conditions prior to the additional modeling complexities for a vane/blade stage analysis in Chapters 7 and 8. This is done to build confidence in the approach at engine operating conditions relative to experimental measurement along with understanding computational cost and accuracy of RANS, HLES, and LES modeling approaches. This approach is extrapolated to higher levels for free-stream turbulence to better understand the role of turbulence on BL, surface heat transfer, and wake formation. Ultimately, the goal is to better understand the impact of turbulence on an actual 3D engine centerline stage design.

LES serves as a computational benchmark for RANS and HLES studies beyond the available experimental data of Arts and Rouvroit [34]. Given the complexity of turbine designs, detailed three-dimensional geometry features must be captured. Therefore, before moving to a full 3D stage geometry that include end-walls and blade tip gaps (Chapter 8), a robust solver and meshing approach needs to be assessed to determine any compromises in accuracy. This is accomplished in the current study by taking an unstructured meshing approach with tetrahedral and prism elements using second-order spatial and temporal schemes in Fluent v16. The accuracy of unstructured meshing using the second-order code Fluent for LES is compared to a

structured high-ordered solvers FDL3DI as part of an ongoing effort at GE [49, 50, 48].

6.1 Zero Inlet Turbulence Generation

Modeling approaches are now assessed at two Reynolds numbers for cases MUR129 and MUR228. Experimental data is available for loading, HTC, and wake total pressure profile. Loading comparisons are first made to confirm operating conditions, inlet flow incident angle, and vane geometry are correctly matched to experimental conditions. This is confirmed for MUR129 in Figure 6-1. Loading profiles are found to be within 1% for each turbulence modeling approach. The largest deviation is found near the throat (approximately $s/C = 0.65$). Due to the choked conditions for MUR228, the impact of the BL state on local shock formation and throat location can be seen. SST model predicts a thicker turbulent BL compared to the other models where the throat has moved upstream. Unsteadiness from the TE wake shedding propagates upstream to the fluidic throat for IDDES-T and WALE models but is not reflected in the mean loading plots. Both BL state and unsteadiness are further discussed later in this section.

Table 6.1. Near wall mesh LES resolution for cases MUR129 and MUR228. Mesh resolution for FDL3DI is included for case MUR228.

Case	Fluent	Fluent	FDL3DI [49]
Case	MUR129	MUR228	MUR228
Mesh Type	Unstructured	Unstructured	Structured
Max $\Delta y+$	0.8	0.5	1.5
Max $\Delta s+$	50	35	65
Max $\Delta z+$	50	35	30

Large computational cost comes at the expense of the near-wall mesh requirement for LES. Previous studies completed by Bhaskaran [35] and Collado [16] have provided meshing targets. These targets were refined for the unstructured second-order solver approach in Chapter 5. Table 6.1 presents the final mesh resolution applied in this chapter. Figure 6-2 shows the WALE near-wall mesh resolution compared to IDDES-T and SST models, quantifying the differences in the desired near-wall mesh density.

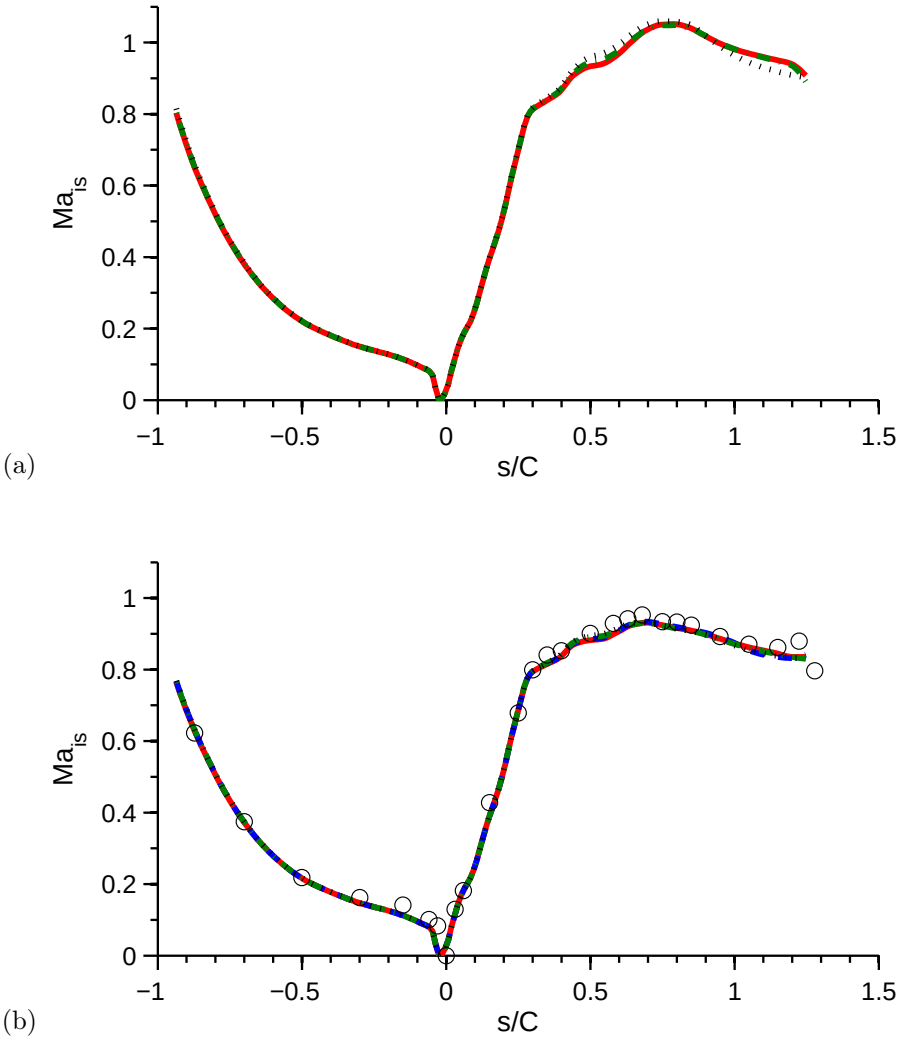

Figure 6-1. Vane loading for no inlet turbulence generation. Cases (a) MUR228 and (b) MUR129 for WALE (——), IDDES-T (- - -), SST-T (· - ·), and SST (· · ·). Experimental measurement for MUR129 (○). IDDES-T only presented for MUR129.

The near-wall mesh requirements for a wall-resolved RANS solution was obtained by reaching a grid independent solution for both SST and SST-T. The WALE near-wall mesh must be refined enough to resolve the transitional and turbulent BL structures resulting in $\Delta s+$ and $\Delta z+$ of 5X less than the RANS cases.

As previously noted, a small deviation in loading is found near the throat (approx $s/C = 0.65$) for the SST model due to the BL state. The mechanical throat is found at the SS surface location of minimum distance to the adjacent vane. Due to the BL

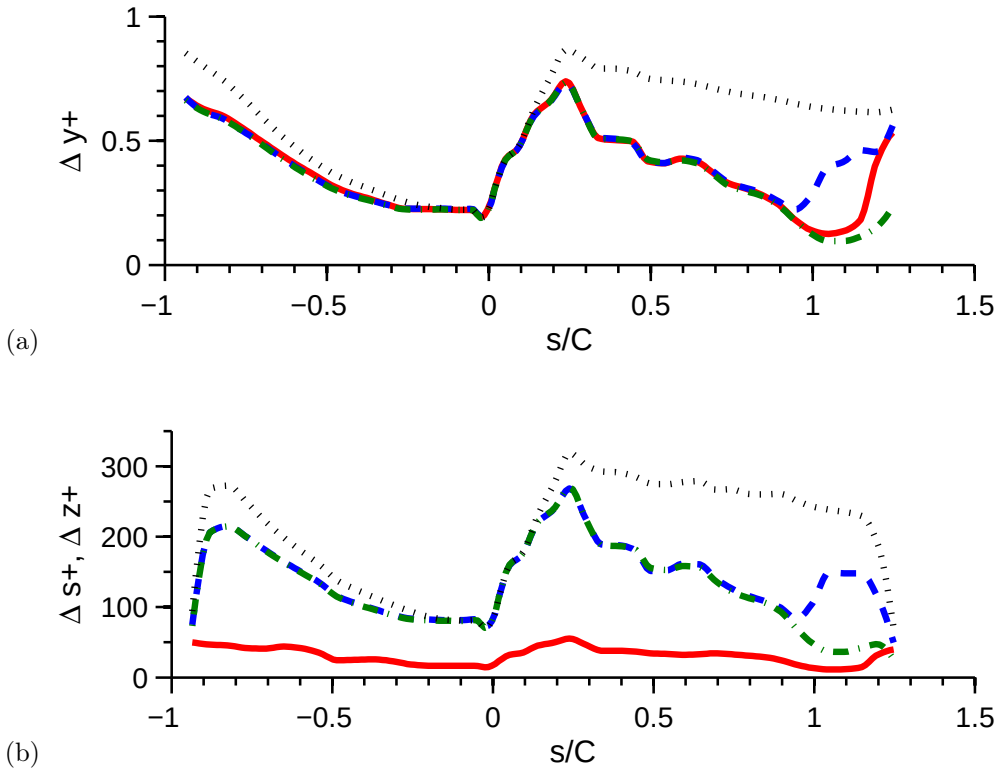

Figure 6-2. Vane (a) $\Delta y+$ and (b) $\Delta s+$ ($= \Delta z+$) for WALE (——), IDDES-T (- - -), SST-T (· - ·), and SST (· · ·) for case MUR129 with no inlet turbulence generation.

thickness, the fluidic throat varies from the mechanical throat, where for MUR228 the fluidic throat is found when the Mach number first reaches 1 on the SS surface.

Figure 6-3 presents surface Nu results for SST, SST-T, IDDES-T, and WALE models for cases MUR129 and MUR228. It is shown that SST predicts a turbulent Nu due to the immediate transition to a turbulent BL on pressure side (PS) and SS of the vane. The turbulent Nu predicted by the SST model shows up to a 4X over-prediction relative to the experimental results. The other three modeling approaches predict a laminar Nu for the majority of the vane, aligning prediction with measurement. This highlights why significant efforts in development of RANS transition models has occurred over the past decades. It is also shown that LES can resolve BL transition at a significant cost increase. However, for HPT conditions of full 3D vane and blade domains, LES can become cost prohibitive for industrial conceptual design studies [9];

therefore, the hybrid LES approach (IDDES-T) is considered. This is assessed for the current case so the approach can be implemented for linear and rotational sliding mesh studies in Chapter 7 and 8.

Overall, Figure 6-3 show that SST-T, IDDES-T, and WALE provide excellent agreement with experimental measurement where small misses are found for each model. SST-T predicts a late transition at the SS TE. This late transition could be in part due to local unsteady shedding at the TE that cannot be captured with a steady RANS model. IDDES-T predicts early transition for case MUR129. This was discussed in detail in Chapter 5. This is due to the model operating in the LES regime given the near-wall mesh resolution and local unsteadiness. This cannot be avoided due to the TE mesh refinement needed to resolve the developing shear flow. Interestingly, this upstream transition point is found for the lower Re case MUR228 that is run at a slightly higher Mach number. This shows the sensitivity of the transition point and the challenge of decoupling it from modeling error.

The WALE model predictions are in good agreement with MUR129, capturing the transition location on the SS. However, the WALE model does over-predict the Nu on the PS as discussed in Chapter 5. This was shown to be caused by over-predicted strength of the Gortler vortex forming on the PS surface. At a lower Re (case MUR228) the Go number is reduced by approximately $2X$, corresponding to a reduced vortex strength. The reduced Go number agrees with the reduced over-prediction for Nu on the PS surface. FDL3DI results of Bhaskaran et al. [49] are included in the comparison to quantify the impact of mesh type and code. Fluent and FDL3DI are found to be in excellent agreement where the largest deviation is found on the vane PS which is within 2X the equivalent experimental uncertainty.

The highest acceleration regions on the vane are found to be on the PS surface at $X/C_{ax} = 0.93$ and the SS surface at $X/C_{ax} = 0.35$. These regions are found to have the thickest thermal BL relative to the velocity BL in Tables 6.2 and 6.3. This effect was predicted by Launder and Lockwood [84] and supported by Sucec and Lu [85]. Launder and Lockwood analytically showed that accelerated flows could have a thermal BL that was up to 8 times thicker than the associated velocity BL,

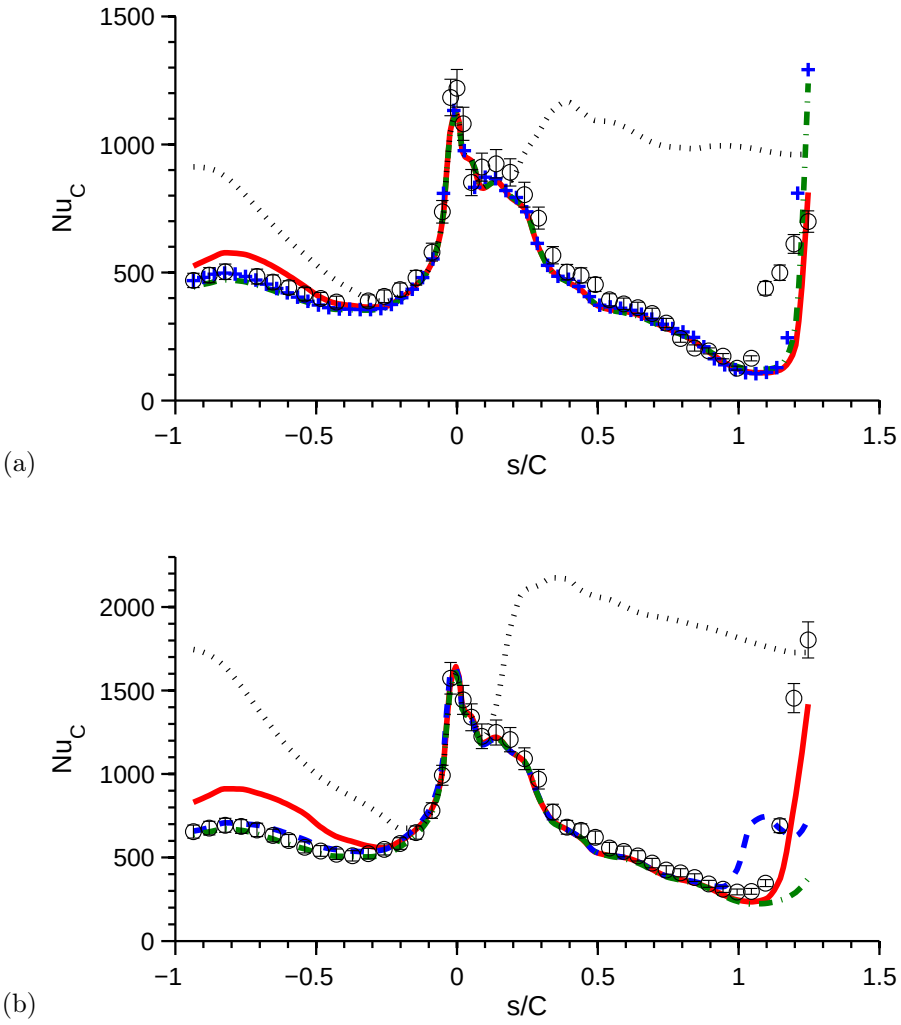

Figure 6-3. Vane mean Nu for no inlet turbulence generation. Experimental cases (a) MUR228 (○) and (b) MUR129 (○) compared to WALE (——), IDDES-T (- - -), SST-T (· - ·), and SST (· · ·). IDDES-T only presented for MUR129. FDL (+) presented for case MUR228.

depending on the strength of the favorable pressure gradient. In regions of near zero acceleration, the BL is expected to be in better agreement with the analytical relationship $\delta_T/\delta \approx Pr^{-1/3}$ [79]. The Pr number for air is 0.71, resulting in $Pr^{-1/3} = 1.12$ which is found to be within 10% of the WALE predictions.

Radomsky and Thole [39] measured the BL profile on a different vane geometry but similar Re and TI level to MUR129. Measurements showed a mean laminar BL profile for the entire PS surface of the vane. The SS surface measurements showed

late transition near the TE where the shape factor, H, locally decreased. Similar profiles and trends are also found for the current WALE BL predictions. However, it should be noted that experiments of Radomsky and Thole [39] were carried out in a low Mach number facility where compressibility effects on BL state are not captured.

Table 6.2. Case MUR228 WALE boundary layer parameters.

Location	δ/D_{TE}	H	δ_T/δ
SS $X/C_{ax} = 0.98$	0.36	3.6	1.20
SS $X/C_{ax} = 0.85$	0.32	2.9	1.10
SS $X/C_{ax} = 0.60$	0.16	2.0	1.22
SS $X/C_{ax} = 0.35$	0.09	1.7	1.35
PS $X/C_{ax} = 0.93$	0.19	1.2	1.35
PS $X/C_{ax} = 0.32$	0.26	1.4	1.22

Table 6.3. Case MUR129 WALE boundary layer parameters.

Location	δ/D_{TE}	H	δ_T/δ
SS $X/C_{ax} = 0.98$	0.33	1.7	1.04
SS $X/C_{ax} = 0.85$	0.19	2.5	1.22
SS $X/C_{ax} = 0.60$	0.12	2.0	1.23
SS $X/C_{ax} = 0.35$	0.07	1.6	1.38
PS $X/C_{ax} = 0.93$	0.10	1.4	1.47
PS $X/C_{ax} = 0.32$	0.21	1.4	1.11

For flat plate laminar boundary layers with zero pressure gradient, the Blasius solution leads to the relationship, $\delta \sim 1/\sqrt{Re_x}$. Increasing the Re from case MUR228 to MUR129 results in a BL reduction ($\sqrt{Re_{MUR228}}/\sqrt{Re_{MUR129}}$) of 0.73. Referring to BL thickness predicted in Tables 6.2 and 6.3, reduction in BL thickness due to increasing Re generally agrees with Blasius flat plat laminar boundary layer solution. WALE BL thickness predictions at X/C_{ax} at 0.32, 0.35, 0.60, and 0.85 are found to agree to within 15% when scaling by Re. The 15% variation from the zero pressure gradient Blasius solution is reasonable given the acceleration for the vane.

Figure 6-4, only the SST model predicts a fully turbulent BL at both the SS and PS TE. All other models predict a laminar BL at the PS TE, where the thickness is found to be around 19% of the TE thickness for MUR228. As the Re is increased the

PS BL thickness decreases as expected, resulting in around 10% of the TE thickness for MUR129. The SS BL is found to range from laminar, transitional, and turbulent depending on the modeling approach. Based on the SS Nu, $X/C_{ax} = 0.98$ is near the experimental transition region explaining the range of BL prediction. SST-T and WALE models predict a transitional BL for cases MUR224. Due to the presence of the adverse pressure gradient, the thickness of the TE SS BL is found to be more than 2X larger than the favorable pressure gradient for the TE PS BL.

It is essential to accurately capture the BL state in order to predict the developing TE wake. Figure 6-5 shows far wake total pressure profile predictions of WALE, IDDES-T, SST-T, and SST for cases MUR129 and MUR228. The profile measurement location is at $X/C_{ax} = 1.44$ downstream of the vane LE. Excellent agreement is found for WALE and IDDES-T relative to experimental measurement for case MUR129, suggesting the BL contribution to the wake development is accurately predicted for the vane. SST-T is found to have mixed results at $X/C_{ax} = 1.44$, where MUR129 provides a reasonable prediction for the wake depth. However, for the lower Re case MUR228, a large deviation is found relative to WALE predictions. This shows SST-T incorrectly predicts the absolute and trend of the mixing loss when varying Re. This is not surprising, as RANS models consistently over-predict wake depth and under-predict wake spreading [62, 53, 17, 46].

Isotropic turbulence is one of the major assumptions for the RANS SST model. The limitations of this assumption are well known, where the WALE model in Figure 6-7 shows the anisotropic behavior in the downstream wake locations of $X/C_{ax} = 1.17$ and $X/C_{ax} = 1.44$ of the vane LE. The three components of resolved Reynold stress are normalized to the kinetic energy, k. The deviation between u'^2/k, v'^2/k, and w'^2/k show the anisotropic turbulence found in the vane down-stream wake.

A comparison between the decay rate of each model is presented in Figures 6-8 and 6-9. The prediction of wake profile and decay for the IDDES with transition model is found to be in good agreement with the WALE model. Improved profile loss prediction and initiation of wake mixing for the IDDES-T model results in similar wake formation to the WALE model. IDDES-T is found to predict a slightly deeper

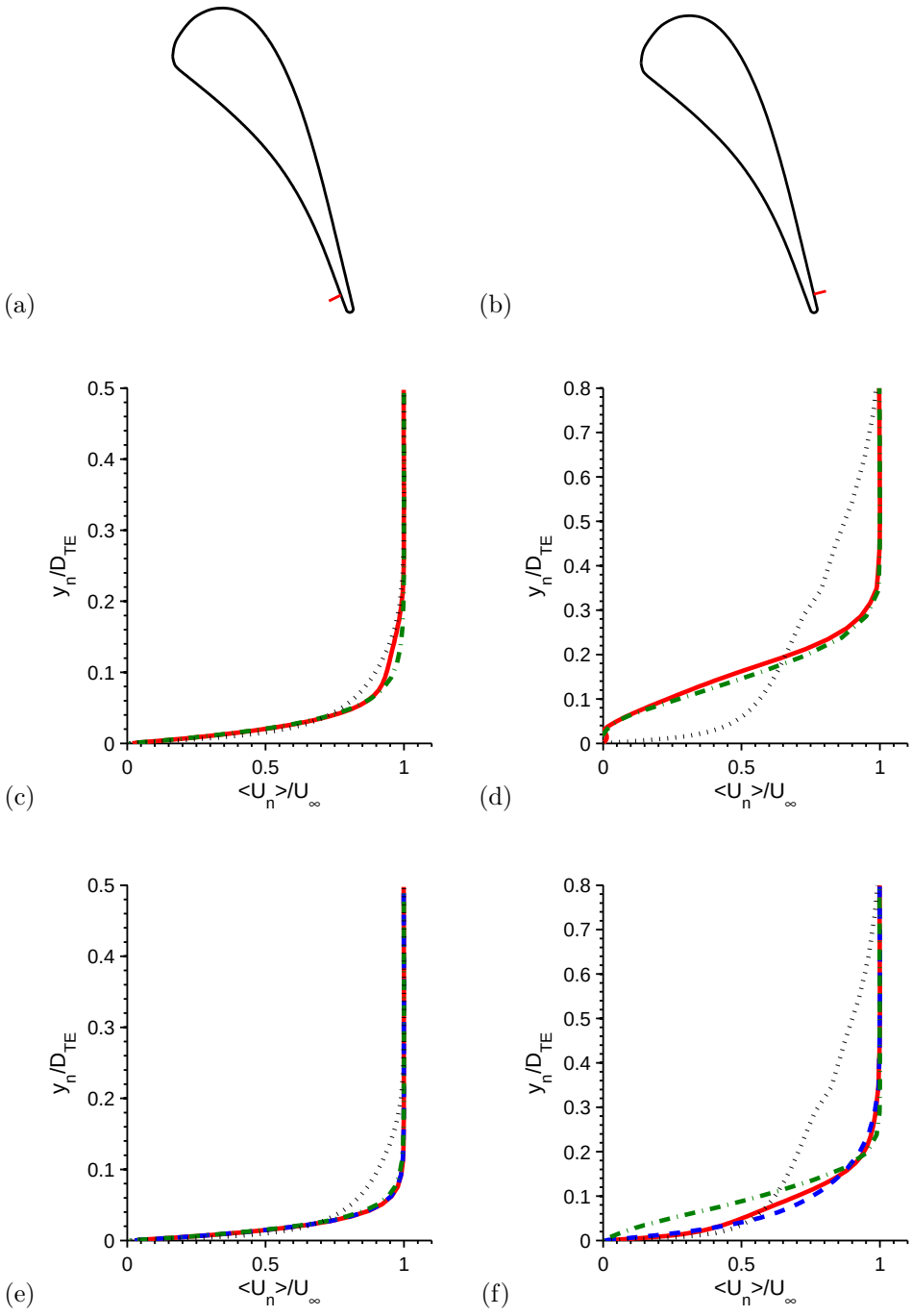

Figure 6-4. Mean velocity boundary layer profiles for WALE (——), IDDES-T (- - -), SST-T (· - ·), and SST (· · ·) with no inlet turbulence. Images shown are (a) PS location $X/C_{ax} = 0.93$, (b) SS location $X/C_{ax} = 0.98$ from the vane LE, (c) case MUR228 PS BL, (d) MUR228 SS BL, (e) MUR129 PS BL, and (f) MUR129 SS BL. IDDES-T only presented for MUR129.

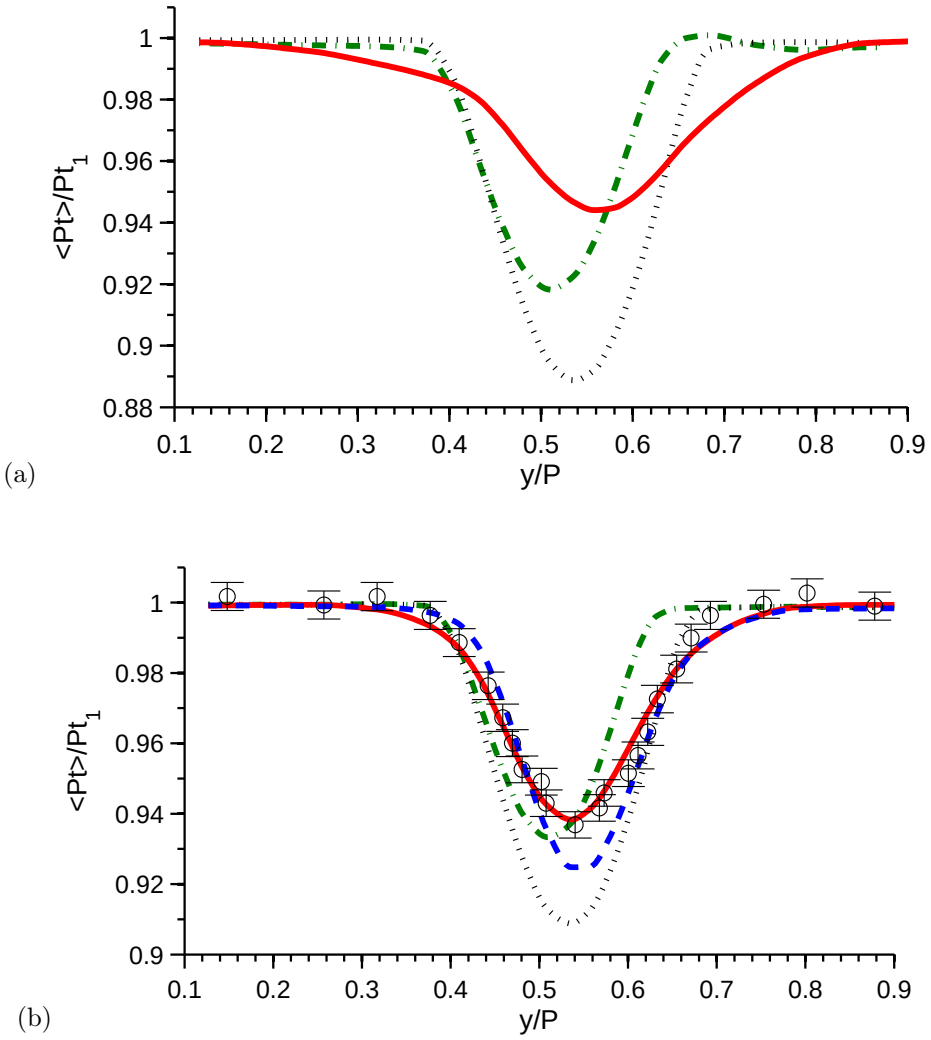

Figure 6-5. Vane normalized mean total pressure profiles for no inlet turbulence at $X/C_{ax} = 1.44$ from the vane LE. Cases (a) MUR228 and (b) MUR129 (○) for WALE (——), IDDES-T (- - -), SST-T (· - ·), and SST (· · ·). IDDES-T only presented for MUR129.

wake which agrees with the higher levels of TI. IDDES-T can be found to have more large coherent structure in the near wake, where small structures begin to form at the TE for the WALE model in Figure 6-10. This leads to earlier break-up of the large energetic structures and lower downstream TI relative to IDDES-T as seen in the wake comparison. The SST-T prediction of peak wake decay is in the best agreement with the WALE predictions in the far wake, $X/C_{ax} = 1.44$. However, poor agreement in the decay rate from the TE to the far wake is found.

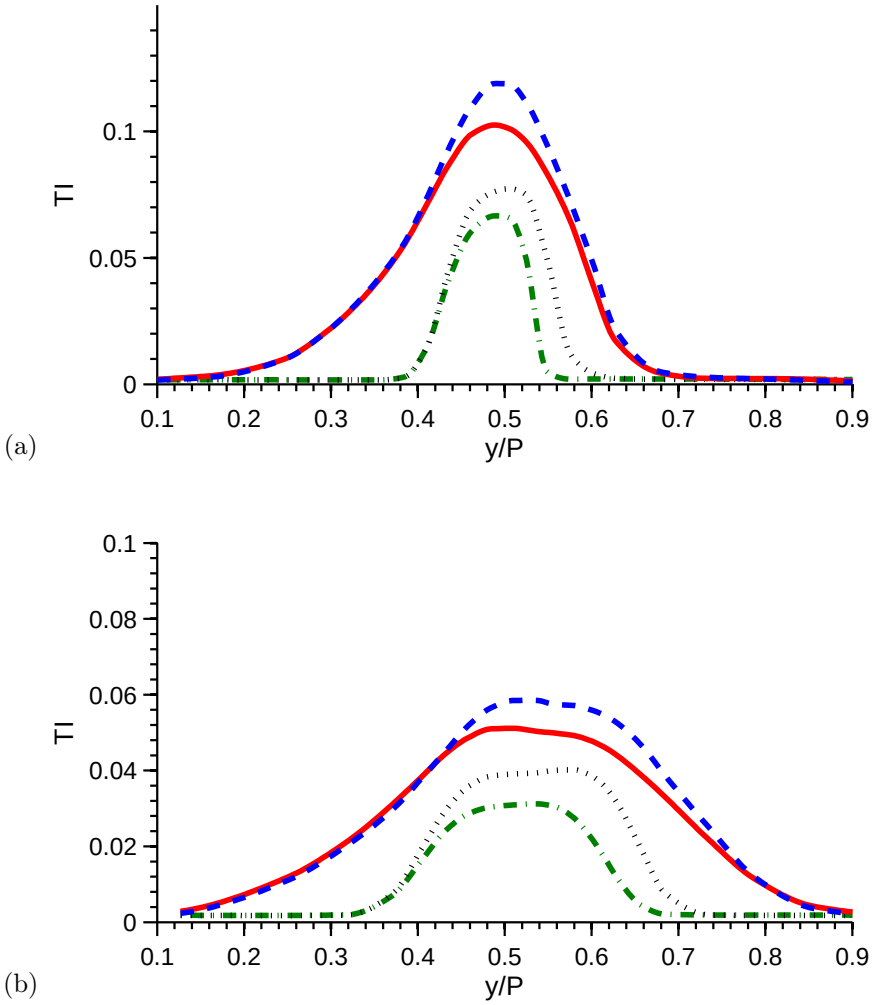

Figure 6-6. Vane local TI profiles for no inlet turbulence at (a) $X/C_{ax} = 1.17$ and (b) $X/C_{ax} = 1.44$ from the vane LE. WALE (——), IDDES-T (- - -), SST-T (· - ·), and SST (· · ·).

The plane mass average total pressure mixing loss at $X/C_{ax} = 1.17$ is summarized in Table 6.4. Relative to the WALE model both IDDES-T and SST-T are within 7% of the predicted loss for case MUR129. When not including transition modeling, SST shows a 50% increase in loss relative to WALE. This highlights the importance in capturing the BL state and the contribution to vane overall total pressure loss. At the lower *Re* case MUR228, SST-T further deviates from the WALE prediction. The mass plane average values can also be misleading in the model's predictive capability, where the SST-T wake profile depth and width are in poor agreement with WALE

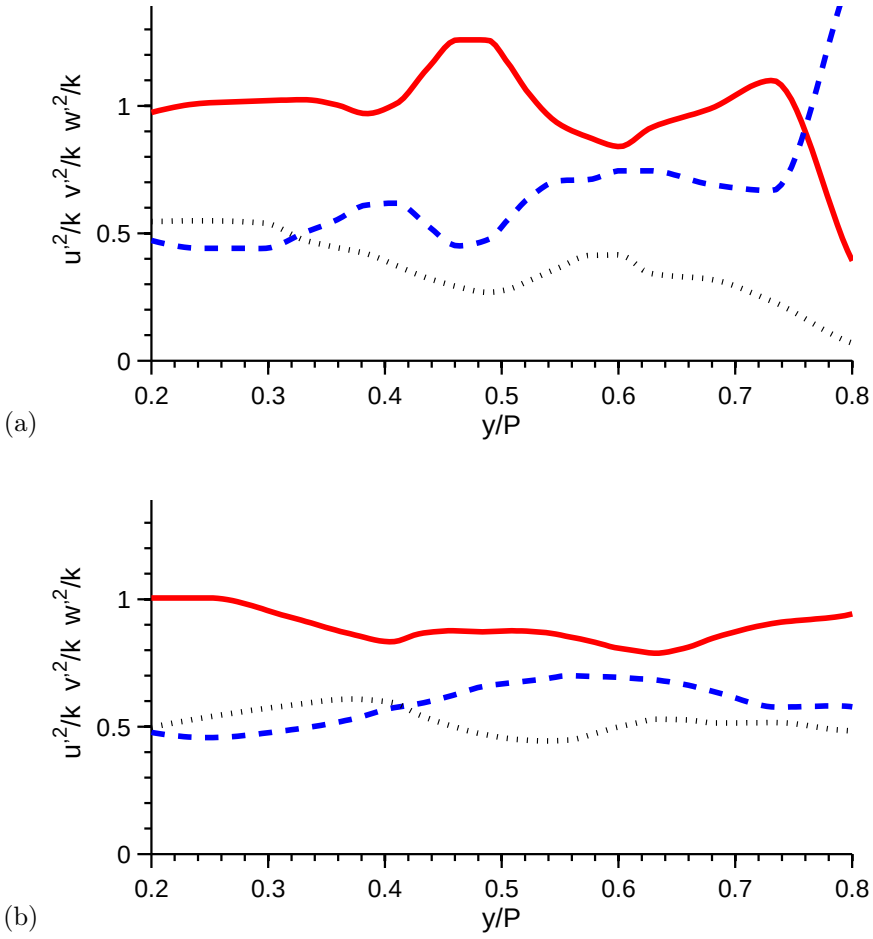

Figure 6-7. Vane local Reynolds Stress profiles for no inlet turbulence at (a) $X/C_{ax} = 1.17$ and (b) $X/C_{ax} = 1.44$ from the vane LE. WALE resolved u'^2/k (——), v'^2/k (- - -), and w'^2/k ($\cdot\ \cdot\ \cdot$) for MUR129.

predictions for MUR129 (Figure 6-5).

Table 6.4. Mass plane average total pressure loss, $1 - \langle Pt \rangle / Pt_1$, at $X/C_{ax} = 1.17$ for no inlet turbulence.

Case	SST	SST-T	IDDES-T	WALE
MUR228	1.80%	1.28%	N/A	1.16%
MUR129	1.47%	1.03%	1.02%	0.96%

It is now important to understand the impact of the unsteady wake on the vane surface. The WALE predictions are used to examine the strength of the unsteadiness from the TE wake shedding that propagates to the vane surface in Figure 6-11.

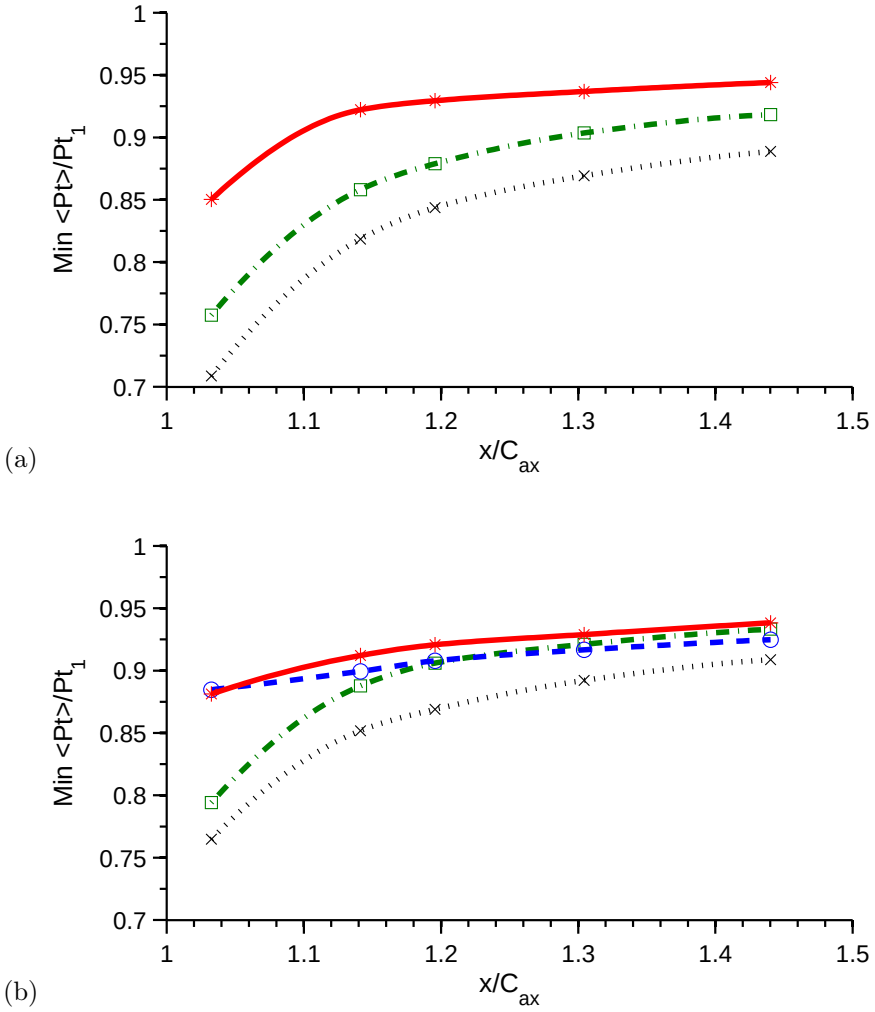

Figure 6-8. Vane wake minimum normalized mean total pressure decay for no inlet turbulence. Cases (a) MUR228 and (b) MUR129 for WALE (——), IDDES-T (- - -), SST-T (· - ·), and SST (· · ·). IDDES-T only presented for MUR129

Frequencies along the SS surface of the vane can be found to match the wake shedding frequency. This is due to the pressure fluctuations from the vane wake shedding propagating across the passage from the adjacent vane. The deterministic signal from the TE shedding can be found at all but one location. At the SS location at $X/C_{ax} = 0.98$ the non-deterministic signal is due to the transitioning of the BL and the chaotic nature of a developing turbulent BL. This shows the unsteady relationship between adjacent vanes. The experimental facility of Arts and Rouvroit [34] cascade

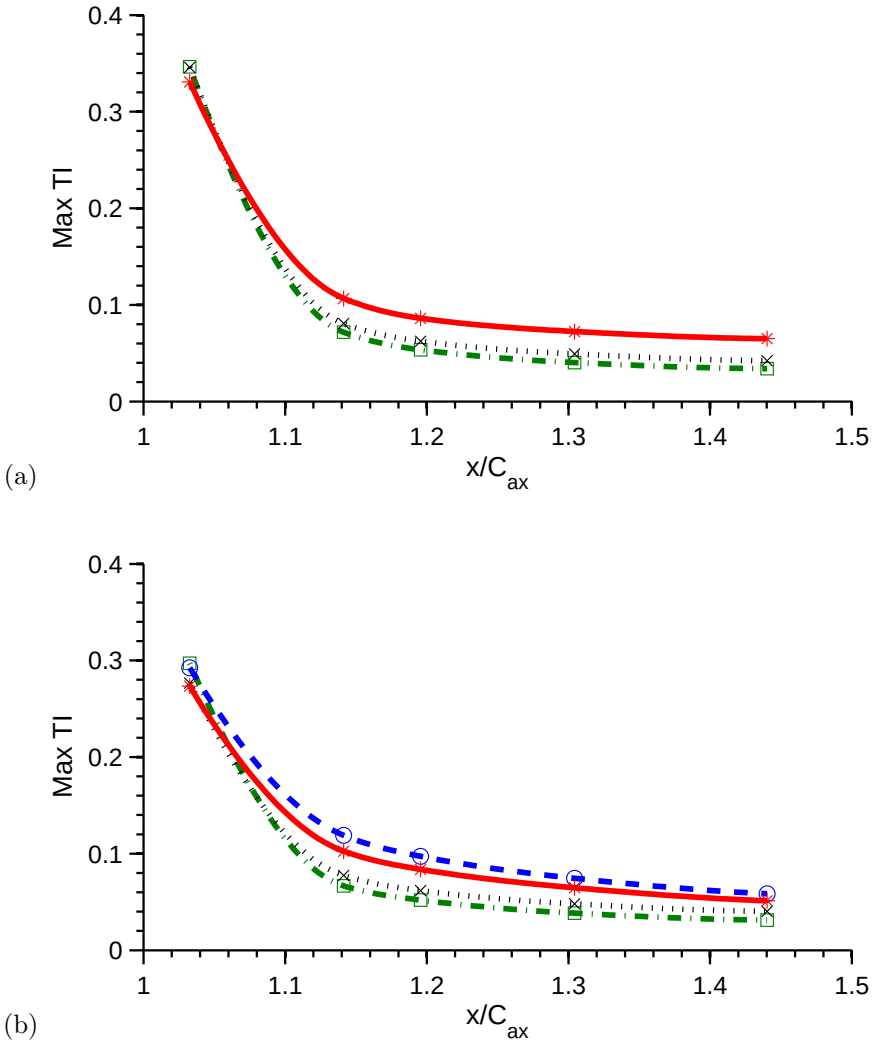

Figure 6-9. Vane wake maximum TI decay for no inlet turbulence. Cases (a) MUR228 and (b) MUR129 for WALE (——), IDDES-T (- - -), SST-T (· - ·), and SST (· · ·). IDDES-T only presented for MUR129.

includes the 5 vane (7 passage) and would have captured this behavior on the center instrumented vane.

Table 6.5 provides a summary for each model's predictive capability for case MUR129. For the quantities where no experimental measurements are available, LES serves as the benchmark. All models provided nearly equivalent accuracy in prediction of Nu. The predicted maximum deviation for the PS surface Nu from the experimental data is 25% for the WALE model where the contribution due to the

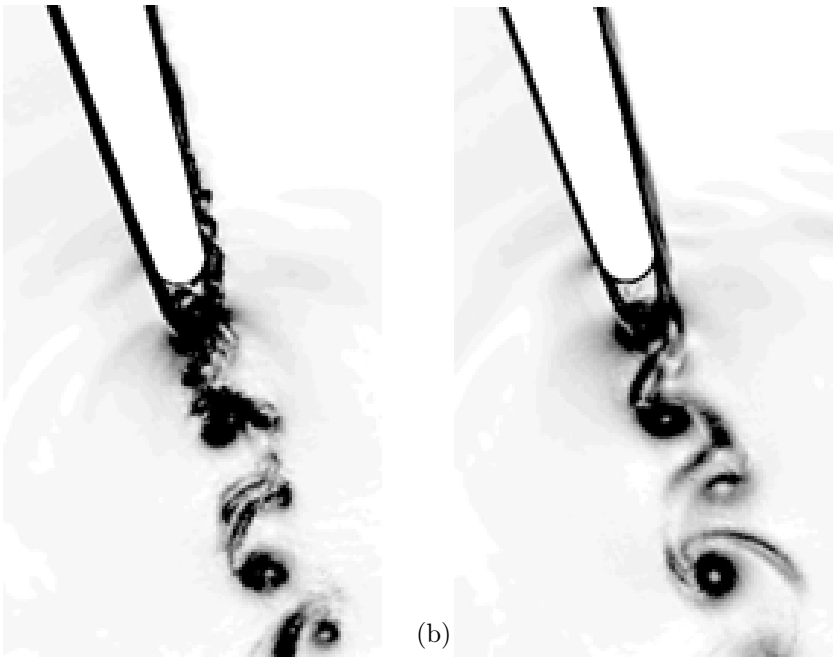

Figure 6-10. Numerical Schlieren of the TE wake for (a) WALE and (b) IDDES-T for MUR129.

over-prediction of the Gortler vortex has been previously discussed. BL transition occurs on the SS surface where the prediction error is based on the difference in s/C relative to the experimental results. The WALE model was shown to predict the surface Nu transition location with 5% of the experimental data.

Next, the wake profile predictions are assessed at the far wake location $X/C_{ax} = 1.44$. SST-T shows the largest deviation from the experimental data of 3%. This is largely due to the model's inability to capture the spread of the wake. The SST-T model most significant limitation is found for the prediction of the wake decay rate. The magnitude of the near wake peak shows a deviation of up to 8% relative to WALE predictions.

Finally, the computational cost is compared on a relative basis to the WALE model. The computational cost for the IDDES-T modeling approach is about 4X less than the WALE modeling approach. This is a result of the reduced near-wall mesh requirement. Identical time step and iteration per time step was used for WALE and IDDES-T modeling approaches. This was driven by the temporal resolution and

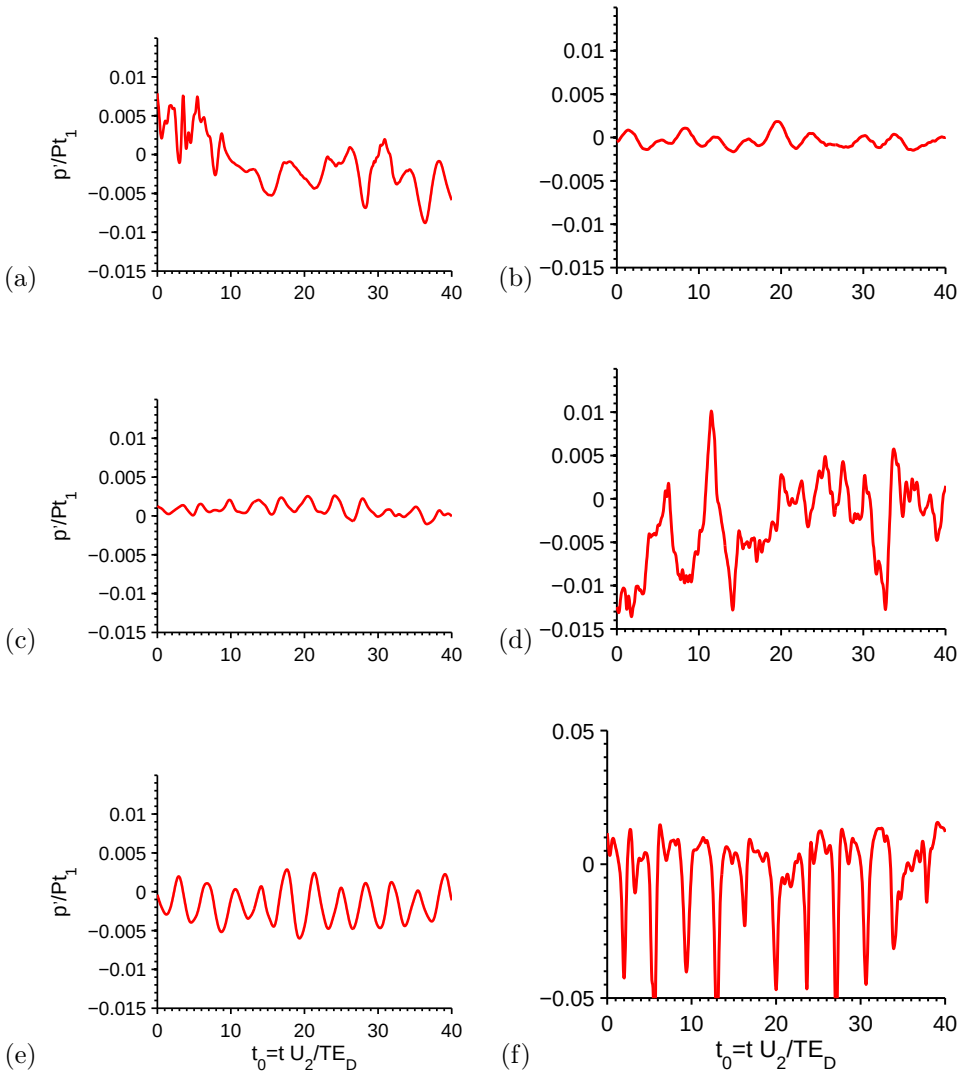

Figure 6-11. WALE case MUR129 p'/Pt_1 on the SS vane surface at (a) $X/C_{ax} = 0.98$,(c) $X/C_{ax} = 0.86$, (e) $X/C_{ax} = 0.72$; the PS vane surface at (b) $X/C_{ax} = 0.93$; the TE of the vane surface at (d) $X/C_{ax} = 1.0$; and in the near wake at (f) $X/C_{ax} = 1.07$.

mesh density required to capture the turbulent mixing in the wake. As expected, the cost is significantly less for the SST-T model. This is driven by the reduction in iteration requirement for the steady RANS solution. This substantial reduction in cost is why RANS modeling remains widely used in industrial flows. However, even after confirming the SST-T solution was grid independent, large modeling inaccuracies were presented. More specifically the ability to capture mixing loss dependency on

Re. This modeling comparison is revisited for cases in the following sections with high free-stream TI.

Table 6.5. Turbulence model predictive summary relative to experimental measurement, otherwise benchmarked to LES (*) for MUR129.

	SST-T	IDDES-T	WALE
PS Nu	$Nu_{Error} < 10\%$	$Nu_{Error} < 10\%$	$Nu_{Error} < 25\%$
SS Nu	$\Delta s/C_{Error} < 10\%$	$\Delta s/C_{Error} < 20\%$	$\Delta s/C_{Error} < 5\%$
Pt Far Wake Profile	$< Pt > /Pt_{Error} < 3\%$	$< Pt > /Pt_{Error} < 1\%$	$< Pt > /Pt_{Error} < 0.5\%$
Pt Wake Decay*	$< Pt > /Pt_{Error} < 8\%$	$< Pt > /Pt_{Error} < 1\%$	Benchmark
Computational Cost*	$< 1/100$	$< 1/4$	Benchmark

6.2 Moderate Inlet Turbulence

Consideration for elevated inlet turbulence is now given where conditions for cases MUR226, MUR224, and MUR235 span two TI and Re numbers. A scale-resolved and RANS approaches are executed for the given inlet turbulence, length scale, and decay. WALE and IDDES-T extend the domain to include the upstream bars that generate an unsteady inlet boundary condition for the vane (Figure 5-2). The locations of the bars are matched to the experimental setup of Arts [76]. Figure 6-12 shows the area plane average TI upstream and through the vane where $X/C_{ax} = 0$ is the LE of the vane. SST and SST-T inlet boundary conditions at $X/C_{ax} = -1.49$ are set to match the experimental reported value of TI. The RANS turbulence decay rate is matched to WALE and IDDES-T predictions by tuning the value of the specific dissipation rate, ω. Figure 6-12 shows that the SST modeled TI matches the decay rate upstream of the vane relative to the resolved TI for the WALE and IDDES-T models. The decay rate up to the vane LE and through the vane is also found to be in agreement with the WALE predictions. The prediction of the modeled turbulent kinetic energy leading up to and through the vane passage is the reasons the SST with the Kato-Launder production term correction was selected.

Frequency peaks near 5,500 and a 2nd harmonic near 11,000 Hz are predicted just downstream of the bars. Based on the free-stream velocity ($U_\infty \approx 60m/s$) and the bar diameter of 3 mm, the Strouhal number is $0.25 - 0.26$ for the 1st harmonic. This

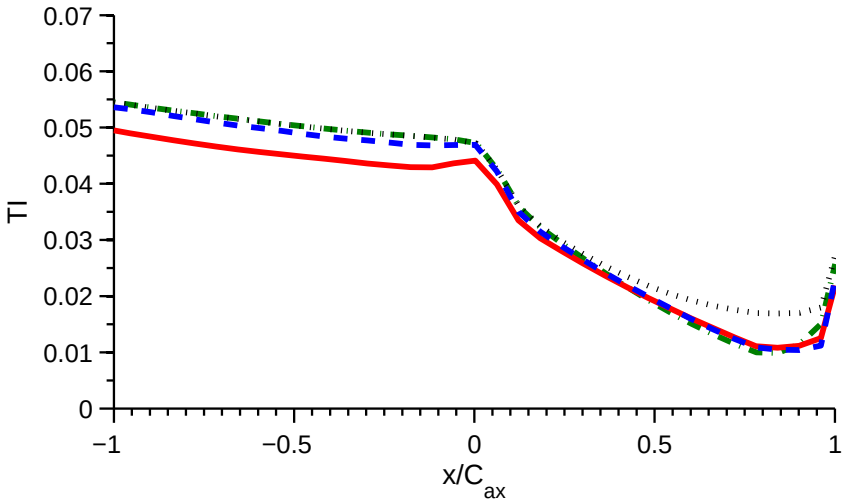

Figure 6-12. Vane turbulence attenuation through the vane for moderate inlet turbulence. MUR235 for WALE (——), IDDES-T (- - -), SST-T (· - ·), and SST (· · ·).

is in good agreement with the experimental measurement of Arts [76]. Using Taylor's hypothesis for frozen turbulence, a length scale of 0.011 meters is found given the bars shedding frequency of 5,500 Hz and free-stream velocity of 60 m/s. This resulted in a 0.16 non-dimensional length scale based on true chord. In addition, the energy spectrum is presented in Figure 6-13 at two locations upstream of the vane LE. The power spectral density (PSD) of U/U_∞ is plotted versus the Strouhal Number based on the bar diameter and free-stream velocity U_∞.

Loading comparisons are made to confirm that operating conditions and geometry are correctly matched for each turbulence model. This is confirmed for MUR226, MUR224, and MUR235 in Figure 6-14. WALE surface Nu in each of the 3 cases, shown in Figure 6-15, predicts a late transition on the SS of the vane. The current study shows that the WALE Nu predictions for the cases at TI=6% (MUR224 and MUR235) have improved agreement to the experimental cases at TI=4% (MUR226 and MUR224). The WALE MUR235 predictions are within the uncertainty of the experimental case MUR217 for inlet TI=4% with exception to the transition on the SS surface at the TE. The SS transition location deviates by s/C of 0.05 from measurement. The improved agreement to measurements taken at lower TI could be due the WALE modeling approach 1) under-prediction of the inlet TI, 2) not accounting

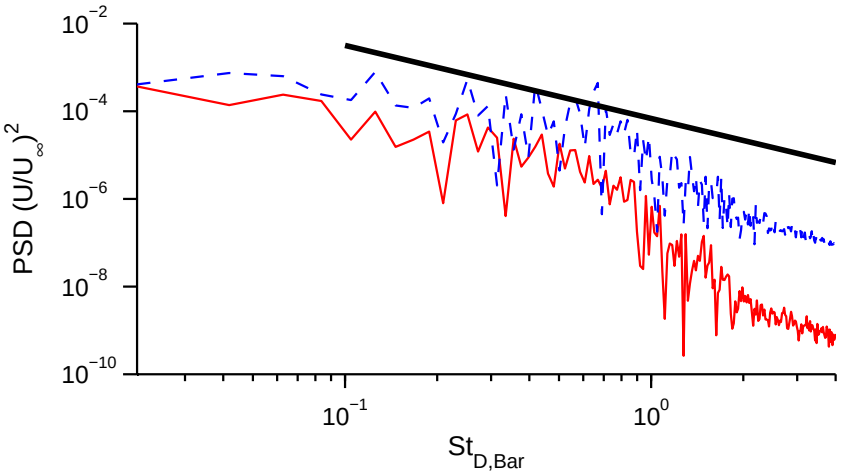

Figure 6-13. WALE vane inlet turbulence energy spectrum for MUR235 at $X/C_{ax} = -1.49$ (——) and $X/C_{ax} = -4.21$ (- - -) relative to the vane LE. Compared to the Kolmogorov's -5/3 Law (——).

for surface roughness, and/or 3) impact of an unstructured mesh using tetrahedral and prism elements. Tetrahedrals and prisms increases the numerical diffusion relative to similar sized hexahedral elements. Case MUR226, FDL3DI on a structure overset hexahedral mesh is included in the comparison to quantify the impact of mesh type and code [49]. Fluent is found to have a slightly lower PS surface Nu relative to FDL3DI. This is equivalent to being within the experimental uncertainty. FDL3DI shows slight improved prediction of the transition location on the SS surface relative to Fluent WALE results. This suggests that for the current comparison, the differences in code and mesh are secondary drivers for the modeling under-prediction of surface Nu. Therefore it is shown for the current resolution and quality of tetrahedral and prism elements with second-order spatial and temporal schemes in Fluent, the predictions are within the equivalent experimental uncertainty relative to FDL3DI predictions. It should also be mentioned that the LES model is different between the Fluent SGS WALE and FDL3DI implicit filtering approach. The contribution of the Fluent SGS WALE model was addressed in Chapter 5. It was found that when setting the SGS constant C_w to zero, a negligible change in Nu and wake mixing prediction was found. Setting C_w to zero eliminates the use of the SGS model where the numerical schemes becomes the LES low-pass filter.

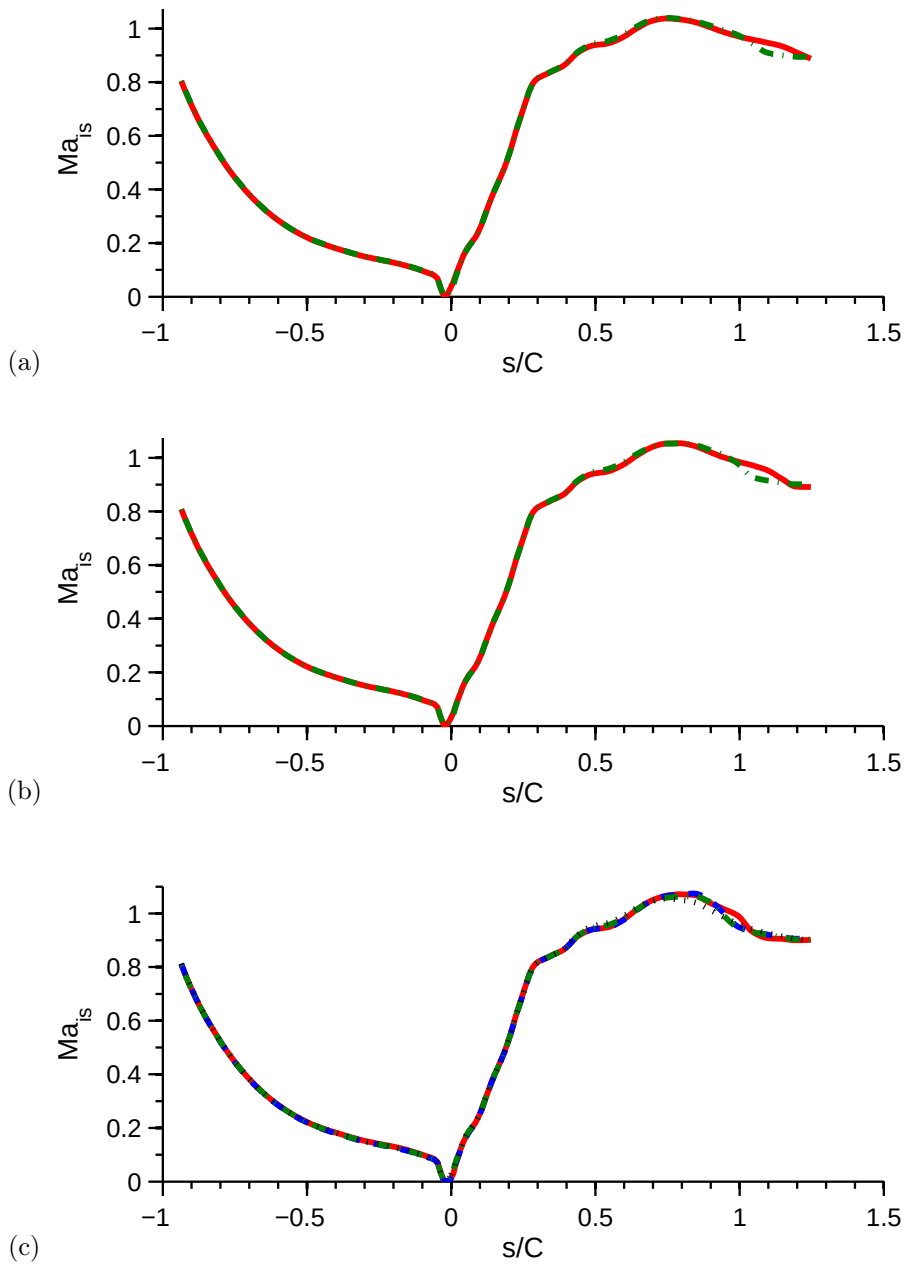

Figure 6-14. Vane loading for moderate inlet turbulence. Cases (a) MUR226, (b) MUR224, and (c) MUR235 for WALE (——), IDDES-T (- - -), SST-T (· - ·), and SST (· · ·). SST and IDDES-T only presented for MUR235.

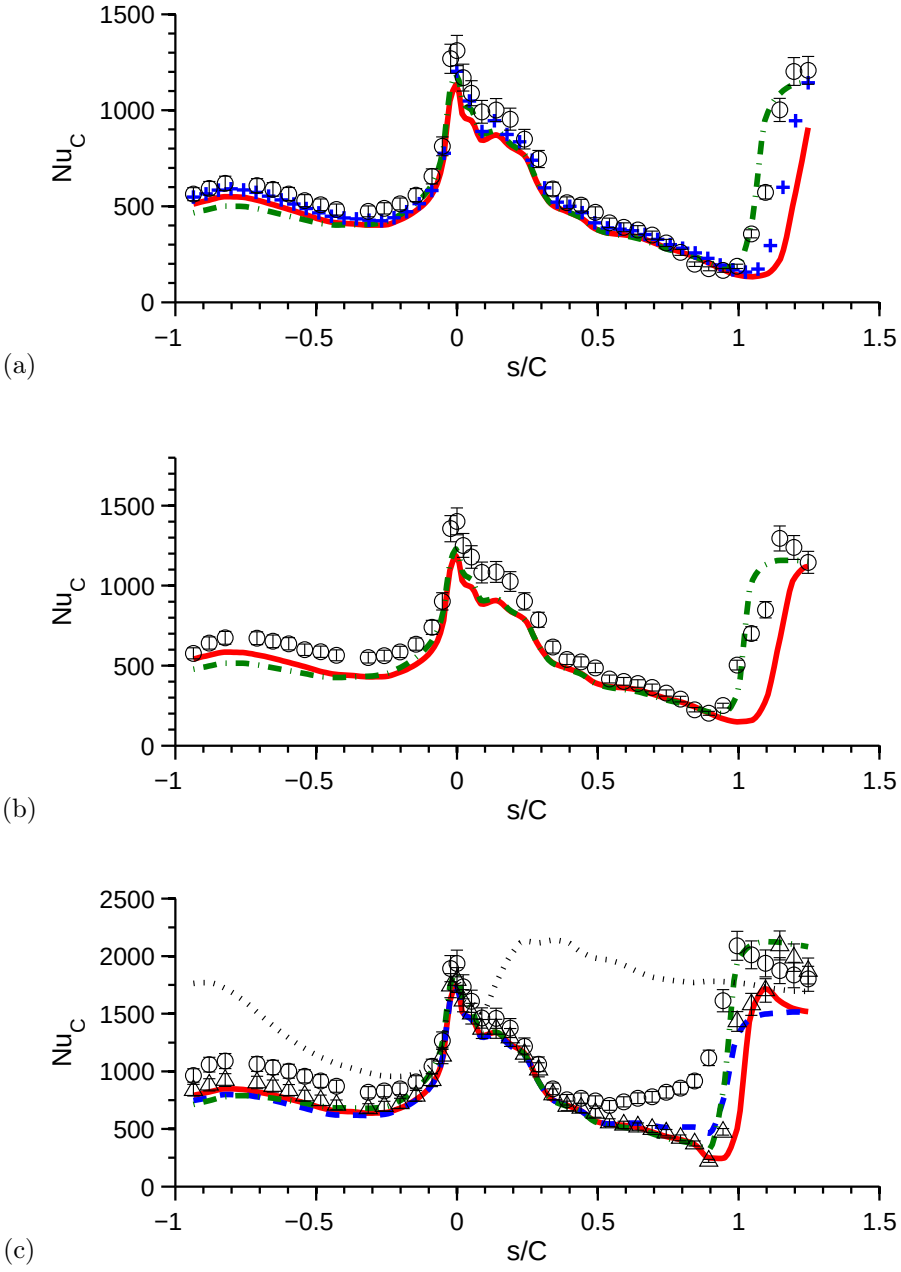

Figure 6-15. Vane mean Nu for moderate inlet turbulence. Experimental cases (a) MUR226 (○), (b) MUR224 (○), and (c) MUR235 (○) and MUR217 (△) compared to WALE (——), IDDES-T (- - -), SST-T (· - ·), and SST (· · ·). SST and IDDES-T only presented for MUR235. FDL (+) presented for case MUR226 [49].

Overall, it is clear that the vane SS transition location is found to be highly sensitive in this Re and TI regime. The SST-T model provides a similar level of accuracy for Nu relative to WALE predictions. It is found when matching the vane inlet turbulence and decay the SST-T provides good predictive capability of the SS surface Nu and transition location. The SST-T, IDDES-T, and WALE all under-predict the SS surface transition location when compared to the experimental case MUR235. As previously stated, improved agreement is found for the lower TI level (MUR217).

Boundary layer plots for the normalized velocity for MUR224 and MUR235 are presented in Figure 6-16. Linear-log plots are used to asses the state of the BL which includes the empirical correlations for the viscous sublayer in Figure 6-17. Both SST-T and WALE models predict a laminar PS and turbulent SS TE BL for case MUR224. The BL shape and thickness are in excellent agreement between the two models. This is not true for the higher Re case MUR235. SST-T and IDDES-T are found to have similar agreement for both the SS and PS BL. However, WALE predicts a higher near-wall velocity for the SS BL. This results in a $u+$ shift of 5 units for the log layer. This is likely due to an under-resolved mesh or a transitional BL state. The under-resolved mesh is an unexpected result where a near-wall mesh sensitivity was completed for MUR224 in Chapter 5 providing $\Delta y+$, $\Delta s+$, and $\Delta z+$ targets for the higher Re case MUR235. Therefore, it appears the $\Delta y+$, $\Delta s+$, and $\Delta z+$ near-wall resolution is not a fixed target value for two Re numbers studies here. The numerical diffusion of the unstructured mesh could also be more dominant at the higher Re. Unfortunately, comparison to the structured high-order code FDL3DI is not currently available at this higher Re case to provide further insight.

Figure 6-18 shows total pressure wake profile predictions of WALE, IDDES-T, SST-T, and SST for the vane for cases MUR226, MUR224 and MUR235. SST-T is found to consistently over-predict wake depth and under-predict wake spreading relative to WALE predictions. This difference is more apparent for the lower Re cases (MUR226 and MUR224). The prediction of wake profile for the IDDES-T model is found to be in good agreement with the WALE predicted wake depth and width. The

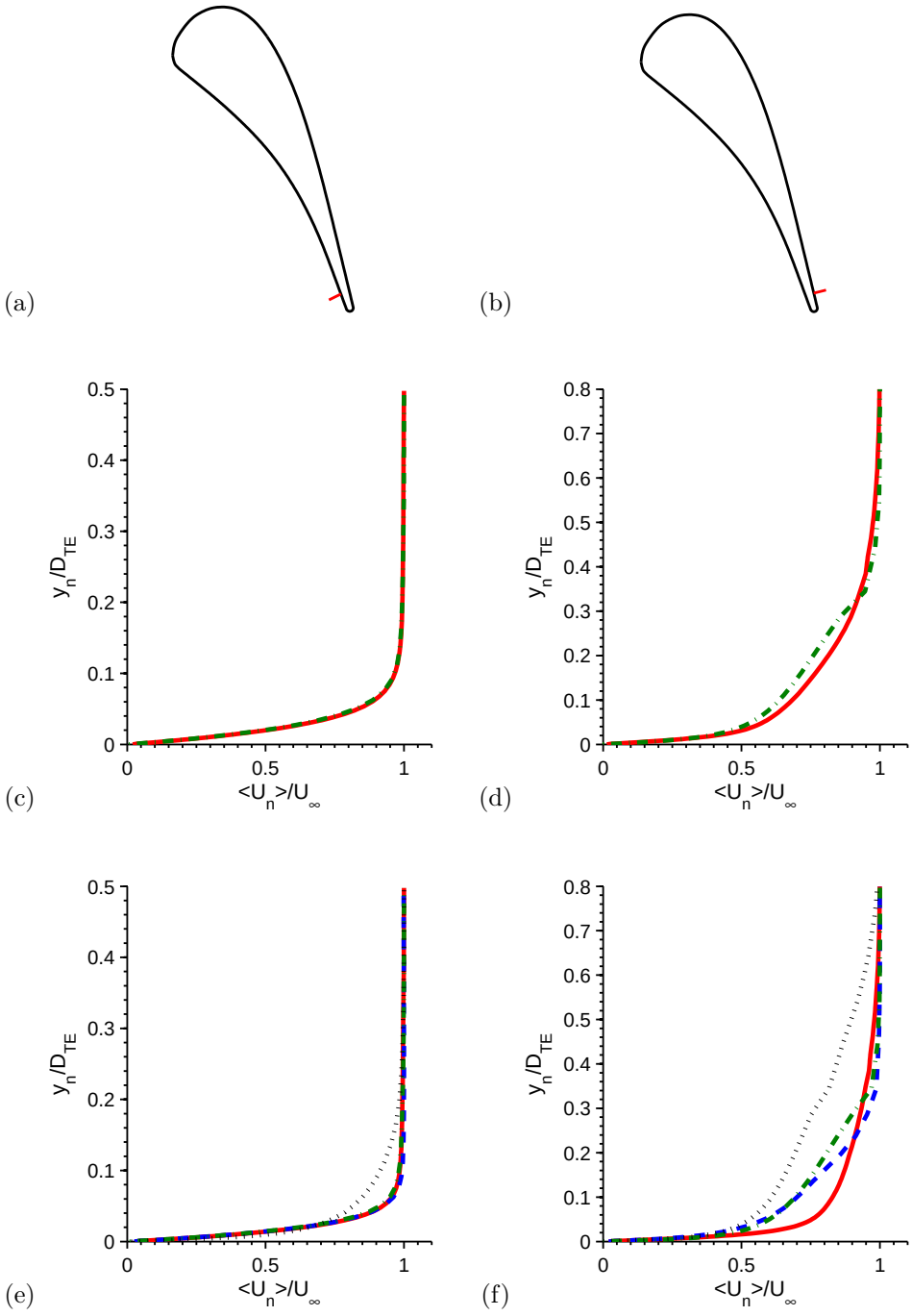

Figure 6-16. Mean velocity boundary layer profiles for WALE (——), IDDES-T (- - -), SST-T (· - ·), and SST (· · ·) with moderate inlet turbulence. Images shown are (a) PS location $X/C_{ax} = 0.93$, (b) SS location $X/C_{ax} = 0.98$ from the vane LE, (c) case MUR224 PS BL, (d) MUR224 SS BL, (e) MUR235 PS BL, and (f) MUR235 SS BL. SST and IDDES-T only presented for MUR235.

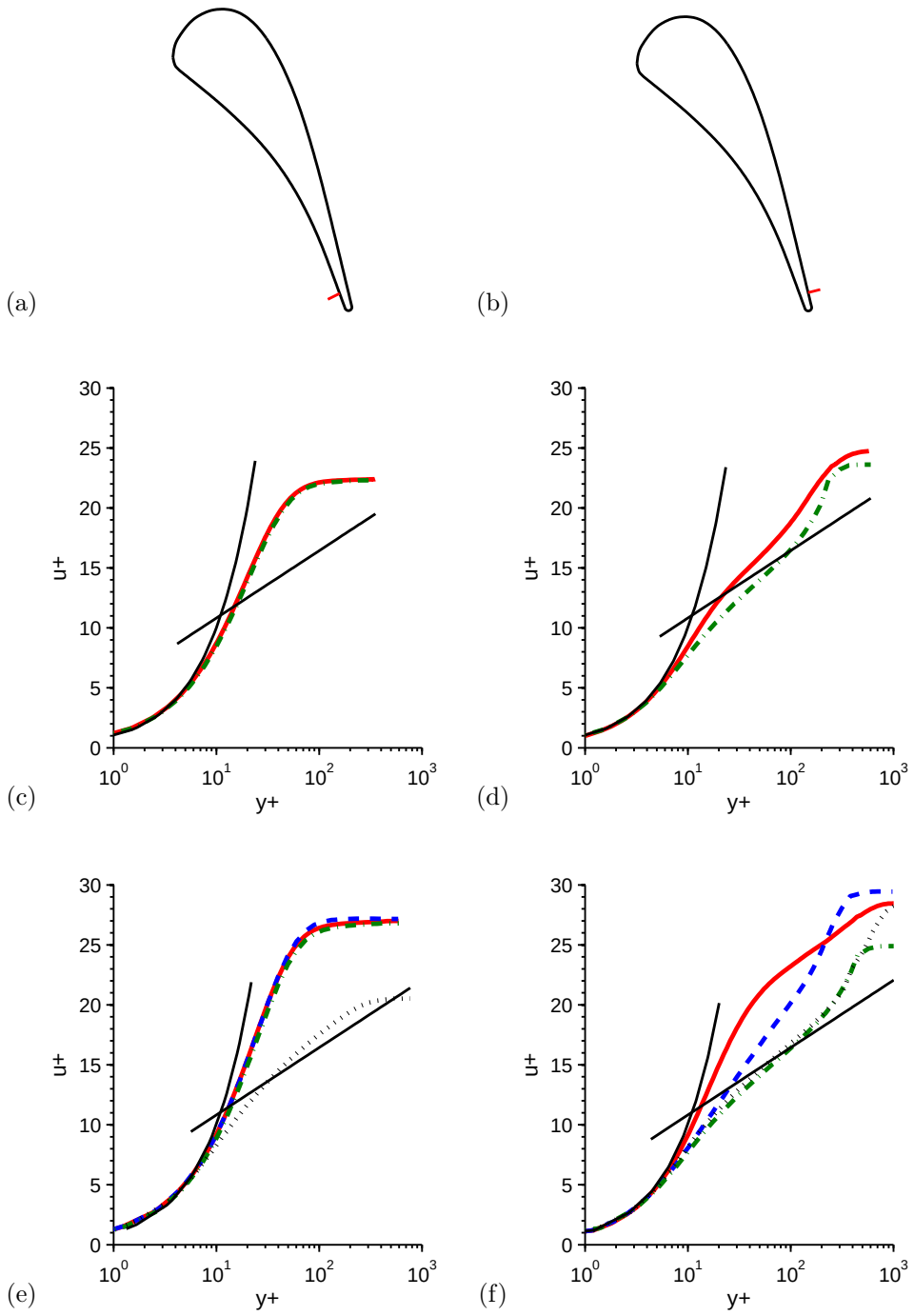

Figure 6-17. Mean velocity linear-log boundary layer profiles for WALE (——), IDDES-T (- - -), SST-T (· - ·), and SST (· · ·) with moderate inlet turbulence. Images shown are (a) PS location $X/C_{ax} = 0.93$, (b) SS location $X/C_{ax} = 0.98$ from the vane LE, (c) case MUR224 PS BL, (d) MUR224 SS BL, (e) MUR235 PS BL, and (f) MUR235 SS BL. SST and IDDES-T only presented for MUR235.

location of the IDDES-T wake is shifted slightly to the SS where we previously saw a deviation in the TE SS BL profile for MUR235. FDL3DI is included in the MUR226 comparison to again quantify the impact of mesh type and code. The wake depth and spreading difference in predictions between Fluent WALE and FDL3DI can be related to 2X the experimental uncertainty.

The plane mass average total pressure mixing loss at $X/C_{ax} = 1.17$ is summarized in Table 6.6. Relative to the WALE model, the SST-T model consistently over-predicts the overall vane loss. For case MUR235, IDDES-T and WALE are within 0.06% of each other for loss. SST-T at the moderated inlet TI is found to further deviate from WALE predictions relative to the previous section with zero inlet TI. Overall, the mass plane average SST-T total pressure loss along with the wake profile depth and width is found to be poor agreement relative to WALE predictions.

Table 6.6. Mass plane average total pressure loss, $1 - \langle Pt \rangle / Pt_1$, at $X/C_{ax} = 1.17$ for moderate inlet turbulence.

Case	SST	SST-T	IDDES-T	WALE
MUR226	N/A	1.33%	N/A	1.13%
MUR224	N/A	1.39%	N/A	1.18%
MUR235	1.69%	1.29%	1.24%	1.18%

6.3 High-Level Inlet Turbulence

High-level inlet turbulence is obtained by moving the upstream bars closer to the vane LE, as shown in Figure 6-19, resulting in TI=20% at $X/C_{ax} = -1.0$. Two cases NB224 and NB129 are modeled ranging from Re of 0.59×10^6 to 1.14×10^6. Additional detail on these cases was provided in Chapter 5. The same modeling approach is taken as the previous section where the WALE and IDDES-T domains include the upstream bars that generate unsteady inlet boundary conditions for the vane. Similar to the moderate inlet turbulence, the non-dimensional length scale is $L_I/C = 0.16$.

Figure 6-20 shows the area plane average TI upstream and through the vane

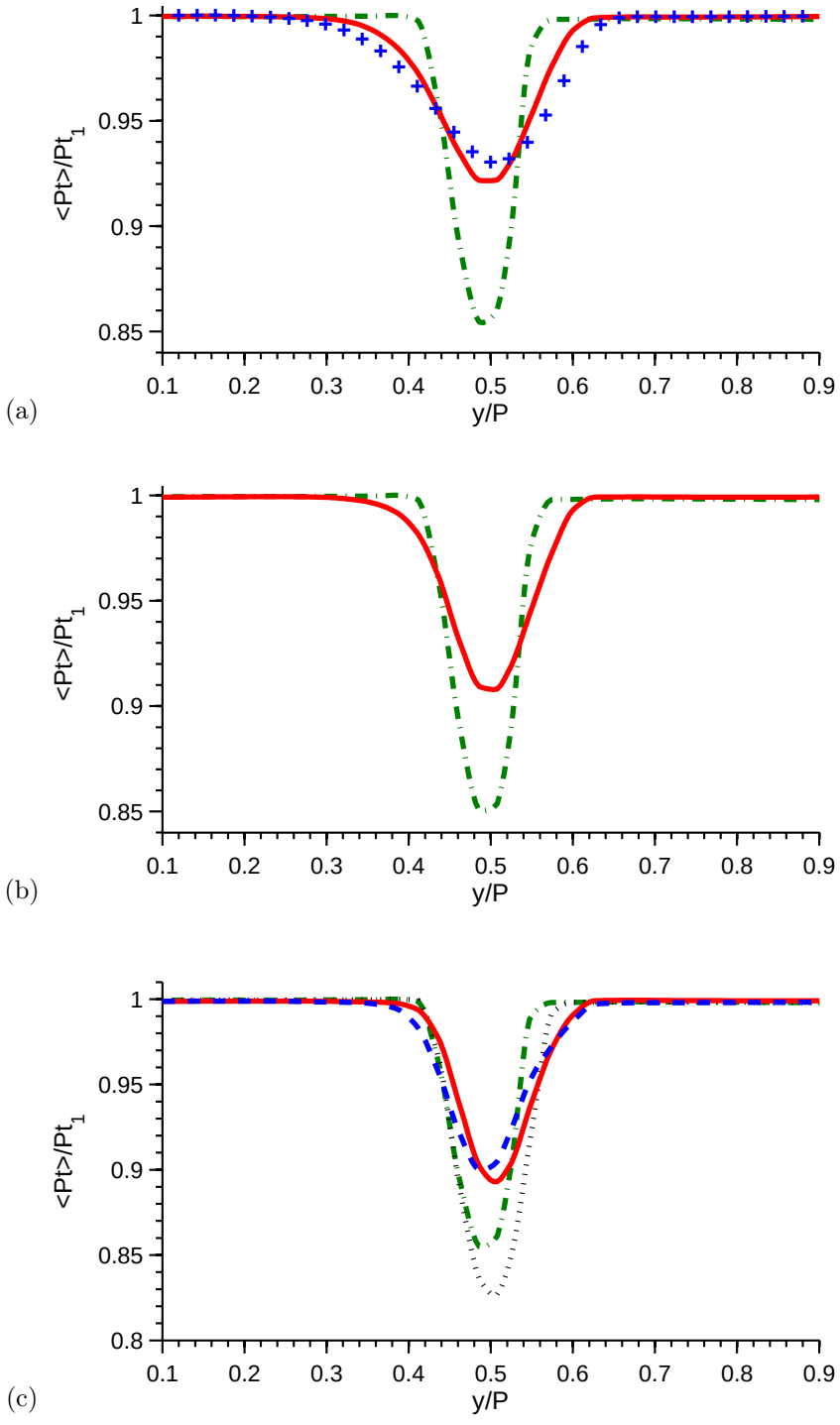

Figure 6-18. Vane normalized mean total pressure profiles for moderate inlet turbulence at $X/C_{ax} = 1.17$. Cases (a) MUR226, (b) MUR224, and (c) MUR235 for WALE (——), IDDES-T (- - -), SST-T (· - ·), and SST (· · ·). SST and IDDES-T only presented for MUR235. FDL (+) presented for case MUR226 [49].

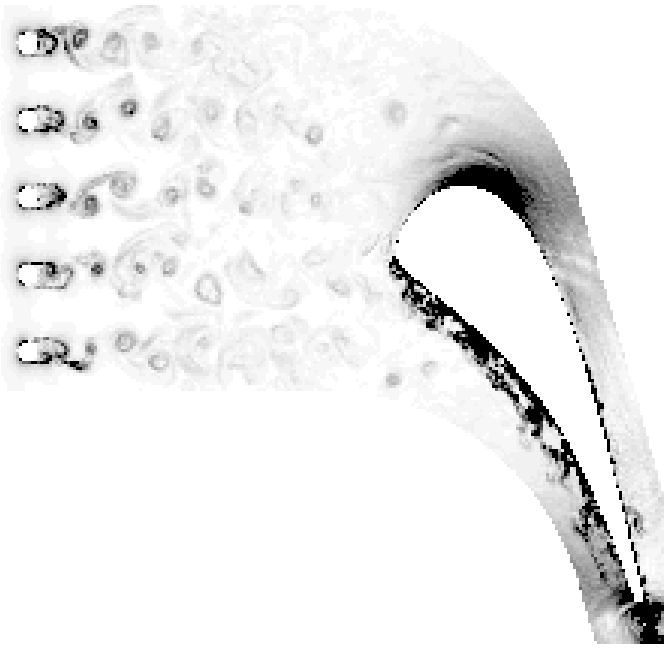

Figure 6-19. High-level inlet turbulence domain. Numerical Schlerien used to show the turbulent structures passed to the downstream vane.

where $X/C_{ax} = 0$ is the LE of the vane. SST and SST-T inlet boundary conditions at $X/C_{ax} = -1.49$ are set to match the WALE model predicted value of TI at $X/C_{ax} = -0.5$. The RANS turbulence decay rate is matched to WALE and IDDES-T predictions by tuning the value of the specific dissipation rate, ω. Figure 6-20 shows that the SST modeled TI matches the decay rate upstream of the vane relative to the resolved TI for the WALE and IDDES-T models. The decay rate through the vane LE is also found to be in agreement for each modeling approach.

Figure 6-21 plots the surface Nu for NB224 and NB129. Large deviation is found between WALE and SST-T that was not found for previous lower free-stream TI cases. For the SST-T modeling approach at the current inlet TI, no experimental data has been used to calibrate or validate the model. Experimental data free-stream TI used to calibrate the $\gamma - Re_\theta$ model ranged from 0-6% [20]. SST and SST-T are found to provide similar levels of Nu since the $\gamma - Re_\theta$ model predicts a fully turbulent Nu over nearly the entire vane surface.

At the current inlet TI=20%, IDDES-T and WALE both predict elevated Nu

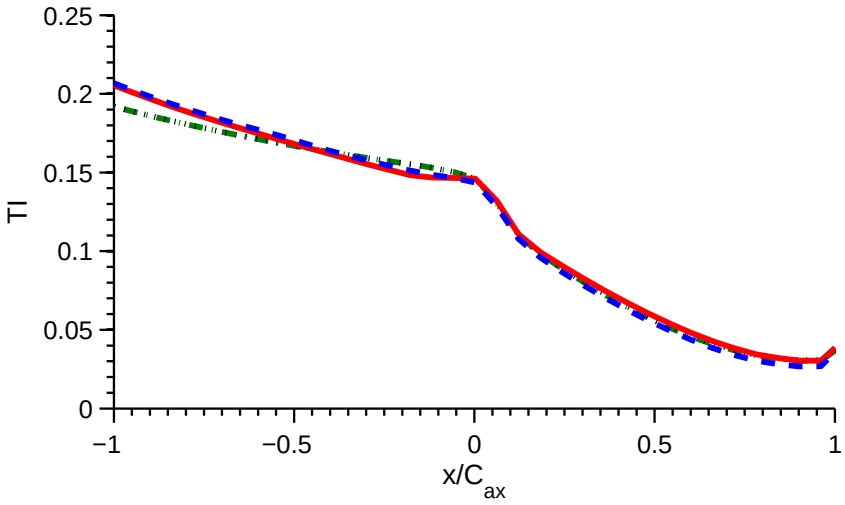

Figure 6-20. Vane turbulence attenuation through the vane for high-level inlet turbulence. NB129 for WALE (——), IDDES-T (- - -), SST-T (· - ·), and SST (· · ·).

compared to low inlet turbulence levels along the SS surface. However, it is clear the Nu doesn't reach a fully turbulent Nu on the PS. The SS TE Nu looks to be nearly fully turbulent but there is no clear transition point along the SS surface. In order to better understand the surface Nu, the vane BL and development is evaluated.

Figure 6-22 shows the WALE and IDDES-T PS BL profiles are found to have non-zero TI levels suggesting a transitional BL state. However, a mean laminar BL is predicted and shown in Figure 6-23. The inability to complete transition is due to the strong favorable pressure gradient. The critical value for the acceleration parameter,

$$K = \nu \frac{\partial U_e}{\partial s} \frac{1}{U_e^2} \tag{6.1}$$

is approximately 3×10^{-6} where U_e is the velocity at the edge of the BL. At values greater than the critical value, the local acceleration can prevent BL transition or relaminarization can occur [86]. K is found to be above this critical value for the entire PS of the vane for cases NB129 and NB224. The inability for a turbulent BL to form is consistent with WALE and IDDES-T predictions where mean laminar velocity profiles are predicted. Laminar mean profiles for inlet TI=20% at similar Re were measured experimentally by both Radomsky [39] and Dees [87] agreeing with

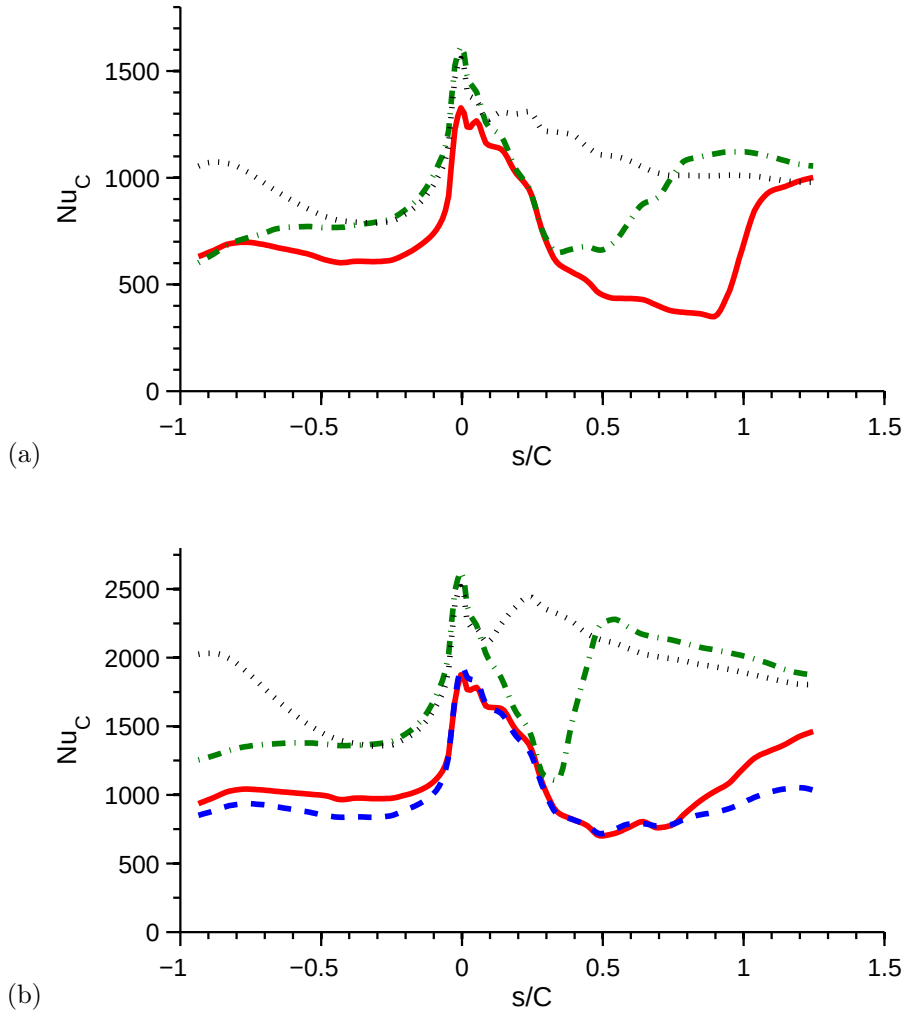

Figure 6-21. Vane mean Nu for high-level inlet turbulence. Cases (a) NB224 (○) and (b) NB129 (○) for WALE (——), IDDES-T (- - -), SST-T (· - ·), and SST (· · ·).

the current findings.

At the SS surface, K only exceeds $3 \times 10^{-}6$ for $0 < s/C < 0.3$. After the high SS curvature (High-C) the near-wall flow sees an adverse pressure gradient and allows for BL transition. This is confirmed with the predicted WALE and IDDES-T BL profile in Figure 6-23 and 6-24. Additionally, the impact of the Re on the boundary layer thickness is accessed to the empirical flat plate relationship for turbulent flow. At the vane SS TE, the scaling of the momentum BL is found to be in agreement with the turbulent flat plate empirical relationship $\delta \sim 1/Re^{1/5}$ [79]. This relationship predicts

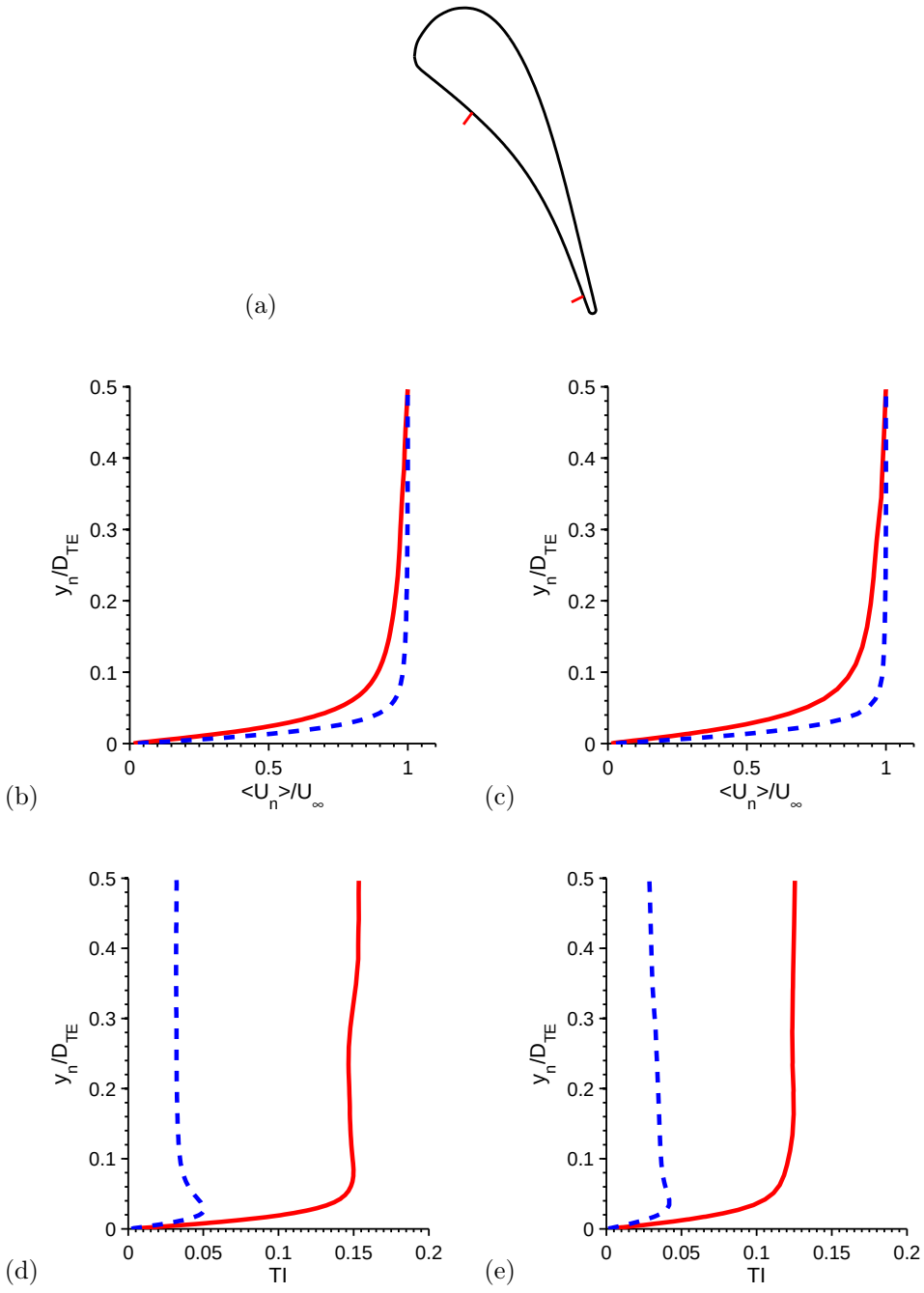

Figure 6-22. Case NB129 boundary layer profiles for WALE (b) mean velocity, (d) TI, and IDDES-T (c) mean velocity, (e) TI with high-level inlet turbulence. Profiles are at $X/C_{ax} = 0.32$ (——) and $X/C_{ax} = 0.93$ (- - -) PS location from the vane LE.

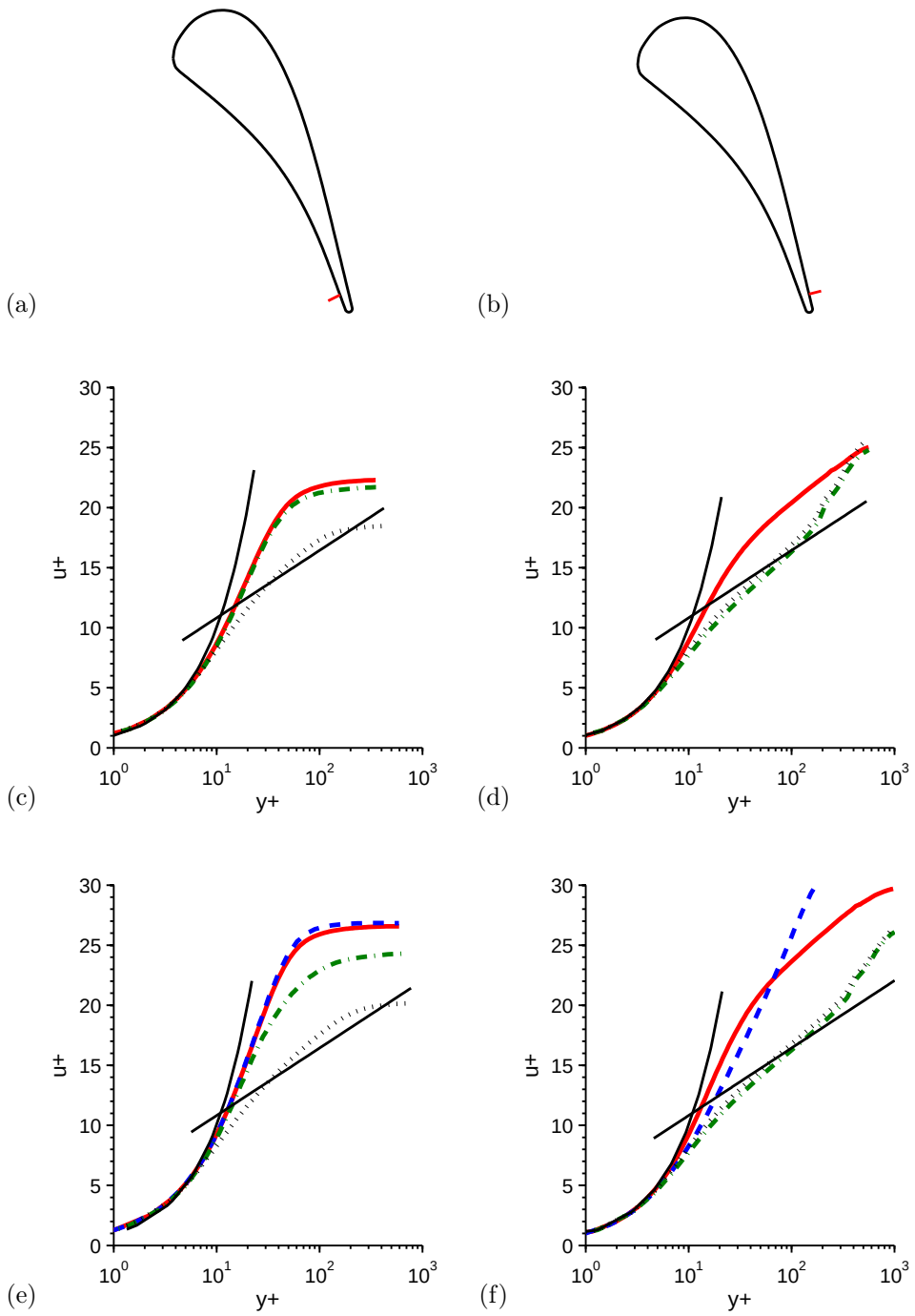

Figure 6-23. Mean velocity linear-log boundary layer profiles for WALE (——), IDDES-T (- - -), SST-T (· - ·), and SST (· · ·) with moderate inlet turbulence. Images shown are (a) PS location $X/C_{ax} = 0.93$, (b) SS location $X/C_{ax} = 0.98$ from the vane LE, (c) case NB224 PS BL, (d) NB224 SS BL, (e) NB129 PS BL, and (f) NB129 SS BL. SST and IDDES-T only presented for NB224.

$\delta_{NB129}/\delta_{NB224}$ to be 0.88, whereas the WALE model predicts 0.92.

Lastly, the relationship between the velocity and thermal BL is considered. Previously, Launder and Lockwood analytically showed that accelerated flows could have thermal boundary layers that were up to 8 times thicker than the associated velocity BL, depending on the strength of the favorable pressure gradient [84]. For lower free-stream TI, it was found that high acceleration regions on the vane led to $\delta_T/\delta > Pr^{-1/3}$ where $\delta_T/\delta = Pr^{-1/3}$ is the analytical relationship assumed for the BL in a zero pressure gradient flow. For the cases with the inlet TI of 20%, the thermal BL was up to 5X thicker than the velocity BL (Table 6.7 and 6.8). For the case of inlet TI=0%, the maximum δ_T/δ was 1.5. This clearly shows the BL dependence on the inlet TI.

Table 6.7. Case NB224 WALE boundary layer parameters.

Location	δ/D_{TE}	H	δ_T/δ
SS $X/C_{ax} = 0.98$	0.76	1.4	1.17
SS $X/C_{ax} = 0.85$	0.44	2.2	1.26
SS $X/C_{ax} = 0.60$	0.21	1.9	1.13
SS $X/C_{ax} = 0.35$	0.10	1.8	1.53
PS $X/C_{ax} = 0.93$	0.21	1.3	3.65
PS $X/C_{ax} = 0.32$	0.27	1.4	3.36

Table 6.8. Case NB129 WALE boundary layer parameters.

Location	δ/D_{TE}	H	δ_T/δ
SS $X/C_{ax} = 0.98$	0.70	1.3	1.27
SS $X/C_{ax} = 0.85$	0.38	1.5	1.38
SS $X/C_{ax} = 0.60$	0.14	1.9	1.32
SS $X/C_{ax} = 0.35$	0.07	1.8	1.85
PS $X/C_{ax} = 0.93$	0.14	1.4	5.07
PS $X/C_{ax} = 0.32$	0.40	1.3	1.93

Wake predictions in Figures 6-25 and 6-26 show large deviation in both depth and width of the total pressure and TI profiles for SST-T compared to WALE. In addition to the known RANS model deficiencies (i.e. assumption of isotropic turbulence), this is also due to the prediction of the BL state and impact on the vane profile loss

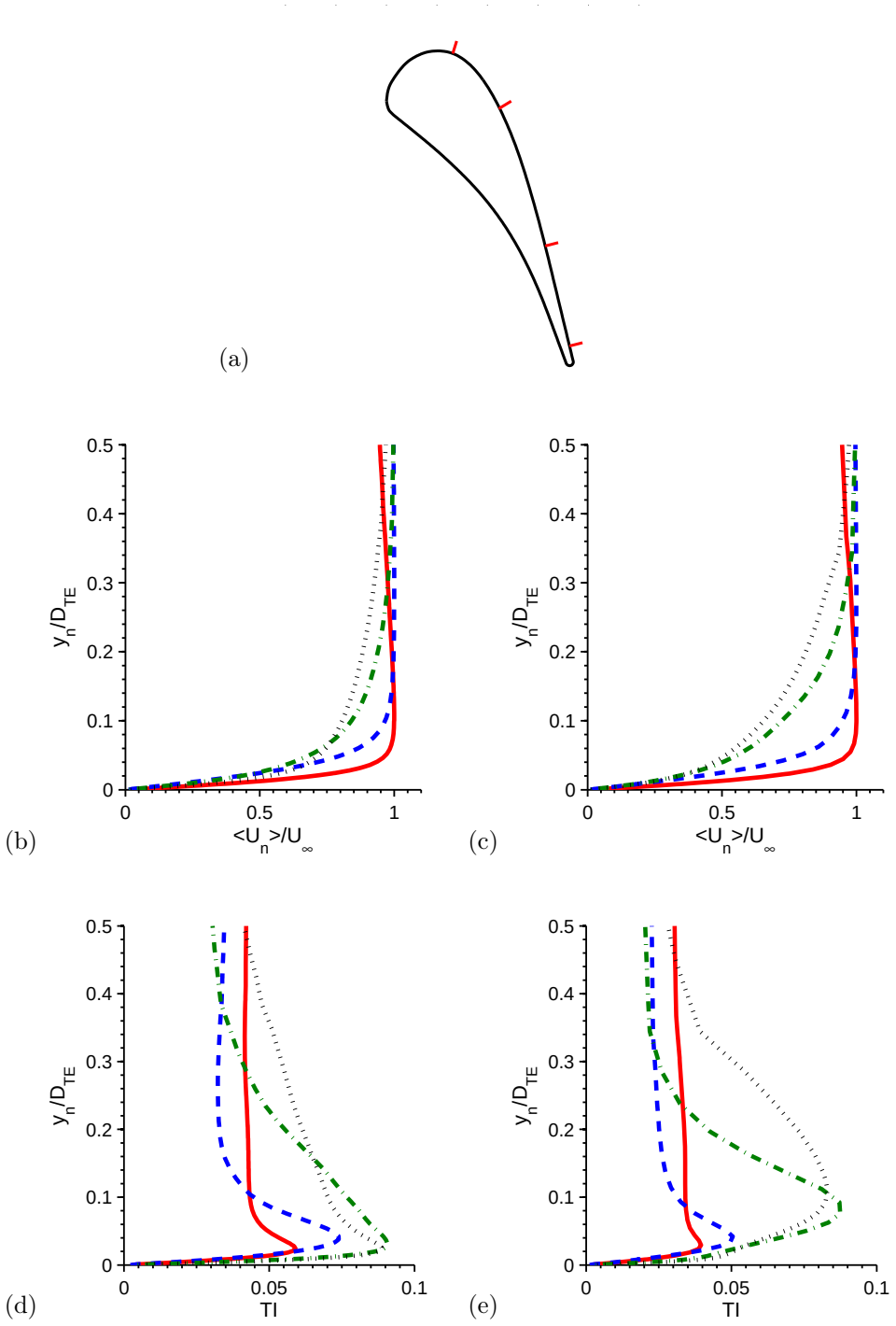

Figure 6-24. Case NB129 boundary layer profiles for WALE (b) mean velocity, (d) TI, and IDDES-T (c) mean velocity, (e) TI with high-level inlet turbulence. Profiles are at $X/C_{ax} = 0.35$ (——), $X/C_{ax} = 0.60$ (- - -), $X/C_{ax} = 0.85$ (· - ·), and $X/C_{ax} = 0.98$ (· · ·) SS location from the vane LE.

and downstream wake mixing. Only agreement in the TI profile is found outside the wake region. IDDES-T is only plotted for case NB129 in Figure 6-25b. Excellent agreement between WALE and IDDES-T in the wake is found within previously discussed experimental uncertainties. This provides confidence in IDDES-T at high-level TI.

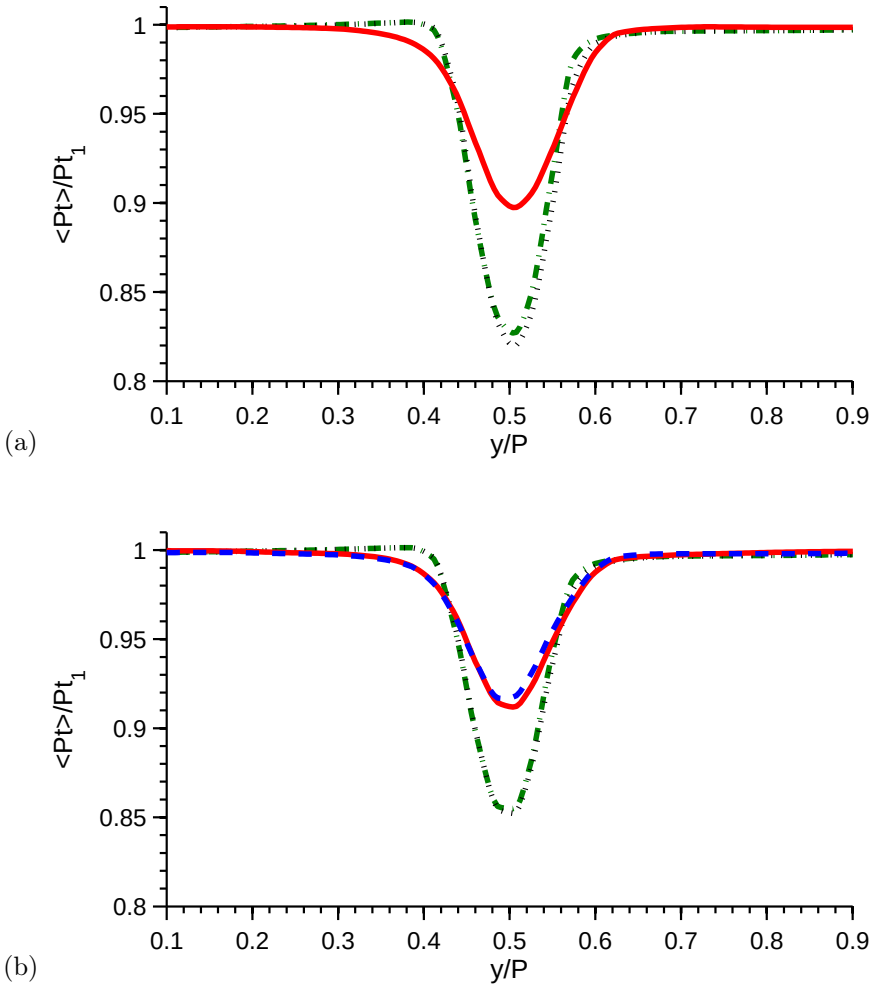

Figure 6-25. Vane normalized mean total pressure profiles for high-level inlet turbulence at $X/C_{ax} = 1.17$ from the vane LE. Cases (a) NB224 and (b) NB129 for WALE (——), IDDES-T (- - -), SST-T (· - ·), and SST (· · ·).

The plane mass average total pressure mixing loss at $X/C_{ax} = 1.17$ is summarized in Table 6.9. Relative to the WALE model, the SST-T and SST models consistently over-predict the overall vane loss due to the early BL transition predicted at high

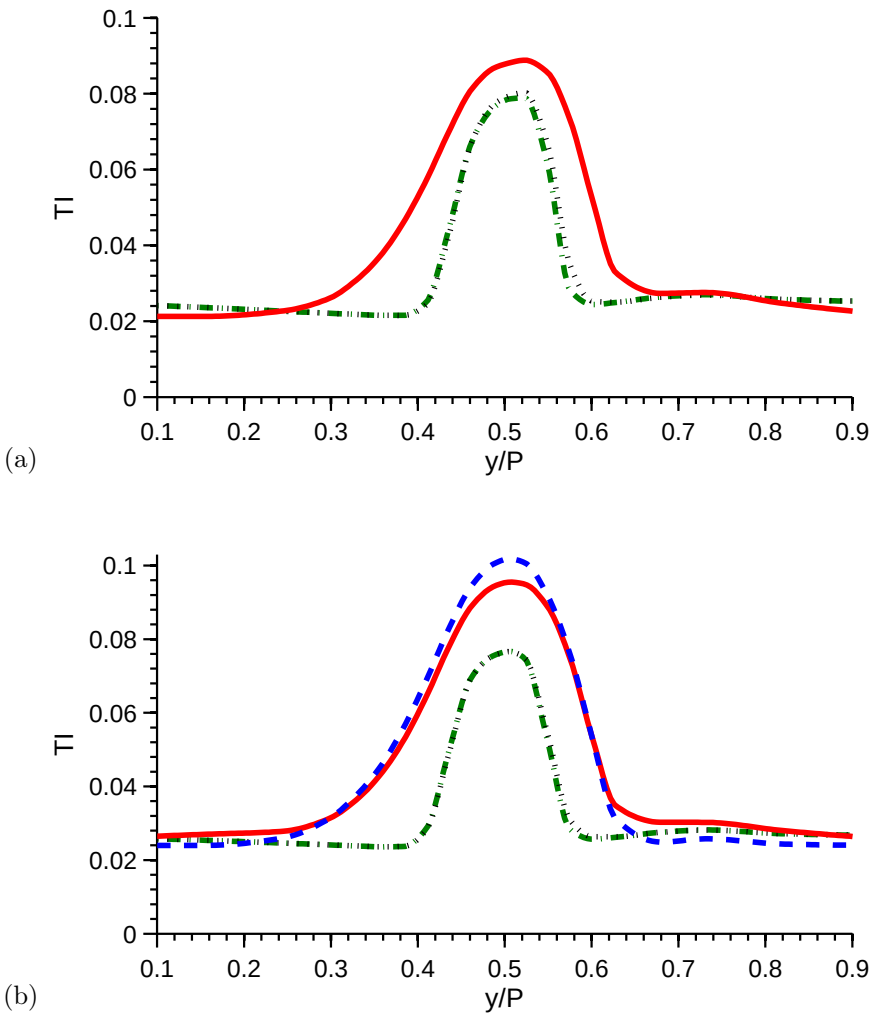

Figure 6-26. Vane local TI profiles for high-level inlet turbulence at $X/C_{ax} = 1.17$ from the vane LE. Cases (a) NB224 and (b) NB129 for WALE (——), IDDES-T (- - -), SST-T (· - ·), and SST (· · ·).

inlet TI. For case MUR235, IDDES-T and WALE are within 3% of each other for the predicted loss.

The relationship between the unsteady wake on the vane surface is now studied at high inlet TI. The WALE predictions are used to examine the strength of the unsteadiness from the TE wake shedding and propagation to the vane surface in Figure 6-27. At zero inlet TI, frequencies along the SS surface of the vane were found to have deterministic frequencies matching the TE wake shedding. This is no longer the case for high inlet TI. All SS surface time series plots are found to have chaotic

signals due to the turbulent or transitional BL. This shows that the high free-stream TI impact dominates the unsteady behavior along the vane surface compared to the unsteady relationship found between adjacent vanes at inlet TI=0%.

Table 6.9. Mass plane average total pressure loss, $1 - \langle Pt \rangle / Pt_1$, at $X/C_{ax} = 1.17$ for high-level inlet turbulence.

Case	SST	SST-T	IDDES-T	WALE
NB224	1.97%	1.85%	N/A	1.45%
NB129	1.63%	1.58%	1.20%	1.23%

Table 6.5 provides a summary for each model's predictive capability for case NB129. No experimental measurements are available, therefore LES serves as the benchmark. It is found that where the SST-T model had previous success in Nu prediction at lower inlet TI levels, the complexity at high TI levels result in significant deviation from WALE predictions. PS surface Nu predictions for IDDES-T are found to be within 5% of the WALE model. At the near wake location $X/C_{ax} = 1.17$, SST-T shows a 7% difference from the WALE predictions. This is largely due to the inability to capture both the BL and wake development where the wake depth is largely over-predicted.

Table 6.10. Turbulence model predictive summary benchmarked to LES for NB129.

	SST-T	IDDES-T
SS Nu	$Nu_{Error} < 120\%$	$Nu_{Error} < 25\%$
PS Nu	$Nu_{Error} < 50\%$	$Nu_{Error} < 5\%$
Pt Near Wake Profile	$< Pt > /Pt_{Error} < 7\%$	$< Pt > /Pt_{Error} < 1\%$
Pt Wake Decay	$< Pt > /Pt_{Error} < 9\%$	$< Pt > /Pt_{Error} < 1\%$
Computational Cost	$< 1/100$	$< 1/4$

6.4 Summary of Inlet Turbulence Impact

The previous section provided a detailed comparison of the SST, SST-T, IDDES-T, and WALE modeling approaches to establish the impact of accuracy at the expense of computational cost. The focus now turns to the impact of inlet TI for the HPT vane.

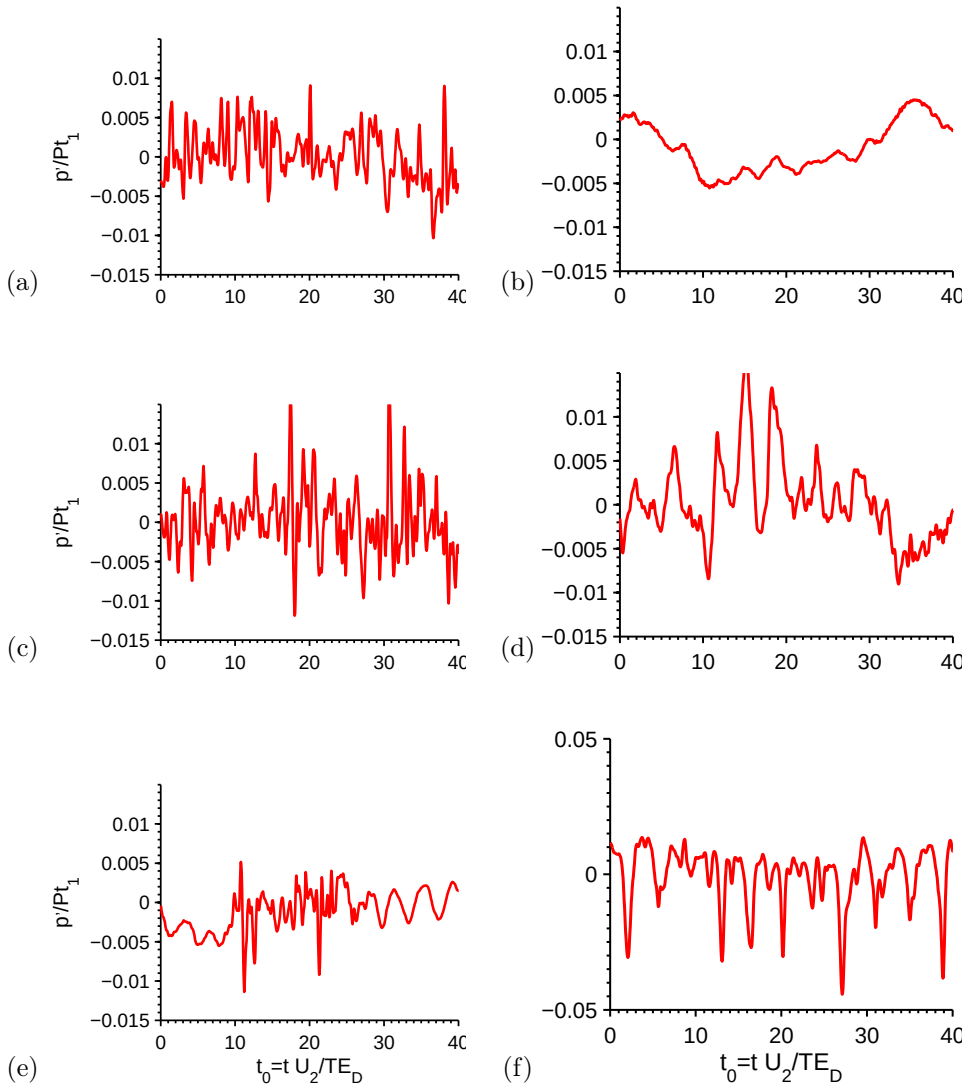

Figure 6-27. WALE case NB129 p'/Pt_1 on the SS vane surface at (a) $X/C_{ax} = 0.98$,(c) $X/C_{ax} = 0.86$, (e) $X/C_{ax} = 0.72$; the PS vane surface at (b) $X/C_{ax} = 0.93$; the TE of the vane surface at (d) $X/C_{ax} = 1.0$; and in the near wake at (f) $X/C_{ax} = 1.07$.

The primary objective of this thesis is to understand the impact of turbulence on BL development, resulting heat transfer, and downstream wake mixing. This section focuses on the vane only geometry before including a downstream blade to study the unsteady stage interaction. Only WALE and IDDES-T models are presented based on the accuracy demonstrated in the previous sections.

Figure 6-28 shows the area plane average TI upstream and through the vane where

$X/C_{ax} = 0$ is the LE of the vane. The accelerated flow through the vane results in local plane average TI levels of less than 5% at the TE for all cases. For the cases with the high free-stream TI, the local TI is reduced by 3X from the LE to the TE of the vane. However, the resolved turbulent kinetic energy increases by approximately 2.5X from the LE to the TE of the vane. Therefore the large fluctuations in velocity are carried through the vane and are seen by the down-stream blade. The impact on the downstream blade is addressed in Chapters 7 and 8.

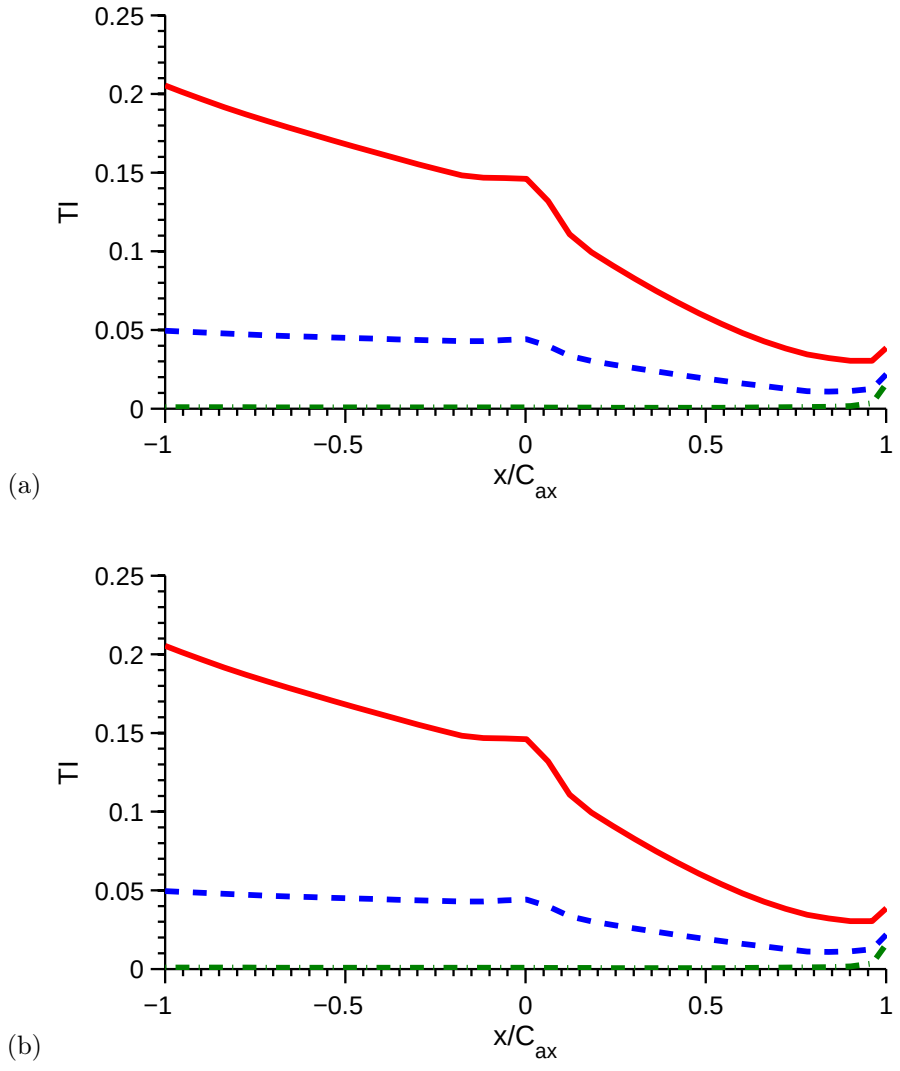

Figure 6-28. Vane turbulence attenuation through the vane for (a) WALE and (b) IDDES-T over range of inlet turbulence at Re_C 1.1×10^6. Turbulence levels shown for high-level (NB129 ——), moderate (MUR235 - - -), and 0% (MUR129 · - ·).

Figure 6-29 shows IDDES-T and WALE both predict similar behavior in the surface Nu due to free-stream TI. Inlet free-stream TI=20% results in Nu increase up to 2X for the PS surface. It was previously shown that the BL had a mean laminar profile but the contribution of the non-zero RMS velocity in the BL results in an elevated Nu which is clearly predicted for the case of TI=20%. Additionally, the WALE PS surface Nu peak value for TI=0% is found to exceed the TI=6% condition. Recall the over-prediction for TI=0% was shown to be caused by the over-prediction of the Gortler vortex along the PS surface. It was hypothesized that a small increase in inlet TI could result in the break-up of the vortex or reduction in strength. This is clearly seen in Figure 6-29 for the WALE predictions when comparing inlet TI of 0% and 6% conditions.

The SS surface for inlet TI=0% shows clear transitioning of the thermal BL near the TE. This is not seen for TI=20% where the Nu is steadily rising. This is indicative of the strong favorable pressure gradient suppressing transition in the high vane curvature (High-C) region on the SS surface. After the vane throat, an adverse pressure gradient is seen by the flow where a turbulent BL can develop. It is important to keep in mind that this study doesn't account for the impact of surface roughness and film cooling which both further promote BL transition. These contributions have been studied by Mayle [28] and Ou [42] and were discussed in Chapter 1.

The momentum (Figure 6-30) and thermal (Figure 6-31) PS BL at the vane TE is found to have a laminar BL with growing non-zero fluctuations due to increasing inlet free-stream TI level. IDDES-T momentum and thermal fluctuation are not resolved near the wall but converge to WALE predictions in the outer BL and free-stream. The difference in TI has a minor impact on the mean momentum and thermal profile, where IDDES-T and WALE show excellent agreement. Notable differences are found along the SS surface (Figures 6-32 and Figure 6-33). The difference in the TI BL is not unexpected due to the near-wall turbulent structures resolved by each model. For the WALE and IDDES-T predictions, similar fluctuations are found in the outer BL as the level convergences to the free-stream value. For the WALE model where the near-wall scales are resolved, equal levels of TI are predicted near the wall for

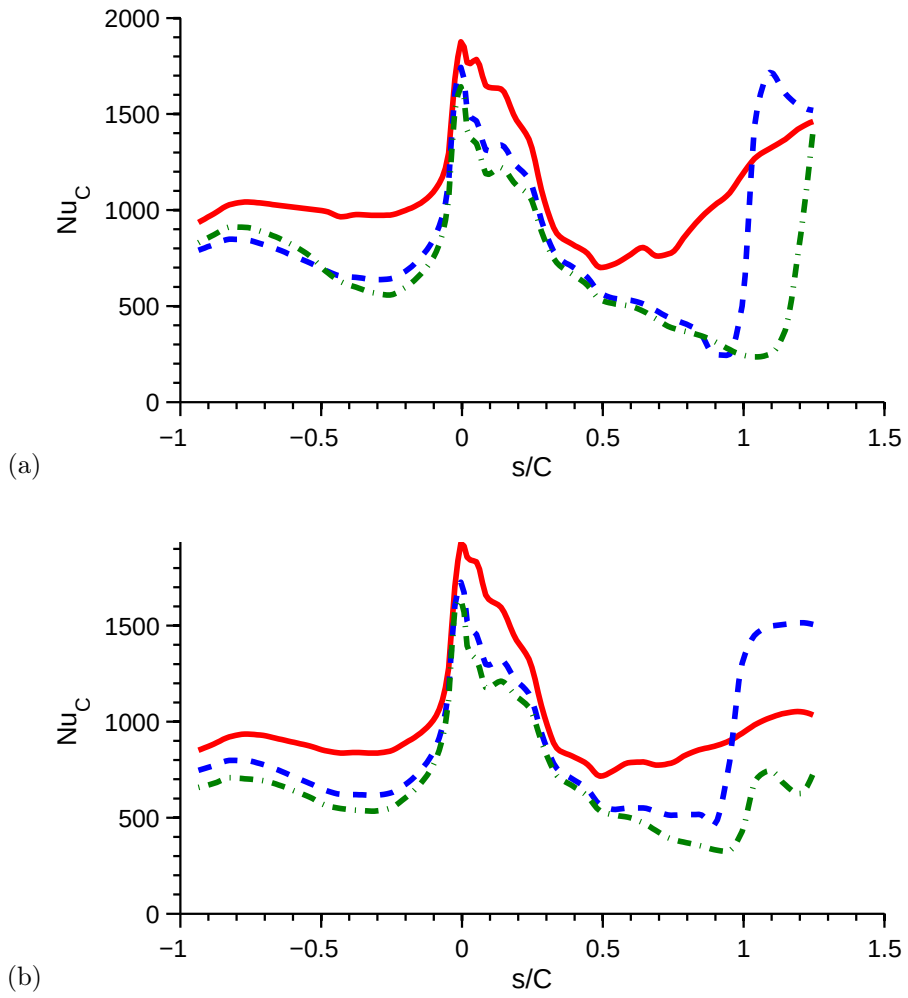

Figure 6-29. Vane mean Nu for (a) WALE and (b) IDDES-T over range of inlet turbulence at Re_C 1.1×10^6. Turbulence levels shown for high-level (NB129 ——), moderate (MUR235 - - -), and 0% (MUR129 · - ·).

TI of 6% and 20% conditions. This shows the fluctuations become independent from increasing free-stream TI levels after a critical flow condition is met for transitioning the BL.

The mean momentum and thermal BL profiles show the WALE model predicts a higher near-wall velocity and temperature compared to IDDES-T. This higher near-wall velocity and temperature results in a shift in the log layer by approximately +5 units for $u+$ and +3 units for $T+$. As previously discussed, this is indicative of a unresolved LES turbulent BL. This shift was not found for the lower Re case MUR224

using the same wall unit meshing targets. This suggests that near-wall mesh targets for $\Delta y+$, $\Delta s+$, and $\Delta z+$ do not remain constant with Re for a turbulent BL.

Tables 6.11 and 6.12 summarize both velocity and thermal BL parameters. The impact of local vane acceleration and free-stream TI is highlighted over the range of conditions. High acceleration regions are found to result in $\delta_T/\delta > Pr^{-1/3}$. This is consistent with the analytical findings of Launder and Lockwood [84] and the experimental findings of Dees [87]. As the free-stream TI is increased from 0% to 6% a $\sim 2X$ increase in the SS momentum BL is found near the TE. This is clearly the impact of inlet TI on the transitioning of the SS BL. There is also $\sim 2X$ increase in the PS momentum BL at $X/C_{ax} = 0.32$ when TI increases from 6% to 20%. This is a region of low acceleration and high TI where the BL is transitional. Downstream of this point the flow is under a strong favorable pressure gradient allowing conditions for relaminarization of the flow where $K >> 3 \times 10^{-}6$. Finally, TI is found to have a significant impact on δ_T/δ. At TI=20% and in regions of high flow acceleration, thermal boundary layers are up to 5X thicker than the velocity BL. This same dependency was experimentally measured by Dees [87] under similar Re but low Mach number conditions.

Table 6.11. WALE boundary layer thickness, δ/D_{TE}, at various inlet TI levels.

Location	$TI = 0$	$TI = 6\%$	$TI = 20\%$
SS $X/C_{ax} = 0.98$	0.33	0.60	0.70
SS $X/C_{ax} = 0.85$	0.19	0.20	0.38
SS $X/C_{ax} = 0.60$	0.12	0.12	0.14
SS $X/C_{ax} = 0.35$	0.07	0.07	0.07
PS $X/C_{ax} = 0.93$	0.09	0.13	0.14
PS $X/C_{ax} = 0.32$	0.21	0.26	0.40

Figures 6-34 and 6-35 show total pressure and TI wake profile predictions for WALE and IDDES-T where profiles over the range of free-stream TI are found to have subtle differences. Going from 0% to 6% inlet TI, the increase spread of the wake reflects the state (thickness) of the TE BL. The wake depth is also found to increase. However, the depth of the wake decreases going from 6% to 20% inlet TI.

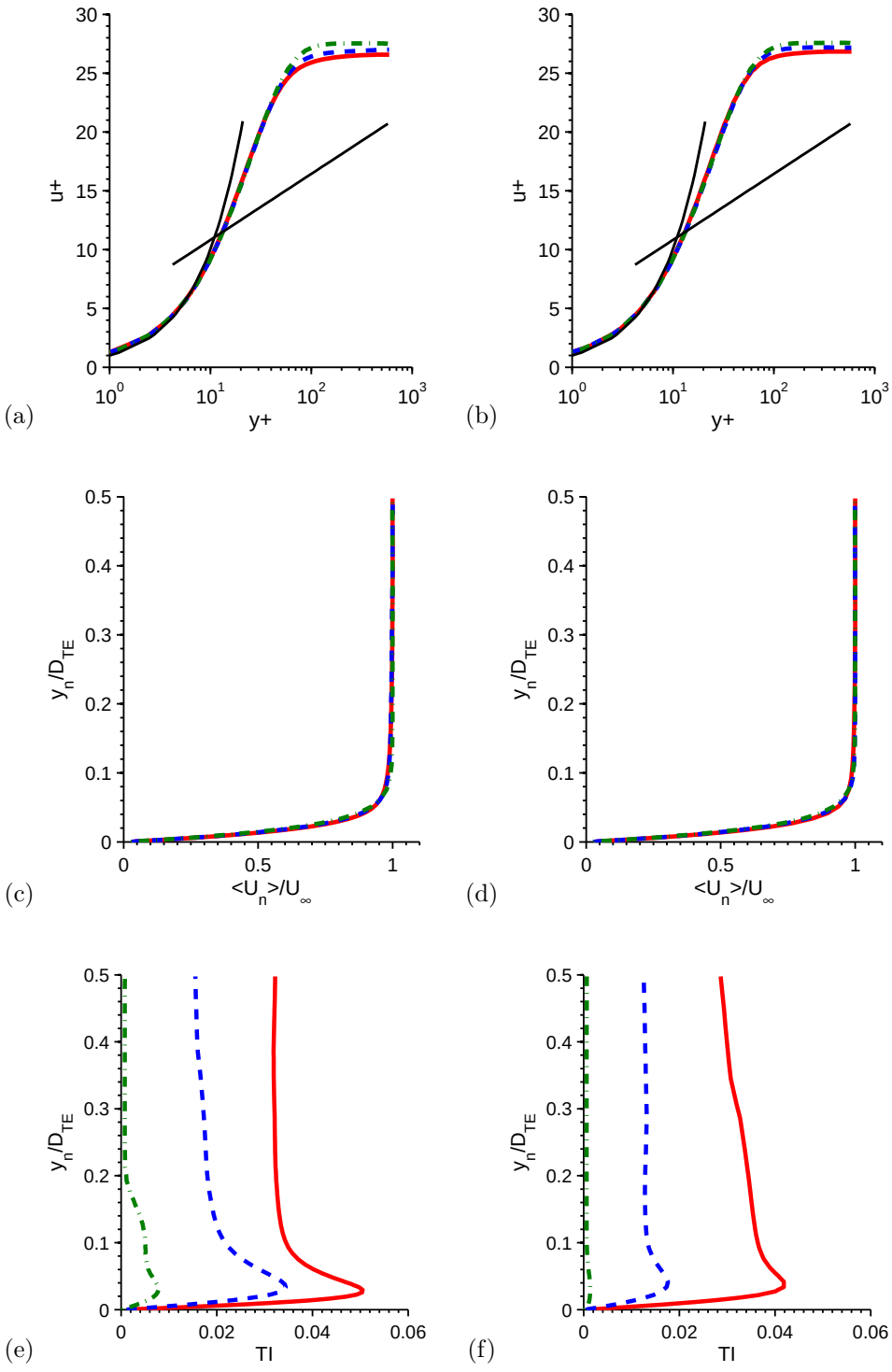

Figure 6-30. PS Boundary layer profiles at $X/C_{ax} = 0.93$ for WALE (a) linear-log mean velocity, (c) mean velocity, (e) TI, and IDDES-T (b) linear-log mean velocity, (d) mean velocity, (f) TI over a range of level inlet turbulence. Turbulence levels shown for high-level (NB129 ——), moderate (MUR235 - - -), and 0% (MUR129 · - ·).

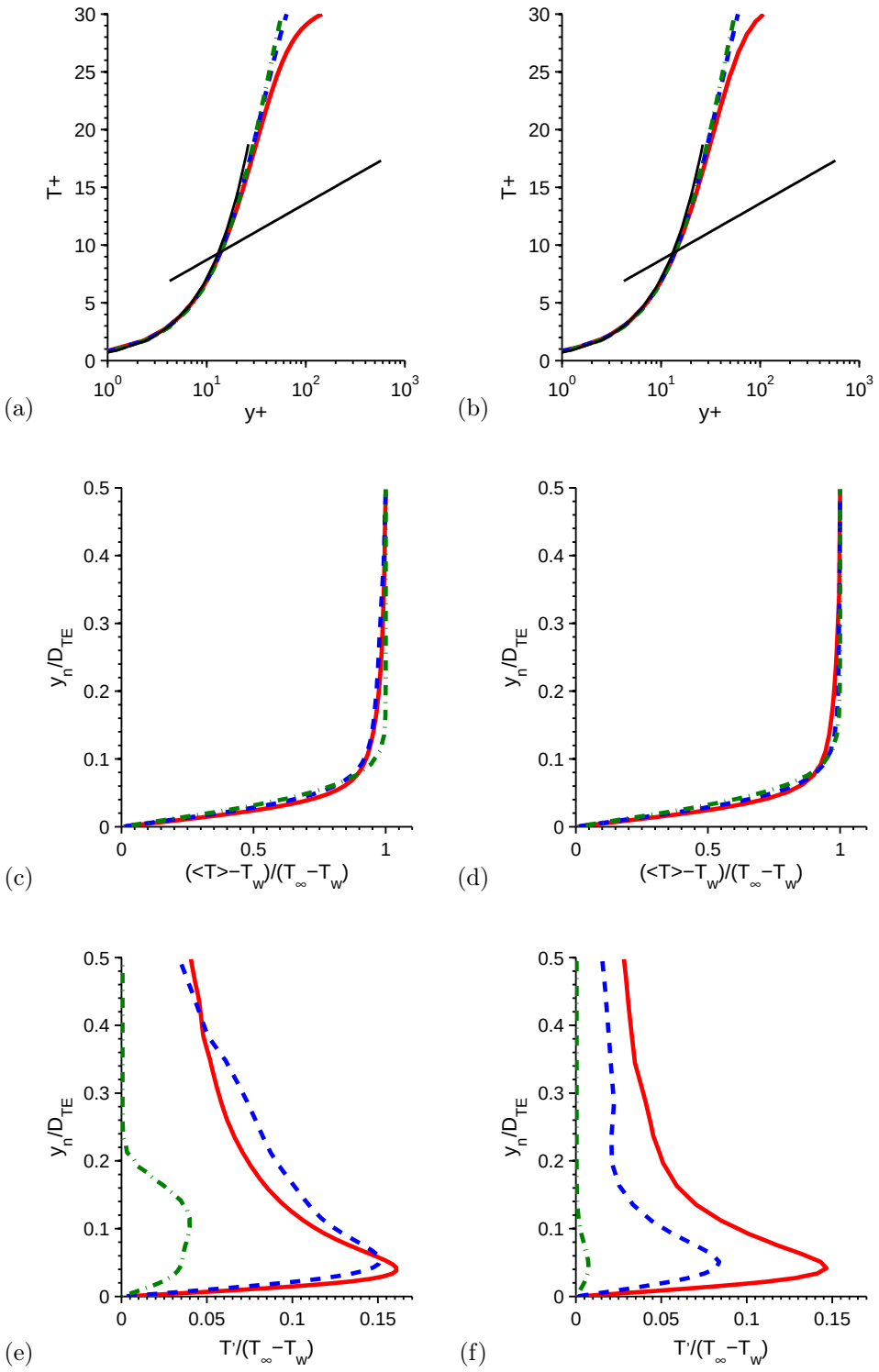

Figure 6-31. PS Boundary layer profiles at $X/C_{ax} = 0.93$ for WALE (a) linear-log mean temperature, (c) mean temperature, (e) $T'/(T_\infty - T_w)$, and IDDES-T (b) linear-log mean temperature, (d) mean temperature, (f) $T'/(T_\infty - T_w)$ over a range of level inlet turbulence. Turbulence levels shown for high-level (NB129 ——), moderate (MUR235 - - -), and 0% (MUR129 · - ·).

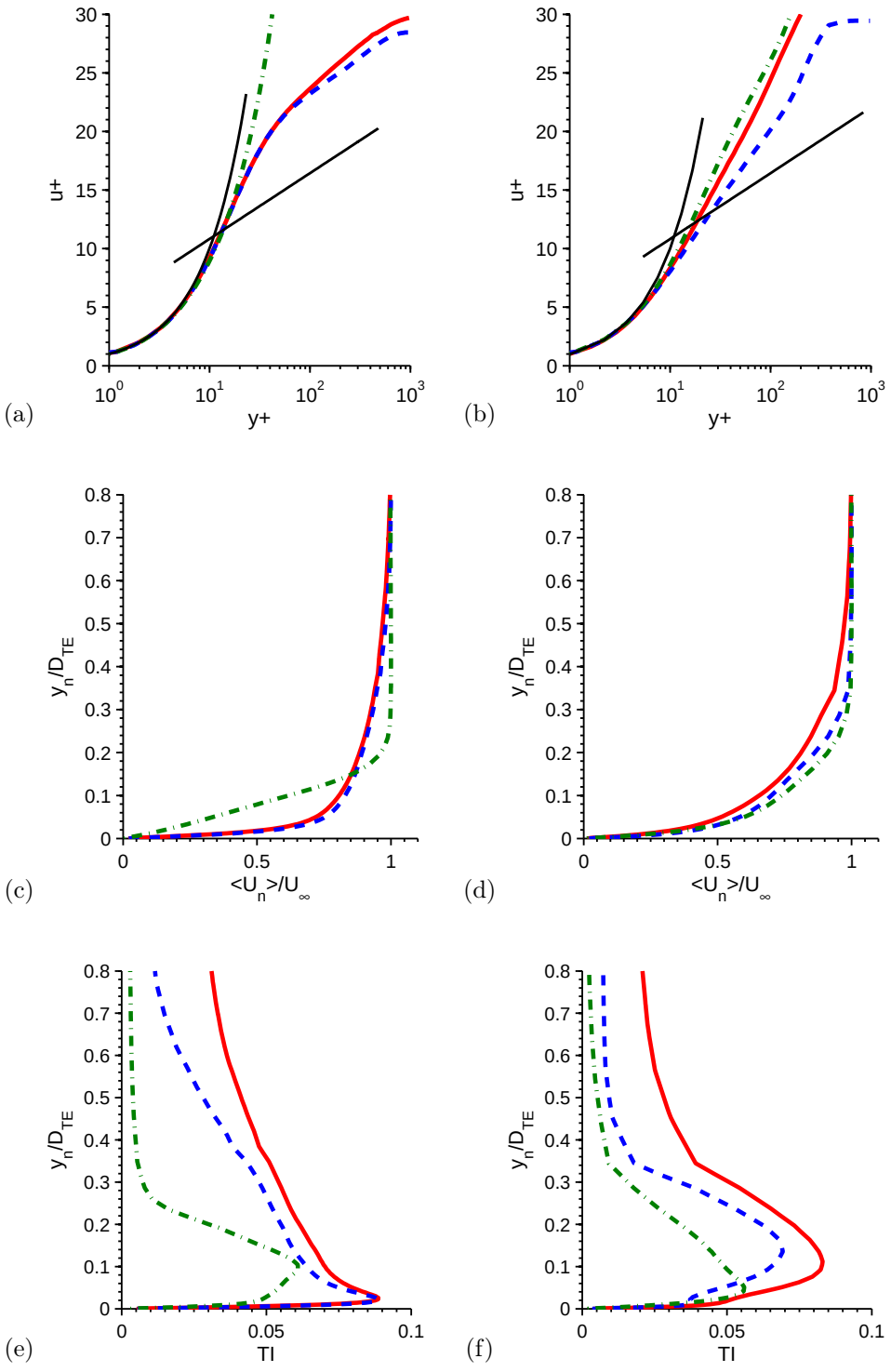

Figure 6-32. SS Boundary layer profiles at $X/C_{ax} = 0.98$ for WALE (a) linear-log mean velocity, (c) mean velocity, (e) TI, and IDDES-T (b) linear-log mean velocity, (d) mean velocity, (f) TI over a range of level inlet turbulence. Turbulence levels shown for high-level (NB129 ——), moderate (MUR235 - - -), and 0% (MUR129 · - ·).

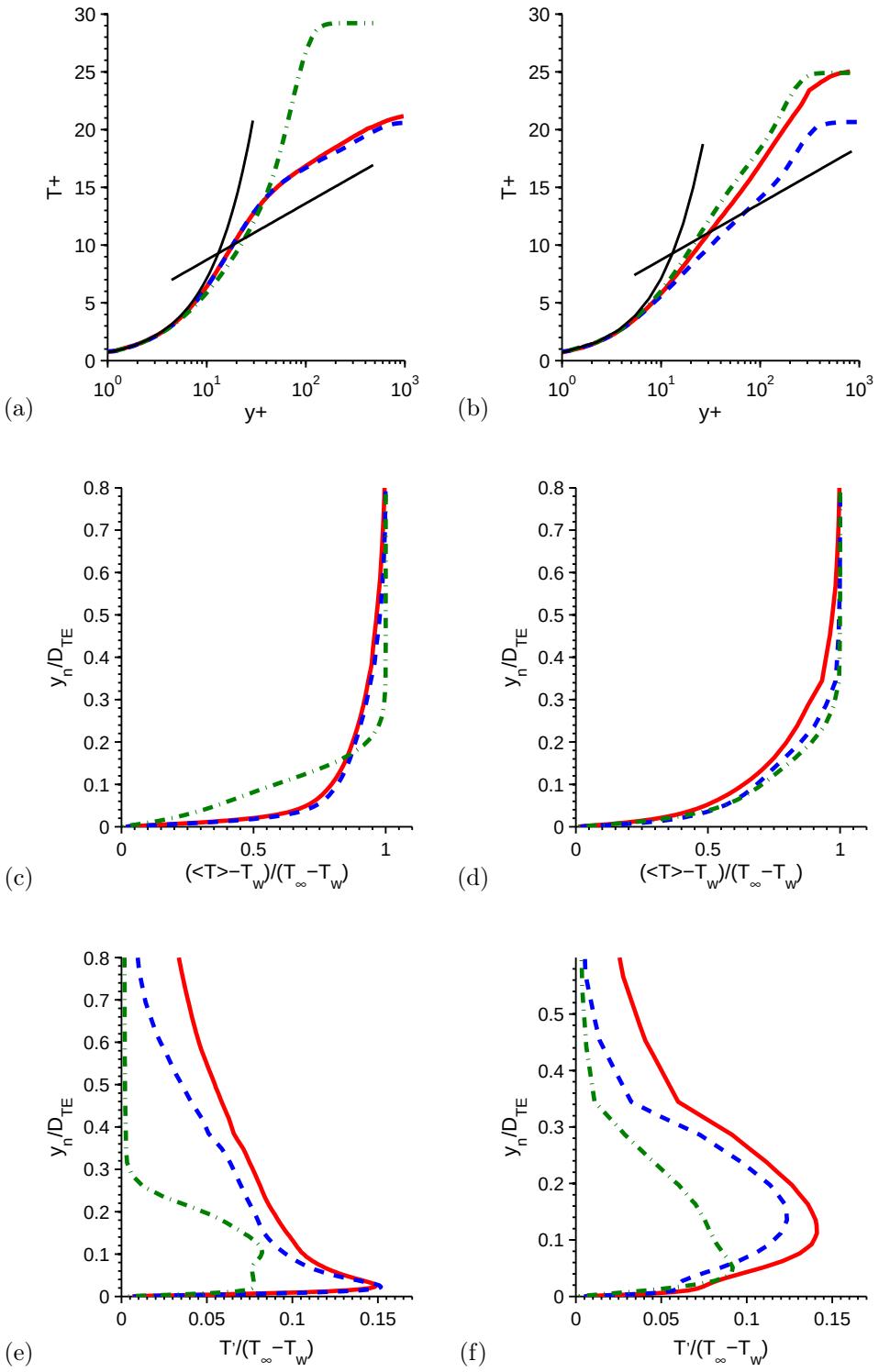

Figure 6-33. SS Boundary layer profiles at $X/C_{ax} = 0.98$ for WALE (a) linear-log mean temperature, (c) mean temperature, (e) $T'/(T_\infty - T_w)$, and IDDES-T (b) linear-log mean temperature, (d) mean temperature, (f) $T'/(T_\infty - T_w)$ over a range of level inlet turbulence. Turbulence levels shown for high-level (NB129 ——), moderate (MUR235 - - -), and 0% (MUR129 · - ·).

Table 6.12. WALE thermal to velocity boundary layer ratio, δ_T/δ, at various inlet TI levels.

Location	$TI = 0$	$TI = 6\%$	$TI = 20\%$
SS $X/C_{ax} = 0.98$	1.04	1.05	1.27
SS $X/C_{ax} = 0.85$	1.22	1.28	1.38
SS $X/C_{ax} = 0.60$	1.23	1.29	1.32
SS $X/C_{ax} = 0.35$	1.38	1.53	1.85
PS $X/C_{ax} = 0.93$	1.47	3.85	5.07
PS $X/C_{ax} = 0.32$	1.11	1.40	1.93

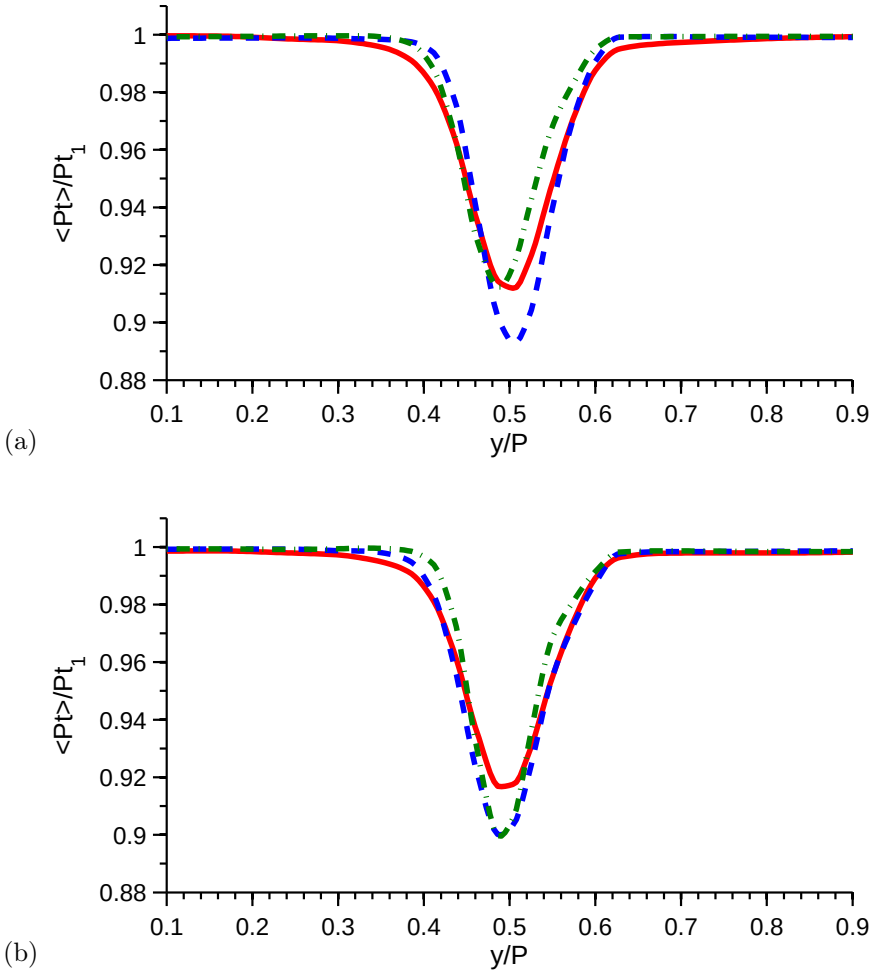

Figure 6-34. Vane normalized mean total pressure profiles for (a) WALE and (b) IDDES-T over range of inlet turbulence at $Re_C \sim 1.1\times10^6$. Profile plotted at $X/C_{ax} = 1.17$ for high-level (NB129 ——), moderate (MUR235 - - -), and 0% (MUR129 · - ·) inlet turbulence.

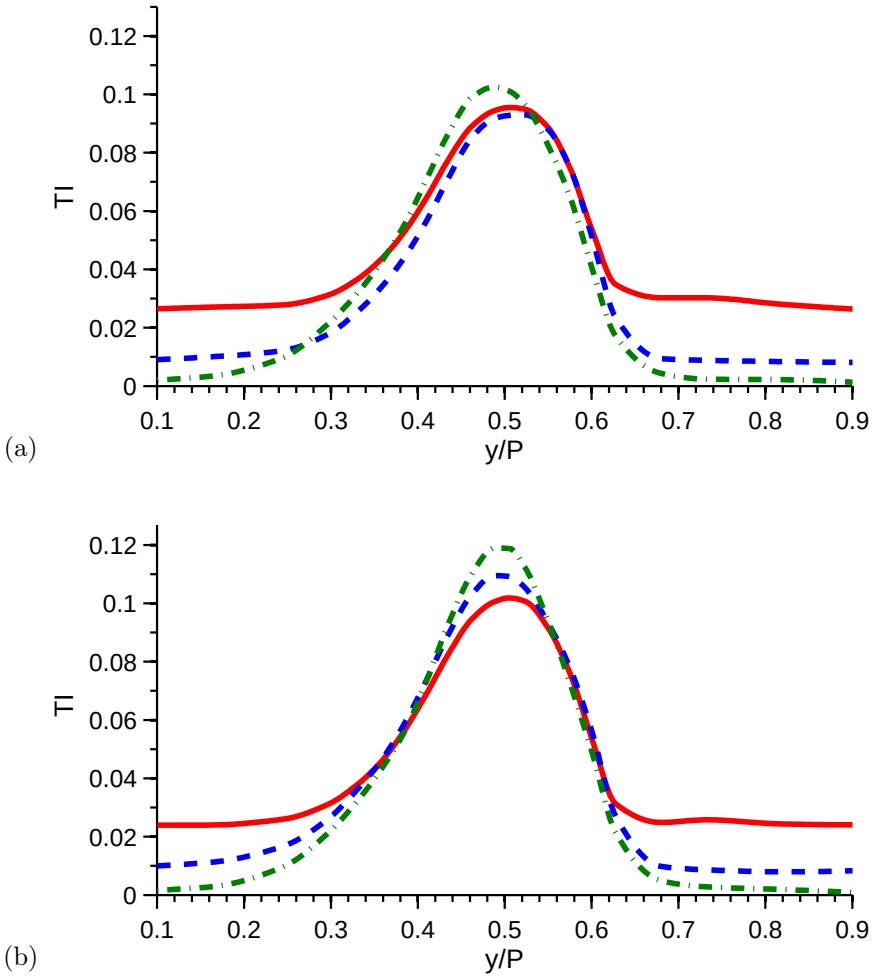

Figure 6-35. Vane local TI profiles for (a) WALE and (b) IDDES-T over range of inlet turbulence at $Re_C \sim 1.1 \times 10^6$. Profile plotted at $X/C_{ax} = 1.17$ for high-level (NB129 ——), moderate (MUR235 - - -), and 0% (MUR129 · - ·) inlet turbulence.

Figure 6-36 shows the comparisons of the wake formation at each inlet TI level. It is found for the case of TI=20%, that the formation of the vortex structures look to have less strength relative to TI=6% based on the local density gradient. Overall similar trends due to the impact of free-stream TI are found for WALE and IDDES-T. Results relative to the experimental uncertainty are found to be within 2X of each other for the range of free-stream TI.

A comparison between the decay rate of each model in presented in Figure 6-37. The prediction of wake decay for the IDDES-T model is found to be in good agreement

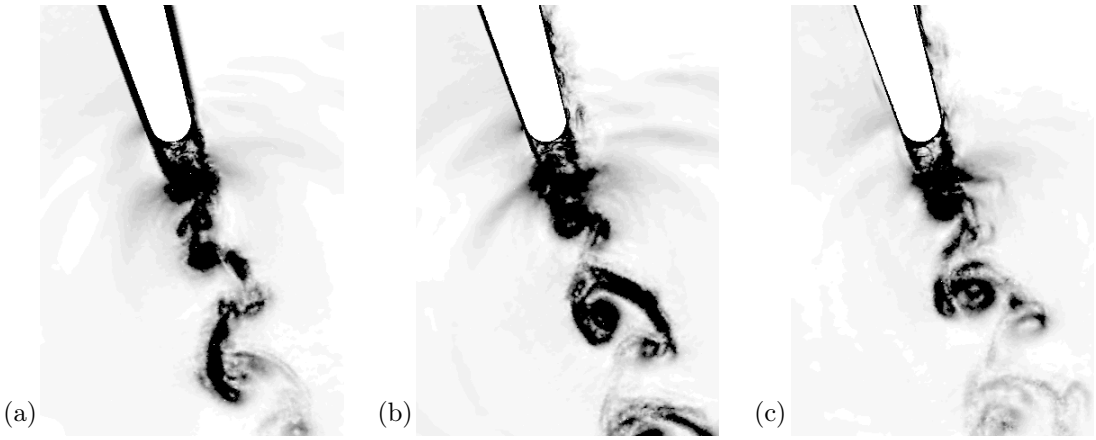

Figure 6-36. Numerical Schlieren of the TE wake for free-stream TI of (a) 0%, (b) 6%, and (c) 20%.

with the WALE model. The largest discrepancy is found for inlet TI=0% where it was shown that the WALE SS BL transition point occurred closer to the TE compared to IDDES-T. This impacts the initial formation of the wake formation predicted for each model. This is also highlighted in the peak of the total pressure wake in Figure 6-34. The plane mass average total pressure mixing loss at $X/C_{ax} = 1.17$ is summarized in Table 6.13. Relative to the WALE model, the IDDES-T is within 0.06% of the predicted loss.

Table 6.13. Mass plane average total pressure loss, $1 - \langle Pt \rangle / Pt_1$, at $X/C_{ax} = 1.17$ for a range of turbulence.

Model	$TI = 0\%$	$TI = 6\%$	$TI = 20\%$
WALE	0.96%	1.18%	1.23%
IDDES-T	1.02%	1.23%	1.20%

6.5 Concluding Remarks

SST, SST-T, IDDES-T, and WALE modeling approaches were preformed for the HPT uncooled vane of Arts and Rouvroit [34]. This was done to build confidence along with understanding computational cost and accuracy. LES served as a computational benchmark for RANS and HLES studies beyond the availability of the experimental

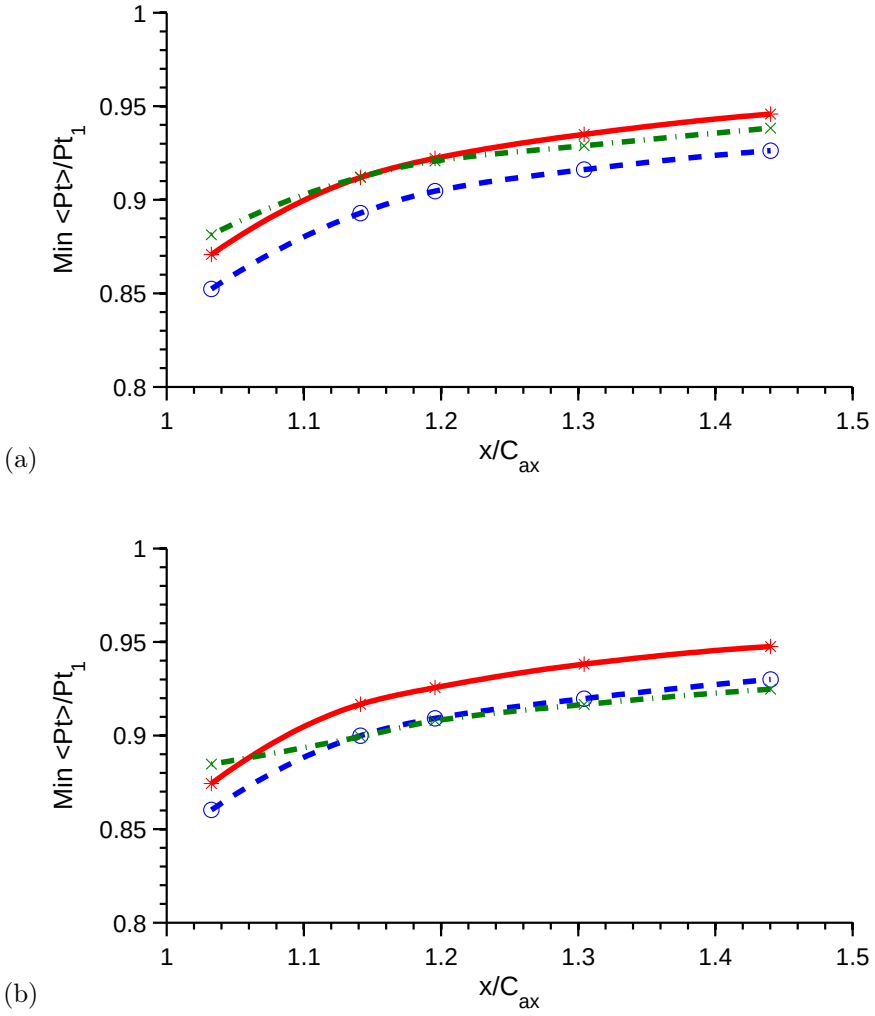

Figure 6-37. Vane wake minimum normalized mean total pressure decay for (a) WALE and (b) IDDES-T over range of inlet turbulence at $Re_C \sim 1.1 \times 10^6$. Turbulence levels shown for high-level (NB129 ——), moderate (MUR235 - - -), and 0% (MUR129 · - ·)

data. This was the case for simulations with high-level free-stream TI. Achieving combustor level turbulence and length scales are both challenging and costly in an experimental facility. However, this was done in a more cost efficient manner by computational matching TI conditions in line with experimental measurements of Barringer et al. [24].

This is the first computational study to expand to high-level TI and provide an understanding of the impact on BL development, surface heat flux, and wake forma-

tion, evaluation, and decay. This study was grounded to experimental data at two Re and inlet TI levels ranging from $0-6\%$. Given the computational cost for LES at high Re HPT conditions, a hybrid LES/RANS approach (IDDES-T) was also studied. The pressented scale-resolved simulation used an unstructured mesh of tetrahedral and prism elements with second-order spatial and temporal schemes in Fluent. Using adequate mesh resolution and quality, predictions from this approach relative to the structured high-order code FDL3DI were within the equivalent experimental uncertainty for surface Nu. This provided confidence in the Fluent WALE predictions and further use of the results as a benchmark for RANS and HLES results.

Up to this point, turbulence boundary conditions have been incomplete computationally where only turbulence level has been based on experimental report values. The current study used turbulence length scale and decay provided by Arts [76] and executed WALE simulations to evaluate the RANS models. SST and SST-T studies showed theses models to be inadequate in the prediction of boundary layer, surface heat flux, and wake total pressure. SST-T was found to provide accurate predictions of Nu at low TI levels. However, SST-T deviated by more than 2X in Nu at high-level TI relative to WALE preditions. Overall, SST and SST-T were unable to predict trends due to varying Re and TI that would be desired for industrial design. The overall total pressure loss was over-predicted by the SST without the transition model by over 1.5X relative to WALE predictions, showing the significant contribution of the BL to the overall loss. In the wake, the resolved TI predicted by the LES model was used to show the inconsistency with the SST model assumption of isotropic turbulence.

WALE was found to provide accurate predictions of all flow field quantities for two Re and inlet TI levels ranging from $0-6\%$ relative to the experimental measurements of Arts and Rouvroit [34]. Predictions were found to be within the equivalent of 2X the experimental uncertainty for the total pressure wake, providing confidence in the results to be further used as a benchmark for RANS and HLES results. The largest variation in surface Nu was found for the SS BL transition point. However, the transition point was found to be extremely sensitive to small variation in free-stream

TI (4-6%), where LES predictions at TI=6% were within 2X experimental uncertainty when compared to experimental measurement at TI=4%. The unknown contribution of surface roughness was also noted as a possible contributor to the difference in Nu prediction and measurement.

The IDDES-T model was able to provide an alternate approach from WALE at 4X cost reduction. IDDES-T was found to be within the equivalent of 2X the experimental uncertainty for wake total pressure and TI development and decay. The most notable differences are found for the TI BL profiles for the SS surface. The difference in the profiles are expected due to the near-wall modeling of turbulent structures by each model. However, the improved agreement in IDDES-T and WALE predictions of the mean momentum and thermal BL is reflected in the agreement in predicted Nu. IDDES-T is therefore selected as the primary approach for reducing cost and maintaining accuracy for the upcoming sliding mesh studies.

Chapter 7

Pitch-line Stage Aero-Thermal Study

7.1 Pitch-line Stage Design: PSD02

The computational study is now extended to include the stage interaction between a vane and downstream blade. An uncooled blade has been designed to pair with the uncooled vane of Arts and Rouvroit [34] to evaluate the impact of free-stream turbulence and vane wake on the downstream blade boundary layer, surface heat transfer, wake formation and evolution. The computational approach is built from the previous chapter that includes benchmarking to experimental measurement.

When including the downstream blade, the stage pressure ratio is set to 2.35. The 2D linear sliding mesh (2DSM) maintains a linear passing blade speed of 250 m/s. The linear vane and blade are extruded in the span direction to maintain computational domain independence where $S/C = 0.24$. The vane to blade gap is set to $X_{gap}/C_{ax} = 0.35$, where C_{ax} is based on the vane axial chord. In order to quantify the impact of stage inlet TI on the downstream blade, the stage design maintains the same vane pressure ratio as MUR129 and NB129. This allows a progressive understanding of the flow field with and without stage interaction. A full description of the stage design and conditions are provided in the Appendix B.

The current study objective is to isolate the contribution of the vane/blade interaction on loss generating mechanisms (i.e. profile and wake mixing) and thermal loading. This is done on a pitch-line section prior to moving to a 3D geometry in

Chapter 8. Limiting the current study to the pitch-line allows for the examination of stage interaction in the absence of endwall secondary flows and rotational effects. HPT stage interactions are further understood by comparing the following cases:

- Vane in absence of downstream blade interaction.
- Blade in absence of upstream vane interaction.
- Fully coupled vane/blade.

WALE and IDDES-T are the coupled sliding mesh modeling approaches to understand the mechanisms contributing to BL, heat transfer, and mixing losses at two levels of stage inlet TI. Finally, given the continued use of RANS for industrial designs, SST and SST-T are the uncoupled approaches.

The two levels of inlet TI match cases MUR129 and NB129, where the inlet TI are 0% and 20% respectively. Upstream bars are again used to generate vane inlet TI for both WALE and IDDES-T models. The blade-only (BO) SST and SST-T inlet boundary conditions come from the vane-only (VO) plane mass averaged mixed out conditions for momentum, enthalpy and turbulence (See Appendix B).

7.2 Zero Inlet Turbulence

The impact of vane/blade interaction is first studied with no inlet TI. Figure 7-1 shows the instantaneous normalized Q-criterion to highlight the generated turbulent structures. Structures are first generated at the TE of the vane and can be found periodically passing through the downstream blade passage. This periodic behavior is examined to understand the impact on BL, surface heat transfer, and wake mixing.

No experimental data is available; however, studies can be tied back to MUR129 VO computational studies and experimental data. Loading comparison are first made to confirm that the condition and geometry are correctly matched. IDDES-T and WALE comparison are made for both VO and sliding mesh domains. This is done to assess any influence the downstream blade has on the upstream vane. The stage design intent was to match the MUR129 VO loading allowing study of the impact

when including the downstream blade (Figure 7-2). Loading profiles are found to be in agreement for each turbulence model and approach. No impact of the downstream passing blade is found on the loading.

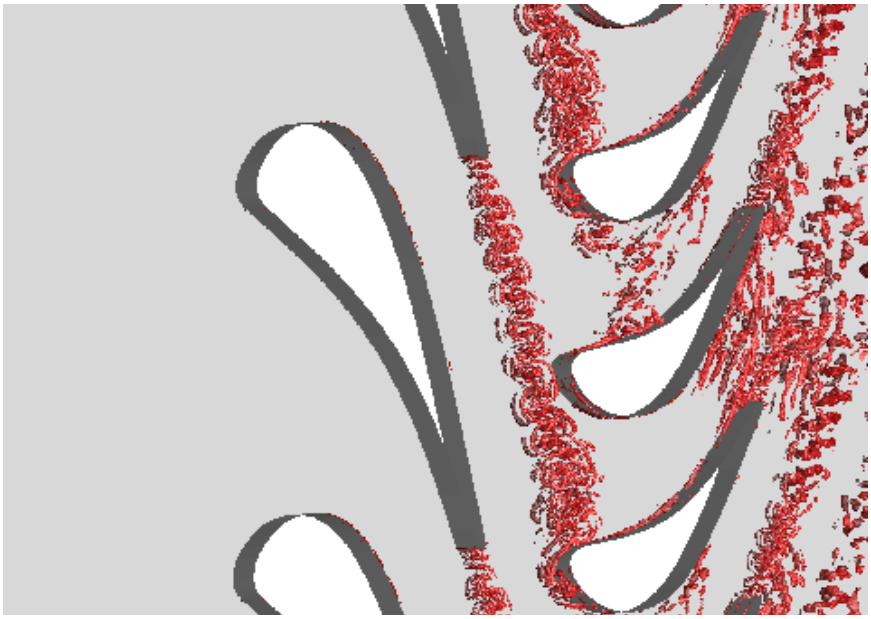

Figure 7-1. Linear sliding mesh domain. Normalized Q-criterion of 0.15 plotted for IDDES-T with no vane inlet turbulence.

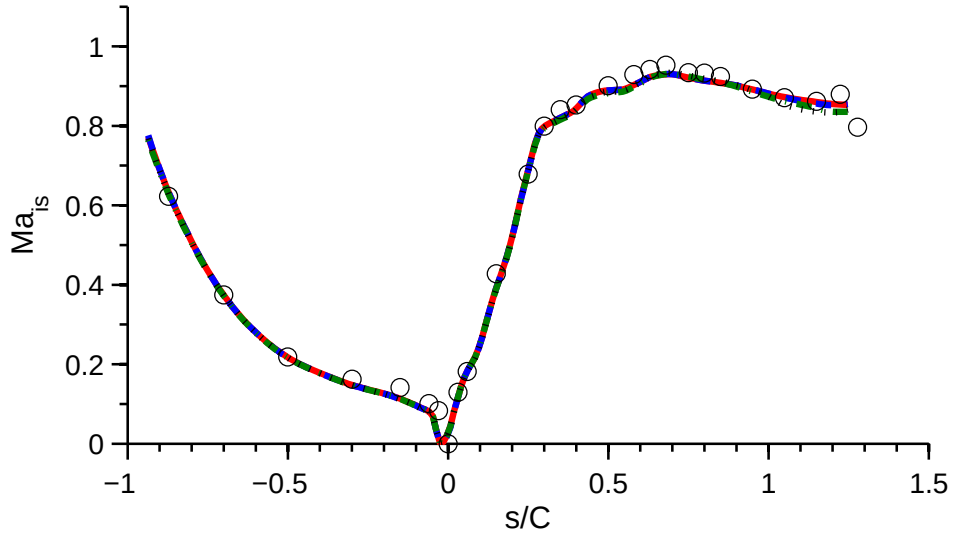

Figure 7-2. Sliding mesh vane loading for WALE (——) and IDDES-T (- - -) compared to vane-only WALE (· - ·) and IDDES-T (· · ·) with no vane inlet turbulence. Experimental vane-only case MUR129(○).

The mean Nu is compared in Figure 7-3 between VO and sliding mesh cases. The SS transition location is found to be delayed for both the WALE and IDDES-T sliding mesh models relative to the VO cases. Additionally, the WALE PS surface Nu is reduced when including the downstream blade interaction. Recall that for the VO case in Chapter 5, the WALE model over-predicted the Nu on the pressure side. This was caused by over-predicted strength of the Gortler vortex forming on the pressure side. The unsteady pressure wave from the periodic passing of the blade is found to dampen the formation of the Gortler vortex.

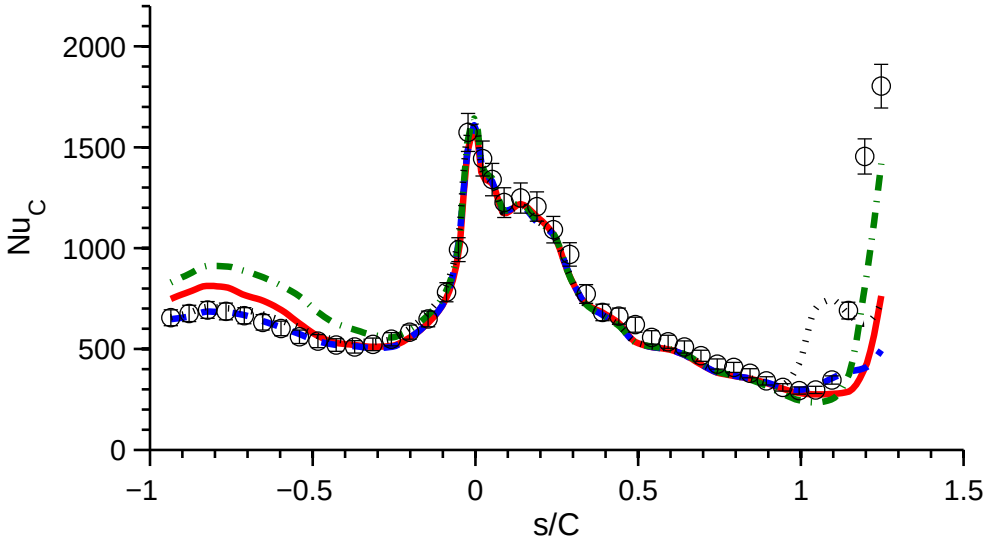

Figure 7-3. Sliding mesh vane mean Nu for WALE (——) and IDDES-T (- - -) compared to vane-only WALE (· - ·) and IDDES-T (· · ·) with no vane inlet turbulence. Experimental vane-only case MUR129(○).

Figure 7-4 shows the pressure fluctuation on the vane TE, PS, and SS surfaces for WALE VO and vane coupled with the downstream blade. Previously, for the VO at zero inlet TI, the deterministic TE shedding frequency from the adjacent vane was found for the SS vane instantaneous pressure on the surface. This is again the case for the vane with a downstream blade including the addition of the blade passing frequency.

Figure 7-5 shows total pressure and TI wake profile predictions. The unsteady pressure wave from the periodic passing of the blade is found to have a negligible impact on the mean total pressure wake profile at $X/C_{ax} = 1.14$ from the vane LE,

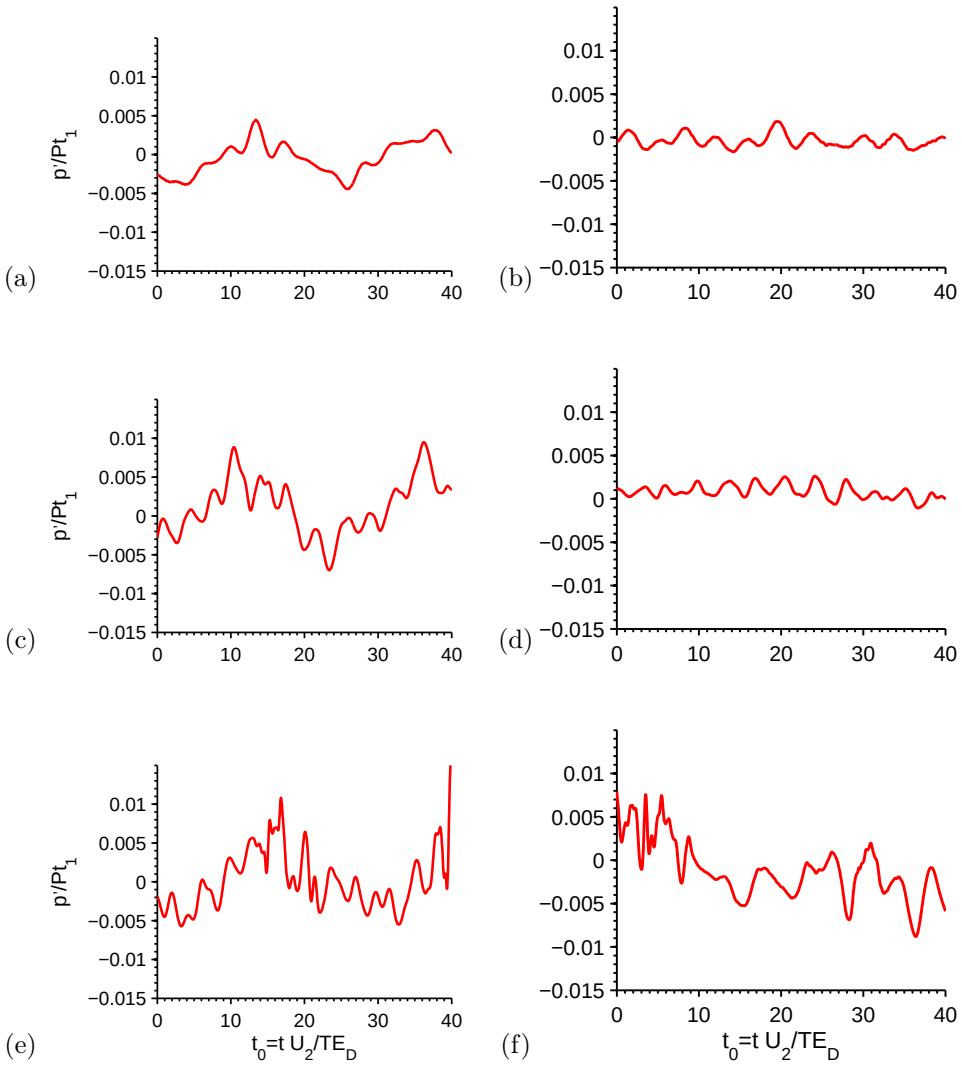

Figure 7-4. Vane surface pressure fluctuation with no vane inlet turbulence. Sliding mesh p'/Pt_1 on the SS vane surface at (a) $X/C_{ax} = 0.98$,(c) $X/C_{ax} = 0.86$, (e) $X/C_{ax} = 0.72$. Vane only p'/Pt_1 on the SS vane surface at (b) $X/C_{ax} = 0.98$,(d) $X/C_{ax} = 0.86$, (f) $X/C_{ax} = 0.72$.

where the blade LE is $X/C_{ax} = 1.35$ from the vane LE. However, differences are found for the TI profiles. Unsteadiness is now present between vane wakes as a result of the downstream blade passing found in the predicted TI. The passing blade creates an unsteady blockage varying the local static pressure. The bow wave interaction drives an additional unsteadiness to the flow field that doesn't exist for the VO case. The vane TE wake decay rate of the peak TI has also increased for the sliding mesh case.

An increase in decay rate is also seen for the peak total pressure wake loss but to a lesser extent as shown in Figure 7-5a.

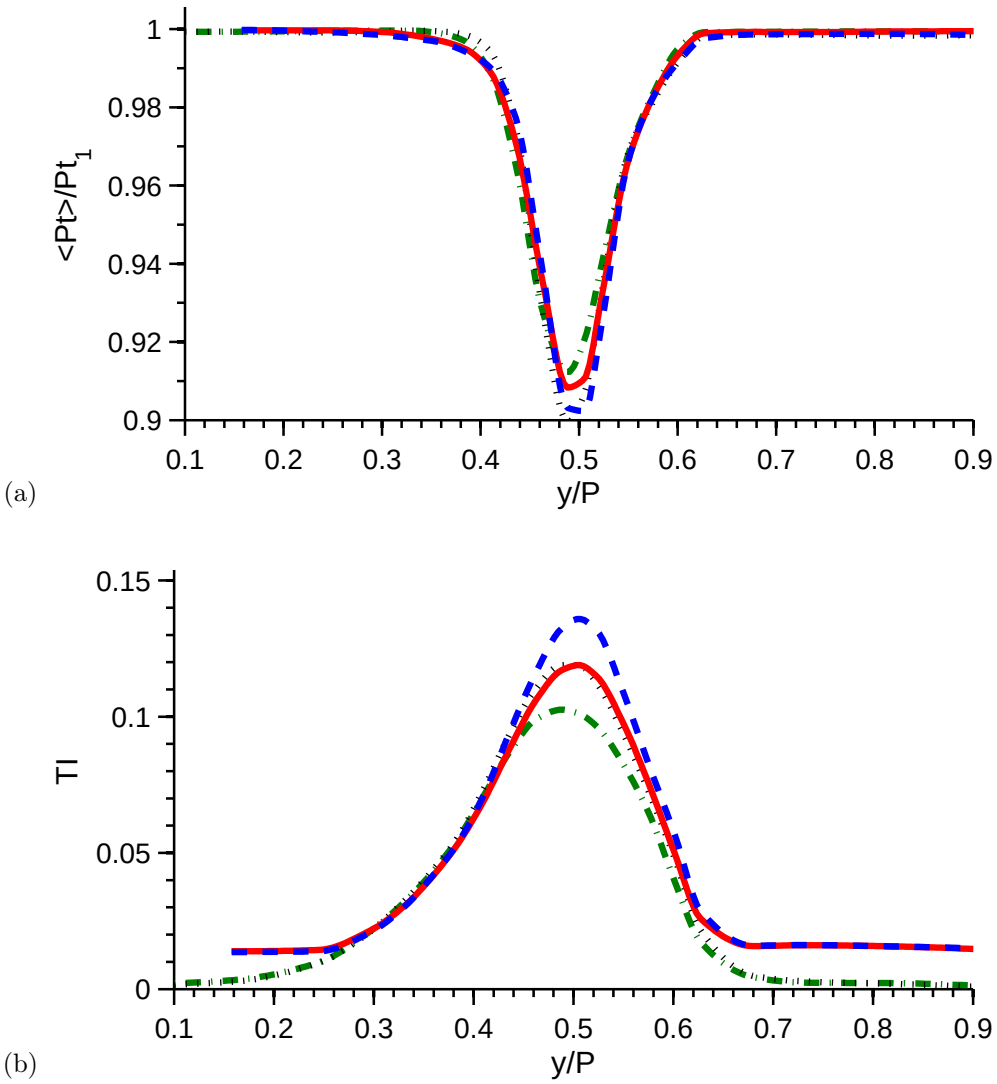

Figure 7-5. Vane (a) normalized mean total pressure and (b) local TI profiles at $X/C_{ax} = 1.14$ from the vane LE. Sliding mesh WALE (——) and IDDES-T (- - -) compared to vane-only WALE (· - ·) and IDDES-T (· · ·) with no vane inlet turbulence.

The study now moves focus to the downstream blade. The coupled interaction between the vane and blade are performed using a linear sliding mesh approach with WALE and IDDES-T. Uncoupled BO steady SST and SST-T are included in the comparison where mixed out boundary conditions are provided from the VO SST

and SST-T results. Matching mean blade inlet boundary conditions for each modeling approach is confirmed by comparing the loading and incident angle in Figure 7-6.

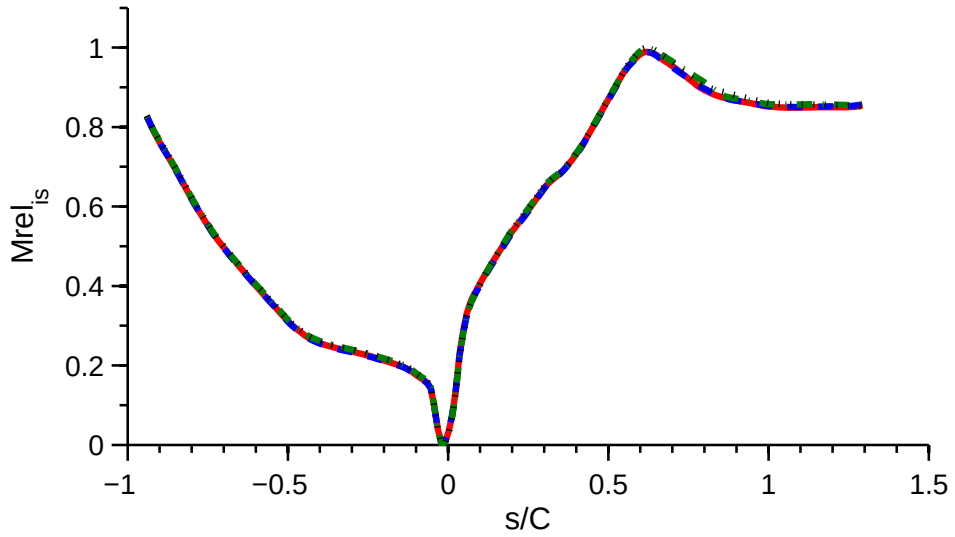

Figure 7-6. Sliding mesh blade loading for WALE (——) and IDDES-T (- - -) compared to blade-only SST-T (· - ·) and SST (· · ·) with no vane inlet turbulence.

Before each of the computational modeling approaches were preformed for the blade, meshing practices from the VO case are upheld. The uncooled vane underwent rigorous mesh and modeling studies in Chapter 5 that is now followed for the blade. The near-wall mesh requirements for a wall-resolved RANS solution was obtained with a grid independent solution for both SST and SST-T was confirmed. Next, the scale-resolved guidelines for mesh resolution, domain extent, time step selection, and convergence criteria are followed for WALE and IDDES-T predictions. First cell values of $\Delta y+$, $\Delta s+$, and $\Delta z+$ are provided in Figure 7-7. Near mesh targets ($\Delta y+$, $\Delta s+$, and $\Delta z+$) for the LES are within those used for the vane.

The mean blade Nu is compared in Figure 7-8 between steady BO and sliding mesh cases. The SST-T model provides a near laminar Nu result for the blade until the BL transitions on the SS. Both WALE and IDDES-T predict a mean Nu above laminar at the LE and PS. This is largely due to resolving the periodic unsteadiness from the passing vane wake and impact on the blade developing BL. IDDES-T is found to slightly under-predict PS surface Nu compared to WALE. The SS surface

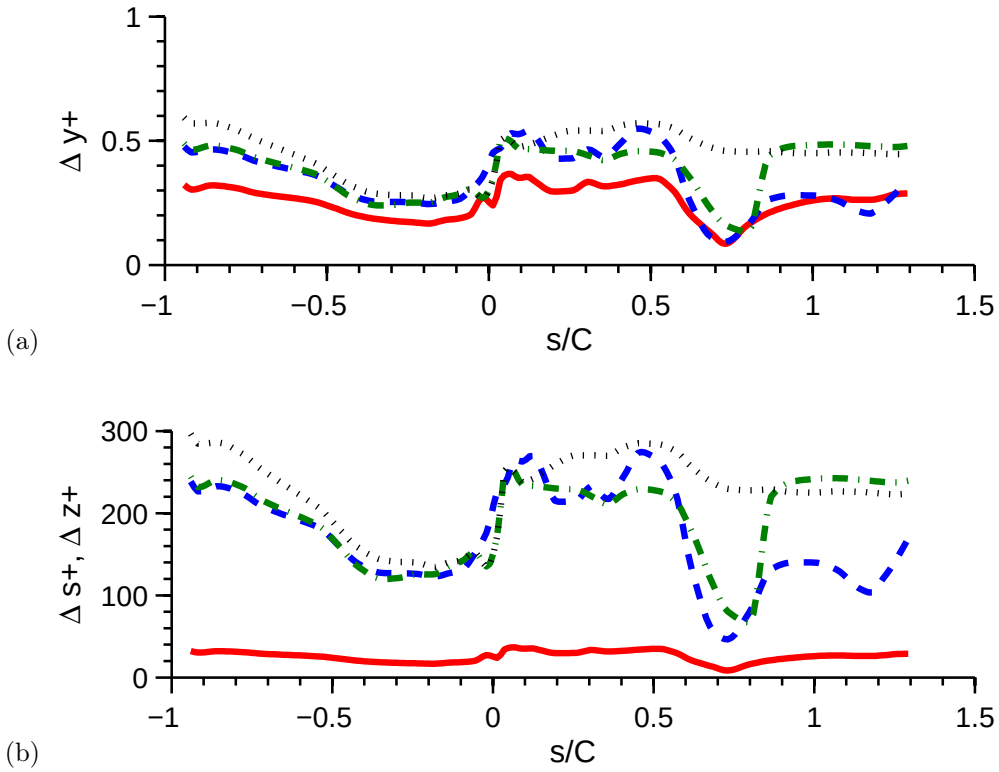

Figure 7-7. Blade (a) $\Delta y+$ and (b) $\Delta s+$ ($= \Delta z+$) for WALE (——), IDDES-T (- - -), SST-T (· - ·), and SST (· · ·) for blade with no stage inlet turbulence generation.

Nu transition location is found to be similar for all modeling predictions except the SST model. This transition point aligns with the peak Mach number at the blade throat where the adverse pressure gradient begins. After the throat, SST-T over-predicts up to 1.5X in surface Nu relative to the WALE predictions.

Interestingly, IDDES-T is found to significantly under-predict the SS surface Nu compared to WALE prediction after the throat. This level of discrepancy was not found in Chapter 6 vane studies with low to high inlet TI. Recall the discussion from Chapter 2 on implementation of the transition model for the IDDES model where the transport equations for the $\gamma - Re_\theta$ transition model is dependent on the modeled kinetic energy. Therefore the impact of the resolved unsteadiness when operating in a WMLES like mode, in the near-wall region, is not directly accounted for by the transition transport equations. The downstream blade surface experiences

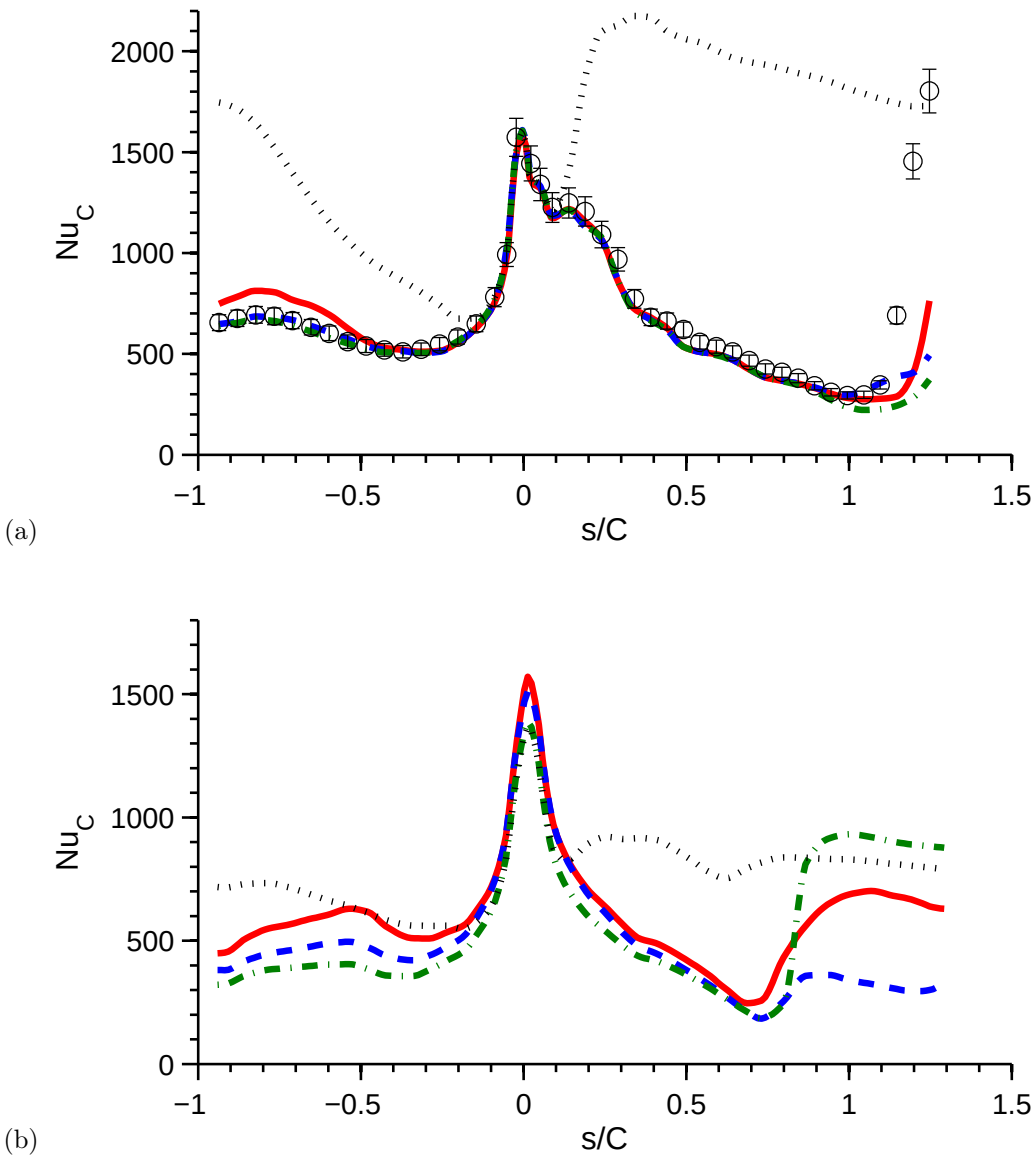

Figure 7-8. Sliding mesh (a) vane and (b) blade mean Nu for WALE (——) and IDDES-T (- - -) compared to (a) vane-only and (b) blade-only SST-T (· - ·) and SST (· · ·) with no vane inlet turbulence.

unsteadiness due the passing of the vane wake, TE wake shedding, and attenuated from stage inlet TI. For the IDDES model, the TI predicted at the blade surface is a combination of the resolved and model kinetic energy resulting for the unsteady flow field.

Figure 7-9 shows the IDDES-T resolved and modeled TI in the SS BL for the

vane and blade TE. For the current case, no inlet TI is provided to the vane. The contributions to the resolved unsteadiness on the vane SS surface is the vane TE shedding and the downstream passing blade. This resolved unsteadiness for TI is found to be on the same order as the model TI. Similar levels of modeled TI are found for the IDDES-T and SST-T predictions. This agreement in the modeled TI leads to similar predictions in the BL state and resulting surface Nu shown in Figure 7-8.

However, for the blade, a notable difference is found for the SS surface Nu for IDDES-T compared to SST-T predictions. This can be explained by the level of modeled versus resolved TI predicted for the blade SS BL with the IDDES-T model. A significant amount of the total TI is contributed by the resolved unsteadiness that doesn't directly contribute to the transport equations for transition. Figure 7-9 shows approximately a 5X reduction in modeled TI for the IDDES-T compared to the SST-T predictions. This is reflected in the reduction in SS surface Nu for the IDDES-T model relative to the SST-T. In addition, relative to the benchmark WALE model, IDDES-T SS surface Nu is under-predicted. This clearly shows the need for a larger dependence on the resolved TI for the IDDES-T approach. This shortcoming in the IDDES-T modeling approach is acknowledged and including the total kinetic energy for a HLES approach with transition modeling should be considered for future model development.

The velocity and thermal BL are shown in Figure 7-10 and 7-11, respectively. WALE and IDDES-T predictions show, in the high acceleration region on the blade PS surface ($X/C_{ax} = 0.93$), the thermal BL to be $\sim 2X$ the thickness of the velocity BL. The larger thermal BL for a favorable pressure gradient is consistent with findings in Chapter 6 for the vane. At the SS TE where a near zero pressure gradient is found, the BL ratio is found to be within 10% of the analytical relationship $\delta_T/\delta \approx Pr^{-1/3}$, where $Pr^{-1/3} = 1.12$ [79].

SST-T, IDDES-T, and WALE models predict a laminar BL on the PS surface where the BL shapes and thicknesses are in excellent agreement. This is not true for the SS BL. The SST-T model predicts a mean turbulent BL based on the comparison

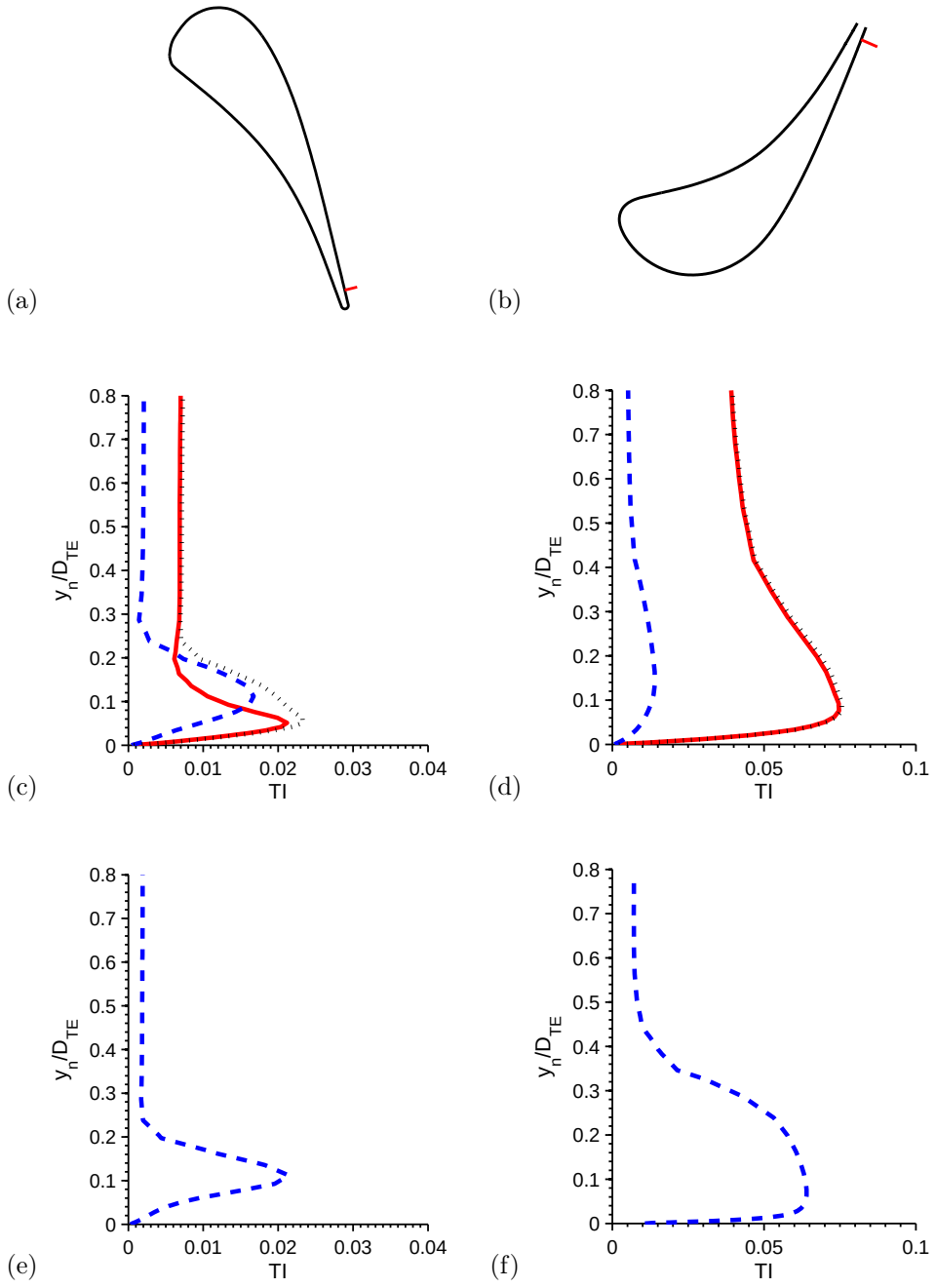

Figure 7-9. Resolved (——), modeled (- - -), and total (· · ·) TI in the BL with no stage inlet turbulence. TI BL profiles for (c) IDDES-T vane, (d) IDDES-T blade, (e) SST-T vane, (f) SST-T blade at SS location $X/C_{ax} = 0.98$ from the vane LE or blade LE.

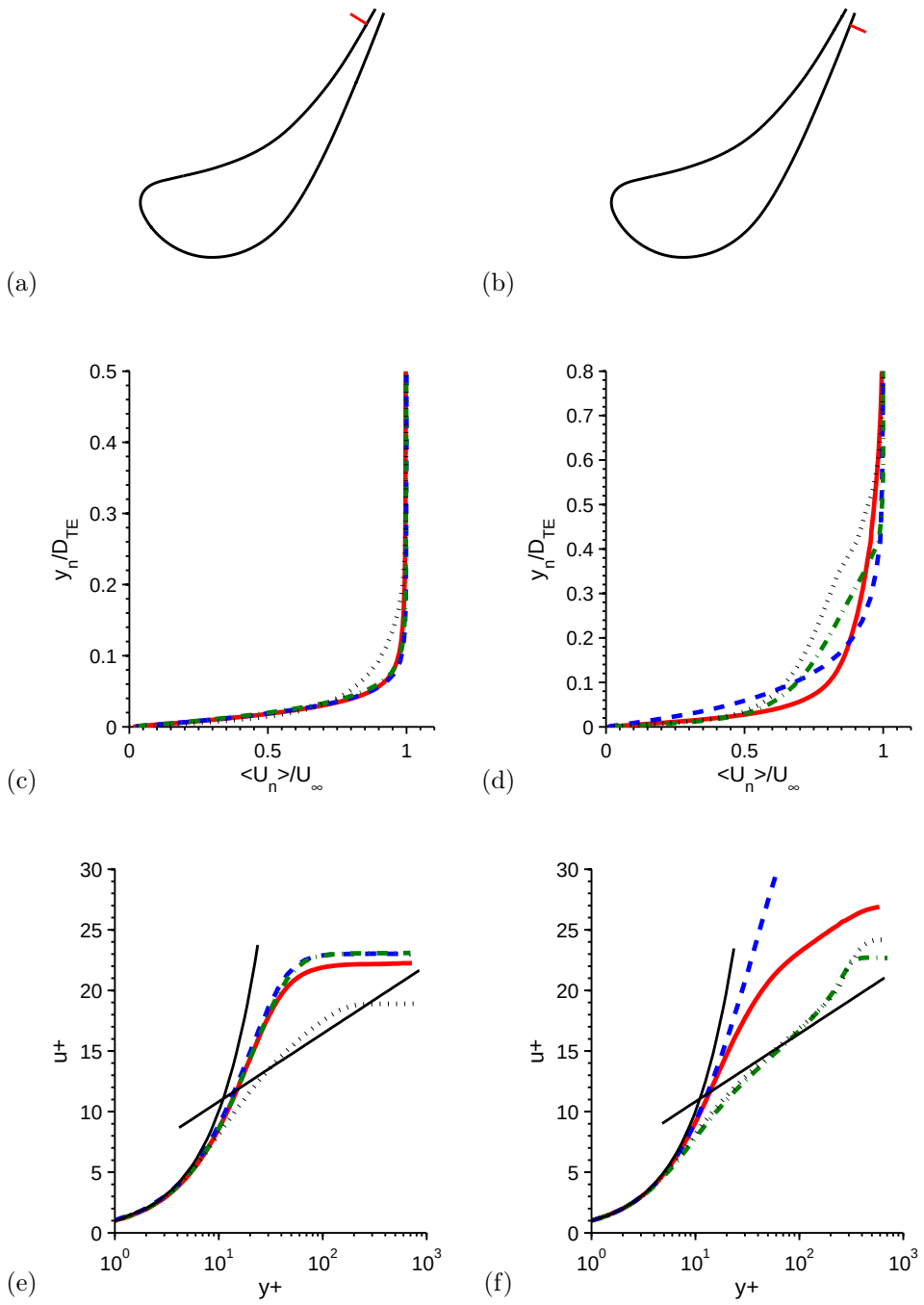

Figure 7-10. Mean velocity boundary layer profiles at (a, c, e) PS location $X/C_{ax} = 0.93$ and (b, d, f) SS location $X/C_{ax} = 0.98$ from the blade LE. Sliding mesh WALE (——) and IDDES-T (- - -) compared to blade-only SST-T (· - ·) and SST (· · ·) with no vane inlet turbulence.

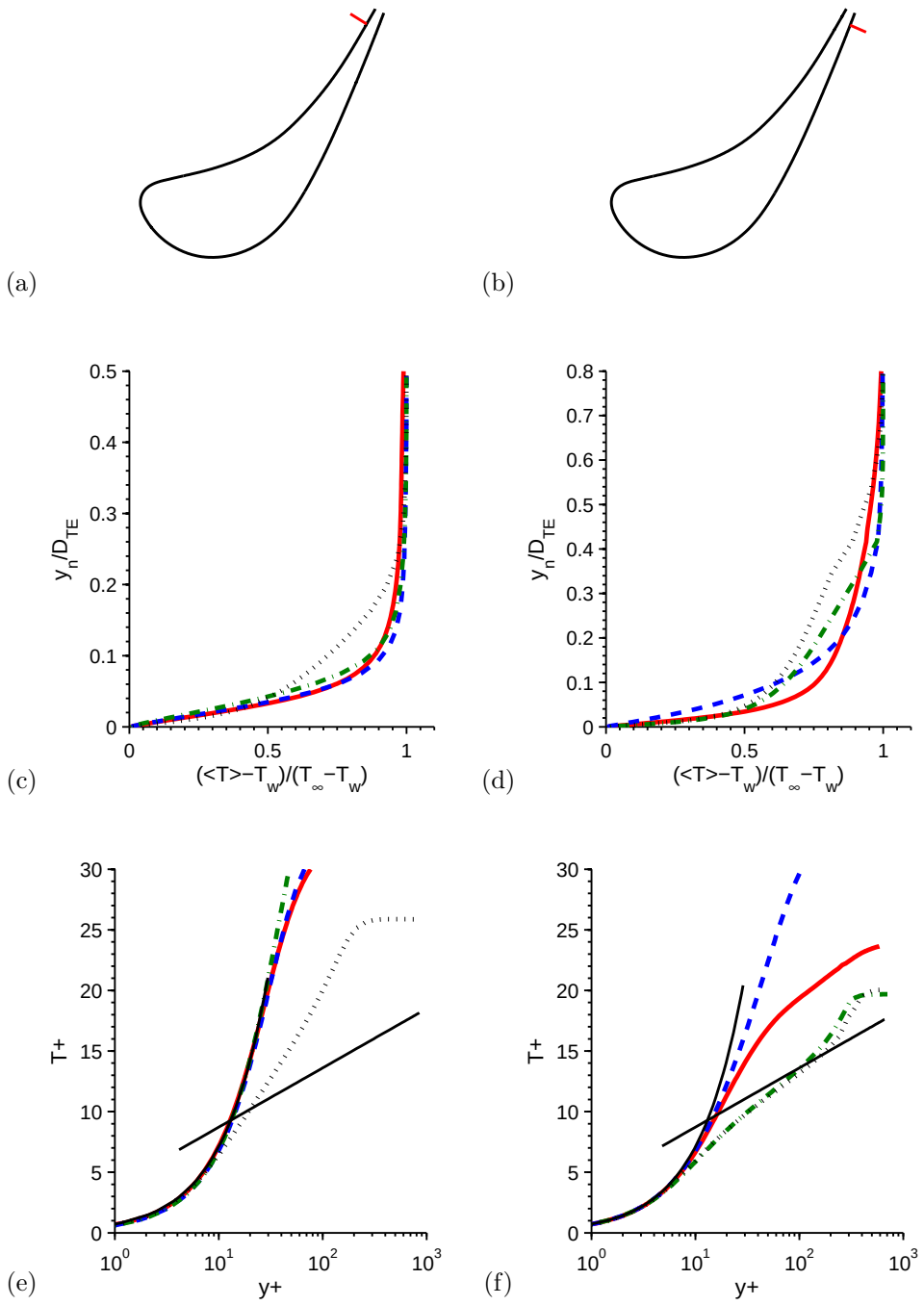

Figure 7-11. Mean temperature boundary layer profiles at (a, c, e) PS location $X/C_{ax} = 0.93$ and (b, d, f) SS location $X/C_{ax} = 0.98$ from the blade LE. Sliding mesh WALE (——) and IDDES-T (- - -) compared to blade-only SST-T (· - ·) and SST (· · ·) with no vane inlet turbulence.

to the log law. However, WALE predicts a higher near-wall velocity for the SS BL. This results in a shift of $+u$ of 5 units for the log layer. This was also found for the vane case MUR235 in Chapter 6. This is again unexpected and the result is indicative of an under-resolved near-wall LES mesh. Referring back to Figure 7-7 $\Delta y+$, $\Delta s+$, and $\Delta z+$ are well within the criteria established on the vane. This suggests the shift in log layer may not be due to near-wall resolution. The IDDES-T SS BL at the TE closely resembles a mean laminar profile. This is likely a result of the low level of modeled TI predicted in the boundary layer and the IDDES-T approach needing a dependency on the total kinetic energy in the near-wall region.

The PS velocity BL near the TE is found to have a mean laminar BL with non-zero fluctuations (Figure 7-12). IDDES-T resolved velocity and thermal fluctuation are dampened near the wall but converge to WALE predictions in the outer BL and free-stream. The difference in near-wall TI has a minor impact on the mean velocity and thermal profile, where IDDES-T and WALE show excellent agreement. Larger differences in TI are found between IDDES-T and WALE for the SS surface BL in Figure 7-13. The difference in the TI BL is not unexpected due to the near-wall turbulent structures resolved by each model. The WALE model predicts a higher near-wall momentum at the TE where TI reaches peak values of 8-10%.

The near-wall peak TI is found to increase with increasing X/C_{ax} along the SS surface for the WALE predictions. This shows the growing unsteadiness in the BL leading to the transition to a turbulent BL at the TE. At $X/C_{ax} = 0.85$ and 0.98, peak TI reaches 8-10% within the log layer. IDDES-T also shows increasing TI along the SS surface where the TI is dampened in the log layer due to the turbulence model blending function near the wall. Only the resolved TI is shown in Figure 7-12.

Figure 7-14 shows total pressure wake and TI profile predictions for WALE, IDDES-T, SST-T, and SST for the blade at $X/C_{ax} = 1.17$ from the blade LE. SST-T and SST is found to consistently over-predict wake depth and under-predict wake spreading relative to WALE and IDDES-T. This is consistent with previous vane wake results.

Previously, it was found that the SST model was able to match the WALE passage

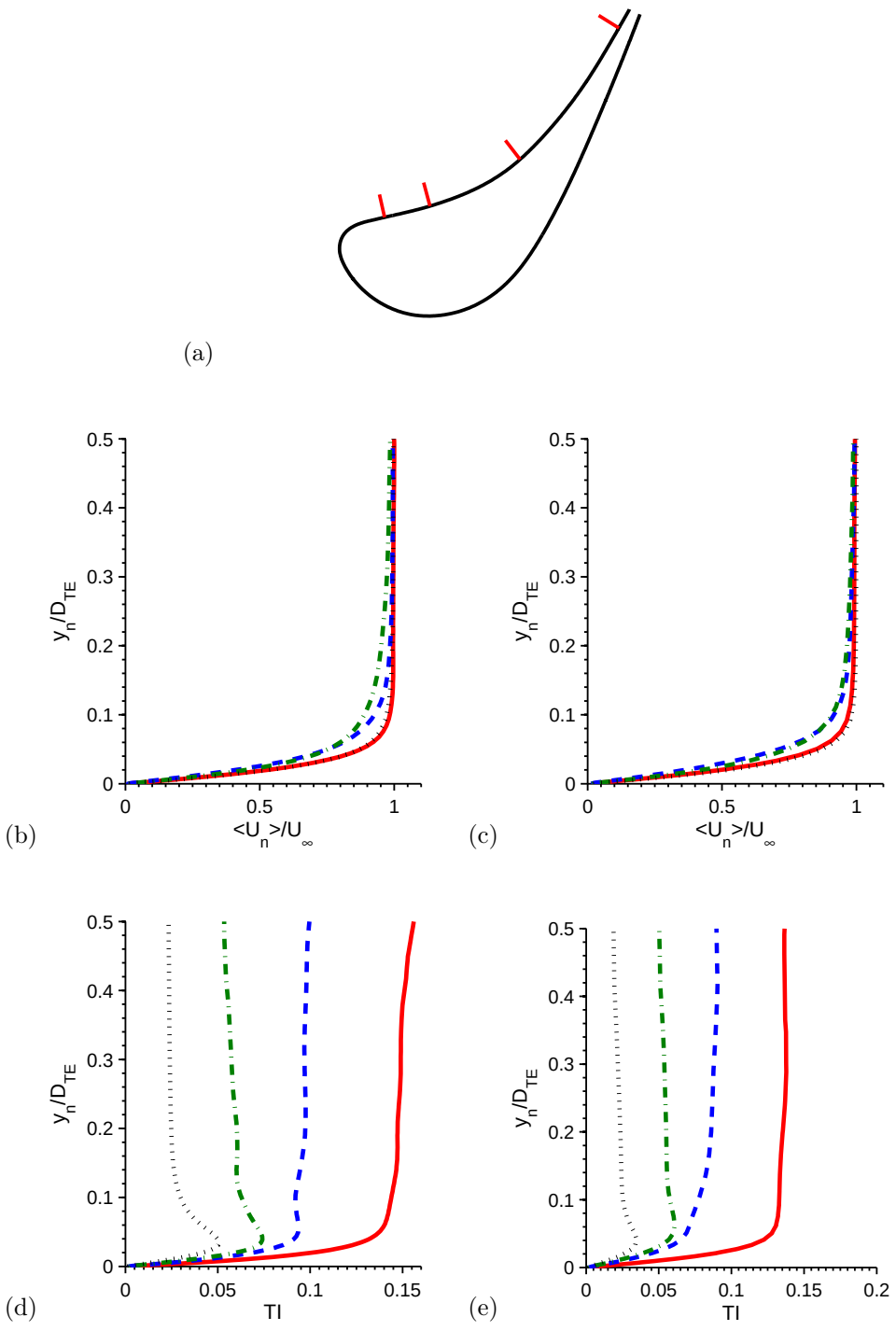

Figure 7-12. Velocity PS boundary layer profiles at $X/C_{ax} = 0.15$ (——), 0.30 (- - -), 0.6 (· - ·), and 0.93 (· · ·) from the blade LE. WALE (b) mean velocity and (d) TI profiles. IDDES-T (c) mean velocity and (e) TI profiles with no vane inlet turbulence.

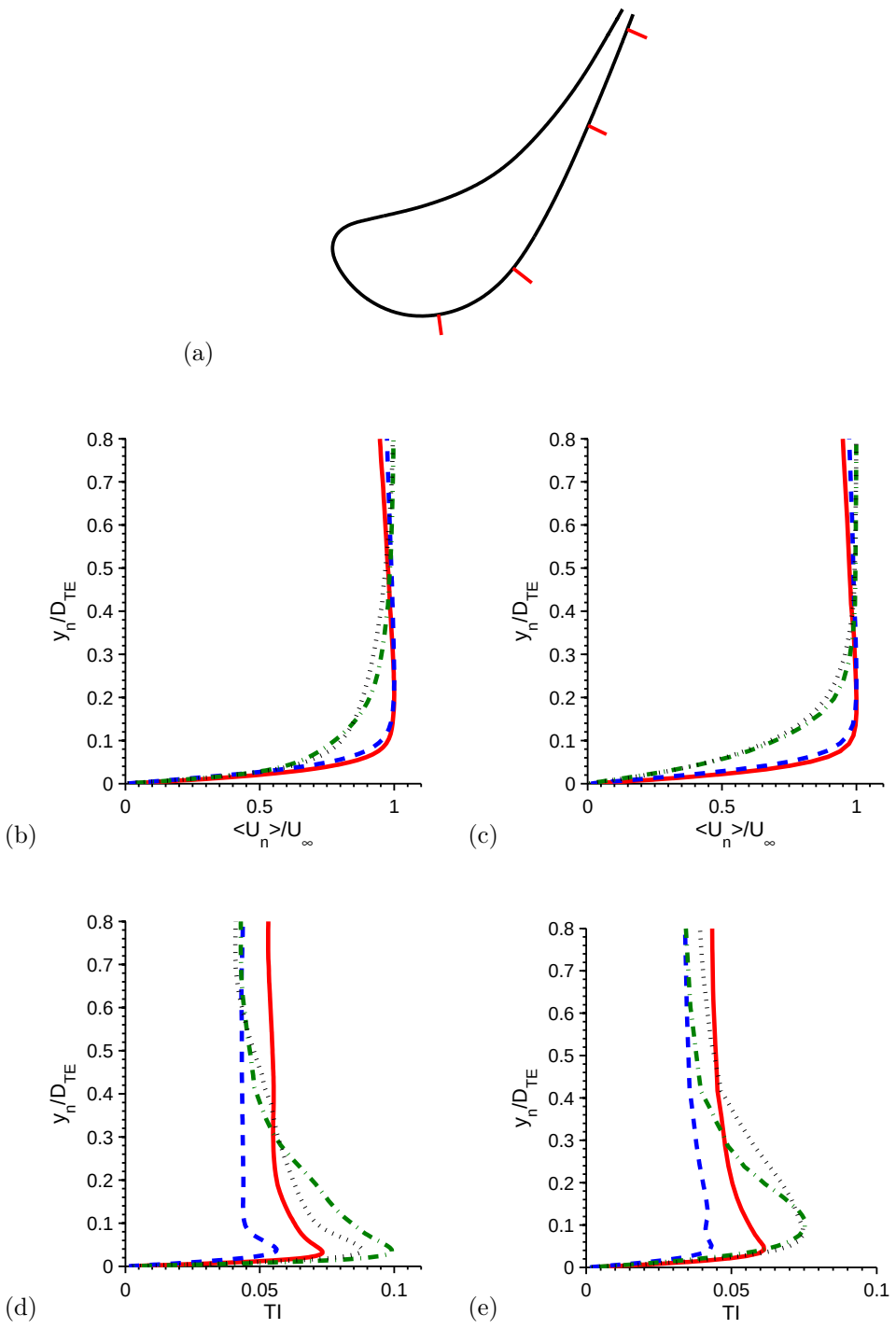

Figure 7-13. Velocity SS boundary layer profiles at $X/C_{ax} = 0.35$ (——), 0.60 (- - -), 0.85 (· - ·), and 0.98 (· · ·) from the blade LE. WALE (b) mean velocity and (d) TI profiles. IDDES-T (c) mean velocity and (e) TI profiles with no vane inlet turbulence.

TI level at the vane exit. This is not the case for the blade which is due to two primary reasons. First, recall that the uncoupled BO steady SST and SST-T mixed out boundary conditions are provided from the VO SST and SST-T results. Therefore the RANS BO cases have a lower plane average inlet TI compared to the WALE and IDDES-T predictions at the vane exit. Second, the periodic unsteadiness that contributes to the overall passage TI generation cannot be captured by a steady RANS modeling approach. Even though the plane average TI level and decay rate is well-matched at the inlet of the vane for all models, the TI generated from the vane wake and through the blade results in the stage exit passage TI under-predicted by 3X compared to WALE predictions.

The prediction of wake profile for the IDDES-T model is found to be in good agreement with the WALE model. Small deviation is the spread in the wake due to SS BL difference between WALE and IDDES-T seen to the left of the wake peak in Figure 7-14. Figure 7-15 highlights the difference in resolved turbulent structures between WALE and IDDES-T. WALE is shown to resolve more near-wall structures for the upper blade due to the higher mesh density and modeling approach compared to IDDES-T. This contributes to the higher prediction of PS surface Nu. This also results in the early break-up on the high energy scales generated from the blade TE.

The mass average vane and blade relative total pressure loss is quantified in Table 7.1. SST predicts the highest loss for the vane and the blade due to turbulent BL on the PS and SS and its contribution to the overall loss. Relative to the WALE model the IDDES-T and SST-T models are within 0.05% for the vane and blade. The mass plane average values can also be misleading in the model's predictive capability, where the SST-T wake profile depth and width is in poor agreement with WALE predictions for the vane and blade.

7.3 High-Level Inlet Turbulence

The same approach from Chapter 6 is used to create high-level turbulence for the stage design. The upstream bars generate TI=20% at $X/C_{ax} = -1.0$ and a non-

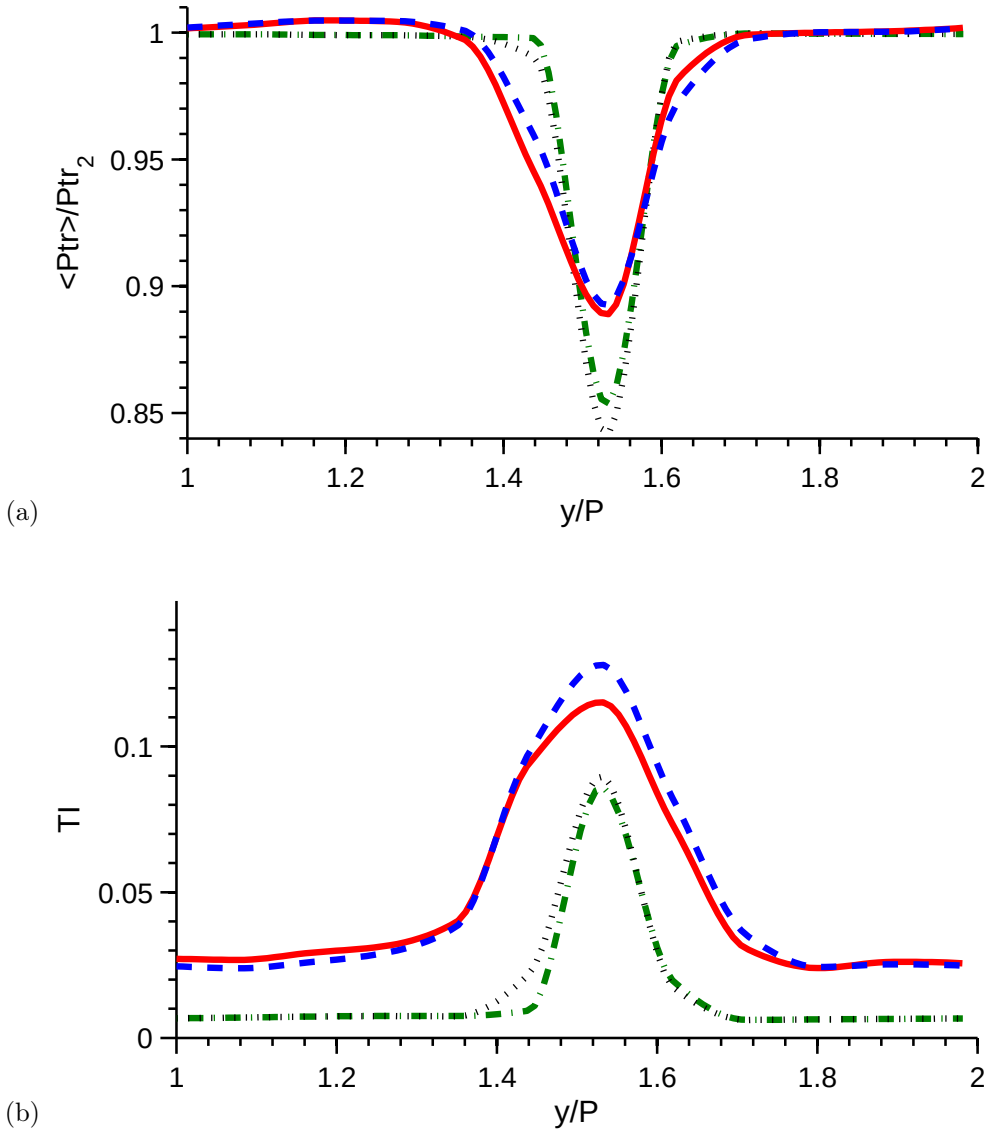

Figure 7-14. Blade (a) normalized mean total relative pressure and (b) local TI profiles at $X/C_{ax} = 1.17$ from the blade LE. Sliding mesh WALE (——) and IDDES-T (- - -) compared to blade-only SST-T (· - ·) and SST (· · ·) with no vane inlet turbulence.

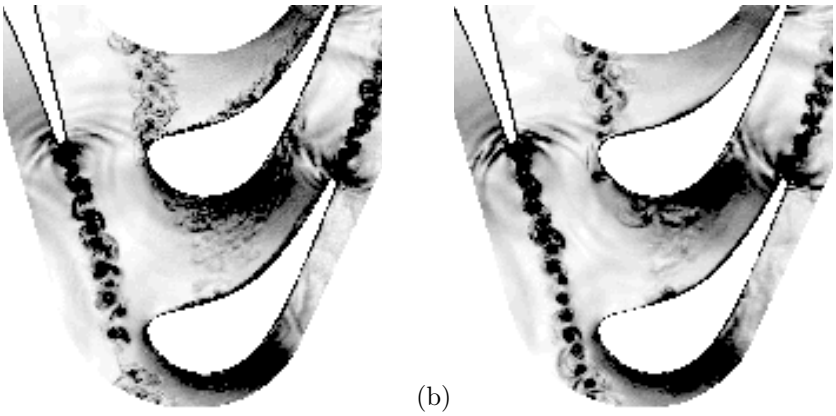

(a) (b)

Figure 7-15. Numerical Schlieren of (a) WALE and (b) IDDES-T pitch-line stage design with no vane inlet turbulence.

Table 7.1. Mass plane average vane total pressure loss, $1 - \langle Pt \rangle / Pt_1$, at $X/C_{ax} = 1.14$ from the vane LE. Mass plane average blade relative total pressure loss, $1 - \langle Ptr \rangle / Ptr_2$, at $X/C_{ax} = 1.17$ from the blade LE for no stage inlet turbulence.

Model	Vane: $1 - \langle Pt \rangle / Pt_1$	Blade: $1 - \langle Pt \rangle / Ptr_2$
WALE	0.99%	1.55%
IDDES-T	1.04%	1.50%
SST-T	1.03%	1.60%
SST	1.47%	1.80%

dimensional length scale of $L_I/C = 0.16$. Conditions at the inlet to the vane match case NB129. IDDES-T domain includes the upstream bars that generate unsteady inlet boundary conditions for the vane along with the downstream blade. WALE sliding mesh was not run for this turbulence case. This was due to the increased cost and the established approach and assessment of the IDDES-T model. Figure 7-16 shows the instantaneous normalized Q-criterion to highlight the generated turbulent structures. Structures are first generated by the upstream bars and pass into the vane. The turbulence structures are stretched as they accelerate through the vane. The TE wake of the vane can be found periodically passing through the downstream blade passage along with remaining structures generated from the bars. This generated stage inlet turbulence combined with periodic vane wake interaction is now examined to understand the impact on BL, surface heat transfer, and wake mixing.

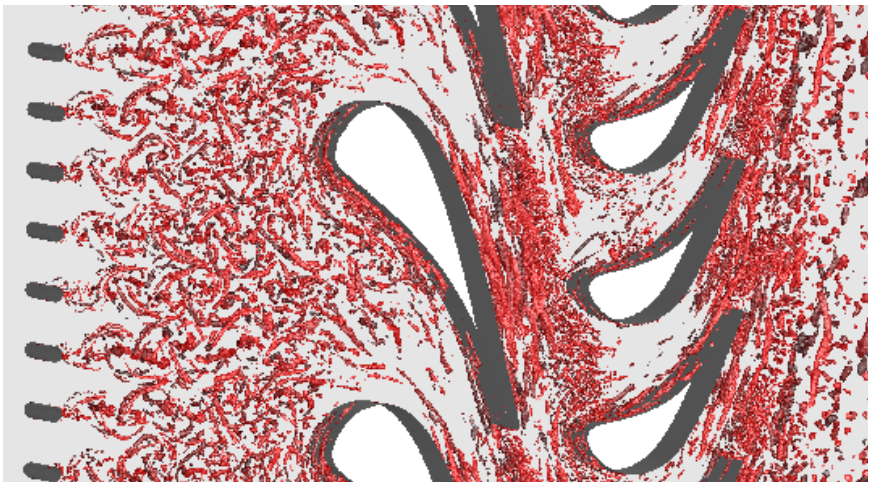

Figure 7-16. Linear sliding mesh domain. Normalized Q-criterion of 0.20 plotted for IDDES-T with high vane inlet turbulence.

Loading comparisons are first made to again confirm conditions and geometry are correctly matched. IDDES-T and WALE comparisons are made for both VO and sliding mesh domains. This is done to assess any influence the downstream blade has on the upstream vane. The stage design intent was to match NB129 VO loading allowing study of the impact when including the downstream blade. This is confirmed in Figure 7-17. Loading profiles are found to be in agreement for each turbulence model and approach. The mean Nu are compared in Figure 7-18 between

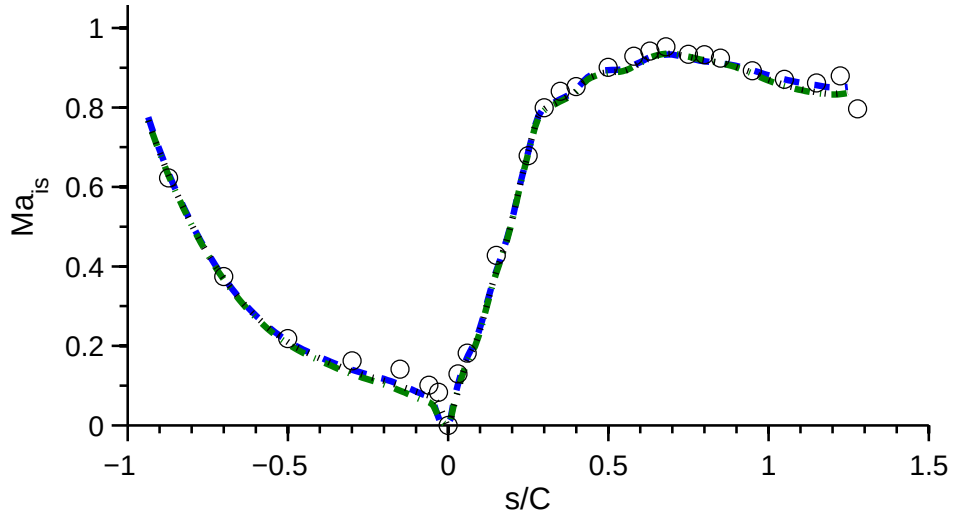

Figure 7-17. Sliding mesh vane loading for IDDES-T (- - -) compared to vane-only WALE (· - ·) and IDDES-T (· · ·) with high-level stage inlet turbulence.

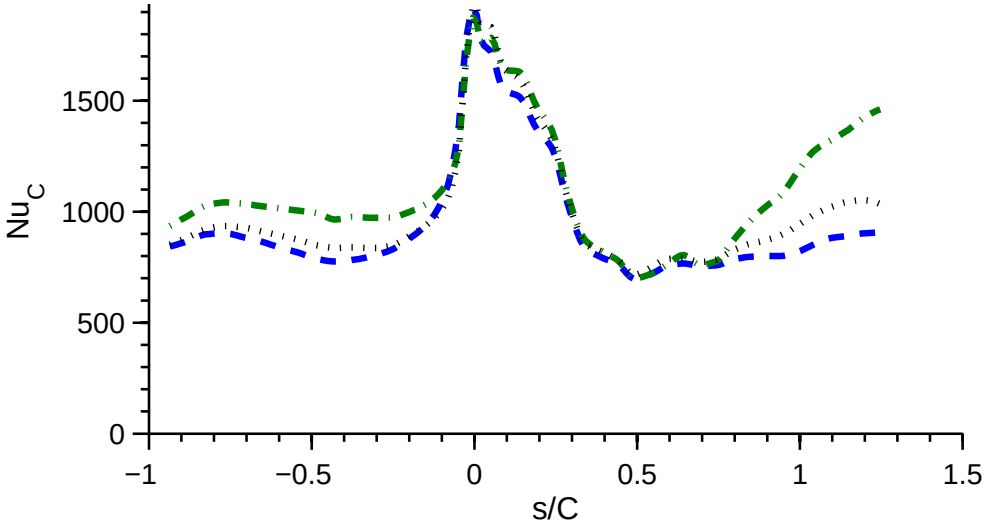

Figure 7-18. Sliding mesh vane mean Nu for IDDES-T (- - -) compared to vane-only WALE (· - ·) and IDDES-T (· · ·) with high vane inlet turbulence.

VO and sliding mesh cases. Overall the IDDES-T predicted surface Nu is found to be slightly reduced due to the downstream blade.

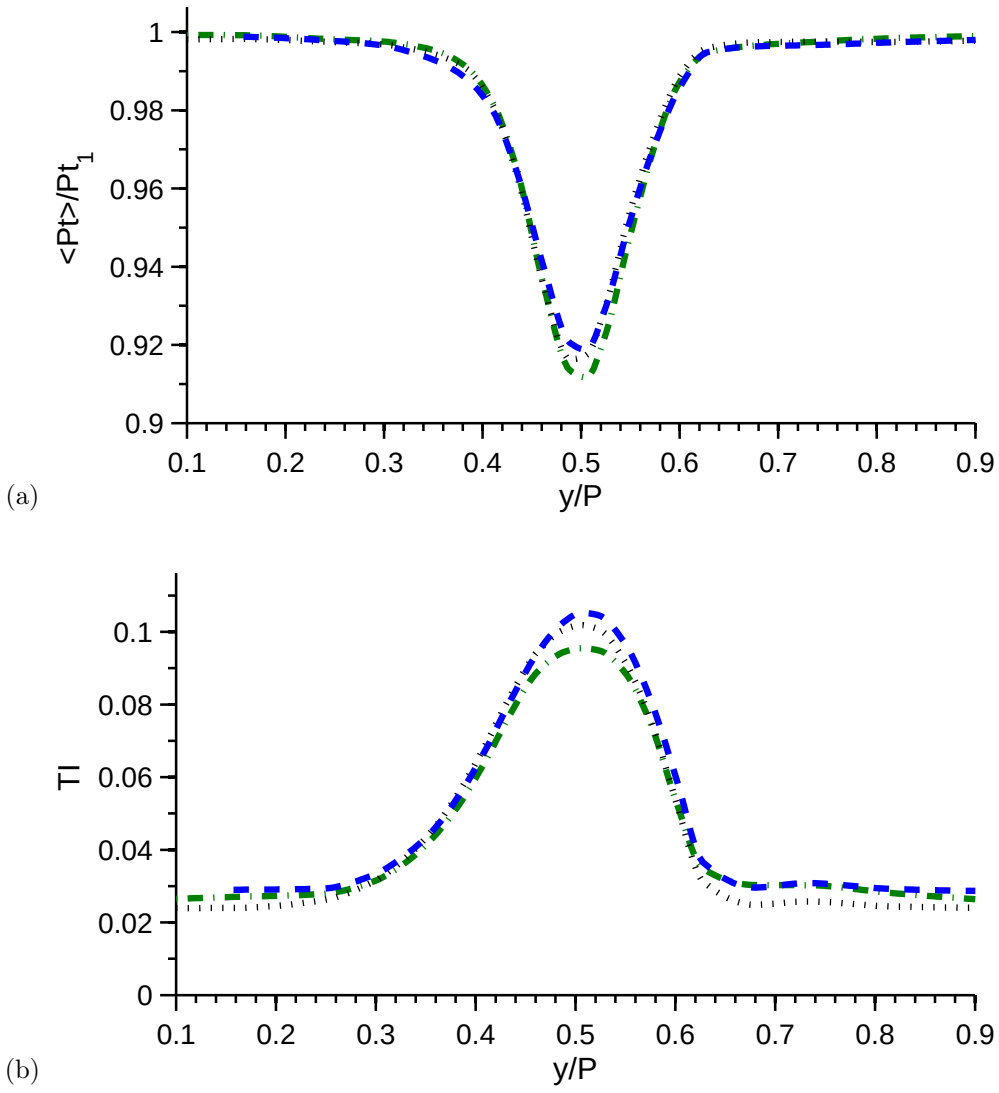

Figure 7-19. Vane (a) normalized mean total pressure and (b) local TI profiles at $X/C_{ax} = 1.14$ from the vane LE. Sliding mesh IDDES-T (- - -) compared to vane-only WALE (· - ·) and IDDES-T (· · ·) with high vane inlet turbulence.

Figure 7-19 shows total pressure and TI wake profile predictions. Findings are similar to the case with no inlet TI where the unsteady pressure wave from the periodic pressure fluctuations from the downstream blade have a negligible impact on the mean total pressure wake profile at $X/C_{ax} = 1.14$. Small differences are again

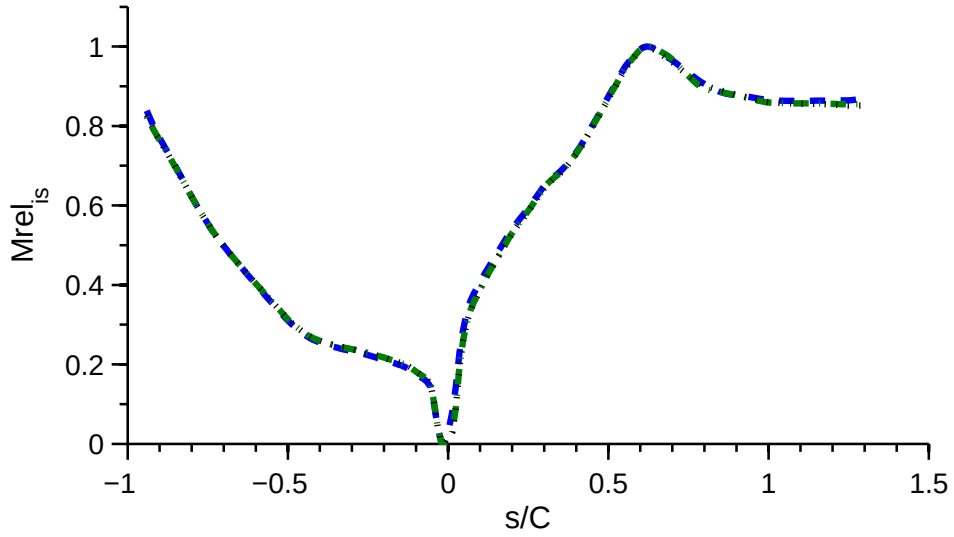

Figure 7-20. Sliding mesh blade loading for IDDES-T (- - -) compared to blade-only SST-T (· - ·) and SST (· · ·) with high vane inlet turbulence.

found for the TI profiles where the passing blade is found to slightly increase the TI outside the vane wake.

The influence of the high-level stage TI on the downstream blade is now considered. The uncoupled BO steady SST and SST-T are again included and compared to the coupled IDDES-T predictions. Matching loading and incident angle is confirmed in Figure 7-20. The mean Nu is compared in Figure 7-21 between steady BO and sliding mesh cases. The SST-T and IDDES-T surface Nu along the PS and LE are found to be in better agreement relative to the previous section where no stage inlet TI was presented. This is due to the elevated blade inlet TI and the SST-T model sensitivity to this boundary condition. The SS surface Nu transition location is found to be similar for SST-T and IDDES-T predictions. This aligns with the peak Mach number at the blade throat where the adverse pressure gradient begins. The SST-T over-predicts Nu by more then 2X relative to IDDES-T. This difference was also found when no TI was provided at the stage inlet where the IDDES-T model is expected to under-predict the SS surface Nu after the throat.

Figure 7-22 shows total pressure wake and TI profile predictions for IDDES-T, SST-T, and SST for the blade at $X/C_{ax} = 1.17$ from the blade LE. SST-T and SST are found to the over-predict wake depth and under-predict wake spreading relative

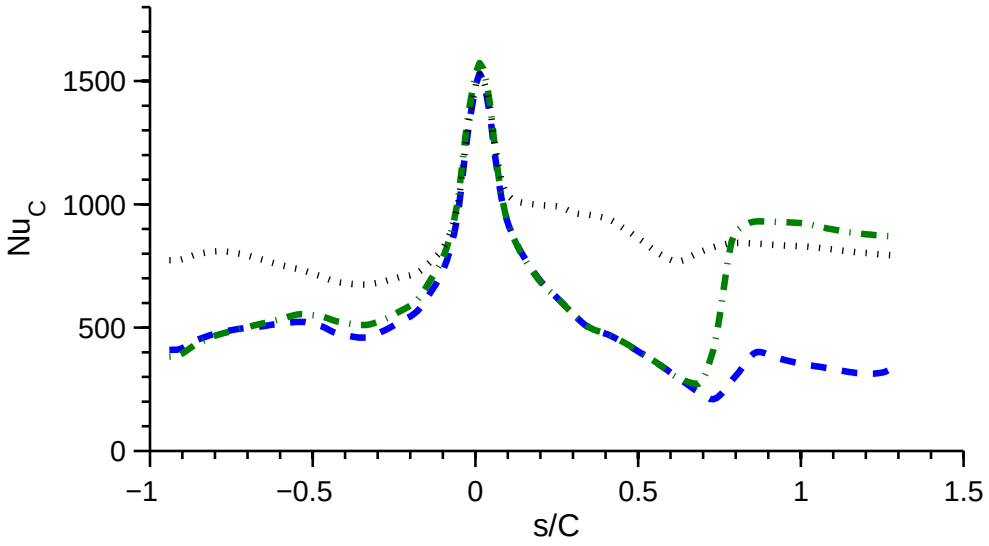

Figure 7-21. Sliding mesh blade mean Nu for IDDES-T (- - -) compared to blade-only SST-T (· - ·) and SST (· · ·) with high vane inlet turbulence.

to IDDES-T predictions. This is consistent with previous wake results for no stage inlet TI. The mass average vane and blade relative total pressure loss is quantified in Table 7.2. SST and SST-T over-predict the loss for the vane relative to IDDES-T due to the turbulent BL on the PS and SS and its contribution to the overall loss. This was also found for the VO WALE predictions in Chapter 6. Relative to the IDDES-T model, the SST-T model is within 0.01% for the blade. The mass plane average values are again misleading, where the SST-T wake profile depth and width are in poor agreement with IDDES-T predictions for the vane and blade.

Table 7.2. Mass plane average vane total pressure loss, $1 - \langle Pt \rangle / Pt_1$, at $X/C_{ax} = 1.14$ from the vane LE. Mass plane average blade relative total pressure loss, $1 - \langle Ptr \rangle / Ptr_2$, at $X/C_{ax} = 1.17$ from the blade LE for high-level stage inlet turbulence.

Model	Vane: $1 - \langle Pt \rangle / Pt_1$	Blade: $1 - \langle Pt \rangle / Ptr_2$
IDDES-T	1.24%	1.69%
SST-T	1.58%	1.70%
SST	1.63%	1.87%

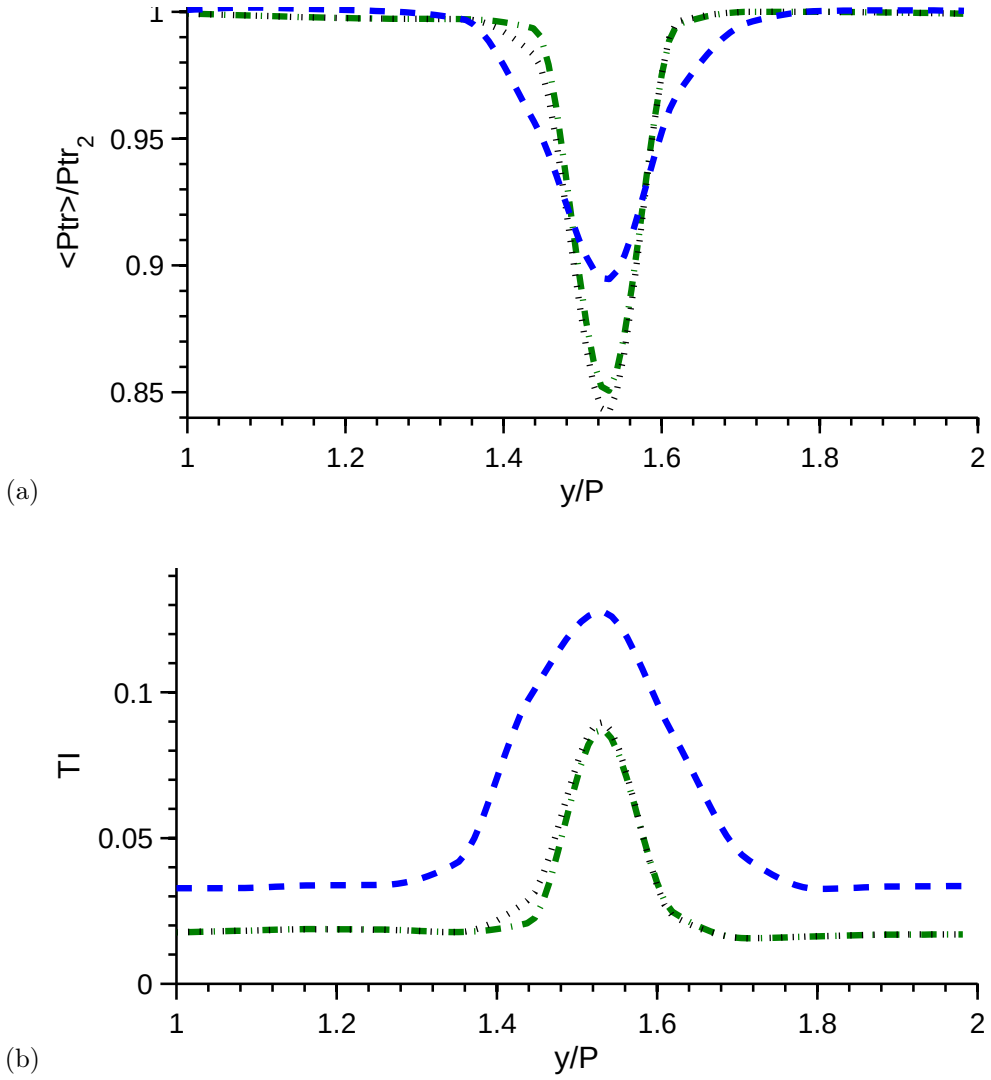

Figure 7-22. Blade (a) normalized mean total relative pressure and (b) local TI profiles at $X/C_{ax} = 1.17$ from the blade LE. Sliding mesh IDDES-T (- - -) compared to blade-only SST-T (· - ·) and SST (· · ·) with high vane inlet turbulence.

7.4 Summary of Inlet Turbulence Impact

For the presented pitch-line study, based on IDDES-T predictions, the impact of stage inlet TI is found to be secondary compared to the periodic unsteadiness generated by the vane wake on the downstream blade surface heat transfer and mixing. Due to the 20% inlet TI, the vane sees on the order of a 1.5X increase in surface Nu in Figure 7-23. However, the blade sees an almost negligible impact for Nu. Less than a 5% increase in PS surface Nu is found for the higher inlet stage TI level and no change in LE Nu is found. The SS shows the same transition location. After this SS location the absolute Nu is again within 5% between the two stage inlet TI levels. However, it was found that a significant amount of the total TI is contributed by the resolved unsteadiness that doesn't directly contribute to the transport equations for transition. Therefore the SS surface Nu after the throat for the IDDES-T model is expected to be under-predicted by nearly 2X based on the WALE predictions for zero stage inlet TI.

It is now important to understand blade surface unsteadiness and the dominant unsteady contributions. The pressure fluctuation, $p' = \langle p \rangle - p$, on the blade LE, PS and SS surfaces for the IDDES-T predictions at the stage inlet TI are presented in Figure 7-24. For the zero inlet TI case, two deterministic frequencies are found. The larger amplitude is the upstream vane passing occurring at approximately every 50 Δt_o. The smaller amplitude is the shedding from the upstream TE vane where the large amplitude is the contribution of the flow from the wake passing. At the high inlet TI the vane TE shedding is dampened due the to high free-stream TI.

Regardless of the stage inlet TI, the blade velocity (Figure 7-25) and thermal (Figure 7-26) mean BL profile are found to be near identical for both the PS and SS surfaces. The velocity and thermal PS BL is found to have mean laminar profiles with non-zero near-wall fluctuations. The SS BL is found to be transitional after the blade throat.

The blade PS and SS BL fluctuations are shown in 7-27. Similar levels of BL TI are found for both levels of inlet stage TI. This is consistent with the surface pressure

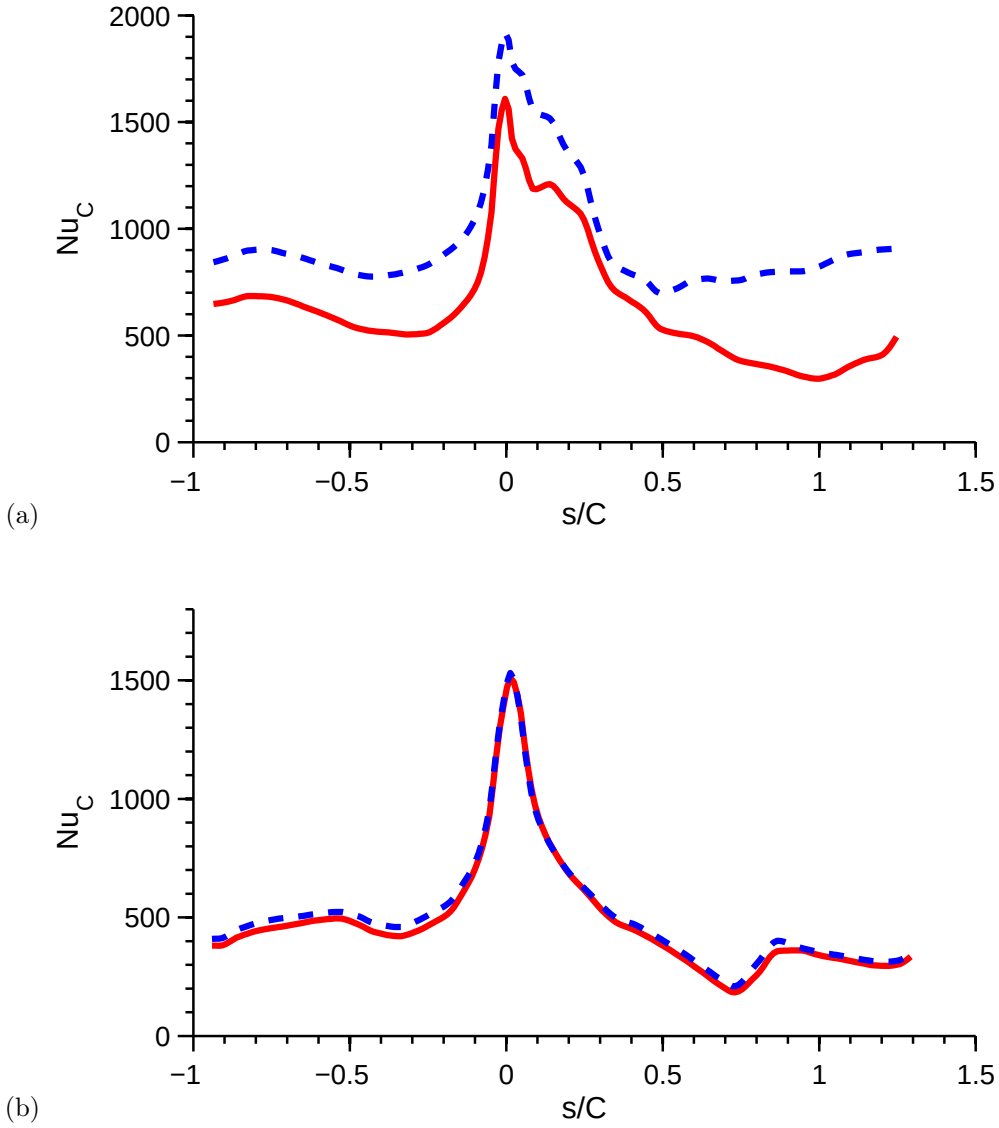

Figure 7-23. IDDES-T sliding mesh surface mean Nu for no stage inlet TI (——) and high-level inlet TI (- - -) for the (a) vane and downstream (b) blade.

fluctuation (Figure 7-24) where the dominant unsteadiness was due to the passing of the upstream vane. Away from the wall, small increases in TI can be found due to the higher stage inlet TI compared to the zero stage inlet TI case. This difference becomes smaller as the flow accelerates and moves closer to the blade TE.

Figures 7-28 and 7-29 compare the vane and blade wake total relative pressure and TI wake profile. The 20% vane inlet TI difference between the two cases has

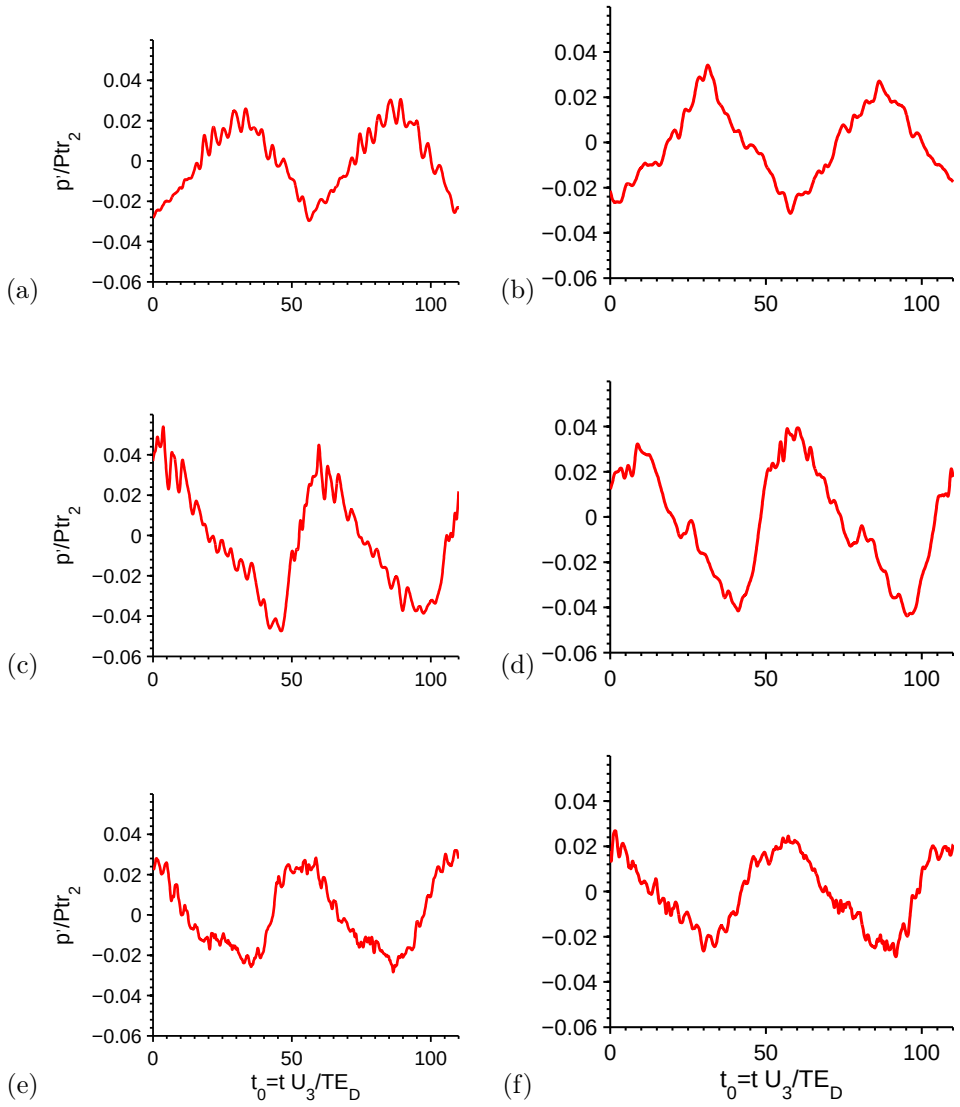

Figure 7-24. IDDES-T Blade surface pressure fluctuation, p'/Pt_1, at (a) PS $X/C_{ax} = 0.69$,(c) LE $X/C_{ax} = 0.0$, and (e) SS $X/C_{ax} = 0.95$ with no stage inlet turbulence. Surface pressure fluctuation at (b) PS $X/C_{ax} = 0.69$,(d) LE $X/C_{ax} = 0.0$, and (f) SS $X/C_{ax} = 0.95$ for high-level stage inlet turbulence.

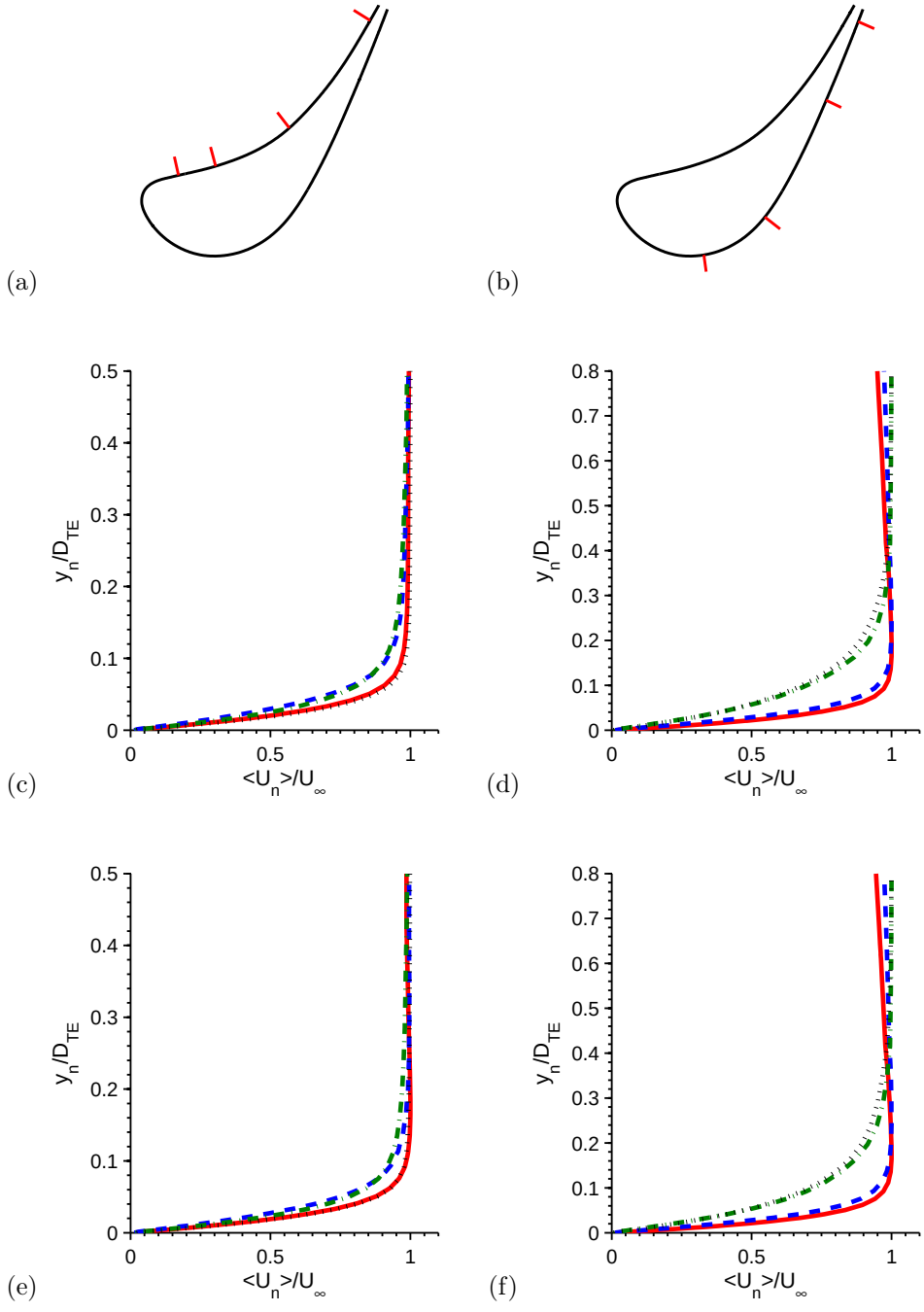

Figure 7-25. IDDES-T blade PS mean velocity boundary layer profiles at $X/C_{ax} = 0.15$ (——), 0.30 (- - -), 0.6 (· - ·), and 0.93 (· · ·) for (c) 0% and (e) 20% stage inlet TI. SS mean velocity boundary layer profiles at $X/C_{ax} = 0.35$ (——), 0.60 (- - -), 0.85 (· - ·), and 0.98 (· · ·) for (d) 0% and (f) 20% stage inlet TI.

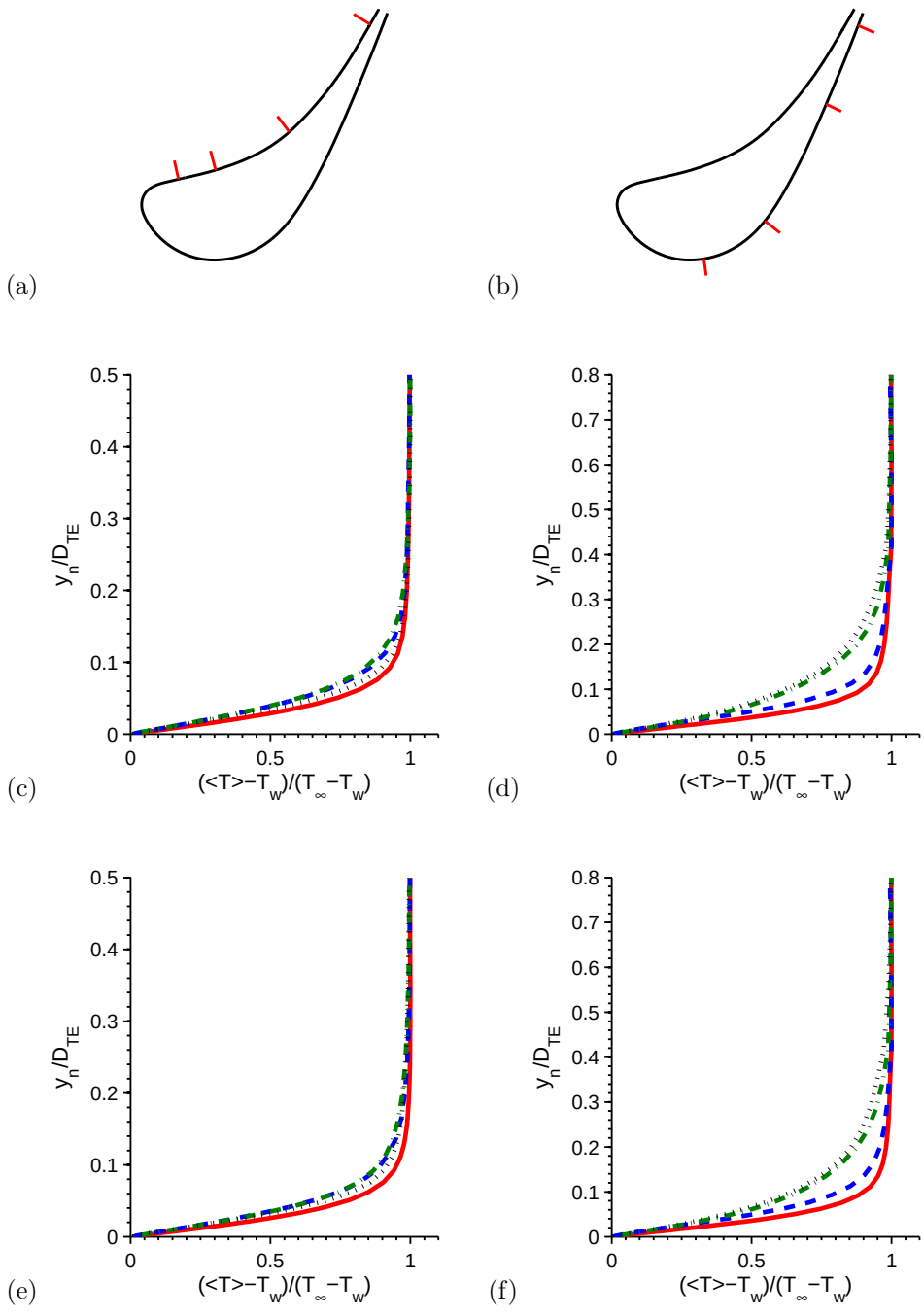

Figure 7-26. IDDES-T blade PS mean temperature boundary layer profiles at X/C_{ax} = 0.15 (——), 0.30 (- - -), 0.6 (· - ·), and 0.93 (· · ·) for (c) 0% and (e) 20% stage inlet TI. SS mean temperature boundary layer profiles at X/C_{ax} = 0.35 (——), 0.60 (- - -), 0.85 (· - ·), and 0.98 (· · ·) for (d) 0% and (f) 20% stage inlet TI.

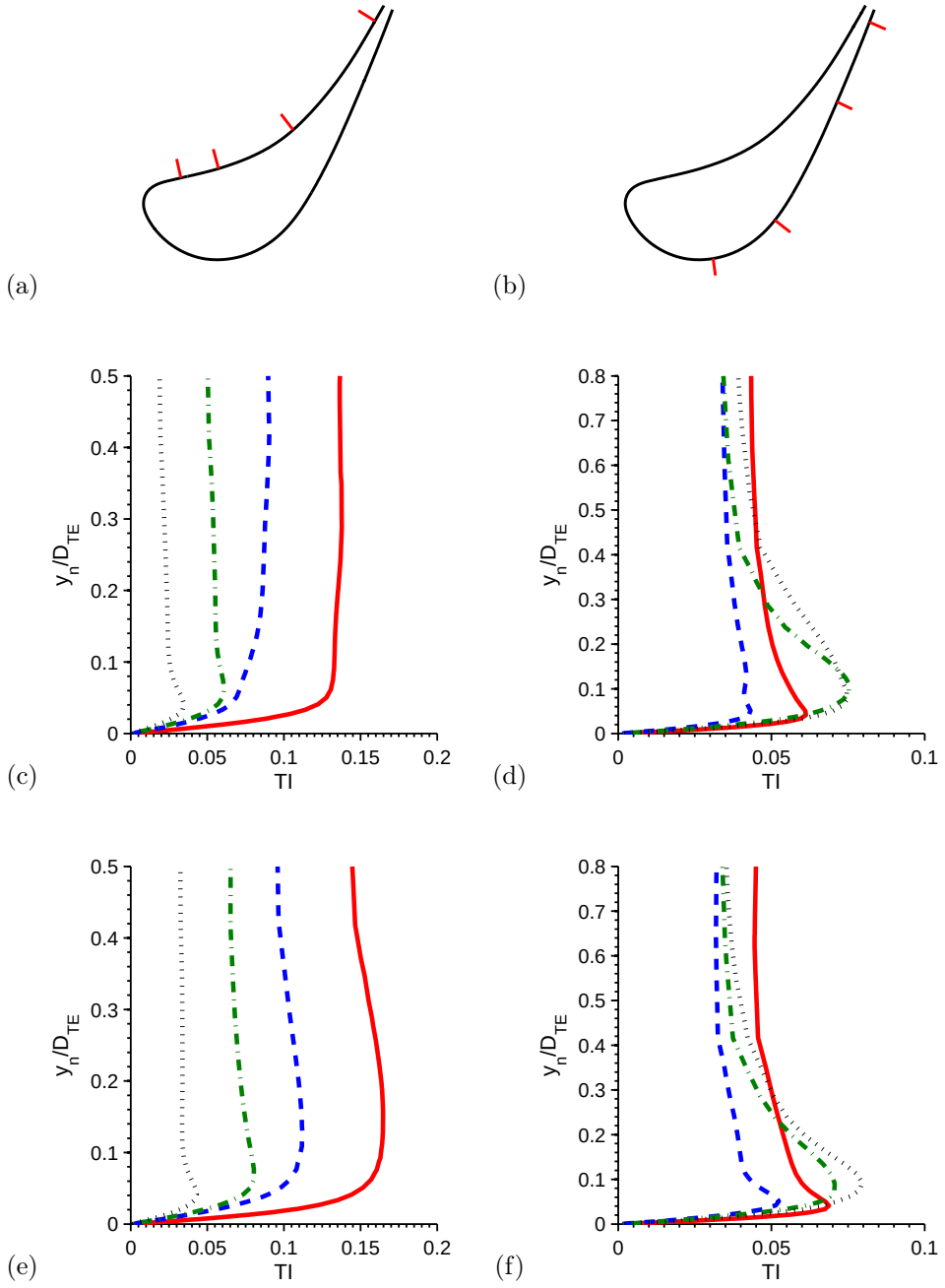

Figure 7-27. IDDES-T blade PS TI boundary layer profiles at $X/C_{ax} =$ 0.15 (——), 0.30 (- - -), 0.6 (· - ·), and 0.93 (· · ·) for (c) 0% and (e) 20% stage inlet TI. SS TI boundary layer profiles at $X/C_{ax} = 0.35$ (——), 0.60 (- - -), 0.85 (· - ·), and 0.98 (· · ·) for (d) 0% and (f) 20% stage inlet TI.

been reduced to a $2-4\%$ difference at the vane exit. Therefore, regardless of the level of turbulence at the inlet of the vane, the downstream blade inlet unsteadiness is found to be dominated by the vane TE wake passing. Overall the blade exit profiles are found to have similar depth and spread where the contribution of higher stage inlet TI is seen in the passage between the blade TE wakes. The mass average vane and blade relative total pressure loss is quantified in Table 7.3. The total pressure wake profile shape for the vane is found to largely deviate for the two levels of TI. This deviation cannot be realized with a simple mass average comparison. The blade is found to have an almost identical wake profile where a mass average difference is found due to an increased loss found in the core of the flow.

Table 7.3. IDDES-T mass plane average vane total pressure loss, $1-\langle Pt\rangle/Pt_1$, at $X/C_{ax}=1.14$ from the vane LE. Mass plane average blade relative total pressure loss, $1-\langle Ptr\rangle/Ptr_2$, at $X/C_{ax}=1.17$ from the blade LE for range of stage inlet turbulence.

IDDES-T	Vane: $1-\langle Pt\rangle/Pt_1$	Blade: $1-\langle Pt\rangle/Ptr_2$
$TI=0\%$	1.04%	1.50%
$TI=20\%$	1.24%	1.69%

The impact of stage inlet TI is found to be of more importance for the vane than the downstream blade for the presented pitch-line stage geometry. When expanding to a 3D domain to include axisymmetric endwalls and tip clearance for the down-stream blade, the secondary flow contribution must be understood. The developing unsteady flow field and impact on the down-stream blade will be tied back to the pitch-line study. The next chapter takes an initial step toward understanding the contribution of 3D geometry and endwall secondary flow impact on BL development, surface heat transfer, and wake development and decay with zero stage inlet TI.

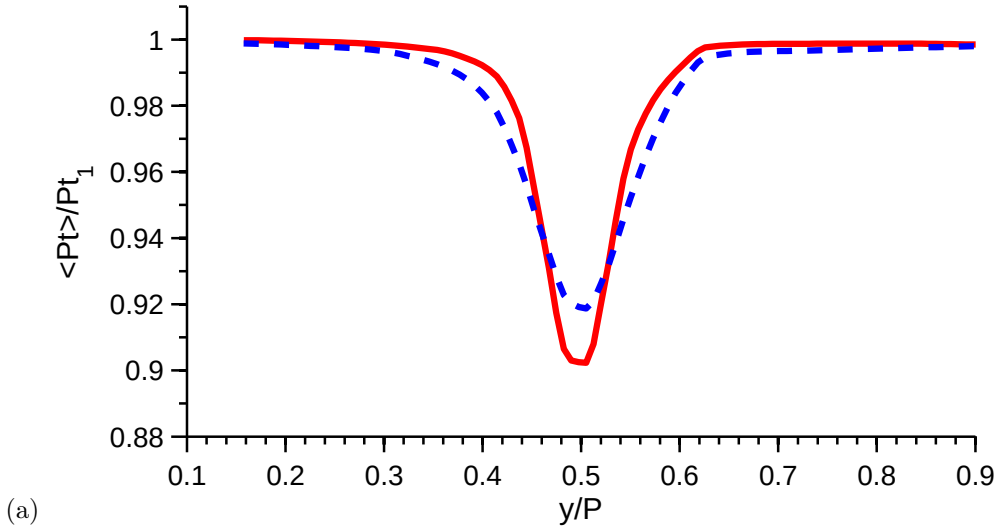

(a)

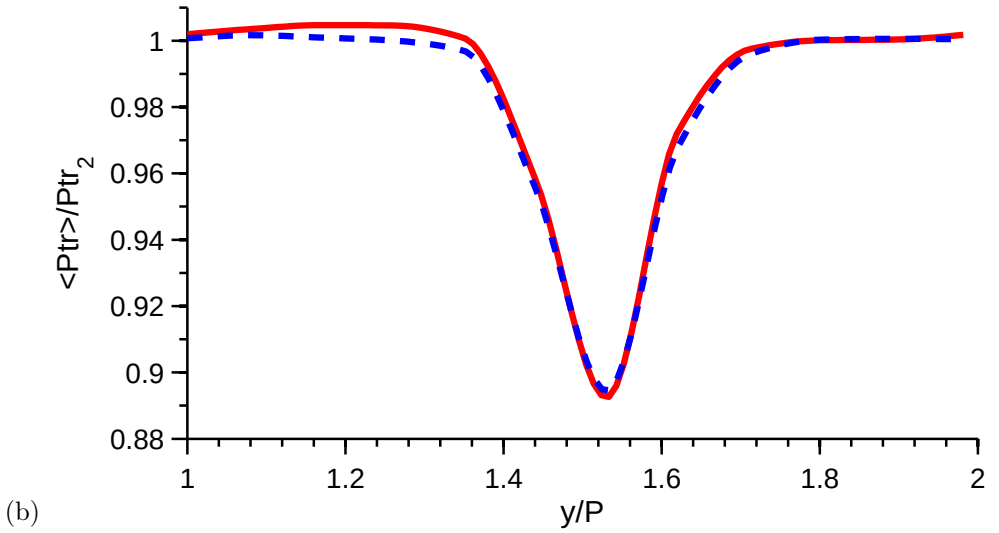

(b)

Figure 7-28. IDDES-T sliding mesh with no stage inlet TI (——) and high-level TI (- - -) normalized mean (a) vane total pressure at $X/C_{ax} = 1.14$ from the vane LE and (b) blade total relative pressure at $X/C_{ax} = 1.17$ from the blade LE.

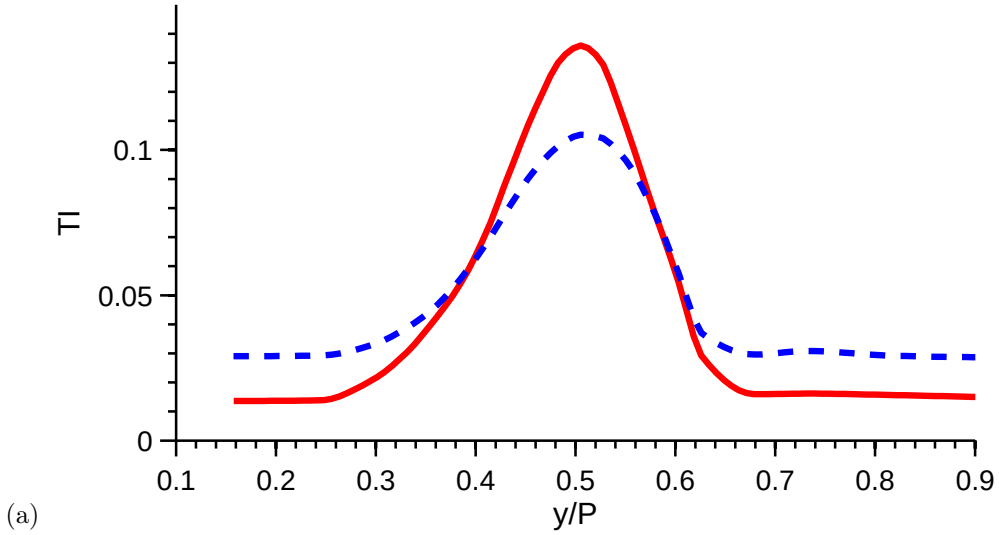

(a)

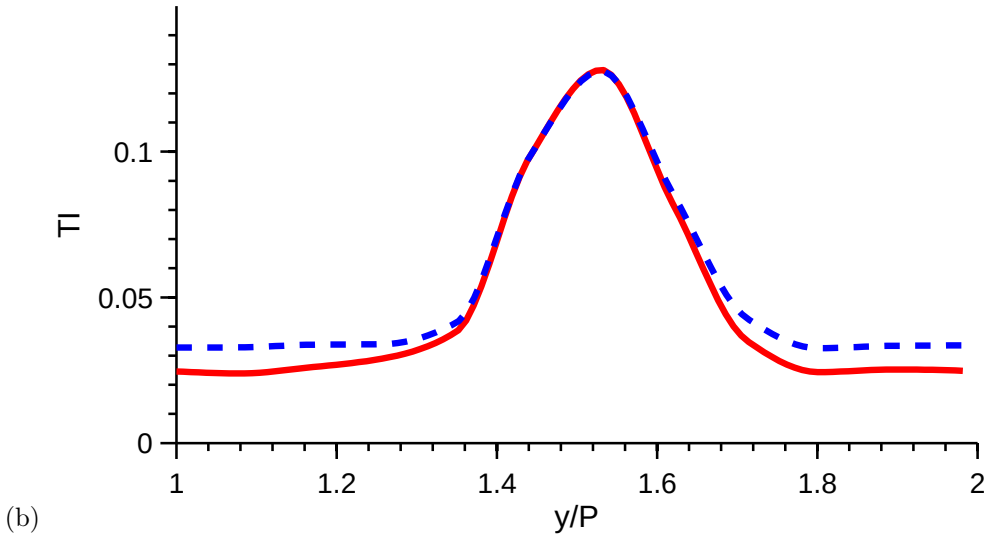

(b)

Figure 7-29. IDDES-T sliding mesh with no stage inlet TI (——) and high-level TI (- - -) for (a) vane exit TI profile at $X/C_{ax} = 1.14$ from the vane LE and (b) blade exit TI profile at $X/C_{ax} = 1.17$ from the blade LE.

Chapter 8

3D Stage Aero-Thermal Study

8.1 3D Stage Design: 3SD02

The computational study is expanded to a 3D stage geometry (Figure 8-1) including axisymmetric endwalls for the vane and an axisymmetric platform with a constant tip clearance 10% of the blade height. The objective is to determine the impact of the secondary flow span-wise penetration on the vane and downstream blade. The vane of Arts and Rouvroit [34] is linearly stacked with the addition of endwall to the computational domain. The 50% span of the 3D vane and blade airfoil geometries are matched to the pitch-line case in Chapter 7. The inlet and exit boundary conditions at the pitch are also matched in order to evaluate the impact of the 3D flow field and rotational effects between the 3D and linear pitch-line geometries. The linear blade speed is matched to the 3D blade's pitch-line tangential speed in order to isolate and study the impact of rotational effects. The blade geometry varies hub to tip to adjust for the variable inlet flow angle. Therefore the blade mechanical incidence angle is decreasing with increasing radius to account for the blade's relative flow incidence angle. The blade was designed to have favorable loading characteristics by minimizing adverse pressure gradients while providing negligible turning after the throat to avoid flow deviation from the desired exit angle [88]. Multiple iterations were performed on the blade using steady RANS with the SST model to achieve the final shape. After completion of the pitch-line section, the same design approach was applied to the hub

and tip of the 3D geometry. Further discussion of the blade geometry can be found in Appendix B.

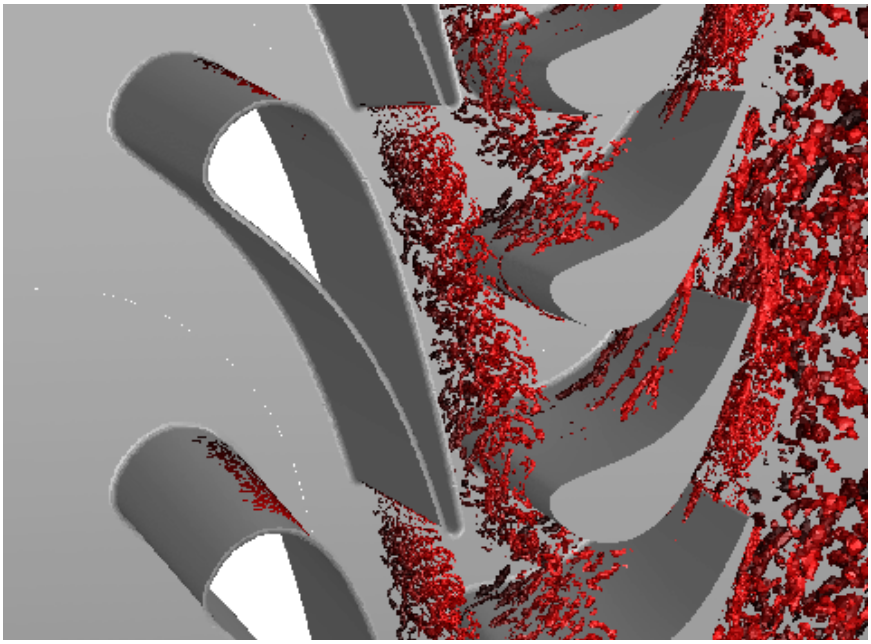

Figure 8-1. 3D Sliding mesh domain. Normalized Q-criterion of 0.15 plotted for IDDES-T from 10% to 90% span.

Chapter 7 focused on isolating a pitch-line geometry in the absence of endwall secondary flows and rotational effects. For the pitch-line geometry it was shown:

- WALE, IDDES-T, and SST-T modeling approaches predicted matching loading for the vane and blade.
- Stage inlet TI of 0 and 20% resulted in up to a 2X increase in vane surface Nu based on IDDES-T predictions.
- Stage inlet TI of 0 and 20% showed negligible change for blade surface Nu based on IDDES-T predictions.
- Stage inlet TI=0% for WALE and IDDES-T vane and blade profile predictions agreed within a delta of 1% for the normalized total pressure. This is smaller than the experiment uncertainty of the vane for Arts and Rouvroit [34].
- Stage inlet TI had a negligible impact on the blade total pressure wake spread and depth. However, increased loss was found in the passage.

Chapter 8 presents results for a stage inlet TI=0% with the addition of endwalls and resulting secondary flows. The developing 3D flow through the vane is examined along with the impact on downstream blade. Impact of stage inlet TI was found to be of secondary importance to the downstream blade relative to the passing vane wake for the presented pitch-line stage geometry. Therefore this chapter takes the next step toward understanding the contribution of 3D geometry on secondary flow development and the impact on BL development, surface heat transfer, and wake mixing at inlet stage TI=0%. In addition, the downstream blade includes a blade tip gap to understand the development of the tip vortex and impact on blade near-wall and downstream flow field.

Previously the linear pitch-line geometry modeling studies were completed for steady SST and SST-T along with scale-resolved unsteady approaches using WALE and IDDES-T models. Therefore, modeling approaches preformed for the 3D geometry leveraged the meshing practices from the previous chapters. For the 3D geometry, IDDES-T is the unsteady coupled modeling approach used to understand the stage interaction given the large domain and computational cost for LES. However, detailed back to back studies between WALE and IDDES-T in Chapters 6 and 7 were completed in order to take an IDDES-T modeling approach here. Finally, given the continued use of RANS for industrial designs, SST and SST-T is the uncoupled approaches. The BO inlet boundary conditions come from the VO plane mass averaged mixed out conditions for momentum, enthalpy and turbulence (See Appendix B).

8.2 Pitch-line Comparison

Before modeling comparisons are made between SST, SST-T, and IDDES-T for the 3D stage geometry, the unsteady modeling approach for IDDES-T is reviewed. In order to reduce the computational cost for the 3D sliding mesh (3DSM) geometry, only IDDES-T was run where the mesh was 2X coarser relative to the linear sliding mesh (2DSM) presented in Chapter 7. The impact of the coarse mesh is qualified in this section along with pitch-line comparisons for the 2DSM and 3DSM. Loading comparison are found

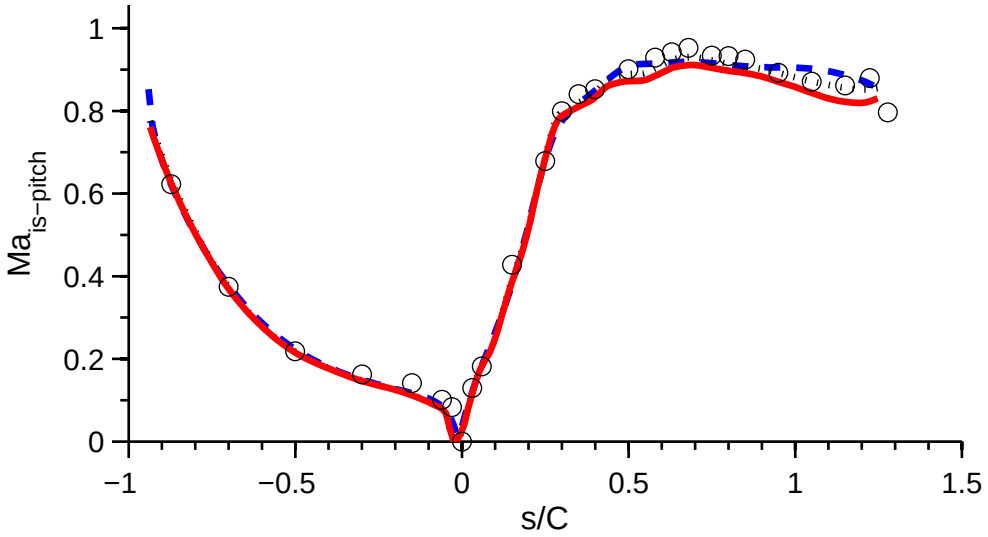

Figure 8-2. Sliding mesh vane loading for 2DSM coarse mesh IDDES-T (——), 3DSM coarse mesh IDDES-T (- - -), and 2DSM desired mesh IDDES-T (· · ·) with no vane inlet turbulence. Experimental vane only case MUR129 (○).

in Figure 8-2. All three case are found to have good agreement in both PS loading and the inlet incidence flow. Small differences in loading are found after the throat location. The deviations between 2DSM and 3DSM are of similar magnitude to the two mesh densities for 2DSM. Therefore, any 3D flow impact on loading at the pitch-line is difficult to distinguish from the contribution of mesh resolution. IDDES-T is also compared back to the pitch-line vane only experimental measurements of Arts and Rouvroit [34], showing minor deviation in loading for the 3D vane. To evaluate the impact of the 3D geometry on the flow around the vane surface, instantaneous streamlines are plotted in Figure 8-3 along with the instantaneous surface pressures, p. The streamlines and pressure field on the PS of the vane resemble 2D like flow field where negligible radial variation is seen. However, the SS surface shows large radial variation where the secondary flow passage vortex is found to have an impact on the vane surface as the flow moves down-stream, highlighting the secondary flow impact on the vane loading.

The predicted Nu in Figure 8-4 remains the same for the majority of the vane. Only at the SS TE does the coarser mesh result in an earlier transition. This shows the

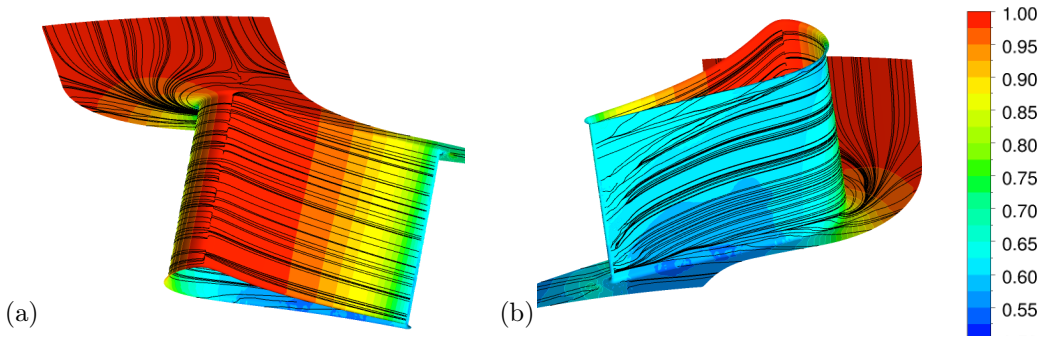

Figure 8-3. Vane IDDES-T surface instantaneous streamlines (a) forward looking aft and (b) aft looking forward with surface contours of instantaneous $p/Pt_{1-50\%span}$.

unfortunate dependency on near-wall mesh resolution for the IDDES-T model where increasing the mesh density by 2X results in a $\Delta s/C = 0.15$ shift in the transition point. The impact of the SS BL looks to be minor on the downstream vane wake in Figure 8-5. Comparing 2DSM and 3DSM coarse mesh Nu surface results, it is shown that the 3D secondary flow field present on the SS surface results in delaying the BL transition.

Larger differences are present in the wake. First, the total pressure outside the

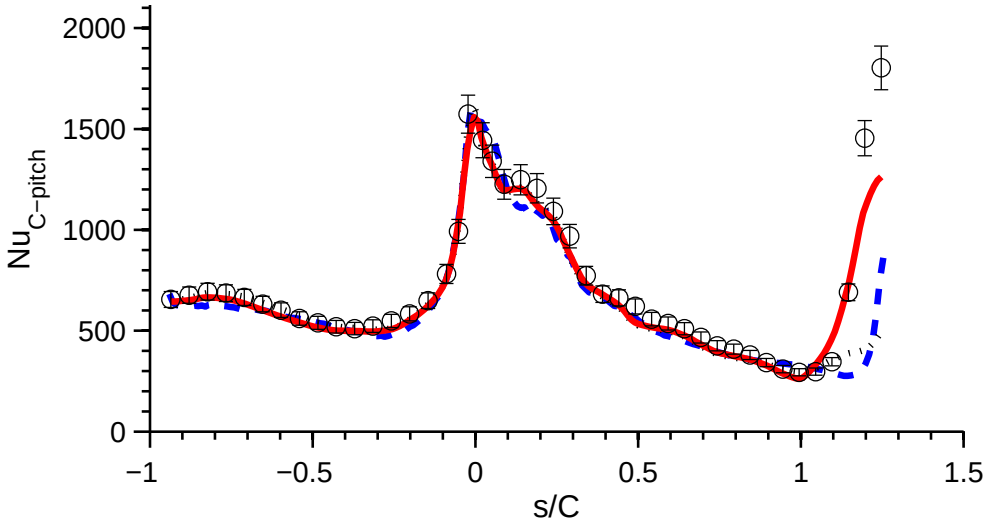

Figure 8-4. Sliding mesh vane mean Nu for 2DSM coarse mesh IDDES-T (——), 3DSM coarse mesh IDDES-T (- - -), and 2DSM desired mesh IDDES-T (· · ·) with no vane inlet turbulence. Experimental vane only case MUR129 (○).

wake is found to be lower. This is due to the annular flow path for the 3D geometry and the addition of the streamline migration and secondary flow through the vane. The total pressure in the free-stream is slightly lower at the exit of the vane at 50% span. Since the profile is normalized to the inlet total pressure, a shift is found in the total pressure outside the wake. A slight increase in the wake spread is found for the 3D geometry compared to the linear case. The major difference is found in the depth

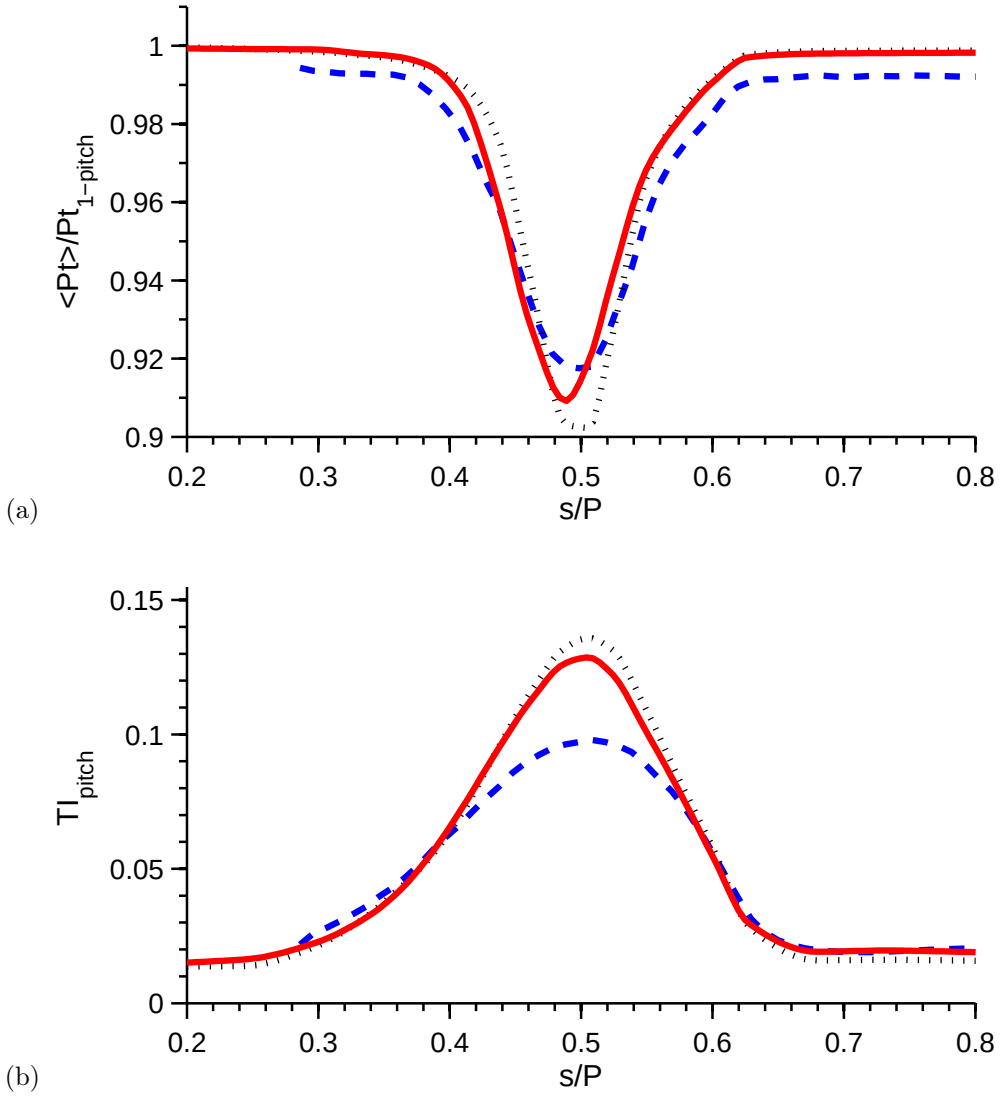

Figure 8-5. Sliding mesh vane (a) normalized mean total pressure and (b) local TI at $X/C_{ax} = 1.14$ from the vane LE for 2DSM coarse mesh IDDES-T (——), 3DSM coarse mesh IDDES-T (- - -), and 2DSM desired mesh IDDES-T (· · ·) with no vane inlet turbulence.

of the wake which would be more significant if the total pressure was normalized to the exit total pressure in the free-stream outside the wake. This shows the first major contributions of 3D flow field effects. The additional centripetal force and the flow migration changes the developing TE wake turbulent structures resulting in increased spreading and wake decay. A closer look at these structures are presented in the next section. The shift in decay rate is also shown for the TI, where the peak TI has reduced by 4% at $X/C_{ax} = 1.14$.

Blade surface Nu is compared in Figure 8-6. The largest difference in blade surface Nu is found on the PS surface. As much as a 20% decrease in PS surface Nu is found for 3D blade geometry. This agrees with the decrease in TI found for the 3D geometry vane wake. Therefore, the turbulent strengthening of the passing vane wake on the downstream blade is reduced, resulting in a lower PS surface Nu. Similar SS surface Nu profiles are found between 2DSM and 3DSM, showing the Nu is again dominated by the favorable pressure gradient before the throat and the adverse pressure gradient after the throat, causing transition.

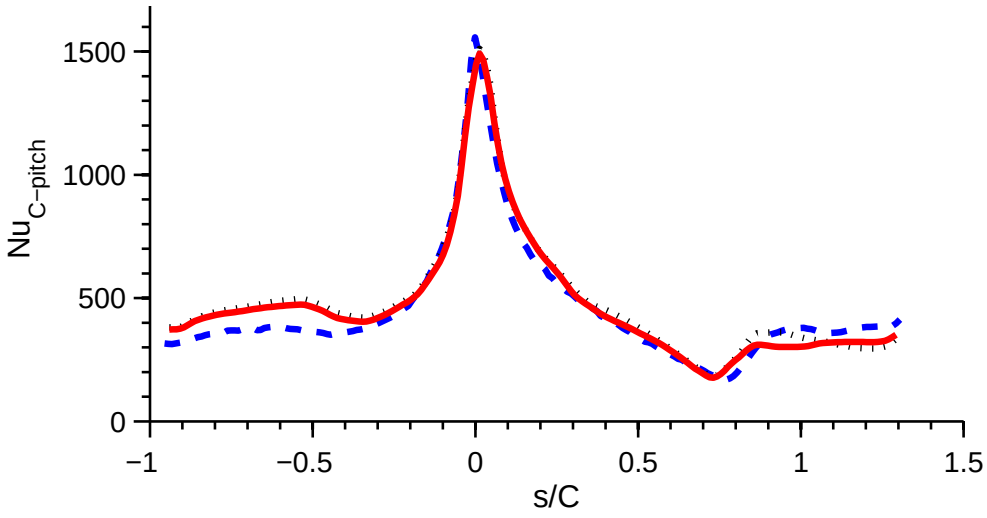

Figure 8-6. Sliding mesh blade mean Nu for 2DSM coarse mesh IDDES-T (——), 3DSM coarse mesh IDDES-T (- - -), and 2DSM desired mesh IDDES-T (· · ·) with no vane inlet turbulence.

The blade surface instantaneous streamlines are plotted in Figure 8-6 along with the instantaneous surface pressures. The streamlines and pressure field on the PS of the blade resemble a 2D like flow field at the mid-span region. Near the hub and

largely at the tip region, radial flow migration is seen on the blade surface. Due to the PS to SS pressure gradient, flow migrates over the tip as a function of the tip gap. This radial migration is found to occur at around 80% span and up on the blade PS surface. On the SS surface, pressure and instantaneous streamlines visually show where the adverse pressure gradient begins and the impact on the near-wall flow and transitioning of the BL. Further discussion on the 3D flow migration and impact on the BL, surface Nu, and wake mixing for the blade is discussed in the next section.

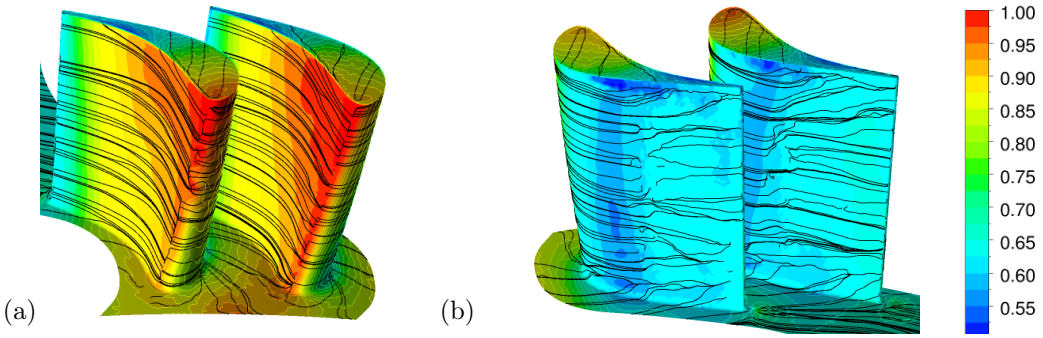

Figure 8-7. Blade IDDES-T instantaneous surface streamlines (a) forward looking aft and (b) aft looking forward with surface contours of instantaneous $p/Ptr_{2-50\%span}$.

8.3 3D Geometry Impact

The endwall contribution to the developing 3D flow field through the vane is now examined along with the impact on downstream blade. Figures 8-8 and 8-9 present both the loading and heat transfer along the 3D vane. Loading is found to be in good agreement across all turbulence modeling approaches, where slight variation is found near the throat at 10, 50, and 90% span. The vane physical throat increases with span. This agrees with the lowest SS TE Mach number found at 90% span. In addition, Figure 8-3 had previously shown the surface pressure distribution on the SS surface, where the pressure is found to increase radially driving the flow migration along the vane surface.

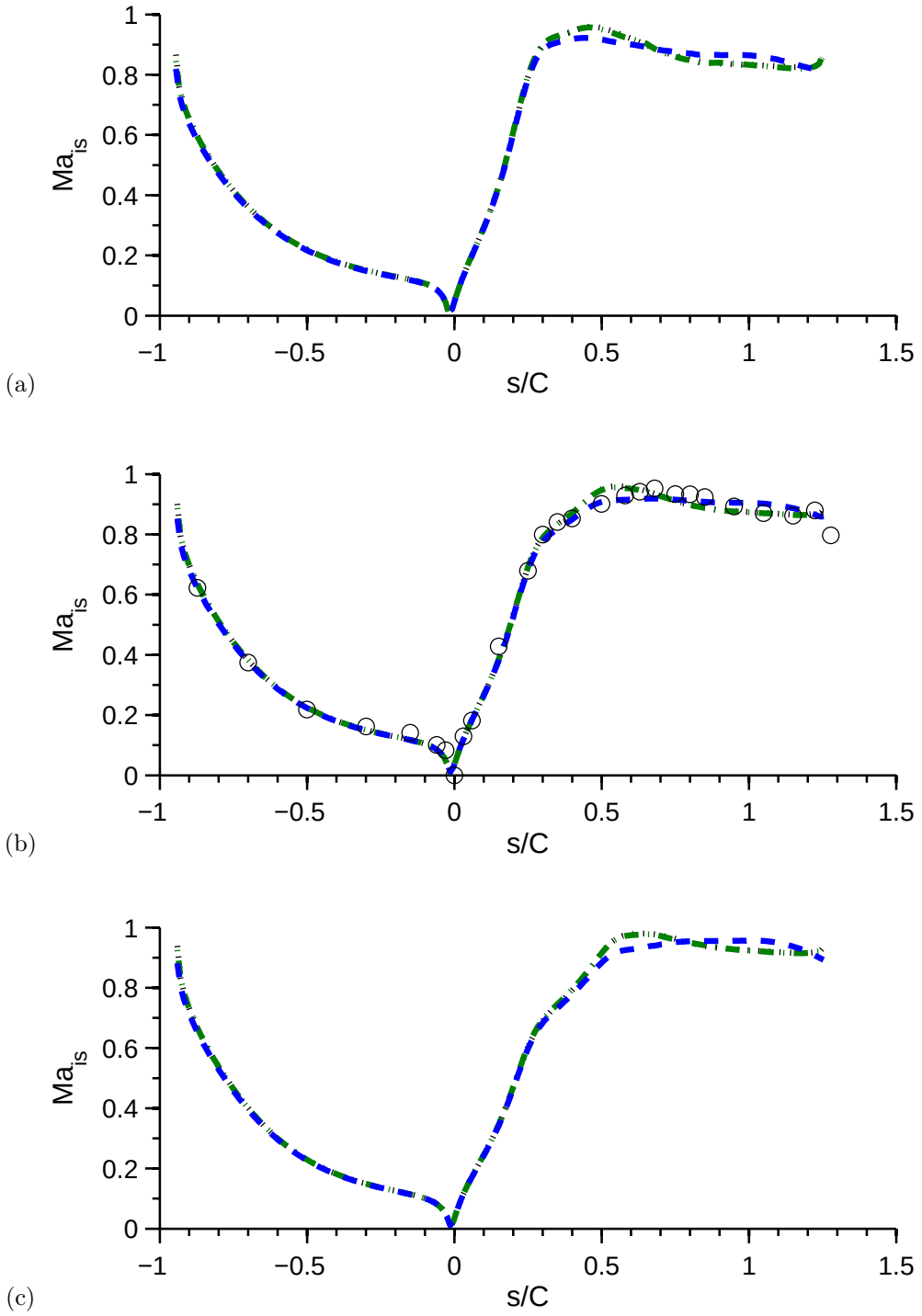

Figure 8-8. 3D vane loading at (a) 90%, (b) 50%, and (c) 10% span for sliding mesh IDDES-T (- - -) compared to vane only SST-T (· - ·) and SST (· · ·) with no vane inlet turbulence.

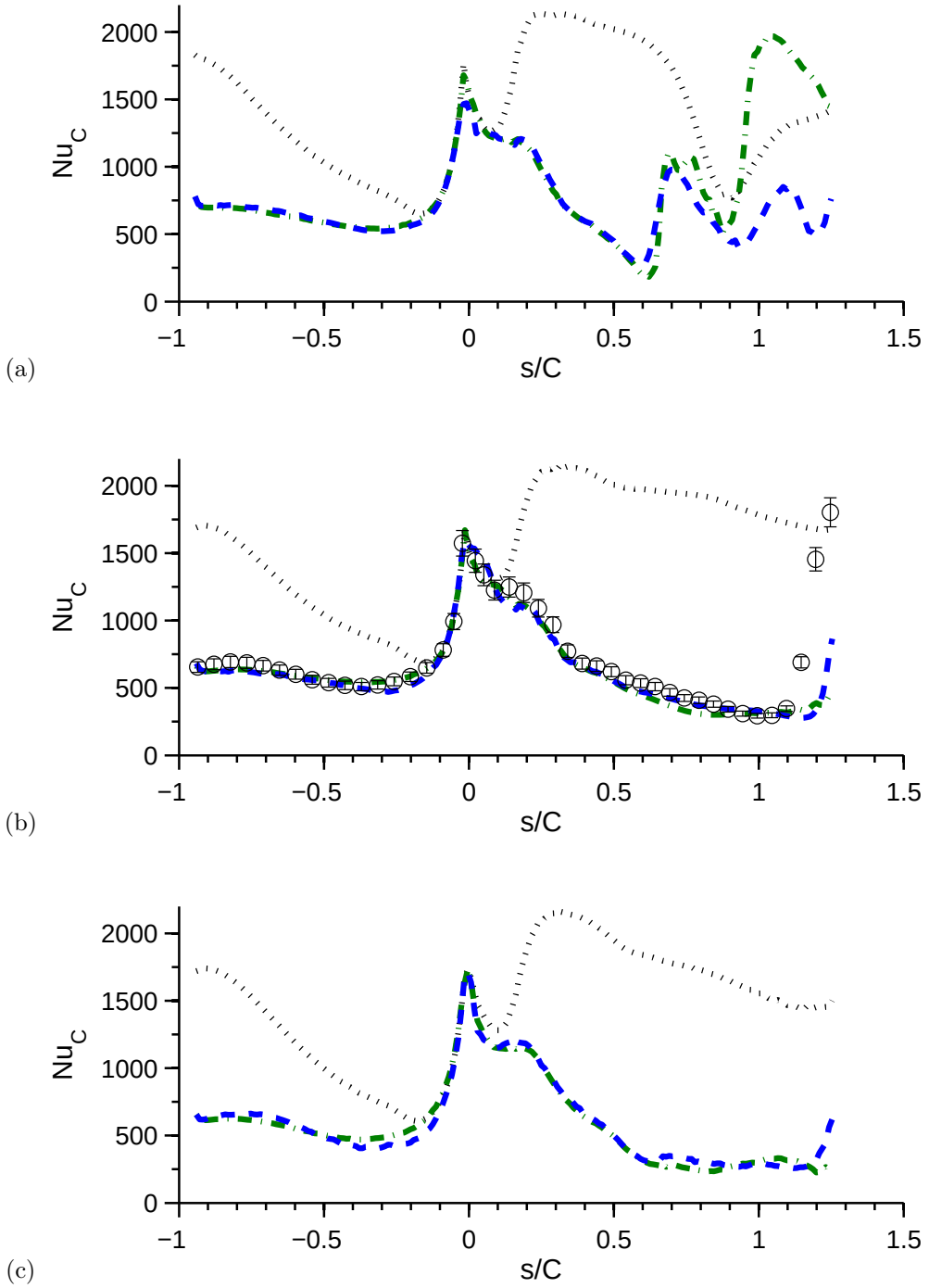

Figure 8-9. 3D vane mean Nu at (a) 90%, (b) 50%, and (c) 10%, span for sliding mesh IDDES-T (- - -) compared to vane only SST-T (· - ·) and SST (· · ·) with no vane inlet turbulence.

The heat transfer along the PS surface is in close agreement between SST-T and IDDES-T. Strong differences are noted on the SS at 90% span, near the outer band. This is due the difference in the strength of the passage vortex between SST-T and IDDES-T. The horseshoe vortex first develops at the LE in the fillet region between the vane and outer band. The impact can be visualized on the vane and endwall surface in Figure 8-10 where an elevated Nu is found at the LE outer band fillet due to the horseshoe vortex. As the vortex wraps around the PS, it enters the vane passage where it migrates to the SS of the adjacent vane due to the PS to SS passage pressure gradient. This also interacts with the LE vortex that wraps around the SS of the adjacent vane. The secondary flow interaction is found visually on the SS of the vane outer span surface where the Nu is locally elevated for SST-T and IDDES-T. The strength of the passage vortex for IDDES-T by the time it reaches the SS surface is minimized relative to SST-T where a 40% lower local Nu is predicted for IDDES-T. Another local spike in Nu is found downstream of the vane TE on both endwalls. This is due to the turbulent flow field generated downstream of the vane wake. IDDES-T predicts a smaller region of elevated Nu leading to a lower thermal gradient at the endwall surface.

The total pressure wake profile is plotted in Figure 8-11 for 10, 50, and 90% span. The profile is normalized to the inlet total pressure at 50% span. IDDES-T is found to have a lower total pressure outside the wake compared to SST and SST-T, showing the additional penetration of mixing loss into the core flow due to the scale-resolved approach. At 50% span, RANS is found to over-predict wake depth and under-predict wake spreading consistent with previous findings on the linear pitch-line geometry. Further deviation is found at 10 and 90% span due to the less mixed out secondary flow contribution to loss predicted by both SST and SST-T. A higher level of TI is predicted for IDDES-T which is contributing to the spreading and decay of the passage secondary flow and its contribution to the vane exit total pressure loss profile. As much as a 2X increase in wake depth is predicted for SST-T compared to IDDES-T at 10% span. For the pitch-line studies in Chapter 6, the WALE predictions were used to show anisotropic TI in the wake where the SST model assumes isotropic

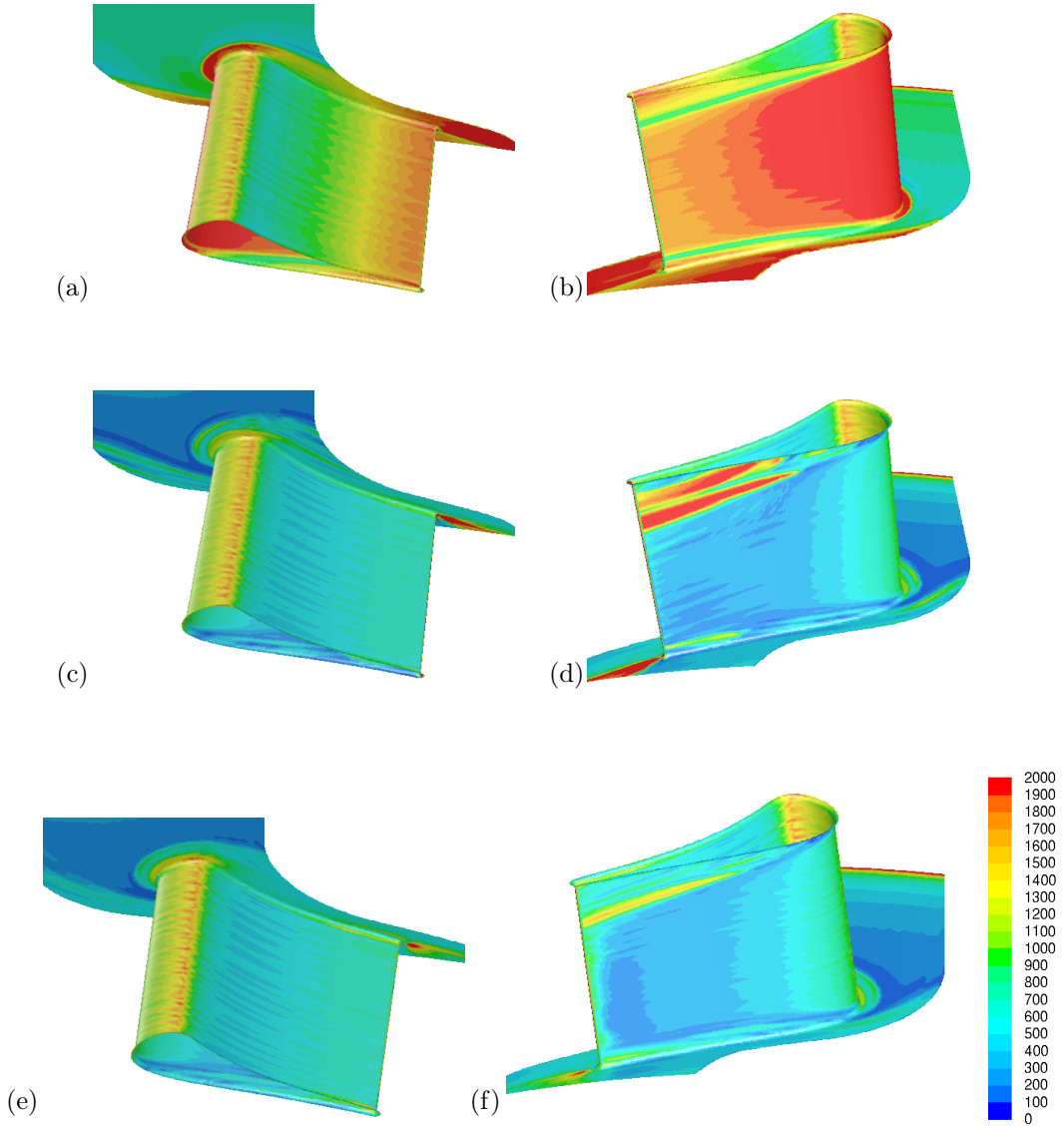

Figure 8-10. Vane SST mean Nu (a) forward looking aft and (b) aft looking forward. SST-T Nu (c) forward looking aft and (d) aft looking forward. IDDES-T Nu (e) forward looking aft and (f) aft looking forward.

turbulence. The addition of secondary flow has been shown to further violate the SST assumption of isotropic TI [89].

Figure 8-13 presents contour plots of normalized total pressure at $X/C_{ax} = 1.14$ downstream of the TE of the vane. The total pressure is normalized based on the circumferentially averaged value at the 50% span at the inlet. As with the 2DSM simulations, the IDDES-T show a wider and more mixed out wake. The figure clearly

shows significant differences in the size and shape of the vane wake. Both the mean and instantaneous total pressure and TI wakes are presented for IDDES-T. The non-uniform turbulent structure qualitatively show the turbulence is not isotropic. The increased spread for the wake for IDDES-T compared to SST and SST-T is shown from the inner to outer span. The passage vortex can be clearly identified for the SST and SST-T predictions near 10% and 90% spans. The strength of the vortex decrease from SST to SST-T is due to the contribution of the different BL state. The strength of the passage vortex is greatly reduced for the IDDES-T prediction due to the mixing of the resolved TE wake shedding and the secondary flow. Not surprisingly, high regions of TI are associated with high regions of loss.

Figures 8-14 and 8-15 present both the loading and heat transfer along the 3D blade. The stagnation point ($s/C = 0$) is at the same physical location on the blade for each radial position, confirming consistent flow incidence for each turbulence modeling approach. For each model, the loading on both the suction and pressure side surface varies as a function of radius due to radial migration and turning in the blade. The blade mechanical turning increases with decrease in span. This is due to the blade relative inlet incident angle decreasing with increasing span to adjust for the higher tangential speed at the tip of the blade. The blade TE is linearly stacked so the mechanical exit angle is held constant resulting in larger turning at the root of the blade. The loading and heat transfer for SST-T and IDDES-T at 50% span are nearly identical, with differences on the suction side surface after the throat. The same results were found for the pitch-line comparison of the SST-T and IDDES-T predictions. However, it was found that a significant amount of the total TI is contributed by the resolved unsteadiness that doesn't directly contribute to the transport equations for the transition model. Therefore, the SS surface Nu after the throat for the IDDES-T model is expected to be under-predicted by nearly 2X based on the WALE pitch-line predictions for zero stage inlet TI in Chapter 6.

The impact of the secondary flows on surface Nu can be visualized on the blade and inner endwall surface in Figure 8-10 where an elevated Nu is found at the LE due the horseshoe vortex. As the vortex wraps around the LE, the secondary flow

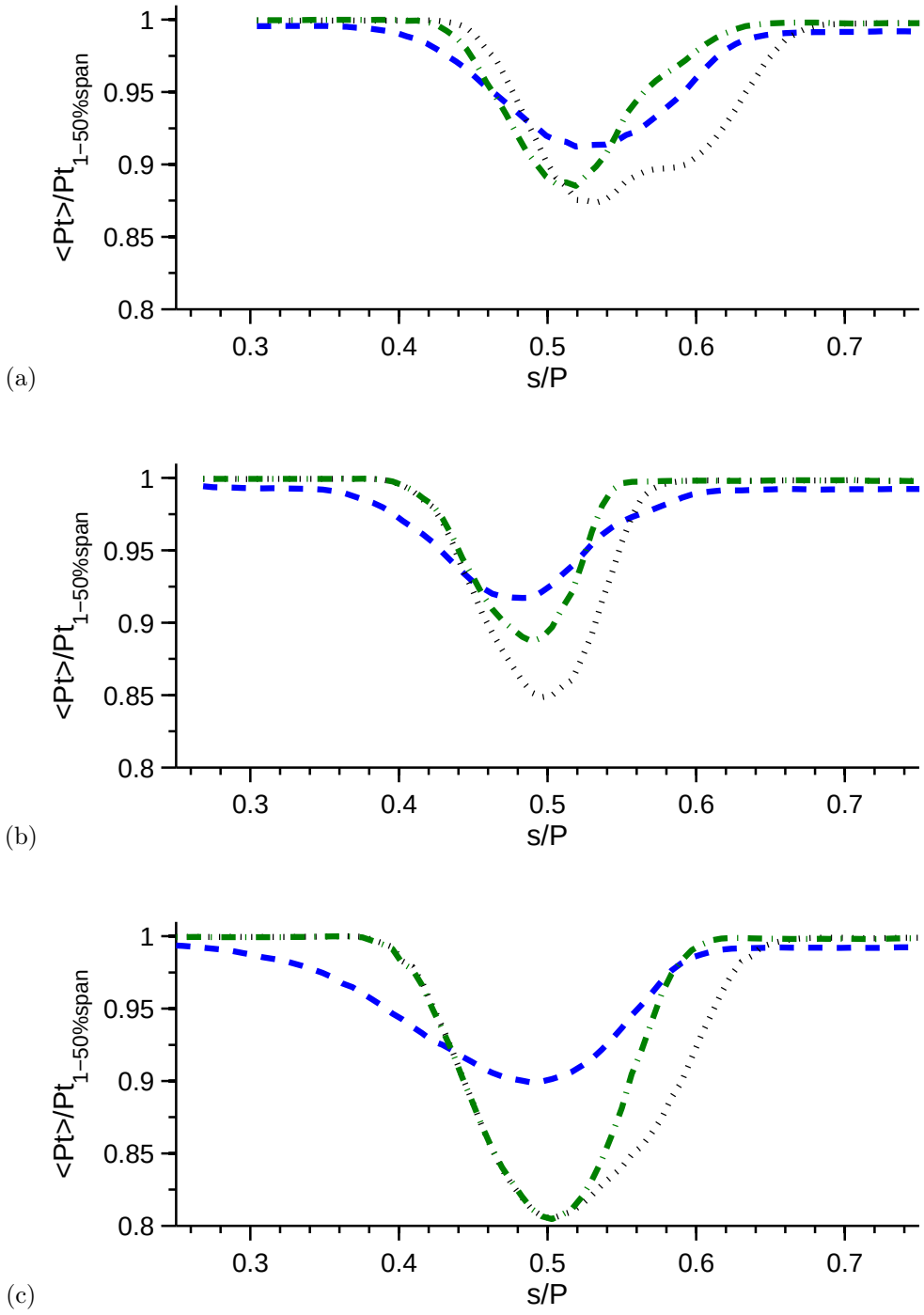

Figure 8-11. 3D vane normalized mean total pressure at $X/C_{ax} = 1.14$ from the vane LE at (a) 90%, (b) 50%, and (c) 10%, span. Sliding mesh IDDES-T (- - -) compared to vane only SST-T (· - ·) and SST (· · ·) with no vane inlet turbulence.

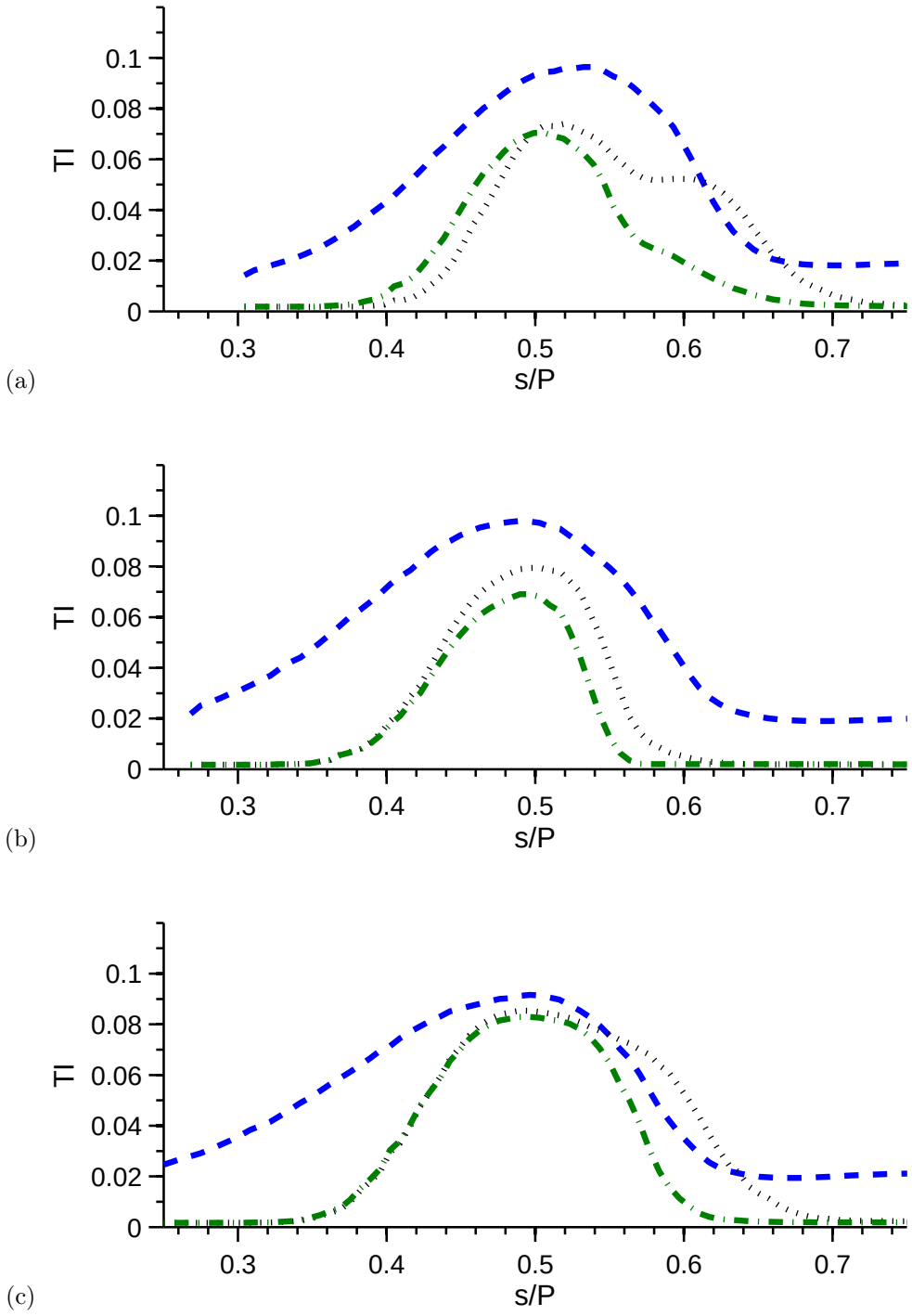

Figure 8-12. 3D vane local TI at $X/C_{ax} = 1.14$ from the vane LE at (a) 90%, (b) 50%, and (c) 10% span. Sliding mesh IDDES-T (- - -) compared to vane only SST-T (· - ·) and SST (· · ·) with no vane inlet turbulence.

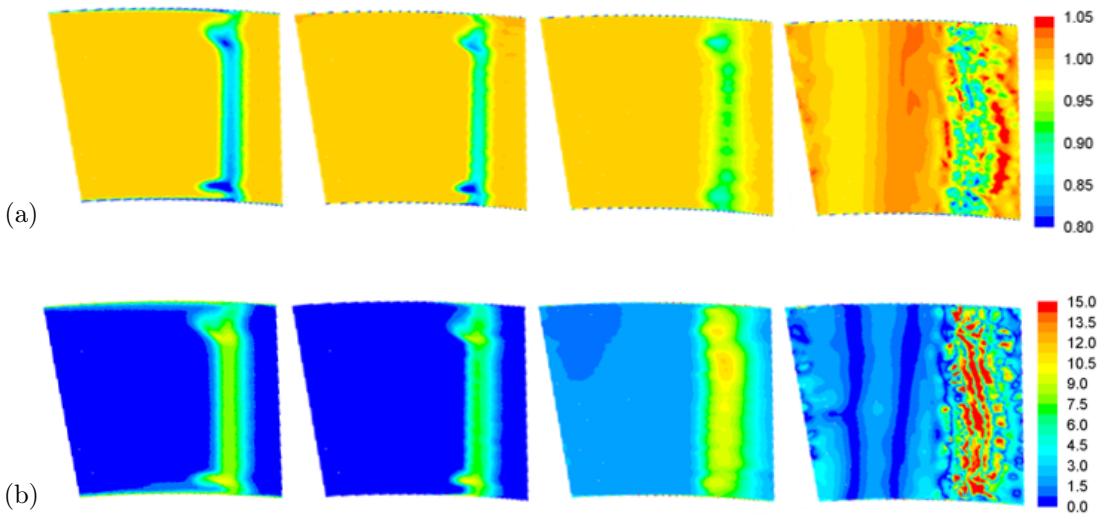

Figure 8-13. 3D vane (a) normalized total pressure and (b) local TI at $X/C_{ax} = 1.14$ from the vane LE. RANS, RANS-T, HLES-T, and instantaneous HLES-T from left to right.

interaction is found visually on the SS of the blade near 10% span on the SS surface. The strength of the passage vortex for IDDES-T by the time it reaches the SS surface is minimized relative to SST-T. The major contribution for secondary flow on the blade surface Nu is found around 80% and up on the SS surface. This is due to the tip vortex developing due to the blade tip gap. IDDES-T predicts a significant reduction in the impact of the tip vortex on the SS surface Nu. The wake profiles highlighting the vortex location and strength are now discussed.

The blade relative total pressure wake profile is plotted in Figure 8-17 for 10, 50, and 90% span. The profile is normalized to the inlet relative total pressure at 50% span. Overall, the SST and SST-T models predict similar wake profiles at each span location. This is due to the similar SS BL state and secondary flow development as suggested by the Nu line (Figure 8-15) and contour (Figure 8-16) plots for the blade. At 50% span, RANS is found to over-predict wake depth and under-predict wake spreading similar to the pitch-line results. Further deviation between models are found at 10 and 90% span due to the higher secondary flow contribution to loss predicted by both SST and SST-T.

In order to further understand the flow field, Figure 8-19 presents contour plots of

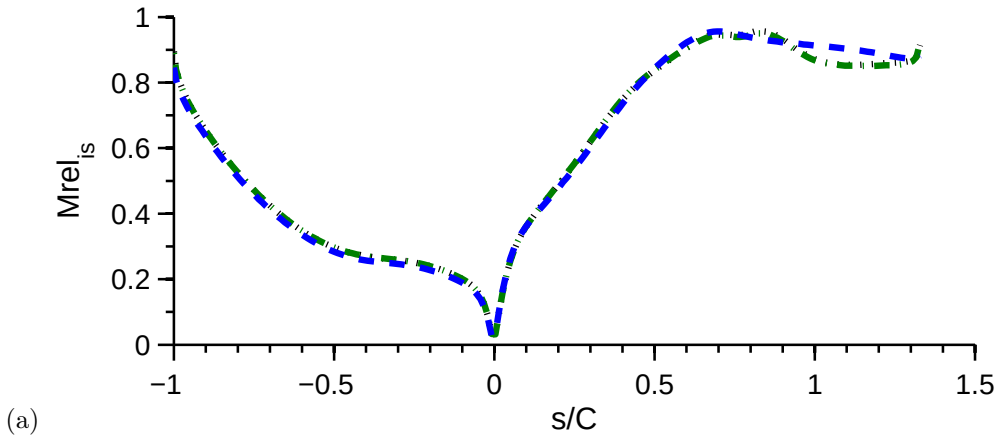

(a)

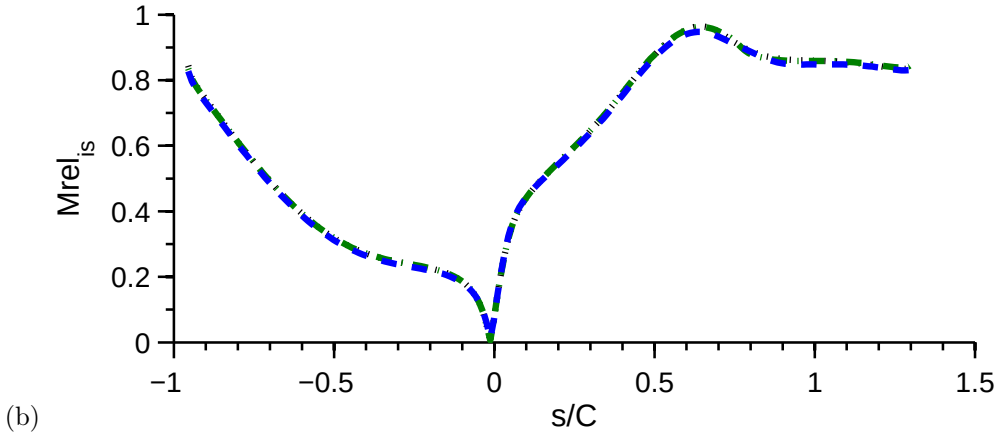

(b)

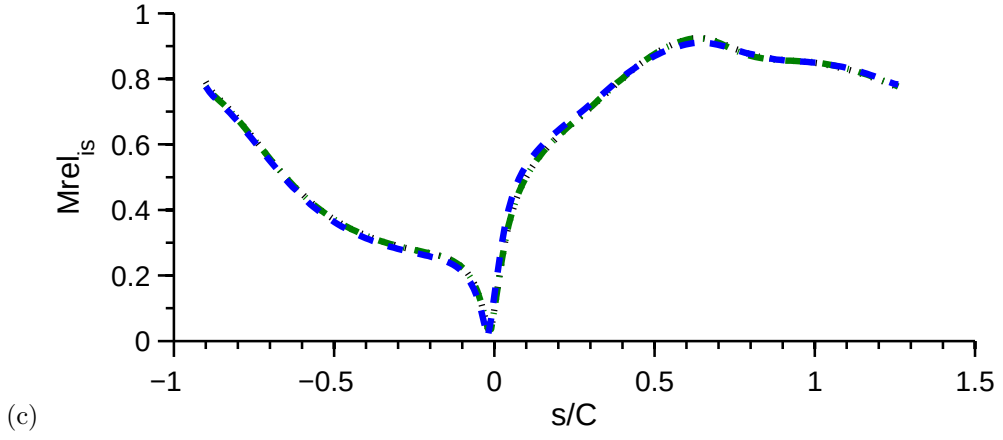

(c)

Figure 8-14. 3D vane loading at (a) 90%, (b) 50%, and (c) 10% span for sliding mesh IDDES-T (- - -) compared to vane only SST-T (· - ·) and SST (· · ·) with no vane inlet turbulence.

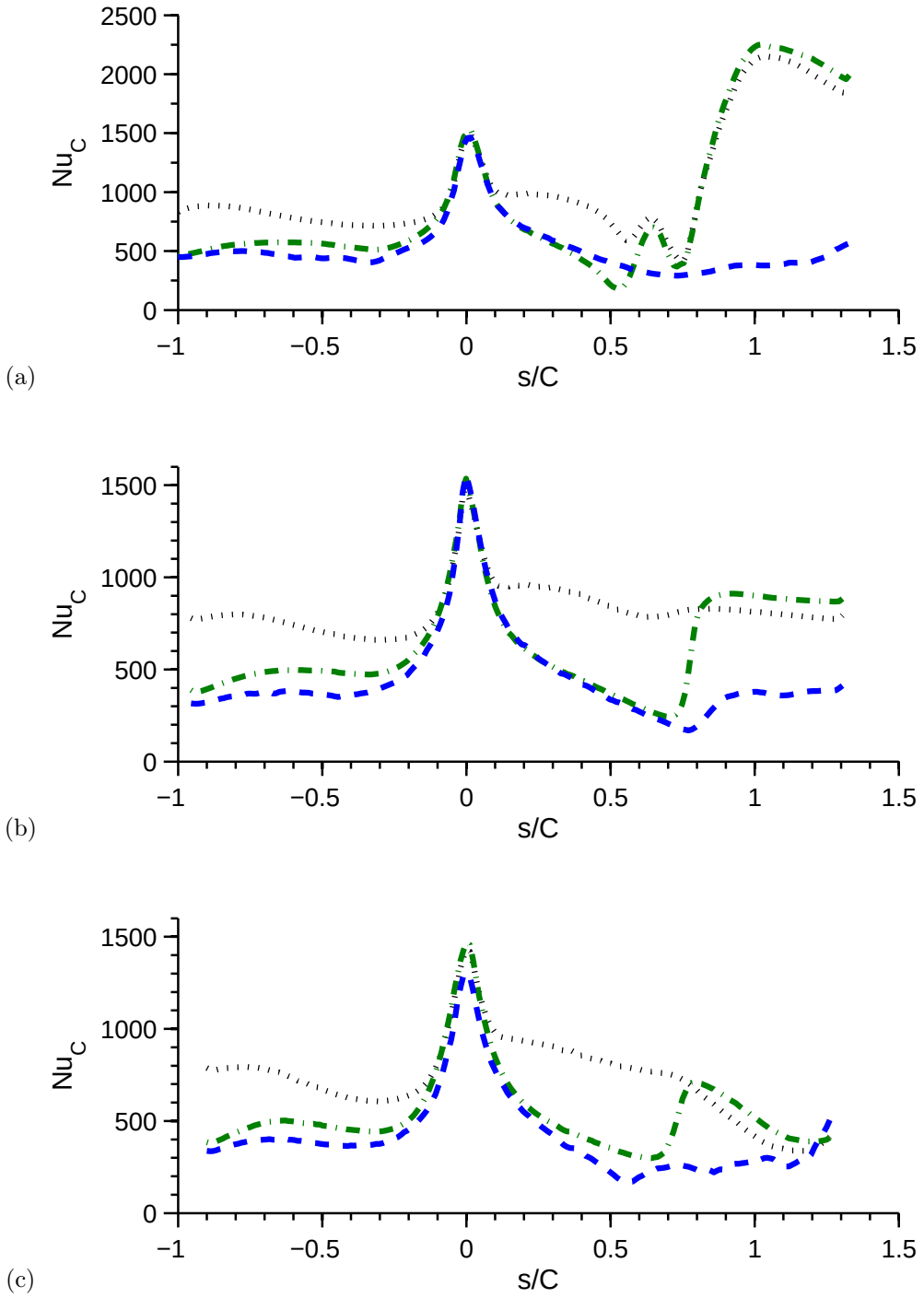

Figure 8-15. 3D vane mean Nu at (a) 90%, (b) 50%, and (c) 10% span for sliding mesh IDDES-T (- - -) compared to vane only SST-T (· - ·) and SST (· · ·) with no vane inlet turbulence.

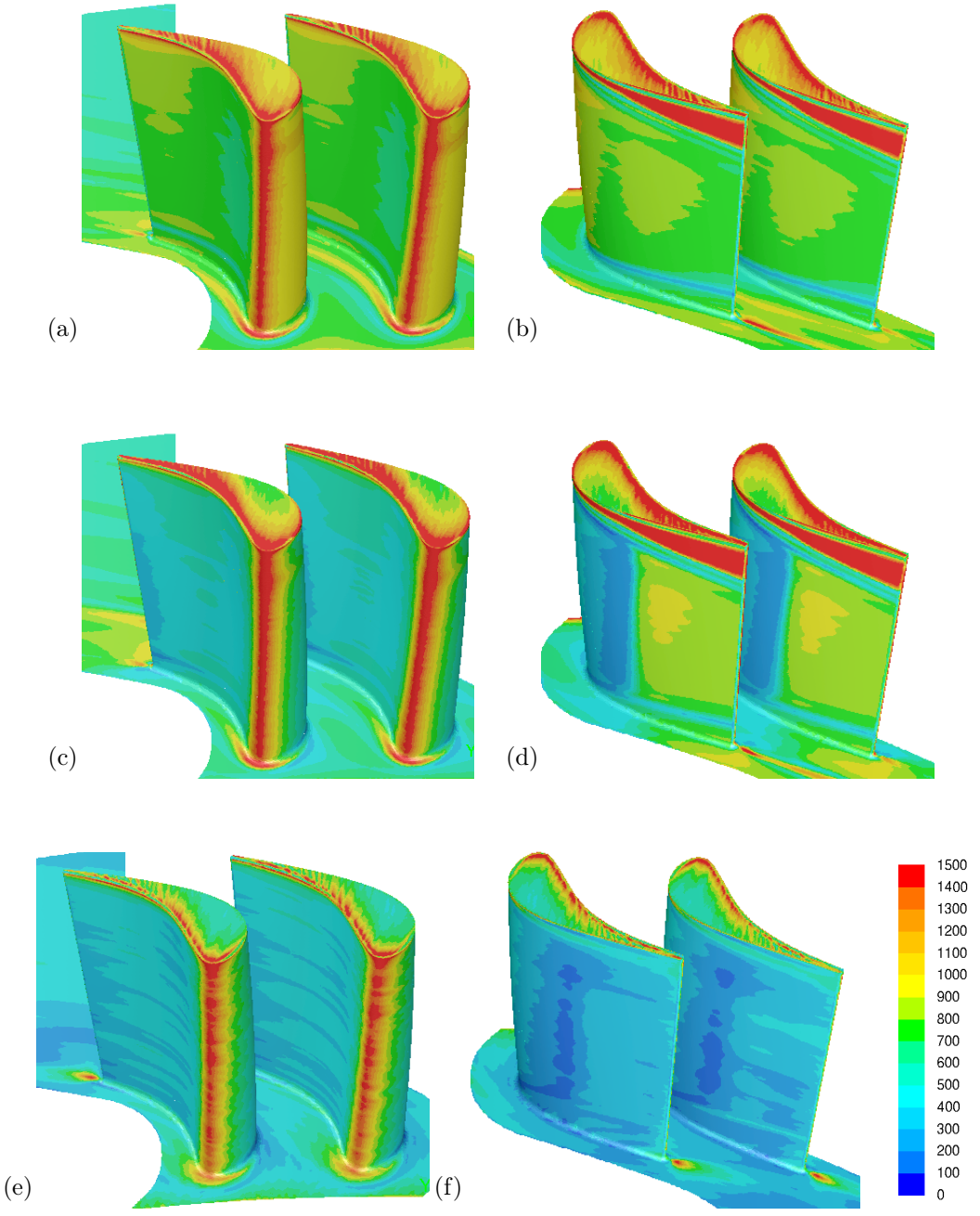

Figure 8-16. Blade SST mean Nu (a) forward looking aft and (b) aft looking forward. SST-T Nu (c) forward looking aft and (d) aft looking forward. IDDES-T Nu (e) forward looking aft and (f) aft looking forward.

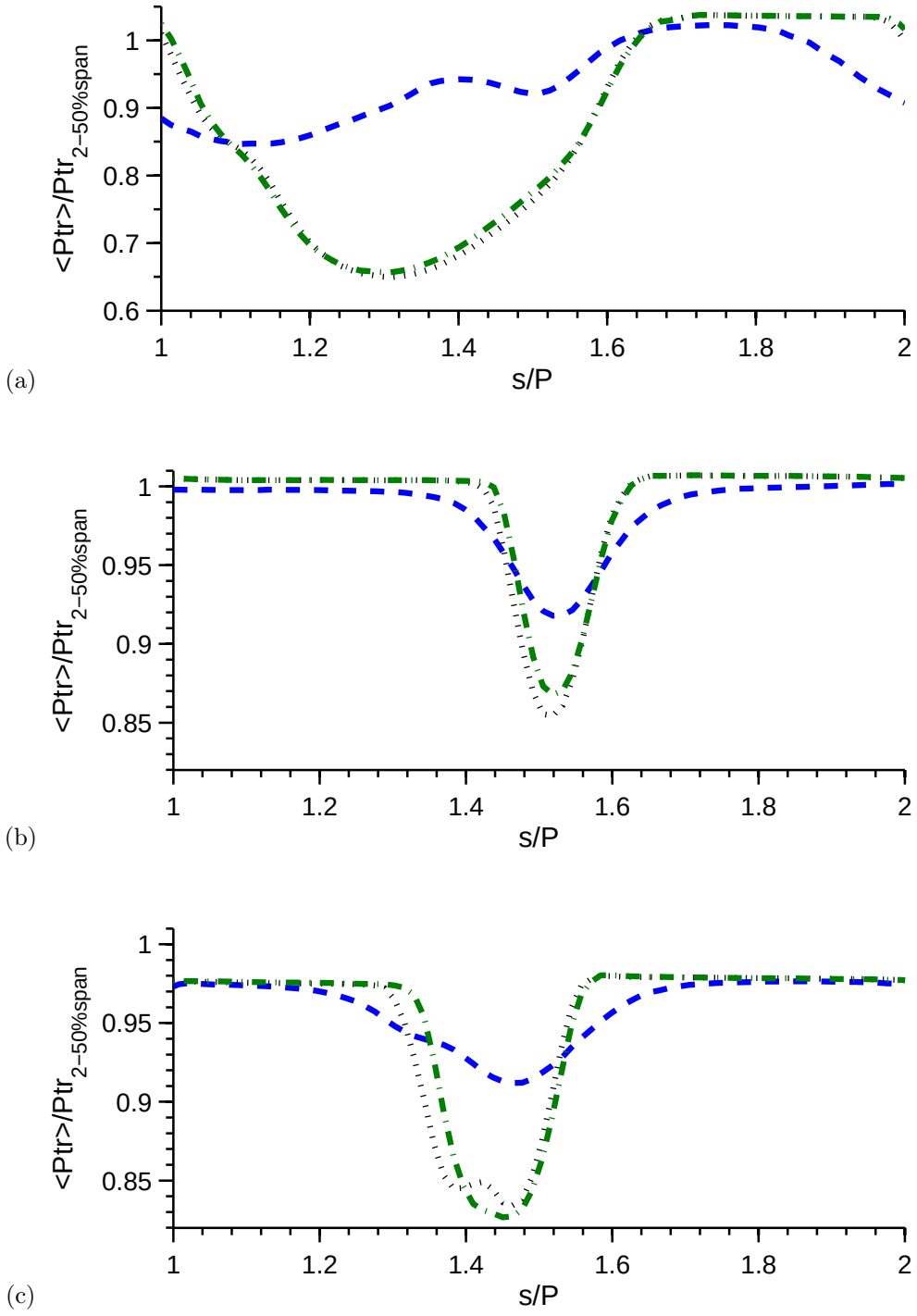

Figure 8-17. 3D vane normalized mean total relative pressure at $X/C_{ax} = 1.17$ from the blade LE at (a) 90%, (b) 50%, and (c) 10% span. Sliding mesh IDDES-T (- - -) compared to vane only SST-T (· - ·) and SST (· · ·) with no vane inlet turbulence.

normalized relative total pressure. The plane is shown at $X/C_{ax} = 1.17$ downstream of the TE of the blade. The total pressure is normalized based on the circumferentially averaged value at the 50% span at the inlet in order to be consistent with the 2DSM simulations discussed previously. As with the 2DSM IDDES-T simulations, the 3DSM shows a wider and more mixed out wake. The figure clearly shows significant differences in the size, shape, location and strength of the tip vortex. SST and SST-T predicts the largest radial penetration of the tip vortex, followed by IDDES-T. The SST and SST-T simulations show the tip vortex extending 50% further into the flowpath then the IDDES-T results. Not surprisingly, high regions of TI are associated with high regions of loss for each model. Near the inner endwall the horseshoe vortex is seen to be much stronger for SST and SST-T than for IDDES-T. Energy separation is found for the blade wake where instantaneous snapshots of non-dimensional total pressure show locations of where values exceed 1.0 [17].

In a shear layer, energy separation due to the imbalance of shear work and heat conduction are small relative to pressure fluctuations found in the wake. Figure 8-18 shows a schematic of the transient pressure change in the trailing-edge wake for the uncooled blade. The front half of the vortex corresponds to a positive dp/dt, where the fluid is gaining energy. The latter half of the vortex corresponds to a negative dp/dt, where the fluid is losing energy. Therefore, local maximums and minimums of the total pressure are found in the outer and center regions of the wake, respectively. These local total pressure regions are found in Figure 8-13a and 8-19a for the vane and blade respectively.

It was found that SST and SST-T predicts a significantly different shape of the tip vortex rolling up relative to IDDES-T. Figure 8-20 shows the impact of the 0% inlet TI and resulting BL state on the formation of the tip vortex for the SST-T model. When the blade inlet TI is set to 0% the SST-T tip vortex more closely matches the IDDES-T tip vortex structure. For the SST-T simulation, it is found that the state of the boundary layer greatly impacts the "detachment" of the tip vortex from the SS surface which directly impacts the magnitude of the Nu at 90% span. This is a significant change in the flow field due to a change of less than 4% in blade inlet TI

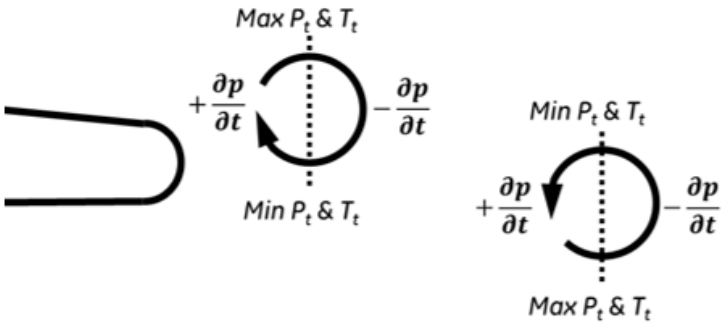

Figure 8-18. Schematic of energy separation due to vane or blade TE vortex shedding.

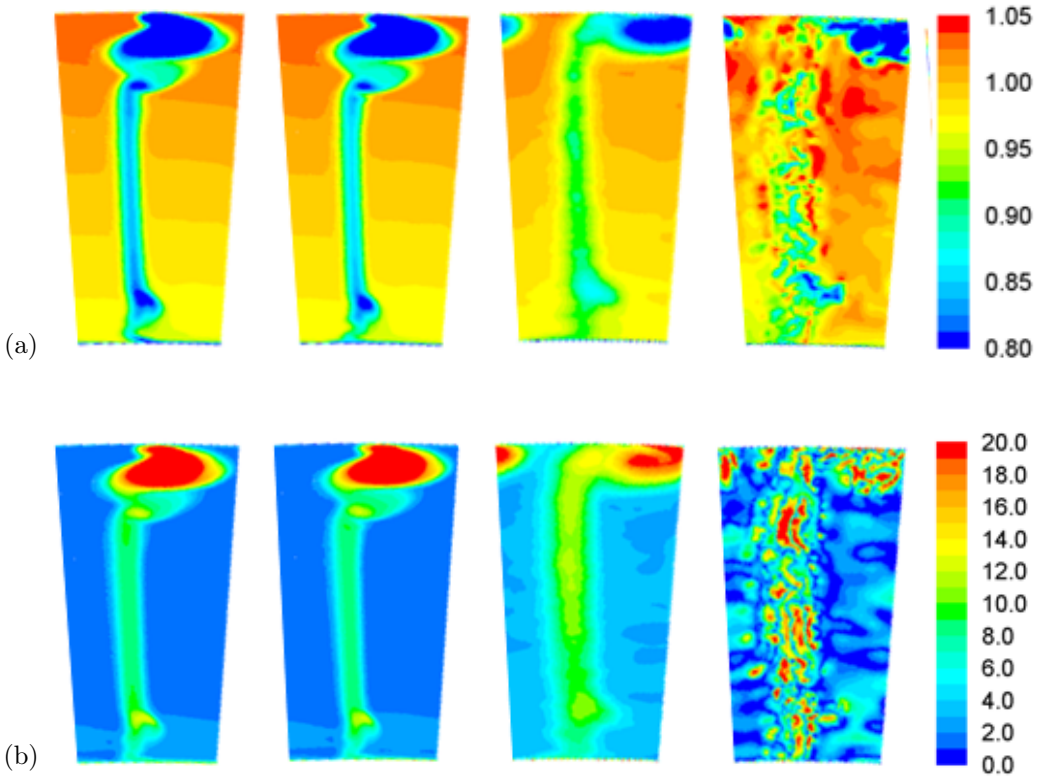

Figure 8-19. 3D blade (a) normalized total relative pressure and (b) local TI at $X/C_{ax} = 1.17$ from the blade LE. RANS, RANS-T, HLES-T, and instantaneous HLES-T from left to right.

for the SST-T model.

Finally, a summary of the predicted stage losses are provided in Table 8.1 for IDDES-T and Table 8.2 for SST-T. The losses for the 3D geometry are compared to the linear pitch-line to quantify the contribution in loss due to secondary flow and

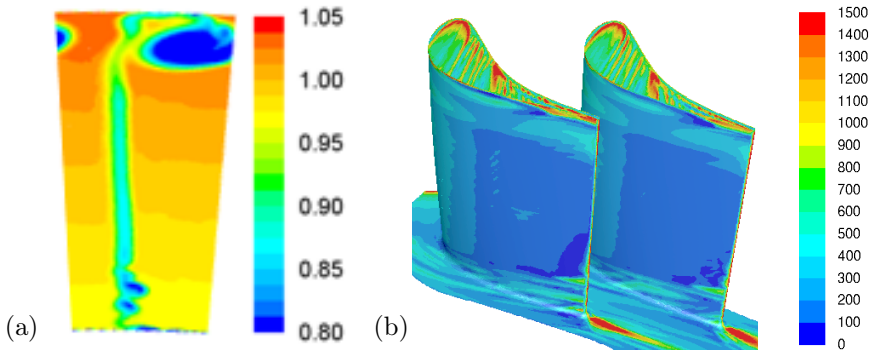

Figure 8-20. 3D blade SST-T (a) normalized total relative pressure at $X/C_{ax} = 1.17$ from the blade LE and (b) mean Nu forward looking aft. No blade inlet TI.

rotation effects. Based on the IDDES-T predictions, the 3D effects contribute to an increase of 0.76% plane mass averaged loss relative to the pitch-line case. Contribution of the passage vortex to the overall vane loss was clearly shown in the contours of the normalize total pressure profile and contour plots at the vane exit. The blade plane mass average loss increases by 1.6% due to the 3D effects. This is largely driven by the tip vortex that is a function of the tip clearance of the blade. The current geometry tip clearance is 10% of the blade height.

Table 8.1. IDDES-T mass plane average vane total pressure loss, $1 - \langle Pt \rangle / Pt_1$, at $X/C_{ax} = 1.14$ from the vane LE. Mass plane average blade relative total pressure loss, $1 - \langle Ptr \rangle / Ptr_2$, at $X/C_{ax} = 1.17$ from the blade LE for 2DSM and 3DSM.

IDDES-T	Vane: $1 - \langle Pt \rangle / Pt_1$	Blade: $1 - \langle Ptr \rangle / Ptr_2$
2DSM	1.04%	1.50%
3DSM	1.80%	3.10%

The SST-T predictions for overall loss are found to be in close agreement with IDDES-T for the liner pitch-line results for the vane and blade. This is not the case for the 3D geometry. Large differences are found in the secondary flow regions contributing to the deviation in loss prediction for the SST-T and IDDES-T model. The loss for the 3D case are predicted to be 0.47% less and 0.65% more for the SST-T model relative to the IDDES-T predictions.

Table 8.2. SST-T mass plane average vane total pressure loss, $1 - \langle Pt \rangle / Pt_1$, at $X/C_{ax} = 1.14$ from the vane LE for 2DVO and 3DVO. Mass plane average blade relative total pressure loss, $1 - \langle Ptr \rangle / Ptr_2$, at $X/C_{ax} = 1.17$ from the blade LE for 2DBO and 3DBO.

SST-T	VO: $1 - \langle Pt \rangle / Pt_1$	BO: $1 - \langle Ptr \rangle / Ptr_2$
2D	1.03%	1.60%
3D	1.33%	3.75%

Due to the selected modeling approach the overall aero-thermal uncertainty due to the IDDES-T or SST-T approach can be quantified. The turbine stage efficiency equation is

$$\eta_t = \frac{Tt_1 - Tt_3}{Tt_1 - Tt_{3s}} \tag{8.1}$$

assuming constant specific heat, Tt_{3s} is the isentropic total temperatures at the stage exit. Tt_1 and Tt_3 are the total temperatures at the inlet and exit of the stage, respectively [88]. This is used to provide a level of uncertainty in the stage efficiency due to the modeling approach. The $\Delta\eta_T$ between IDDES-T and RANS-T is about 3%. The thermal impact can be quantified by applying an energy balance to determine the internal vane or blade cooling flow variation due to the given predicted external heat flux. The energy balance equation is

$$q = \dot{m} c_p (\Delta T_c) \tag{8.2}$$

where q is the overall heat flux on the vane or blade surface, $\dot{m}$ is the internal cooling flow rate for the vane or blade, c_p is the constant specific heat, and ΔT_c is the increase in the internal cooling flow temperature [90]. Assuming ΔT_c remains constant, the cooling flow rate is proportional to the change in surface heat flux necessary to maintain the same vane or blade bulk temperature. The vane and blade surface total area averaged heat flux is calculated from the IDDES-T and SST-T predictions. The total heat flux ratio for IDDES-T divided by the SST-T predictions are 0.95 for the vane and 0.71 for the blade. This results in a 5% and 29% uncertainty in cooling flow for the vane and the blade between the two modeling approaches, respectively.

Chapter 9

Conclusion

Simulations have been used to systematically understand the impact of turbulence and the uncoupled and coupled vane/blade interaction on BL development, resulting heat transfer, and downstream wake mixing in the absence of cooling. Leading up to these studies, a building block approach was taken to gain confidence in the modeling method and understand the accuracy to computational cost trade-off of RANS, HLES, and LES modeling approaches.

Chapter 3 presented evaluations of different turbulence modeling approaches conducted on a cylinder in cross-flow under low Mach and Reynolds number conditions. Scale-resolved approaches were demonstrated using an unstructured mesh of tetrahedral and prism elements with second-order spatial and temporal schemes in Fluent. WALE predictions compared to PIV measurements of Konstantinidis et al. [71] were found to be within the experimental uncertainty for first-order and second-order statistics with the exception of u'^2 at $X/D = 0.7$. Provided the established meshing approach and resolution, equivalent accuracy was demonstrated for the unstructured and structured meshing approaches. The WALE model was used to demonstrate the anisotropic behavior in the wake and the SST model deficiency due to the isotropic turbulence assumption. Next, the IDDES model was able to provide mean flow predictions within the experimental uncertainty with the exception of $X/D = 1.5$. The cross-stream fluctuating velocity prediction was within $1.5X$ of the experimental uncertainty at locations $X/D = 1.5$ and 2.0. All other locations are within experimental

uncertainty for IDDES. These flow conditions and simple geometry facilitated quick turn-around for modeling assessment before moving the HPT vane study at high Re and Mach number conditions.

A key motivation for the current work was to understand the capability of executing scale-resolved simulations with a second-order code on a mesh of prisms and tetrahedral. Established meshing practices for wall-resolved LES for boundary layers were initially considered. However, in support of this work, additional near-wall mesh studies have been executed to access the accuracy of LES and HLES modeling approaches for a second-order code using prisms and tetrahedral elements. Robust meshing approaches must be able to resolve complex HPT geometry while maintaining mesh quality adequate for scale-resolved simulations. Therefore a robust solver and meshing approach was assessed to determine any compromises in accuracy. The accuracy of LES using an unstructured mesh of prisms and tetrahedral with the second-order commercial solver Fluent was compared to the structured high-ordered solvers FDL3DI as part of an ongoing effort at GE [49, 50]. Relative to FDL3DI, Fluent WALE results were found to be within the equivalent experimental uncertainty provided adequate mesh resolution and quality. This gave validity to the current LES modeling approach to assess the impact of turbulence and the uncoupled and coupled vane/blade interaction on BL development, resulting heat transfer, and downstream wake mixing. In addition, modeling sensitivities were completed for RANS, HLES, and LES modeling approaches establishing clear guidelines for mesh resolution, domain extent, time step selection, and convergence criteria.

Computational modeling approaches were then assessed for accuracy relative to the HPT uncooled vane experimental studies of Arts and Rouvroit [34]. Previous studies have evaluated the impact of low (0-6%) free-stream turbulence on Nu. This was the first computational study to expand to high-level TI to provide an understanding of the impact on BL development, surface heat flux, and the resulting wake formation, evolution, and decay. In addition, when compared to LES computational cost reductions of 100X and 4X were found for RANS and HLES approaches, respectively. The current study used turbulence length scale and decay provided by

Arts [76] and WALE predictions to properly characterize the inlet turbulence. These results were also used to determine the inlet k and ω inlet conditions for the SST and SST-T models. The SST and SST-T models were found to be inadequate in the prediction of boundary layer, surface heat flux, wake total pressure, and TI development. SST-T was only found to provide accurate predictions of Nu at low TI levels. Overall, SST and SST-T approaches were unable to predict trends due to varying Re and TI that would be desired for industrial design.

WALE was found to provide accurate predictions of all flow field quantities. The approach was found to be within the equivalent of 2X the experimental uncertainty for the total pressure wake, providing confidence in the Fluent WALE predictions and further use of the results as a benchmark for RANS and HLES results. The largest variation in surface Nu was found for the SS BL transition point. However, the transition point was found to be extremely sensitive to small variations in free-stream TI (4-6%). An example of this was where LES predictions run at TI=6% fell within 2X experimental uncertainty when compared to experimental measurements made at TI=4%. The unknown contributions of surface roughness was also noted as possible contributors to the difference in Nu prediction and measurement. Finally, the IDDES-T model was able to provide an alternate approach from WALE at 4X cost reduction. IDDES-T was found to be within the equivalent of 2X the experimental uncertainty for wake total pressure. This provided justification for the IDDES-T model as it reduced cost while maintained accuracy.

Next, the impact of 0 and 20% inlet turbulence was assessed for SST, SST-T, IDDES-T, and WALE for the vane. IDDES-T and WALE showed that free-stream of $TI = 20\%$ results in Nu increased up to 2X for the PS surface. However, the BL had a mean laminar profile where the non-zero RMS velocity led to an elevated Nu. The SS surface for inlet $TI = 0\%$ showed clear transitioning of the thermal BL near the TE. This was not seen for $TI = 20\%$ where the Nu was steadily rising. After the vane throat, an adverse pressure gradient was seen by the flow where a turbulent BL developed. At $TI = 20\%$ and in regions of high flow acceleration, thermal boundary layers were found to be 5X thicker than the velocity BL. This same dependency

was experimentally measured by Dees [87] under similar Re but low Mach number conditions.

Chapter 7 focused on stage interaction of the vane/blade for a pitch-line section. A downstream blade was designed to be coupled with the upstream uncooled vane of Arts and Rouvroit [34]. The level of stage inlet TI was found to have a larger impact on the vane than the downstream blade. The impact of stage inlet TI is found to be secondary compared to the periodic unsteadiness generated by the vane wake on the downstream blade surface heat transfer and mixing. Due to the high-level TI, the vane saw on the order of a 1.5X increase in surface Nu. However, the blade saw an almost negligible impact for Nu. Less than 5% increase in PS surface Nu was found for the higher inlet stage TI level and no change in LE Nu was found based on IDDES-T predictions. The suction side showed the same transition location, where after transition began, the absolute Nu was again within 5% between the two stage inlet TI levels. The transition location was found after the throat in the region of the adverse pressure gradient. However, it was found that a significant amount of the total TI is resolved which doesn't directly contribute to the modeled kinetic energy used by the transition model transport equations. Therefore the SS surface Nu after the throat for the IDDES-T model was expected to be under-predicted by nearly 2X based on the WALE predictions for zero stage inlet TI. Overall the blade exit profiles for 0 and 20% stage inlet TI were found to have similar depth and spread where the loss contribution of higher stage inlet TI was seen in the passage between the blade TE wakes. A 0.16% mass average increase in loss across the blade was found due to an increased loss found in the core of the flow due to the higher passage TI.

Ultimately, the goal was to better understand the impact of turbulence on a 3D engine centerline stage design with axisymmetric endwalls and a blade tip clearance. Comparison back to the linear pitch-line stage geometry was done to isolate the impact on loss generating mechanisms (i.e. profile and wake mixing) and thermal loading due to endwall secondary flows and rotational effects. First modeling approaches were compared between IDDES-T, SST-T, and SST. Overall, IDDES-T predicted a faster decay rate for secondary flow through the vane and blade passage compared to

SST and SST-T predictions. For example, the modeling approach for SST-T and the predicted size and the strength of the secondary flow showed up to a 3X local increase in surface Nu due to the tip vortex. The SST-T simulations showed the tip vortex extending 50% further into the flowpath than the IDDES-T results. When the blade inlet TI was set to 0% the SST-T tip vortex better matched the IDDES-T tip vortex structure. This showed the sensitivity and impact of the TI boundary condition for the SST-T modeling approach.

The vane IDDES-T predictions showed 3D flow field effects that contributed to a plane mass average increase of 0.76% in total pressure loss relative to the pitch-line case. Contribution of the passage vortex to the overall vane loss was clearly identified in contours of the total pressure and the vane exit. The blade normalized total pressure loss increased by 1.6% due to the 3D effects, largely driven by the tip vortex. This resulted in over a 2X increase in the mass average loss at the exit of the blade for the 3D geometry relative to the linear pitch-line geometry.

Lastly, for the 3D geometry, the aero-thermal uncertainty due to the IDDES-T or SST-T modeling approach was quantified. Based on the turbine stage efficiency, the $\Delta\eta_T$ between IDDES-T and SST-T was found to be 3%. The thermal impact was quantified by applying an energy balance to determine the internal vane or blade cooling flow variation due the predicted external heat flux. Assuming ΔT_c remains constant, the cooling flow rate is proportional to the change in surface heat flux necessary to maintain the same vane or blade bulk temperature. The vane and blade surface total area averaged heat flux is calculated from the IDDES-T and SST-T predictions. The total heat flux ratio for IDDES-T divided by the SST-T predictions are 0.95 for the vane and 0.71 for the blade. This results in a 5% and 29% uncertainty in cooling flow for the vane and the blade between the two modeling approaches, respectively.

Nomenclature

Upper-case Roman:

C	Airfoil true chord
C_{ax}	Airfoil axial chord
C_w	WALE SGS model constant
D	Diameter
F_{IDDES}	IDDES switching function
Go	Gortler number
H	Shape factor, δ^*/θ
L_e	Dissipation turbulent length scale, k/e
L_I	Integral turbulent length scale
M	Mach number
Nu	Nusselt number
P	Pressure
St	Strouhal number
Re	Reynolds number
R_x	Stage reaction
R_{zz}	Spanwise velocity correlation function
S	Span or Local strain rate invariant, $(2S_{ij}S_{ij})^{1/2}$
S_{ij}	Strain rate tensor, $0.5\left(\partial U_i/\partial x_j + \partial U_j/\partial x_i\right)$
$\widetilde{S}_{ij}$	Favre averaged or LES Favre filter strain rate tensor, $0.5\left(\partial \widetilde{U}_i/\partial x_j + \partial \widetilde{U}_j/\partial x_i\right)$
T	Temperature
TI	Turbulence intensity, $(2k/3)^{1/2}/U_{ref}$
$\boldsymbol{U}$	Velocity magnitude
U	Axial velocity or wheel speed
U_∞	Free-stream velocity or velocity at edge of boundary layer
U_n	Wall normal velocity
V	Pitch velocity parallel to the inlet flow plane
W	Spanwise velocity

Lower-case Roman:

c_p	Specific heat at constant pressure
f	Frequency
g	Airfoil pitch
h	Heat transfer coefficient or enthalpy
k	Turbulent kinetic energy, $(u_i u_i)/2$
n	Normal component
o	Airfoil throat
q	Heat flux
u	Fluctuating axial velocity $u = U - \langle U \rangle$
u_τ	Shear velocity, $\sqrt{\tau_w/\rho}$
u'	RMS velocities
$u+$	Velocity wall coordinates, u/u_τ
r	Radial coordinate from engine centerline
s	Surface distance
t	Time
v	Fluctuating pitch velocity, parallel to the inlet flow plane
w	Fluctuating spanwise velocity
x	Axial coordinate normal to the inlet flow plane
y	Pitch coordinate, parallel to the inlet flow plane
$y+$	Distance in wall coordinates, $\rho y \mu_\tau / \mu$
z	Spanwise coordinate

Symbols:

$\langle U \rangle$	Mean of axial velocity
$\langle U \rangle_z$	Spanwise average of Mean of axial velocity
$\overline{U}$	Reynolds averaged or LES filter (resolved) axial velocity
$\widetilde{U}$	Favre averaged or LES favre filter (resolved) axial velocity
$+$	Wall units

Δx	Grid spacing
Δ_{SGS}	Explicit SGS filter size
α	Absolute frame flow angle
β	Relative frame flow angle
ε	Turbulence dissipation
δ	Velocity boundary layer thickness
δ_T	Thermal boundary layer thickness
δ^*	Displacement thickness
η_t	Turbine stage efficiency
γ	Ratio of specific heats
κ	von Karman constant
μ	Molecular viscosity
μ_t	Turbulent eddy viscosity
μ_{SGS}	SGS Eddy viscosity
ϕ	Scalar or Flow coefficient
$\overline{\phi}$	Reynolds averaged component, $\overline{\phi} = \phi - \phi'$
$\widetilde{\phi}$	Favre averaged component, $\widetilde{\phi} = \phi - \phi$"
ϕ'	Reynolds decomposition fluctuating component
ϕ"	Favre Reynolds decomposition fluctuating component
ρ	Density
τ_R	Rotational Mach number
τ_{ij}	Stress tensor, $\mu\left(\partial U_i/\partial x_j + \partial U_j/\partial x_i - 2/3 \cdot \partial U_k/\partial x_k \delta_{ij}\right)$
θ	Momentum thickness or circumferential angle component
ω	Specific turbulence dissipation rate
Ω	Local rate of rotation invariant, $\left(2\Omega_{ij}\Omega_{ij}\right)^{1/2}$
Ω_{ij}	Rate of rotation, $0.5\left(\partial U_i/\partial x_j - \partial U_j/\partial x_i\right)$

Subscripts:

ax	Axial
b	Blade

bl	Along the line true chord
c	Coolant value
n	Wall normal direction
is	Isentropic
r	Relative frame
t	Total or stagnation
v	Vane
1	Inlet to vane
2	Outlet to nozzle/Inlet to blade
3	Outlet of blade
∞	Freestream

Abbreviations:

2DSM	Two-dimensional linear sliding mesh
3D	Three-dimensional
3DSM	Three-dimensional annular sliding mesh
BL	Boundary layer
BO	Blade only domain
CBC	Convection boundedness criterion
FD	Finite difference
GT	Gas turbine
HPT	High pressure turbine
HTC	Heat transfer coefficient
IDDES	Improved delayed detached eddy simulation
IDDES-T	IDDES with $\gamma - Re_\theta$ transition model
KL	Kato-Launder
LE	Leadedge
LES	Large eddy simulation
LPT	Low pressure turbine
NVD	Normalized variable diagram

PL	Production limiter
PS	Pressure-side
RANS	Reynolds averaged Navier-Stokes
SGS	Subgrid scale
SS	Suction-side
SST	Shear stress transport
SST-T	SST with $\gamma - Re_\theta$ transition model
TE	Trailing edge
TKE	Turbulent kinetic energy
TI	Turbulence intensity
URANS	Unsteady Reynolds averaged Navier-Stokes
VO	Vane only domain
WALE	Wall Adapted Local Eddy

Appendix A

RANS Modeling Coefficients

Table A.1. RANS modeling coefficients for compressible flow

$k-\omega$	Value	SST	Value
α_o	1/9	α_o	1/9
α_∞	0.52	α_∞	0.52
α^*_∞	1/9	$\beta_{i,1}$	0.075
β_i	0.072	$\beta_{i,2}$	0.0828
β^*_∞	0.09	β^*_∞	0.09
σ_k	2.0	κ	0.41
σ_ω	2.0	$\sigma_{k,1}$	1.176
ζ^*	1.5	$\sigma_{k,2}$	1.0
R_β	8.0	$\sigma_{\omega,1}$	2.0
R_k	6.0	$\sigma_{\omega,2}$	1.168
R_ω	2.95	ζ^*	1.5
M_{to}	0.25	a_1	0.31
–	–	R_β	8.0
–	–	R_k	0.61
–	–	R_ω	2.95
–	–	M_{to}	0.25

Appendix B

Stage Design

A downstream blade is designed for this study to be coupled with the upstream uncooled vane of Arts et al. [34]. An overview of the stage design is provided in this section. The pitch-line blade design will be referred to as PBD02 (Pitch-line Blade Design 02) and 3D blade design is 3BD02 (3D Blade Design 02). Primary references for this design are the VKI BRITE EURAM TATEF Project [91] and transonic single turbine stage (TTM-Stage) BRITE EURAM DITTUS Project [92]. For brevity, the two projects will be referred to as VKI BRITE and TTM BRITE, respectively. The VKI BRITE geometry is not fully disclosed; however, the overall conditions and non-dimensional geometry can be inferred from Denos et al. [91]. The TTM BRITE project fully discloses the conditions and geometry and can be found in Erhart [92]. The design points for both references are transonic turbine designs. The current design varies from the primary reference cases for the following reasons:

- Desired to pursue passage Mach numbers < 1 to avoid numerical complexities for transonic flow [93]. Therefore, requiring a lower stage pressure ratio.
- Blade/Vane count of 2:1 to maintain computational periodic boundary conditions.
- Given the blade loading coefficient of 0.6, the stage reaction was increased closer to 0.5 to obtain peak stage efficiency [88].
- The blade axial chord was set to meet an optimal value based on Zweifel's criteria. A Zweifel number of approximately 0.8 is found to correlate with

minimal loss [88].

The 2D computational stage domain is held to a pitch-line section that includes no centrifugal forces. The stage geometry is intended to study the fundamental vane/blade interaction in a computationally cost efficient manner. To achieve the above design criteria, a 2D stage analysis is performed. The analysis procedure and defining design parameters, as described by Dixon [88], are briefly discussed below.

Descriptions of the vane/blade stations are provided in Figure B-1. Station 1 is located at the LE of the vane and station 3 is located at the TE of the blade. The non-dimensional parameters used for the stage design are the following:

- Loading coefficient:

$$\psi = \frac{\Delta H}{2U^2} \tag{B.1}$$

- Zweifel number:

$$\Psi_\tau = 2\left(\frac{g}{C_{ax}}\right)\cos\left(\alpha_2\right)^2\left(\tan\alpha_1 + \alpha_2\right) \tag{B.2}$$

  For the blade $\alpha_1 \rightarrow \beta_2$ and $\alpha_2 \rightarrow \beta_3$

- Stage Reaction:

$$R_x = \frac{h_2 - h_3}{h_{o1} - h_{o3}} \tag{B.3}$$

- Flow coefficient:

$$\phi = \frac{C_{x3}}{U} \tag{B.4}$$

- Blade Rotational Mach number:

$$\tau_R = \frac{U}{\sqrt{\gamma R T_3}} \tag{B.5}$$

Condition MUR129 from Arts and Rouvroit [34] was selected as the vane design operating point in order to satisfy the subsonic Mach number criteria. Table B.1 compares vane conditions to the reference designs. The Reynolds number is in close agreement with the VKI BRITE. Knowing the flow conditions for the vane exit, velocity vector diagrams are used to initial design the downstream blade. Table B.2 provides the PBD02 blade's design and conditions achieved by following the design

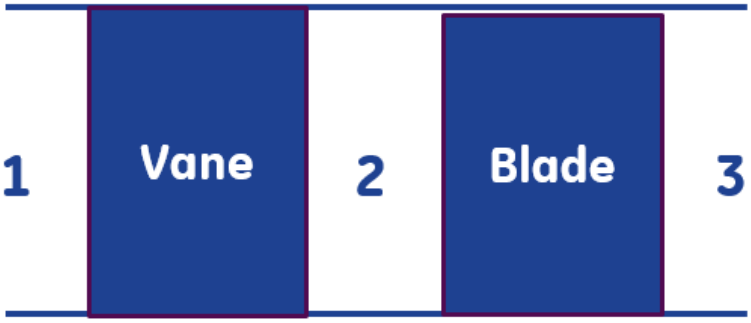

Figure B-1. HPT stage station diagram.

criteria for this study. Similar to the vane, the Reynolds number of the PBD02 blade is consistent to the VKI BRITE.

Table B.1. Vane design parameters.

Vane	TTM BRITE	VKI BRITE	Arts et al. [34]
Turning (deg)	68	74	75
Zweifel (Ψ_τ)	0.74	0.67	0.78
Exit Mach (M_2)	1.15	1.05	0.84
$Re_{C,2}$	2.5×10^6	1.0×10^6	1.1×10^6
$Re_{TE,2}$	5.2×10^4	2.5×10^4	2.4×10^4

Table B.2. PBD02 Blade design parameters.

Blade	TTM BRITE	VKI BRITE	PBD02
Turning (deg)	102	117	101
Zweifel (Ψ_τ)	1.01	1.01	0.82
Exit Mach $M_{r,3}$	0.99	0.92	0.82
$Re_{C,3}$	1.2×10^6	4.6×10^5	5.1×10^5
$Re_{TE,3}$	4.0×10^4	1.6×10^4	1.5×10^4
Flow Coef. (ϕ)	0.59	0.51	0.42
Rot. Mach (τ_R)	0.75	0.70	0.70

After completing the 2D stage design at the selected stage operating condition, a blade profile must be determined in an iterative manner. The blade was designed to have favorable loading characteristics by minimizing adverse pressure gradients and providing negligible turning after the throat to avoid flow deviation from the desired exit angle [88]. Multiple iterations were performed on the blade using steady RANS

with the SST model to achieve the final shape. After completion of the 2D design the approach was extrapolated to a 3D geometry. The vane of Arts and Rouvroit [34] is linearly stacked with the addition of constant radius end-wall to the computational domain. The 50% span of the 3D vane and blade airfoil geometries are matched to the pitch-line case PSD02. The 2D linear blade speed is matched to the 3D blade's pitch-line tangential speed in order to isolate and study the impact of rotational effects. The blade geometry varies hub to tip to adjust for the variable inlet flow angle. Therefore the blade mechanical incidence angle is decreasing with increasing radius to account for the blade's relative flow incidence angle. Coordinates for both the 2D and 3D designs are found in Table B.3.

The vane to blade axial gap has been set to $X_{gap}/C_{ax} = 0.35$, where C_{ax} is based on the vane axial chord. Computational studies by Denos et al. [91] on the VKI BRITE geometry increased X_{gap}/C_{ax} from 0.35 to 0.5 highlighting the decrease in amplitude of the fluctuations near the blade leading edge region. The author has decided to focus on $X_{gap}/C_{ax} = 0.35$ spacing providing a stronger impact on the blade flow conditions due to the proximity to the upstream vane wake. The final 2D (PBD02) and 3D (3BD02) blade geometry is provided in Table B.4.

B.1 CFD Boundary Conditions

Simulations with the PSD02 and 3SD02 geometries were completed in Chapter 7 and 8, respectively. Sliding mesh domain were used for IDDES-T and WALE. Blade-only (BO) and vane-only (VO) domains were used for SST and SST-T simulations. The domain summary is provided in Table B.5.

Boundary conditions for the RANS VO runs are provided in Table B.6. The BO inlet boundary conditions come from the VO plane mass averaged mixed out conditions for momentum, enthalpy, and turbulence for the 2D pitch-line PBD02 geometry. The 3BD02 geometry inlet conditions use circumferentially averaged radial profiles. These conditions are provided in Table B.7. Final, the IDDES-T and WALE sliding mesh boundary conditions are provided in Table B.8.

Table B.3. 2DSM (PBD02) and 3DSM (3BD02) blade Coordinates in mm.

2DSM		3DSM (90% Span)			3DSM (50% Span)			3DSM (10% Span)		
X	Y	X	Y	Z	X	Y	Z	X	Y	Z
80.56	-31.52	79.15	-47.76	383.42	79.34	-44.74	363.32	80.57	-42.77	343.09
80.09	-32.73	78.15	-49.78	383.16	78.69	-45.85	363.18	80.09	-43.96	342.94
79.41	-34.47	76.47	-52.93	382.74	77.86	-47.23	363.01	79.42	-45.60	342.72
78.25	-37.34	74.40	-56.33	382.26	76.71	-49.07	362.76	78.54	-47.68	342.44
76.81	-40.79	72.26	-59.23	381.82	74.98	-51.65	362.40	77.35	-50.35	342.06
75.20	-44.54	69.18	-62.45	381.31	72.45	-54.94	361.92	75.70	-53.77	341.54
73.45	-48.32	66.26	-64.62	380.94	69.07	-58.40	361.38	73.52	-57.80	340.88
71.54	-51.97	63.10	-66.30	380.65	65.57	-60.92	360.96	71.30	-61.34	340.26
69.49	-55.29	59.86	-67.59	380.43	61.36	-62.88	360.62	68.46	-64.93	339.59
66.87	-58.23	56.69	-68.71	380.23	57.29	-64.07	360.41	65.32	-67.60	339.07
63.63	-60.24	53.29	-69.96	380.00	53.69	-64.95	360.26	61.01	-69.29	338.73
59.79	-61.06	50.64	-71.86	379.64	50.73	-66.50	359.97	56.84	-69.03	338.78
55.78	-60.33	51.54	-75.29	378.98	51.27	-70.09	359.29	53.42	-67.28	339.13
53.18	-58.72	54.75	-77.71	378.49	53.66	-72.48	358.82	51.11	-64.60	339.66
51.39	-56.71	57.95	-78.73	378.28	57.26	-74.14	358.48	50.64	-61.27	340.27
50.43	-54.29	61.31	-78.71	378.28	61.14	-74.35	358.43	53.58	-59.31	340.62
51.84	-51.96	64.67	-77.53	378.53	64.80	-73.12	358.69	57.54	-58.54	340.75
54.40	-51.17	67.77	-75.14	379.01	68.23	-70.34	359.24	62.02	-57.46	340.94
57.60	-50.44	70.15	-72.15	379.59	70.87	-66.72	359.93	65.93	-55.84	341.21
61.62	-49.24	72.11	-68.76	380.22	72.88	-63.09	360.59	69.73	-53.38	341.60
65.73	-47.36	73.69	-65.43	380.81	74.68	-59.37	361.22	72.72	-50.62	342.02
69.33	-44.66	75.07	-62.20	381.35	76.65	-54.97	361.91	75.04	-47.94	342.41
72.34	-41.46	76.67	-58.21	381.98	78.03	-51.69	362.40	76.69	-45.79	342.70
74.76	-38.35	78.16	-54.32	382.55	78.99	-49.32	362.73	77.91	-44.11	342.92
76.81	-35.24	79.48	-50.77	383.03	79.73	-47.44	362.98	78.81	-42.86	343.08
78.08	-33.09	80.32	-48.47	383.33	80.29	-46.02	363.16	79.49	-41.88	343.20
78.94	-31.61	80.88	-46.95	383.52	80.71	-44.92	363.30	79.82	-41.42	343.25
79.53	-30.57	80.91	-46.87	383.53	80.91	-44.40	363.36			

Table B.4. 2D and 3D stage geometry summary.

Geometry	PBD02	3BD02
Vane Cax [mm]	36.8	36.8
Blade Cax [mm]	30.6	30.6
Stage Gap [mm]	13.6	13.6
Blade Tip Gap [mm]	N/A	0.508
Airfoil Fillet Radius [mm]	N/A	1.016
Passage Height [mm]	N/A	50.8

Table B.5. Domain summary.

Nomenclature	Geomerty	Periodic
2DVO	2-D Vane-Only	Linear
2DBO	2-D Blade-Only	Linear
2DSM	2-D Sliding Mesh	Linear
3DVO	3-D Vane-Only	Rotational
3DBO	3-D Blade-Only	Rotational
3DSM	3-D Sliding Mesh	Rotational

Table B.6. Vane-only boundary conditions.

Vane	2DVO	3DVO
P_{t1} [kPa]	184.9	184.9
T_{t1} [K]	409	409
k $[m^2/s^2]$	0.34	0.34
ω [1/s]	355	355
Inlet Flow [deg]	0	0
T_{wall} [K]	300	300
P_{s2} [kPa]	116.5	3DSM Radial Profile (Avg=115)

Table B.7. Blade-only SST and SST-T boundary conditions for no vane inlet TI (MUR129).

Blade	2DBO	3DBO
P_{tr2} [kPa]	2DVO (122.0)	3DVO Radial Profile (Avg=121.2)
T_{tr2} [K]	2DVO (363)	3DVO Radial Profile (Avg=363)
Inlet Flow [deg]	2DVO (33.4)	3DVO Radial Profile (Avg=30.8)
k $[m^2/s^2]$	2DVO (50)	3DVO Radial Profile (Avg=59)
ω [1/s]	2DVO (2.9E5)	3DVO Radial Profile (Avg=2.9E5)
T_{wall} [K]	300	300
P_{s3} [kPa]	78.6	78.6

Table B.8. Sliding mesh LES and HLES boundary conditions.

Sliding Mesh	2DSM	3DSM
P_{t1} [kPa]	184.9	184.9
T_{t1} [K]	409	409
Inlet Flow	0	0
T_{wall} [K]	300	300
P_{s3} [kPa]	78.6	78.6
Blade Speed	250 [m/s]	683 [rad/s]

Bibliography

[1] Bureau of Transportation Statistics, 2015. United States Department of Transportation. Office of the assistant secretary for research and technology. `www.transtats.bts.gov/fuel.asp`

[2] Federal Aviation Administration, June 2014. The economic impact of civil aviation on the US economy.

[3] Boeing, 2014. Current market outlook 2014.

[4] GEA, 2014. Taps II combustor, Final report. United States Department of Transportation. Federal Aviation Administration.

[5] Federal Aviation Administration, 2015. Continuous lower energy, emissions, and noise (CLEEN) program. `www.faa.gov/`

[6] Seventh Framework Programme, 2015. Insight on combustor-turbine interactions. `www.factor-fp7.eu/`

[7] Bunker, R., 2005. "A review of shaped hole turbine film-cooling technology". *Journal of Heat Transfer,* ***127***, pp. 441–453.

[8] Wilcock, R., Young, J., and Horlock, J., 2005. "The effect of turbine blade cooling on the cycle efficiency of gas turbine power cycles". *Journal of Engineering for Gas Turbines and Power,* ***127***, pp. 109–120.

[9] Slotnick, J., Khodadoust, A., Alonso, J. Darmofal, D., Gropp, W., Lurie, E., and Mavriplis, D., 2014. CFD vision 2030 study: A path to revolutionary computational aerosciences. Tech. rep., NASA.

[10] Martins, J., and Lambe, A., 2013. "Multidisciplinary design optimization: A survey of architecture". *AIAA Journal,* ***51***, pp. 2049–2075.

[11] Zlatinov, M., and Laskowski, G., 2015. "Hybrid large-eddy simulation optimization of a fundamental turbine blade turbulated cooling passage". *Journal of Propulsion and Power,* ***31***, pp. 1292–1297.

[12] Levy, D., Laflin, K., Tinoco, E., Vassberg, J., Mani, M., Rider, B., Rumsey, C., and Wahls, R., 2012. "Summary of data form the fifth aiaa CFD drag prediction workshop". *50th AIAA Aerospace Science Meeting, Nashville, TN, January 2012.*

[13] Claus, R., Townsend, S., Carney, D., Horowita, J., and Turner, M., 2006. "A case study of high fidelity engine system simulation". *42nd AIAA/ASME/SAE/ASEE Joint Propulsion Conference, Sacramento, CA, July 2006*.

[14] Tinoco, E., Bogue, D., Kao, T.-J., Yu, N., Li, P., and Ball, D., 2005. "Progress toward CFD for full flight envelope". *The Aeronautical Journal*, pp. 451–460.

[15] Medic, G., Joo, J., Lele, S., and Sharma, O., 2012. Prediction of heat transfer in a turbine cascade with high levels of free-stream turbulence. Tech. rep., Center for Turbulence Research, Stanford, CA.

[16] Collado Morata, E., Gourdain, N., Duchaine, F., and Gicquel, L., 2012. "Effects of free-stream turbulence on high pressure turbine heat transfer predicted by structured and unstructured LES". *International Journal of Heat and Mass Transfer,* ***55***, Jan., pp. 5754–5768.

[17] Kopriva, J., Laskowski, G., and Sheikhi, M. R. H., 2013. "Assessment of high pressure cooled and uncooled turbine blade wakes via RANS and URANS at engine scale conditions". *ASME Turbo Expo, San Antonio, TX, June 2013*.

[18] Stock, H., and Haase, W., 2006. "Navier-stokes airfoil computations with en transition prediction including transitional flow regions". *AIAA Journal,* ***38***, pp. 2059–2066.

[19] Langtry, R., and Menter, F., 2009. "Correlation-based transition modeling for unstructured parallelized computational fluid dynamics codes". *AIAA Journal,* ***47***, pp. 2894–2906.

[20] Langtry, R., Menter, F., Likki, S., Suzen, Y., Huang, P., and Volker, S., 2006. "A correlation-based transition model using local variables-part II: Test cases and industrial applications". *Journal of Turbomachinery,* ***128***, pp. 423–432.

[21] ANSYS, 2014. Solver Theory Guide release 15.

[22] Arts, T., Rouvroit, M., and Rutherford, A., 1990. Aero-thermal investigation of a highly loaded transonic linear turbine guide vane cascade. Tech. rep., von Karman Institue for Fluid Dynamics, Belgium.

[23] Bunker, R., 2008. Gas turbine engines: Turbine cooling 2008. Tech. rep., GE Global Research Center Class 1 Report, Niskayuna, NY.

[24] Barringer, M. D., Richard, O. T., Walter, J. P., Stitzel, S. M., and Thole, K. A., 2002. "Flowfield simulations of a gas turbine combustor". *Journal of Turbomachinery,* ***124***, pp. 508–516.

[25] Giel, P., Bunker, R., van Fossen, G., and Boyle, R., 2000. "Heat transfer measurements and predictions on a power generation gas turbine blade". *ASME Turbo Expo, Munich, Germany, May 2000*.

[26] Polanka, M., 1999. "Detailed film cooling effectiveness and three component velocity field measurements on a first stage turbine vane subject to high freestream turbulence". Ph.D. Thesis, Department of Mechanical Engineering, University of Texas at Austin, Austin, TX.

[27] Thole, K., Bogard, D., and Whan-Tong, J., 1994. "Generating high freestream turbulence levels". *Experiments in Fluids,* ***17***, pp. 375–380.

[28] Mayle, R., 1991. "The role of laminar-turbulent transition in gas turbine engines". *Journal of Turbomachinery,* ***113***, pp. 509–537.

[29] Mee, D., Baines, N., and Oldfield, L., 1990. "An examination of the contributions to loss on a transonic turbine blade in a cascade". *Journal of Turbomachinery,* ***114***, pp. 155–162.

[30] Rehder, H.-J., 2012. "Investigation of trailing edge cooling concepts in a high pressure turbine cascade - aerodynamic experiments and loss analysis". *Journal of Turbomachinery*, p. 051029.

[31] Sieverding, C., and Heinemann, H., 1990. "The influence of boundary layer state on vortex shedding from flat plates and turbine cascades". *Journal of Turbomachinery,* ***112***, pp. 181–187.

[32] Cicatelli, G., and Sieverding, C., 1997. "The effect of vortex shedding on the unsteady pressure distribution around the trailing edge of a turbine blade". *Journal of Turbomachinery,* ***119***, pp. 810–819.

[33] Sieverding, C., Rischard, H., and Desse, J., 2003. "Turbine blade trailing edge flow characteristics at high subsonic outlet mach number". *Journal of Turbomachinery,* ***125***, pp. 298–309.

[34] Arts, T., and Rouvroit, M., 1992. "Aero-thermal performance of a two-dimensional highly loaded transonic turbine nozzle guide vane: A test case for inviscid and viscous flow computations". *Journal of Turbomachinery,* ***114***, pp. 147–154.

[35] Bhaskaran, R., 2010. "Large eddy simulation of high pressure turbine cascasde". Ph.D. Thesis, Department of Mechanical Engineering, University of Stanford, Stanford, CA.

[36] Wheeler, P., Sandberg, R., Pichler, R., Michelassi, V., and Laskowski, G., 2015. "Direct numerical simulations of a high-pressure turbine vane". *ASME Turbo Expo, Montreal, Canada, May 2015.*

[37] Pichler, R., Kopriva, J., Michelassi, V., Sandberg, R., and Laskowski, G. M., 2016. "Highly resolved LES of a linear HPT vane cascade using structured and unstructured codes". *ASME Turbo Expo, Seoul, South Korea, June 2016.*

[38] Nix, A., 2003. "Effects of high intensity, large-scale freestream combustor turbulence on heat transfer in transonic turbine blades". Ph.D. Thesis, Department of Mechanical Engineering, Virginia Polytechnic Institute and Stage University.

[39] Radomsky, R., and Thole, K., 2002. "Detailed boundary layer measurements on a turbine stator vane at elevated freestream turbulence levels". *Journal of Turbomachinery,* ***124***, pp. 107–118.

[40] Dees, J., Bogard, D., Ledezma, G., and G., L., 2013. "Overall and adiabatic effectiveness values on a scaled up, simulated gas turbine vane: Part I - experimental measurements". *Journal of Turbomachinery,* ***135***, p. 051017.

[41] Laskowski, G., Ledezma, G., Tolpadi, A., and Ostrowski, M., 2008. "CFD simulations and conjugate heat transfer analysis of a high pressure turbine vane utilizing different cooling configurations". *ISROMAC-12 Conference, Honolulu, HI, February 2008.*

[42] Ou, S., and Han, J. C., 1994. "Unsteady wake effect on film effectiveness and heat transfer coefficient from a turbine blade with one row of air and CO2 film injection". *Journal of Turbomachinery,* ***116***, pp. 921–928.

[43] Didier, F., Denos, R., and Arts, T., 2002. "Unsteady rotor heat transfer in a transonic turbine stage". *Journal of Turbomachinery,* ***124***, pp. 614–622.

[44] Sharma, O., Pickett, G., and Ni, R., 1992. "Assessment of unsteady flows in turbines". *Journal of Turbomachinery,* ***114***, pp. 79–90.

[45] Wang, G., Papadogiannis, D., Duchaine, F., N., G., and Gicquel, L., 2013. "Towards massively parallel large eddy simulation of turbine stages". *ASME Turbo Expo, San Antonio, TX, June 2013.*

[46] Kopriva, J., Laskowski, G., and Sheikhi, M. R. H., 2015. "Hybrid LES of a high pressure turbine". *ERCOFTAC Workshop DLES 10, Limassol, Cyprus, May 2015.*

[47] Kopriva, J., Laskowski, G., and Sheikhi, M. R. H., 2014. "Computational assessment of inlet turbulence on boundary layer development and momentum/thermal wakes for high pressure turbine vanes and blade at engine scale conditions". *ASME IMECE, Montreal, Canada, November 2014.*

[48] Talnikar, C., Wang, Q., Kopriva, J., and Laskowski, G. M., 2016. "Future directions of high-fidelity CFD for aero-thermal turbomachinery research, analysis and design". *46th AIAA Fluid Dynamics Conference, Washington, DC, June 2016.*

[49] Bhaskaran, R., Jia, F., Laskowski, G., Wang, Z., and Paliath, U., 2017. "Towards high-order large eddy simulation of aero-thermal flows for turbomachinery applications". *ASME Turbo Expo, Charlotte, NC, June 2017.*

[50] Wang, Z., Li, Y., Jia, F., Laskowski, G. M., Kopriva, J., Paliath, U., and Bhaskaran, R., 2017. "Recent progresses in large eddy simulation with the FR/CPR method". *Computer and Fluids*.

[51] Talnikar, C., Wang, Q., Kopriva, J., and Laskowski, G. M., 2017. "Unsteady adjoint for coupled large eddy simulation of a turbine vane-blade". *ASME Turbo Expo, Charlotte, NC, June 2017*.

[52] Kopriva, J., and Laskowski, G., 2017. "Hybrid large eddy simulations of an uncooled high pressure turbine stator-rotor stage". *European Turbomachinery Conference, Stockholm, Sweden, May 2017*.

[53] Wilcox, D., 2006. *Turbulence Modeling for CFD*. DCW Industries, Incorporated, La Canada, CA.

[54] Menter, F., 1993. "Zonal two equation k-w turbulence models for aerodynamic flows". *24th AIAA Fluid Dynamics Conference, Orlando, FL, July 1993*.

[55] Menter, F., 1994. "Two-equation eddy-viscosity turbulence models for engineering applications". *AIAA Journal,* ***32***, pp. 1598–1605.

[56] Nicoud, F., and Ducros, F., 1999. "Subgrid-scale stress modeling based on the square of the velocity gradient tensor". *Flow, Turbulence, and Combustion,* ***62***, pp. 183–200.

[57] Shur, M., Spalart, P., Strelets, M., and Travin, A., 2008. "A hybrid RANS-LES approach with delayed-DES and wall-modelled LES capabilities". *International Journal of Heat and Fluid Flow,* ***29***, pp. 1638–1649.

[58] Chapman, D., 1979. "Computational aerodynamics development and outlook". *AIAA Journal,* ***17***, pp. 1293–1313.

[59] Piomelli, U., Balaras, E., Pasinato, H., Squires, K., and Spalart, P., 2003. "The inner-outer layer interface in large-eddy simulations with wall-layer models". *Heat and Fluid Flow,* ***24***, pp. 538–550.

[60] Menter, F., Langtry, R., Likki, S., Suzen, Y., Huang, P., and Volker, S., 2006. "A correlation-based transition model using local variables-part I: Model formulation". *Journal of Turbomachinery,* ***128***, pp. 413–422.

[61] Winoto, S., 1991. "The ULTIMATE conservative difference scheme applied to unsteady one-dimensional advection". *Computer Methods in Applied Mechanics and Engineering,* ***88***, pp. 17–74.

[62] Durbin, P., 2011. *Statistical Theory and Modeling for Turbulent Flows*. Wiley, Cambridge, UK.

[63] Tavoularis, S., and Corrsin, S., 1981. "Experiments in nearly homogeneous turbulent shear flow with a uniform mean temperature gradient. Part 1". *Journal of Mechanics,* ***104***, pp. 311–347.

[64] Tucker, H., 1970. "The distortion of turbulence by irrotational strain". Mechanical engineering 70-7, McGill University.

[65] Kato, M., and Launder, B. E., 1993. "The modeling of turbulent flow around stationary and vibrating square cylinders". *Proceeding of the 9th Symposium on Turbulent Shear Flows, Kyoto, Japan, August 1993.*

[66] Grinstein, F., Margolin, L., and Rider, W., 2007. *Implicit Large Eddy Simulation.* Cambridge University Press.

[67] Li, Y., and Wang, Z., 2016. "A priori and a posteriori evaluations of sub-grid scale models for the burgers' equation". *Computers and Fluids,* ***139***, pp. 92–104.

[68] Frohlich, J., and von Terzi, D., 2008. "Hybrid LES/RANS methods for the simulation of turbulent flows". *Progress in Aerospace Sciences,* ***44***, pp. 349–377.

[69] Mentor, F., 2015. Best Practice: Scale-Resolving Simulations in ANSYS CFD.

[70] Gritskevich, M., Garbaruk, A., and Menter, F., 2003. "Fine-tuning of DDES and IDDES formulations to the k-w shear stress transport model". *Progress in Flight Physics,* ***5***, pp. 23–42.

[71] Konstantinidis, E., Balabani, S., and Yianneskis, M., 2003. "The effect of flow perturbations on the near wake characteristics of a circular cylinder". *Journal of Fluid Structures,* ***18***, pp. 367–368.

[72] Konstantinidis, E., Balabani, S., and Yianneskis, M., 2005. "Conditional averaging of PIV plane wake data using a cross-correlation approach". *Experimental Fluids,* ***39***, pp. 38–47.

[73] Mohammad, A., Wang, Z., and Liang, C., 2010. "Large eddy simulation of flow over a cylinder using high-order spectral difference method". *Advances in Applied Mathematics and Mechanics,* ***2***, pp. 451–466.

[74] Nakamura, H., and Igarashi, T., 2004. "Unsteady heat transfer from a circular cylinder for reynolds numbers from 3000 to 15,000". *International Jouranl of Heat and Fluid Flow,* ***25***, pp. 741–748.

[75] Bose, S., Wang, B., and Saeedi, M., 2012. Prediction of unsteady heat transfer from a cylinder in crossflow. Tech. rep., Center for Turbulence Research, Stanford, CA.

[76] Arts, T., 2014. Private Communication.

[77] Walter, D., and Cokljat, D., 2008. "A three-equation eddy-viscosity model for reynolds-averaged navier-stokes simulations of transitional flow". *Journal of Fluids Engineering,* ***130***, p. 121401.

[78] Chima, V., 1995. "A k-w turbulence model for quasi-three-dimensional turbomachinery flows". *NASA.*

[79] Kays, A., Crawford, M., and Weigand, B., 2005. *Convective Heat and Mass Transfer*. McGraw-Hill, New York.

[80] Ledezma, G., Bhaskaran, R., Laskowski, G. M., and Kopriva, J., 2017. "Large eddy simulation of a film cooled vane at different turbulence levels". *AIAA SciTech. Dallas, TX*.

[81] Gortler, H., 1955. "Dreidimensionales zur stabilitatstheorie laminarer grenzschichten". *Journal of Applied Mathematics and Mechanics,* ***35***, pp. 362–363.

[82] Saric, W., 1994. "Gortler vortices". *Annual Review of Fluid Mechanics,* ***26***, pp. 379–409.

[83] Winoto, S., 1983. "Qualitative investigation on goertler vortices". *8th Australasian Fluid Mechanics Conference, Newcastle, New South Wales, November 1983*.

[84] Launder, B., and Lockwood, F., 1969. "An aspect of heat transfer in accelerating turbulent boundary layers". *Journal of Heat Transfer,* ***91***, pp. 229–234.

[85] Sucec, J., and Lu, J., 1990. "Heat transfer across turbulent boundary layers with pressure gradients". *Journal of Heat Transfer,* ***112***, pp. 906–912.

[86] White, F., 1974. *Viscous Fluid Flow*. McGraw-Hill, New York.

[87] Dees, J., 2010. "Experimental measurements of conjugate heat transfer on a scaled-up gas turbine airfoil with realistic cooling configuration". Ph.D. Thesis, The University of Texas at Austin.

[88] Dixon, S. L., 1998. *Fluid Mechanics and Thermodynamics of Turbomachinery*. Butterworth-Heinemann.

[89] Pope, S., 2003. *Turbulent Flows*. Cambridge University Press, Cambridge, UK.

[90] Incropera, F., and DeWitt, D., 2006. *Fundamentals of Heat and Mass Transfer*. WILEY.

[91] Denos, R., Arts, T., Paniagua, V., Michelassi, V., and Martelli, F., 2000. "Investigation of the unsteady rotor aerodynamics in a transonic turbine stage". *Journal of Turbomachinery,* ***123***, pp. 81–89.

[92] Erhart, J., 2000. "Design, construction and commissioning of a transonic test-turbine facility". Ph.D. Thesis, Graz University of Technology.

[93] Tannehill, J. C., Anderson, D. A., and Pletcher, R. H., 1997. *Computational Fluid Mechanics and Heat Transfer*. Taylor and Francis, Philadelphia, PA, USA.